

A SEARCH FOR TOP QUARK DECAYS TO A CHARGED
HIGGS BOSON IN PROTON-ANTIPROTON COLLISIONS AT A
CENTER-OF-MASS ENERGY OF 1.8 TeV

Brendan Bevensee

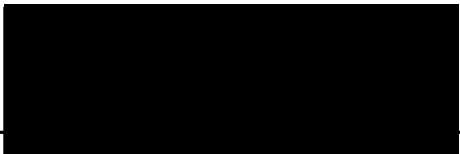
A DISSERTATION
in
PHYSICS AND ASTRONOMY

PRESENTED TO THE GRADUATE FACULTY OF THE UNIVERSITY OF
PENNSYLVANIA IN PARTIAL FULFILLMENT OF THE REQUIREMENTS FOR THE
DEGREE OF DOCTOR OF PHILOSOPHY

1999



Professor H.H. Williams
Supervisor of Dissertation



Professor Nigel Lockyer
Graduate Group Chairman

UMI Number: 9926097

UMI Microform 9926097
Copyright 1999, by UMI Company. All rights reserved.

**This microform edition is protected against unauthorized
copying under Title 17, United States Code.**

UMI
300 North Zeeb Road
Ann Arbor, MI 48103

Acknowledgements

I thank my advisor Brig Williams for his guidance and support during the past seven years, and also for giving me the freedom to pursue topics that I found interesting. I appreciate his warm friendship, enthusiasm for physics, and constant optimism. I am appreciative of all the Penn professors involved with CDF for creating an informal and stimulating environment for our group. Nigel Lockyer and Joe Kroll have always been very accessible for physics discussions and advice.

This thesis builds upon the work done by many other physicists. I thank the members of the Top Group and the Exotics Group at CDF who have constructively criticized this analysis. Rob Roser and Mark Kruse have been particularly helpful. I appreciate John Conway and David Stuart for monitoring my results and being supportive on many occasions.

Michelangelo Mangano has made many good recommendations for this analysis, and helped me understand many of the theoretical issues. Torbjörn Sjöstrand gave me a lot of good advice about simulating the charged Higgs signal using PYTHIA, and helped me alter his code.

I am also very grateful to Wasiq Bokhari, Fumi Ukegawa, and Guillaume Unal, for always being willing to discuss my analysis with me. I would like to thank Owen Long, Scott Metzler, Chris Holck, and Ed McKigney for being outstanding office mates, and for their generous friendship.

I have enjoyed interacting with the members of the Penn HEP Engineering Group during the past several years. I am extremely grateful to Mitch Newcomer and Rick Van Berg, unmatched stylists of instrumentation, for being so patient as they educated me.

On a personal note, I thank Jim Olsen for his friendship over the past 10 years,

and for all the fun we have had while learning physics together. I also want to thank Rad, Bill, Alex, Doug and the rest of my classmates, as well as Peter, Mark, Richard and Paul for their camaraderie. [REDACTED]

[REDACTED]

[REDACTED]

ABSTRACT

A SEARCH FOR TOP QUARK DECAYS TO A CHARGED HIGGS BOSON
IN PROTON-ANTIPROTON COLLISIONS
AT A CENTER-OF-MASS ENERGY OF 1.8 TeV

Brendan Bevensee

Advisor: H.H. Williams

In comparison to the standard model (SM), where the top quark decays to $W^\pm b$ almost exclusively, a large top quark branching fraction $\mathcal{B}(t \rightarrow H^\pm b)$ can suppress $t\bar{t}$ decay rates to dilepton final states, as well as lepton+jets final states. Furthermore, if the decay $H^\pm \rightarrow cs$ dominates, then the ratio of dilepton events to lepton+jets events will be much smaller than the SM value. However, the observed lepton+jets and dilepton event rates, and the observed ratio of these events, are consistent with $\mathcal{B}(t \rightarrow W^\pm b) = 1.0$.

At small values of $\tan\beta$, if the decay $H^\pm \rightarrow cs$ dominates, $\mathcal{B}(t \rightarrow H^\pm b) \leq 32\%$ at the 95% C.L. assuming the theoretical value $\sigma_{t\bar{t}} = 5.0$ pb. Without assuming a value for $\sigma_{t\bar{t}}$, I find that $\mathcal{B}(t \rightarrow H^\pm b) \leq 71\%$ at the 95% C.L. These results are valid if $M_{H^\pm} < 120$ GeV/ c^2 . At larger values of M_{H^\pm} , the three-body decay mode $H^\pm \rightarrow W^\pm b\bar{b}$ becomes dominant, preventing low- $\tan\beta$ limits to be set for $M_{H^\pm} > 140$ GeV/ c^2 .

At large values of $\tan\beta$, where $H^\pm \rightarrow \tau\nu$, $\mathcal{B}(t \rightarrow H^\pm b) \leq 36\%$ at the 95% C.L., if $M_{H^\pm} \leq 165$ GeV/ c^2 and $\sigma_{t\bar{t}} = 5.0$ pb. These high- $\tan\beta$ limits take into account a large H^\pm width.

These results are invalid for non-perturbative values of $\tan\beta$, and regions where the top quark width exceeds 15 GeV. They have been reviewed by the members of the CDF Collaboration, and presented by the author at several conferences [1, 2].

Contents

Acknowledgements	ii
Abstract	iv
List of Tables	xi
List of Figures	xiv
1 Introduction	1
1.1 Gauge Symmetries	1
1.2 The Higgs Field and Mass	4
1.3 The Charged Higgs Boson and the Top Quark	5
1.4 Search Strategy for a Charged Higgs Boson	11
1.4.1 Absolute Rate Method	12
1.4.2 Relative Rate Method	14
1.5 Thesis Overview	15
2 Theoretical and Experimental Framework	16
2.1 The Unbroken $SU(2)_L \times U(1)_Y$ Model	16
2.2 Hidden Symmetries and the Higgs Mechanism	19
2.3 The Minimal Standard Model	21
2.3.1 The Higgs Sector	22
2.3.2 The Gauge Boson Mass Spectrum	22
2.3.3 Yukawa Couplings - Masses for the Fermions . . .	24
2.4 The Two-Higgs-Doublet Extension to the SM	26

2.4.1	The Higgs Sector	26
2.4.2	Gauge Boson mass spectrum	28
2.4.3	The Yukawa Couplings of H^\pm to Fermions	30
2.5	Properties of the Top Quark Decay $t \rightarrow H^\pm b$	32
2.5.1	Decays of the Top Quark and the H^\pm	33
2.5.2	The Perturbative Range of $\tan\beta$	35
2.5.3	Large Top Quark and H^\pm Widths	36
2.6	Top Quark Production	38
2.7	Tevatron Top Quark Results	42
2.7.1	The Dilepton and Lepton+Jets Decay Modes	42
2.7.2	Cross Section Measurements	44
2.7.3	Top Mass Measurements	45
2.7.4	Kinematics of Events	47
2.8	Existing Limits for H^\pm Production	49
2.8.1	Direct Searches at the Tevatron and LEP2	49
2.8.2	Indirect Searches using $b \rightarrow s\gamma$	51
2.8.3	Indirect Searches using Other Low-Energy Processes	53
3	The CDF Detector	58
3.1	The Tevatron	58
3.1.1	Luminosity	60
3.2	An Overview of the CDF Detector	61
3.2.1	The CDF Coordinate System	63
3.3	The Tracking System	64
3.3.1	Silicon Vertex Detector (SVX)	65
3.3.2	Vertex Drift Chamber (VTX)	68
3.3.3	Central Tracking Chamber (CTC)	70

3.3.4	Track Reconstruction	73
3.4	Calorimeters and Jet Identification	73
3.4.1	The Central Electromagnetic Calorimeter (CEM)	75
3.4.2	The Central Hadronic Calorimeters (CHA and WHA)	79
3.4.3	Jet Identification	81
3.4.4	Jet Energy Corrections	82
3.4.5	Missing Energy (E_T) Measurement	83
3.5	Muon Chambers	84
3.6	Beam-Beam Counters and Luminosity	88
3.7	Trigger and Data Acquisition Systems	90
3.7.1	Level 1 Trigger	91
3.7.2	Level 2 Trigger	93
3.7.3	Data Acquisition	95
3.7.4	Level 3 Trigger and Raw Top Data Samples	97
4	Selection Criteria, SM Efficiencies, and Non- $t\bar{t}$ Backgrounds	100
4.1	The High- P_T Electron and Muon Samples	100
4.1.1	Electron Identification	101
4.1.2	Muon Identification	104
4.2	The Lepton+Jets Channel	107
4.2.1	The Primary Vertex	108
4.2.2	SECVTX - the Displaced Vertex Tagging Algorithm	109
4.2.3	Lepton+jets Selection Efficiency for $t\bar{t} \rightarrow WbW\bar{b}$	111
4.2.4	Non- $t\bar{t}$ Backgrounds in the Lepton+Jets Sample .	116
4.2.5	The Background for the Charged Higgs Analysis .	119
4.3	The Dilepton Channel	120

4.3.1	Dilepton Selection Efficiency for $t\bar{t} \rightarrow WbW\bar{b}$. . .	124
4.3.2	Non- $t\bar{t}$ Backgrounds in the Dilepton Sample	125
5	Modeling $t\bar{t}$ Events with H^\pm Decays	128
5.1	$H^\pm \rightarrow c\bar{s}$	129
5.2	$H^\pm \rightarrow W^\pm b\bar{b}$	129
5.3	$H^\pm \rightarrow \tau^\pm \nu$: Modeling Large Γ_H	134
5.4	Modeling a Large Top Quark Width	136
6	Selection Criteria Efficiency for the Signal	140
6.1	Regions in which Large Widths are Simulated	140
6.2	$t\bar{t}$ with $H^\pm \rightarrow cs$ or $\tau\nu$ Decays	142
6.2.1	Systematic Uncertainties	146
6.3	$t\bar{t}$ with $H^\pm \rightarrow W^\pm b\bar{b}$ Decays	149
6.4	$t\bar{t}$ with a Large H^\pm Width	150
6.5	$t\bar{t}$ with a Large Top Quark Width	154
6.6	The Total $t\bar{t}$ Efficiency - Dependence on M_{H^\pm} and $\tan\beta$	156
7	Limits using the Absolute Rate of Events	160
7.1	Assumptions	160
7.2	Methods for Combining the Channels	162
7.3	Method 1: Sum the Events from Each Channel	163
7.3.1	Correlated Systematic Errors	165
7.4	Method 2: Use a Product-of-Probabilities Approach . . .	169
7.5	Results	171
7.5.1	Features of the Limit Plots	174
7.5.2	Comparison to the $D\emptyset$ Limits	175

8	Limits using the Relative Rate of Events	177
8.1	Reconstructing $\sigma_{t\bar{t}}$	181
8.1.1	Trial-Experiments Method	181
8.1.2	Log-Likelihood Approach	182
8.2	Limits Using the Number of Dilepton Events	184
8.3	Results	185
9	Conclusion	187
9.1	Summary	187
9.2	Comparison to Indirect Searches	189
9.3	Effect of Radiative Corrections on the Limits	190
9.4	Prospects for Run II	191
9.5	Alternative Search Strategies	192
9.5.1	A Direct Search for $H^\pm \rightarrow cs$	193
9.5.2	Transverse Mass in Lepton+Jets Events	196
A	Partial Widths for the Top Quark and H^\pm	200
A.1	The H^\pm Partial Widths	200
A.2	The Top Quark Partial Widths	202
A.3	The m_b used for the QCD-Corrected $\Gamma_{t \rightarrow Hb}$	203
B	Yukawa Couplings for Higgs Bosons	207
B.1	Standard Model Higgs-Fermion Couplings	207
B.2	Couplings of the H^\pm to Fermions	209
C	The Fermilab Tevatron	212
C.1	Proton Acceleration	212
C.2	Antiproton Acceleration	216

C.3	$p\bar{p}$ Tevatron Collisions	219
D	The Decay Rate $\Gamma(t \rightarrow H^{+*} b \rightarrow \tau^+ \nu b)$	221
D.1	Setting up the Matrix Element	221
D.2	Evaluating the Traces	222
D.3	The Decay Rate	224
D.4	Phase Space	225
D.5	Predicted M_{H^\pm} Distribution	226
D.6	Cross Check - The Narrow Width Approximation	227
E	Numerical Values of Efficiencies for $t\bar{t}$ Events With H^\pm Decays	228
F	Cross Checks of Efficiencies for $t\bar{t}$ with $H^\pm \rightarrow cs, \tau\nu$ Decays	231
G	Systematic Errors for $t\bar{t}$ with H^\pm Decay	235
	Bibliography	239

List of Tables

1.1	The $t\bar{t}$ decay modes, their expected topologies, and their approximate branching fractions within the minimal SM.	8
1.2	The expected number of signal events from $t\bar{t}$ production in the top dilepton and lepton+jets channels, assuming only SM $t\bar{t}$ decays. . .	9
2.1	The $SU(2)_L \times U(1)_Y$ doublets and singlets within the SM.	18
2.2	Three theoretical calculations of $\sigma_{t\bar{t}}$, for $M_{\text{top}} = 175 \text{ GeV}/c^2$	41
2.3	The H^\pm limits at the 95% C.L. from the four LEP2 experiments. .	51
3.1	The luminosity from Run 1A and Run 1B.	61
3.2	Summary of the CDF calorimeter properties.	74
3.3	Summary of the ten Level 1 triggers.	92
3.4	Summary of Level 2 triggers for CMU and CMU-CMP muons used in the Run 1B top analyses.	95
3.5	Run 1B Level 3 triggers used to create the top samples.	99
4.1	The selection cuts for central electrons.	103
4.2	The selection cuts for muons.	106
4.3	SVX track quality cuts used by the SECVTX algorithm, the requirements for a good SVX cluster, and final cuts imposed on a displaced vertex.	110
4.4	The SM efficiencies for $t\bar{t}$ decays to satisfy the lepton+jets selection cuts.	113
4.5	Systematic errors in each channel for the product $\epsilon\mathcal{L}$	114

4.6	The expected number of background events, $t\bar{t}$ events, and the observed number of events, in each jet multiplicity bin of the lepton+jets channel.	117
4.7	The SM efficiencies for $t\bar{t}$ decays to satisfy the dilepton selection cuts.	124
4.8	The expected number of background events and $t\bar{t}$ events in the dilepton channel, compared with the observed number.	126
5.1	A comparison of the multiplicity of b -quarks that pass a set of kinematic cuts, for Monte Carlo $t\bar{t} \rightarrow WbH\bar{b}$ decays.	131
6.1	Efficiency of successive cuts in the lepton+jets channel, compared for $M_{H^\pm} = 80$ and $140 \text{ GeV}/c^2$	145
6.2	Efficiency of successive cuts in the dilepton channel, compared for $M_{H^\pm} = 80$ and $140 \text{ GeV}/c^2$	146
7.1	Correlated and uncorrelated systematic uncertainties in the $t\bar{t}$ efficiency.	165
7.2	The 95% C.L. limits assuming $\sigma_{t\bar{t}} = 5.0 \text{ pb}$ and 7.5 pb , for the two methods of combining the dilepton and lepton+jets channels. . . .	168
8.1	Limits derived from comparing the observed balance of dilepton and lepton+jets events, with the balance predicted within the two-Higgs-doublet model.	186
A.1	The QCD-corrected value of m_b , as a function of m_b , renormalization scale μ , and Λ	206
E.1	Efficiencies for $t\bar{t}$ with H^\pm decays in the lepton+jets channel. . . .	228
E.2	Efficiencies for $t\bar{t}$ with H^\pm decays in the lepton+jets channel. . . .	229
E.3	Efficiencies for $t\bar{t}$ with H^\pm decays in the lepton+jets channel. . . .	230

E.4	Efficiencies for $t\bar{t}$ with H^\pm decays in the lepton+jets channel. . . .	230
F.1	Comparison of lepton+jets channel efficiencies for $t\bar{t}$ topologies with H^\pm decays, and efficiencies for the same decay modes where the W^\pm boson replaces the H^\pm	232
F.2	Comparison of dilepton channel efficiencies for $t\bar{t}$ topologies with H^\pm decays, and efficiencies for the same decay modes where the W^\pm boson replaces the H^\pm	232
G.1	Systematic errors in each channel for the product $\epsilon\mathcal{L}$	235
G.2	Differences in $t\bar{t}$ efficiencies between the extremes of no initial-state radiation and no final-state radiation.	236
G.3	The change in $t\bar{t}$ efficiencies when the jet energy scale is shifted from -10% to +10% of its nominal value.	237
G.4	The change in $t\bar{t}$ efficiencies when the jet energy scale is shifted from -10% to +10% of its nominal value.	238
G.5	Differences in $t\bar{t}$ efficiencies between the extremes of no initial-state radiation and no final-state radiation.	238

List of Figures

1.1	Top quark pair production, followed by SM $t\bar{t}$ decay.	7
1.2	The $\sigma_{t\bar{t}}$ and top mass measured at the Tevatron.	10
1.3	The expected number of events as a function of $\tan\beta$ for $M_{H^\pm} = 120 \text{ GeV}/c^2$	12
1.4	The predicted ratio of (dilepton / lepton+jets) events as a function of $\tan\beta$ for $M_{H^\pm} = 120 \text{ GeV}/c^2$	14
2.1	The Higgs potential energy curve.	20
2.2	The tbH^+ Yukawa coupling at small and large values of $\tan\beta$	33
2.3	Regions in the M_{H^\pm} vs. $\tan\beta$ plane for which $\mathcal{B}(t \rightarrow H^\pm b) > 25\%$, and the dominant decay mode of H^+ in these regions.	34
2.4	The width of the top quark and the H^\pm as a function of $\tan\beta$	37
2.5	The currently accepted view of the proton.	38
2.6	The parton densities $xf(x, Q^2 = M_{\text{top}}^2)$ for quarks and gluons. . . .	40
2.7	The leading order (α_s^2) diagrams for $t\bar{t}$ production in $p\bar{p}$ collisions. . . .	41
2.8	The values of $\sigma_{t\bar{t}}$ measured by the CDF and DØ Collaborations. . . .	44
2.9	The values of M_{top} measured by the CDF and DØ Collaborations. . . .	45
2.10	The top mass measured by CDF using the lepton+jets sample. . . .	46
2.11	The dijet mass spectrum of the two untagged jets in double b -tagged lepton+jets events.	48
2.12	“Penguin” diagrams for the decay $B \rightarrow X_s \gamma$	52
2.13	Supersymmetric diagrams containing a scalar top quark (\tilde{t}) and a chargino (X^\pm) that contribute to the rate for $b \rightarrow s\gamma$	52

2.14	The decay $B \rightarrow \tau\nu$ ordinarily occurs via W^\pm exchange, but can be enhanced by the presence of the H^\pm	54
2.15	Summary of all existing 95% C.L. limits on H^\pm production.	57
3.1	The Tevatron accelerator complex.	59
3.2	A three-dimensional view of the CDF detector.	62
3.3	A side view of one quadrant of the CDF detector.	62
3.4	One of the barrels of the SVX detector, and a schematic of several microstrips.	66
3.5	The SVX detector display for a top lepton+jets event.	67
3.6	One segment of the VTX.	68
3.7	A VTX event display for a top dilepton event.	69
3.8	The CTC endplate, and one of the CTC cells.	70
3.9	A CTC event display showing a top $e\text{-}\mu$ dilepton event.	72
3.10	The geometry of a calorimeter wedge.	77
3.11	A calorimeter wedge, with the CEM light collection system and the CES strip chamber indicated.	77
3.12	A schematic of the CES.	78
3.13	The distribution of transverse energy deposited in the calorimeters by a top dilepton event candidate.	79
3.14	A CMU module consists of four layers of drift cells.	85
3.15	The coverage in $\eta - \phi$ space of the three different muon systems.	86
3.16	A top dilepton candidate, as viewed in many of the detector systems including the CMU, CMP and CMX detectors.	87
3.17	One of the BBC counters.	89
3.18	A simplified block diagram of the Run 1B data acquisition system.	97

4.1	An illustration of two SVX tags. One has a positive decay length L_{xy} , and another has a negative L_{xy}	111
4.2	An example of a higher-order diagram for $Wb\bar{b}$ production.	118
4.3	The azimuthal angle between the \vec{E}_T and the closest lepton or jet, versus the \vec{E}_T , for Z^0 data events.	122
4.4	The azimuthal angle between the \vec{E}_T and the closest lepton or jet, versus the \vec{E}_T , for data events passing all the dilepton selection cuts except for the \vec{E}_T cuts.	123
5.1	The $H^\pm \rightarrow W^\pm b\bar{b}$ phase space in the m_{23}^2 vs. m_{12}^2 plane for $M_{H^\pm} = 140 \text{ GeV}/c^2$, and the matrix element squared for this decay.	130
5.2	The P_T spectrum of the b - and \bar{b} -quarks from the three-body decay $H^\pm \rightarrow W^\pm b\bar{b}$, where $M_{H^\pm} = 140 \text{ GeV}/c^2$	132
5.3	The expected distribution of $m_{\tau\nu}$ (effective H^\pm mass) from the decay $t \rightarrow \tau\nu b$, for $M_{H^\pm} = 150 \text{ GeV}/c^2$ and various values of $\tan\beta$	135
5.4	The top mass distribution for three different values of Γ_H , and $M_{H^\pm} = 80 \text{ GeV}/c^2$	137
5.5	The dependence of $\mathcal{B}(t \rightarrow \tau\nu b)$ on M_{top} for $M_{H^\pm} = 140 \text{ GeV}/c^2$, and $\tan\beta = 150$	139
6.1	Efficiencies for $t\bar{t}$ topologies containing $H^\pm \rightarrow cs$ and $H^\pm \rightarrow \tau\nu$ decays, to pass the selection criteria of the dilepton and lepton+jets channels.	143
6.2	The P_T of electrons and muons from $H^\pm \rightarrow \tau^\pm\nu$ decay, for $M_{H^\pm} = 80$ and $140 \text{ GeV}/c^2$	144
6.3	The jet E_T spectrum of jets arising from b -quarks from $t \rightarrow H^\pm b$ decay, and the SVX tagging efficiency for jets from b -quarks with two SVX tracks.	144

6.4	The P_T spectrum of leptons, and the P_T spectrum of b -quarks, from $t \rightarrow W^\pm b$ and $H^\pm \rightarrow W^\pm b\bar{b}$ decays.	147
6.5	The jet energy spectrum for jets from b -quarks, for the three different types of decays that generate b -quarks at low $\tan\beta$ and $M_{H^\pm} = 150 \text{ GeV}/c^2$	148
6.6	Jet multiplicity for jets with $E_T > 15 \text{ GeV}$, assuming $M_{H^\pm} = 150 \text{ GeV}/c^2$, and $\mathcal{B}(t \rightarrow H^\pm b \rightarrow W b\bar{b}) = 0.85$	150
6.7	Efficiencies for $t\bar{t}$ topologies containing $H^\pm \rightarrow W^\pm b\bar{b}$ decays, to pass the selection criteria of the dilepton and lepton+jets channels. . . .	151
6.8	A comparison of lepton P_T and b -jet E_T spectrums for two different values of Γ_H , assuming $M_{H^\pm} = 150 \text{ GeV}/c^2$ and $t\bar{t} \rightarrow \tau\nu b\tau\nu\bar{b}$	152
6.9	The $t\bar{t}$ efficiency in each channel as a function of $\tan\beta$ and Γ_H , for $M_{H^\pm} = 150 \text{ GeV}/c^2$	153
6.10	The $t\bar{t}$ efficiency in each channel as a function of $\tan\beta$ and Γ_{top} , for $M_{H^\pm} = 80 \text{ GeV}/c^2$	154
6.11	The total $t\bar{t}$ efficiency as a function of $\tan\beta$, for $M_{H^\pm} = 120 \text{ GeV}/c^2$. 156	
6.12	The $t\bar{t}$ efficiency in each channel as a function of $\tan\beta$, for $M_{H^\pm} = 120 \text{ GeV}/c^2$	158
6.13	The $t\bar{t}$ efficiency in each channel as a function of $\tan\beta$, for $M_{H^\pm} = 150 \text{ GeV}/c^2$	159
7.1	The number of expected dilepton events and lepton+jets events as a function of $\tan\beta$, for $M_{H^\pm} = 120 \text{ GeV}/c^2$	161
7.2	Predicted distribution of dilepton events, lepton+jets events, and the sum of these events in many trial experiments, for an assumed point in parameter space.	163

7.3	The expected number of (dilepton + lepton+jets) events as a function of $\tan\beta$, for $M_{H^\pm} = 120$ and $150 \text{ GeV}/c^2$	167
7.4	Probability for observing N or more events vs. N , for the dilepton channel and the lepton+jets channel, assuming a particular point in parameter space.	170
7.5	CDF excluded regions in the M_{H^\pm} vs. $\tan\beta$ plane.	172
7.6	CDF excluded regions in the M_{H^\pm} vs. $\mathcal{B}(t \rightarrow H^\pm b)$ planes.	173
7.7	$D\bar{D}$ excluded regions in the M_{H^\pm} vs. $\tan\beta$ plane.	176
8.1	The predicted ratio of dilepton to lepton+jets events as a function of $\tan\beta$, for $M_{H^\pm} = 100 \text{ GeV}/c^2$	178
8.2	Distributions for the number of dilepton events, lepton+jets events, and the ratio of these events in many trial experiments where $M_{H^\pm} = 80 \text{ GeV}/c^2$, and $\tan\beta = 0.62$	179
8.3	The $\sigma_{t\bar{t}}$ reconstructed in the lepton+jets channel using trial experiments, and also a log-likelihood approach.	182
8.4	The $\sigma_{t\bar{t}}$ measured separately using the observed number of dilepton events, and the observed number of lepton+jets events, assuming that $M_{H^\pm} = 80 \text{ GeV}/c^2$ and $\tan\beta = 0.62$	183
8.5	The measured value of $\sigma_{t\bar{t}}$, assuming $M_{H^\pm} = 80 \text{ GeV}/c^2$ and $\tan\beta = 0.62$, and the predicted distribution of dilepton events.	185
9.1	The dijet mass of the two jets without b -tags, in Monte Carlo $t\bar{t}$ events that pass the lepton+jets selection cuts, have two b -tags, and two other jets.	195
9.2	Transverse mass M_T formed between the \cancel{E}_T and lepton P_T in lepton+jets events.	197

C.1	The Tevatron accelerator complex, and a summary of the steps in the acceleration process of protons and antiprotons.	213
C.2	The proton target station.	217
D.1	The phase space in the m_{23}^2 vs. $m_{\tau\nu}^2$ plane for the three-body decay $t \rightarrow H^* b \rightarrow \tau \nu b$, and the matrix element squared for this decay. . .	225
F.1	Angular distribution of charged particles emitted in tau decays. . .	233
F.2	The P_T spectrums of leptons from tau decay, for taus that originate from W^+ decay or H^+ decay.	234

Chapter 1

Introduction

To date, there exists an overwhelming amount of experimental evidence [3] suggesting that the forces between fundamental particles, such as electrons, neutrinos and quarks, respect a class of symmetries called gauge symmetries. The fundamental property of mass for these particles violates gauge symmetry, unless it arises as a consequence of a special mechanism called the Higgs mechanism. This mechanism predicts the existence of a class of particles called Higgs bosons, which have never been observed. In this introductory chapter, beginning with the concept of gauge symmetries, I describe the motivation for searching for top quark decays to a charged Higgs boson. Then I outline the search strategy employed in this thesis, and the organization of later chapters.

1.1 Gauge Symmetries

Symmetry plays an important role in physics because of its intimate connection with conservation laws. The basis of a symmetry principle is the assumption that a certain quantity is not measurable in a physical system, and this implies an invariance of the system to a related transformation. Such invariance under a *continuous* symmetry transformation, in turn, implies the existence of a conserved quantity, according to Noether's theorem [4]. For example, it is believed that there is no absolute origin of space-time coordinates, which means that a physical system is invariant under arbitrary displacements in these coordinates. By enforcing this

invariance, conservation laws for energy and momentum can be derived [5]. Similarly, the assumption that an absolute direction in space is unobservable implies an invariance under rotations of a system in space, which in turn yields a conserved law for angular momentum [6].

In the second half of this century, more abstract and profound symmetries such as strangeness conservation, isospin rotation invariance and gauge invariance have been observed. Unlike symmetries associated with space-time, these operate on internal degrees of freedom, and have no classical analog. One of the most interesting and powerful symmetries is called gauge invariance. In Quantum Electrodynamics (QED), we know that charge and current are conserved. The corresponding symmetry transformation, under which the electromagnetic interaction must be invariant in form, is a change of phase factor for the complex wavefunction ψ that represents a charged field, $\psi \rightarrow e^{i\alpha}\psi$. In other words, by demanding the Lagrangian (which yields the equations of motion) to be invariant under these so-called gauge transformations, one can deduce charge and current conservation. Of course, this is no explanation of why nature chooses to respect this abstract symmetry!

Invariance under phase rotation $\psi \rightarrow e^{i\alpha}\psi$ is an example of a global symmetry, since the transformation $e^{i\alpha}$ is independent of position in space and time. There is a more powerful type of symmetry, called a “local” symmetry, for which the transformations can vary freely from point to point. In our example of QED, local gauge invariance is achieved by making the phase rotation factor α an arbitrary function of space-time, $\alpha = \alpha(x)$. To preserve local gauge invariance, it is necessary to counteract the variation of α with x by introducing a field A_μ , called a gauge field. This turns out to be the photon field (electromagnetic vector potential). The coupling strength e of this field to a charged particle is also specified, so that the classical prescription [7] for obtaining the motion of a charged particle in an electromagnetic field, $\vec{p} \rightarrow \vec{p} - (q/c)\vec{A}$, is predicted. Finally, a gauge invariant

term for the kinetic energy of the photon field must be added to the Lagrangian, ensuring that Maxwell's equations can be derived from it. Thus, while local gauge symmetry may not be an *a priori* principle of physics, in a sense it specifies the entire interacting field theory of QED.

Our example of the phase transformation in QED is called a $U(1)$ gauge symmetry, since a simple phase change is equivalent to multiplication by a 1×1 unitary matrix. The extension to more complicated groups was made by Yang and Mills in a classic 1954 paper [8], who showed how to construct an $SU(2)$ gauge theory of strong interactions. " $SU(2)$ " is the group of symmetry operations consisting of 2×2 unitary matrices, which are special because they have determinant unity. Eventually, it was recognized that the strong interactions respect the symmetry of the group $SU(3)$, rather than $SU(2)$. Despite this, in 1967, Weinberg was able to build on the work of Yang and Mills, and develop a model of weak and electromagnetic interactions that simultaneously respects types of $SU(2)$ and $U(1)$ symmetries [9]. This model, which will be discussed in the next chapter, predicts three gauge fields in addition to the photon field, which give rise to the intermediate vector bosons W^\pm and Z^0 . These bosons are exchanged between quarks and leptons in order to transmit the weak force. This is a central feature of the *standard model* (SM) of particle physics.

Today, it is believed that all fundamental particles and their interactions obey local gauge symmetries. These symmetries prescribe the strength and structure of the interaction of one particle with another, which takes place via the exchange of force-carrying particles associated with the gauge fields, called gauge bosons. The four forces are known to be gauge invariant, with gravity as an exception. These include the electromagnetic force, responsible for all light and radio phenomena and mediated by the exchange of photons; the weak force, at work in radioactive decay, and transmitted by the massive intermediate vector bosons W^\pm and Z^0 ;

and the strong force, responsible for holding the nucleus of an atom together, and “carried” from one quark to another by massless objects called gluons.

1.2 The Higgs Field and Mass

For the Lagrangian describing a fermion (*e.g.*, quark, electron or neutrino) to be invariant under gauge transformations, both the fermion and the gauge fields acting on it must be massless. While the photon is known to be massless, the intermediate vector bosons, as well as all the charged fermions, are observed to be massive. This seems to invalidate the notion that their interactions arise due to gauge symmetries. The key point is that the Lagrangian alone is not sufficient to describe a perturbative quantum field theory, for which particle states are built from the lowest energy (vacuum) state [10]. The symmetry properties of such a theory require specification of the symmetry for the vacuum state, as well as that of the Lagrangian [6]. The way that a gauge field can acquire a mass without breaking gauge invariance rests on the observation that a field theory Lagrangian and the vacuum state of that field theory need not have the same invariances. This is called spontaneous symmetry breaking, and an example of it will be given in the next chapter.

The standard model (SM) hypothesizes the existence of a “doublet” of scalar fields called the Higgs field, in order to accommodate massive vector bosons and fermions. The Higgs field has two roles to play. First, it is subject to a potential energy that is spontaneously broken. Secondly, quarks and leptons are initially taken to be massless, but are assumed to have couplings to the Higgs field, called Yukawa couplings. When spontaneous symmetry breaking occurs, the vector bosons acquire masses through a process called the Higgs mechanism. The Yukawa couplings result in fermion masses. A byproduct of the Higgs mechanism

is a massive scalar neutral boson, called the Higgs boson. While the masses of the W^\pm and Z^0 are essentially predicted by this model, the mass of the Higgs boson is a free parameter.

The SM has been confirmed over the last 30 years with steadily improving precision, with the discovery of the W^\pm and Z^0 bosons having occurred over 15 years ago. However, the Higgs sector is the least understood aspect of electroweak gauge theory. The Higgs boson, a key ingredient of the SM, remains undetected. However, the Higgs boson coupling to a fermion is predicted to be proportional to the fermion mass. This property makes the Higgs boson a difficult particle to discover, since the most experimentally accessible particles are light fermions such as electrons, and the u and d quarks inside protons, which couple to the Higgs boson only very weakly. The heavier fermions couple more strongly to the Higgs, but are difficult to produce themselves.

1.3 The Charged Higgs Boson and the Top Quark

Up to this point only the *minimal standard model* (SM) has been described, which contains the simplest possible Higgs sector with only one doublet of Higgs fields. Given that there is no experimental information on the Higgs sector, it is prudent to explore the implications of more complicated Higgs models. For example, it is possible that there exists two doublets of Higgs fields, rather than just one. In this scenario, symmetry breaking produces three neutral Higgs bosons and two charged Higgs bosons (H^\pm).

This model is particularly attractive for several reasons. First, it is an extension of the minimal model that adds the new phenomena of charged Higgs bosons, while remaining theoretically consistent with all known experimental observations [11]. Secondly, there are a number of theoretical reasons to suppose that the SM itself

is part of a larger theory called supersymmetry [12]. Supersymmetry, generally considered to be the leading candidate for a theory that extends the SM, requires a two-doublet Higgs sector. Thus, the observation of a charged Higgs boson would be direct evidence for symmetry breaking, and could indicate the existence of physics beyond the SM.

The H^\pm couples preferentially to the most massive fermion pair that is kinematically available to it. The top quark, the sixth quark to be discovered, has a mass of about $175 \text{ GeV}/c^2$, much larger than any of the other fermions. For this reason, the the phenomenology of the charged Higgs boson and the top quark are intimately connected [11]. Within the SM, the top quark decays to a W^\pm boson and a b quark almost 100% of the time. The W^\pm boson subsequently decays into a pair of leptons $e\nu_e, \mu\nu_\mu$, or $\tau\nu_\tau$, or a pair of light quarks ud or cs , with the following approximate branching fractions.

$$t \rightarrow W^\pm b \qquad W^\pm \rightarrow \underbrace{e\nu_e, \mu\nu_\mu, \tau\nu_\tau}_{1/9 \text{ each}}, \underbrace{ud, cs}_{1/3 \text{ each}} \quad (1.1)$$

However, if a charged Higgs boson exists, the decay mode $t \rightarrow H^\pm b$ competes with the SM decay mode $t \rightarrow W^\pm b$, as long as its kinematically allowed to do so ($M_{H^\pm} \lesssim M_{\text{top}} - m_b$). The H^\pm may decay to the lepton pair $\tau\nu$, the light quark pair cs , or to a W^\pm boson and a pair of bottom quarks:

$$t \rightarrow W^\pm b, H^\pm b \qquad H^\pm \rightarrow \tau\nu, cs, W^\pm b\bar{b} \quad . \quad (1.2)$$

A key parameter in the theory is $\tan\beta$, the ratio of vacuum expectation values of the two Higgs doublets, which will be covered in more detail in the next chapter. The Higgs mass M_{H^\pm} and $\tan\beta$ determine the branching fractions for the top quark and H^\pm decays given above. The formulas for these branching fractions are given in Appendix A.

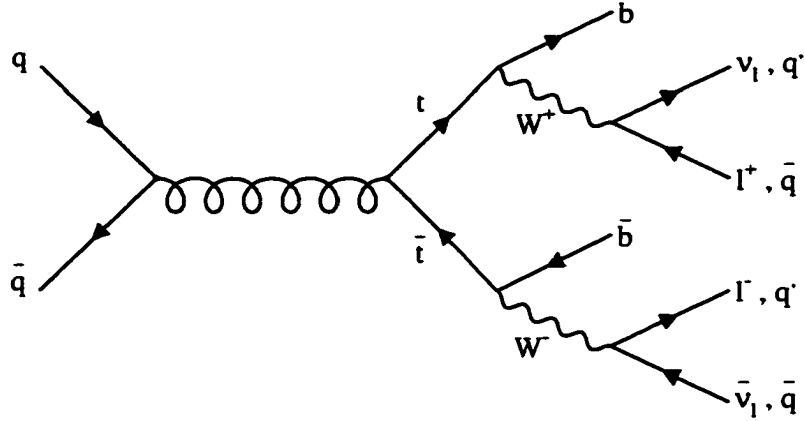


Figure 1.1: Top quark pair production, followed by SM $t\bar{t}$ decay. A quark from a proton annihilates an antiquark from an antiproton, temporarily producing a gluon, denoted by the curly line, which in turn decays to $t\bar{t}$. The rate for this process is proportional to the $t\bar{t}$ production cross section $\sigma_{t\bar{t}}$. If charged Higgs bosons H^\pm exist, they could replace the W^\pm bosons in this decay.

This search exploits the fact that the spectrum of topologies, from $t\bar{t}$ events containing a charged Higgs boson, will be much different from SM $t\bar{t}$ events, since the H^\pm decays very differently from a W^\pm boson. The H^\pm signatures are unique enough to be found, if the top quark branching fraction $\mathcal{B}(t \rightarrow H^\pm b)$ is large enough. This search also exploits the extraordinarily large top quark mass M_{top} of about $175 \text{ GeV}/c^2$, and the Tevatron's current monopoly on the top quark, to perform a search for H^\pm over a range of masses that significantly extends beyond the reach of other experiments such as LEP2.

In 1995, the CDF [13] and DØ [14] collaborations announced the discovery of top quark pair production, via the observation of events with topologies consistent with the SM decay $t\bar{t} \rightarrow W^+ b W^- \bar{b}$, as shown in Fig. 1.1. A SM $t\bar{t}$ decay can

SM $t\bar{t}$ Decay Topologies

name	topology	signature	branching fraction
all-hadronic	$t\bar{t} \rightarrow q\bar{q}q\bar{q}b\bar{b}$	6 jets	36/81 (44%)
lepton+jets	$t\bar{t} \rightarrow \ell\nu_\ell\bar{q}q\bar{b}\bar{b}$	1 e/μ + \cancel{E}_T + 4 jets	24/81 (30%)
tau+jets	$t\bar{t} \rightarrow \tau\nu\bar{q}q\bar{b}\bar{b}$	1 τ + \cancel{E}_T + 4 jets	12/81 (15%)
dilepton	$t\bar{t} \rightarrow \ell\nu_\ell\ell\nu_\ell\bar{b}\bar{b}$	2 e/μ + \cancel{E}_T + 2 jets	4/81 (5%)
tau dilepton	$t\bar{t} \rightarrow \tau\nu\ell\nu_\ell\bar{b}\bar{b}$	1 e/μ + 1 τ + \cancel{E}_T + 2 jets	4/81 (5%)
ditau	$t\bar{t} \rightarrow \tau\nu\tau\nu\bar{b}\bar{b}$	2 τ + \cancel{E}_T + 2 jets	1/81 (1%)

Table 1.1: The $t\bar{t}$ decay modes, their expected topologies, and their approximate branching fractions within the minimal SM. Here $\ell\nu_\ell$ denotes $e\nu_e$ or $\mu\nu_\mu$. Missing transverse energy is denoted by \cancel{E}_T .

be categorized by the decay modes of the two W^\pm bosons in the event, since each W^\pm can decay into a pair of leptons or light quarks. The different top decay topologies are indicated in Table 1.1. Most often both W^\pm bosons in a $t\bar{t}$ event will decay to a quark-antiquark pair, leading to a fully hadronic final state containing six quarks. Nominally, each of these quarks will hadronize to produce a “jet” of collimated particles in the detector. This happens for 44% of $t\bar{t}$ decays. However, a large background rate from other non- $t\bar{t}$ processes, which also produce events with multiple jets, makes isolation of this signal very difficult [15]. The background rate is significantly reduced if the event contains at least one high transverse momentum (or “high- P_T ”) electron (e) or muon (μ), which can be easily identified in the detector. When just one of the W^\pm bosons in a $t\bar{t}$ event decays to $e\nu$ or $\mu\nu$, then the final state includes a charged lepton with high transverse momentum (high- P_T), an imbalance of energy from the undetected neutrino, referred to as *missing transverse energy* (\cancel{E}_T), and four or more jets from the hadronization of the quarks.

Number of Expected and Observed SM $t\bar{t}$ Events

assume	dilepton channel	lepton+jets channel
$\sigma_{t\bar{t}} = 5.0\text{pb}$	4.0 ± 0.5 events	20.0 ± 3.0 events
$\sigma_{t\bar{t}} = 7.5\text{pb}$	6.1 ± 0.7 events	30.0 ± 4.5 events
observed:	6.5 ± 3.0 events	23.4 ± 6.0 events

Table 1.2: The expected number of signal events from $t\bar{t}$ production in the top dilepton and lepton+jets channels, assuming only SM $t\bar{t}$ decays ($\mathcal{B}(t \rightarrow Wb) = 1.0$). Results are shown for two different $t\bar{t}$ cross sections, along with the observed number of events, after background subtraction of non- $t\bar{t}$ processes [16].

This “lepton+jets” mode occurs about 30% of the time. When both W^\pm bosons in a $t\bar{t}$ event decay leptonically to $e\nu$ or $\mu\nu$, the final state includes two high- P_T leptons, \cancel{E}_T from the two neutrinos, and two jets from the hadronization of the b -quarks. This “dilepton” state occurs about 5% of the time. Decays of W^\pm bosons to the the tau lepton are not explicitly included in these searches, unless the tau subsequently decays to an electron or a muon. This analysis examines both the lepton+jets and dilepton decay topologies.

The observed number of events is consistent with the expected number of events in each of these decay channels, assuming that $t\bar{t}$ decays exclusively to $WbW\bar{b}$. CDF observes 9 dilepton events above a non- $t\bar{t}$ background of 2.5 events, and 34 lepton+jets events above a non- $t\bar{t}$ background of 10.6 events [16]. Table 1.2 lists the observed number of events above background in each channel. Also shown is the predicted number of events for several values of the $t\bar{t}$ cross section $\sigma_{t\bar{t}}$, a quantity that is proportional to the rate of $t\bar{t}$ production. Predictions are made for $\sigma_{t\bar{t}} = 5.0$ pb and 7.5 pb, assuming only SM decays. The value 5.0 pb lies within the range of theoretical values $\sigma_{t\bar{t}} = 4.9\text{--}5.5$ pb [17, 18, 19], calculated for

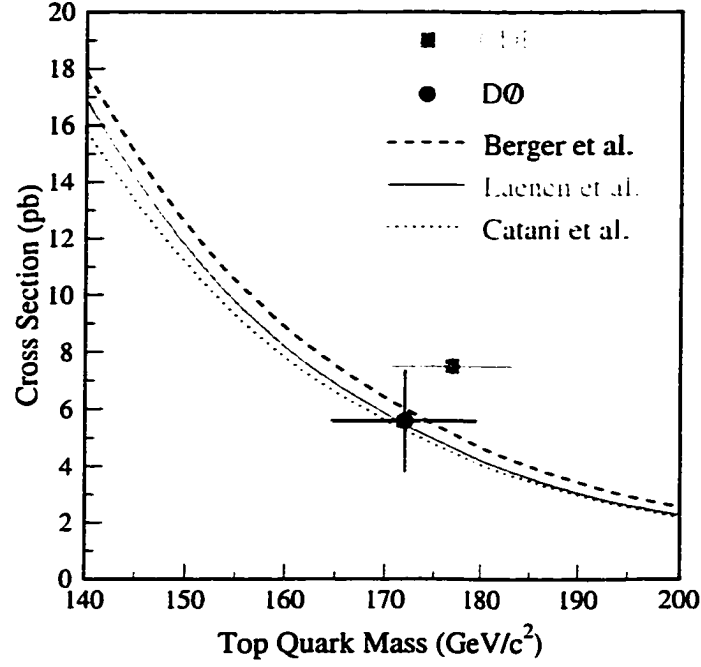


Figure 1.2: The $\sigma_{t\bar{t}}$ and top mass measured at the Tevatron. Each experiment combines all of its applicable $t\bar{t}$ decay channels that are observed, in order to obtain the measurement with the smallest error.

the measured top mass of $175 \text{ GeV}/c^2$ [20, 21]. The second value of 7.5 pb is taken to be 50% larger to illustrate sensitivity to this assumed value. The measured value of the $t\bar{t}$ cross section is $7.6^{+1.8}_{-1.5}$ pb using all the $t\bar{t}$ decay channels observed at CDF [22]. The $\sigma_{t\bar{t}}$ is measured to be $8.2^{+4.4}_{-3.4}$ pb using only the observed number of dilepton events [23], and $6.2^{+2.1}_{-1.7}$ pb using only the observed number of lepton+jets events [22]. Each of these rates is consistent with the theoretical range of $\sigma_{t\bar{t}}$. The $\sigma_{t\bar{t}}$ measurements made by the CDF and DØ Collaborations are shown as a function of M_{top} in Fig 1.2, along with theoretical curves. For these measurements, each experiment has combined all of its applicable decay modes.

1.4 Search Strategy for a Charged Higgs Boson

I have described how the observed rates for $t\bar{t}$ decays to dilepton final states and lepton+jets final states are consistent with the theoretical predictions for these rates, assuming that the top quark decays exclusively to $W^\pm b$. This thesis examines the effect that frequent top quark decays to $H^\pm b$ would have on these event rates. The top dilepton and lepton+jets channels each contain enough events, and have a large enough signal/background ratio, to separate real $t\bar{t}$ rate effects from background fluctuations. In addition, the backgrounds from SM sources other than $t\bar{t}$ production are well understood. For these reasons, this search uses identical selection criteria to those used for the CDF top discovery [13], and the CDF top cross section [22] measurement.

In this search, two predictions of the two-Higgs-doublet model are exploited to exclude the possibility of a large top quark branching fraction $\mathcal{B}(t \rightarrow H^\pm b)$. First of all, a large $\mathcal{B}(t \rightarrow H^\pm b)$ suppresses $t\bar{t}$ decay rates to dilepton final states and lepton+jets final states, so they are significantly smaller than the corresponding SM predictions for these rates. This is true whether H^\pm decays predominantly to the light quark pair cs or the tau-neutrino pair $\tau\nu$, but not if H^\pm decays frequently to the $W^\pm b\bar{b}$ final state. Limits are set where the number of predicted $t\bar{t}$ events is too small to account for the observed number of events. The second method for excluding H^\pm relies on the fact that a large $\mathcal{B}(t \rightarrow H^\pm b)$ results in a ratio of dilepton events to lepton+jets events that is much smaller than the SM value. Parameter space is excluded based on the fact that the observed ratio agrees with the SM prediction.

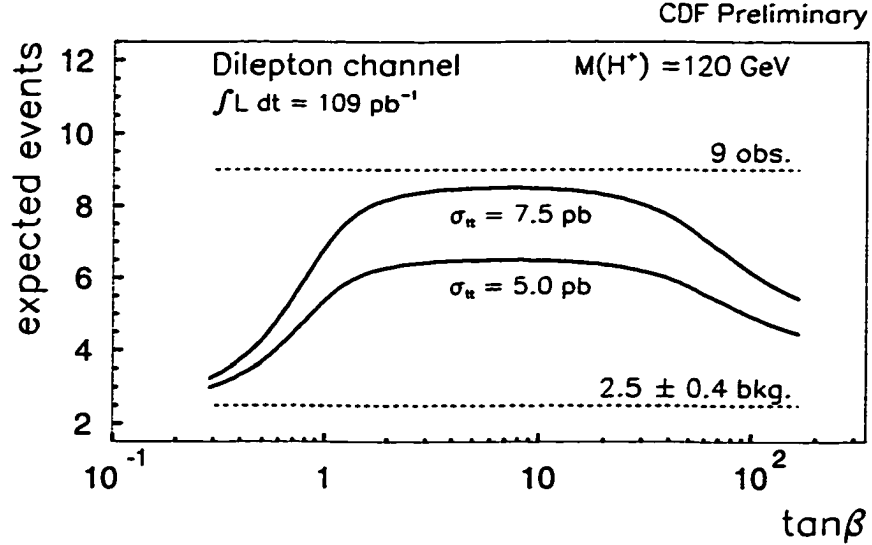


Figure 1.3: The expected number of events as a function of $\tan\beta$ for $M_{H^\pm} = 120 \text{ GeV}/c^2$, assuming the validity of the charged Higgs scenario. Curves are given for the theoretical value of $\sigma_{t\bar{t}}$, and a value that is 50% higher. The number of observed events is also shown. A deficit of events is predicted near $\tan\beta = 0$, where $t \rightarrow H^\pm b \rightarrow csb$ decays are prevalent, and also near $\tan\beta = 100$, where $t \rightarrow H^\pm b \rightarrow \tau\nu b$ decays are prevalent. At the maximum of the curves, near $\tan\beta = 10$, $\mathcal{B}(t \rightarrow H^\pm b) \approx 0$, and only SM $t\bar{t}$ decays are expected.

1.4.1 Absolute Rate Method

The $t\bar{t}$ events that contain one or two $H^\pm \rightarrow cs$ or $H^\pm \rightarrow \tau\nu$ decays will have markedly reduced efficiencies for passing the selection criteria of the dilepton and lepton+jets channels, compared to SM decays. If $\mathcal{B}(t \rightarrow H^\pm b)$ is large, and $H^\pm \rightarrow cs$, then the following topologies will be prevalent:

$$\begin{array}{cc}
\bar{t}\bar{t} \longrightarrow \text{HbH}\bar{b} & \bar{t}\bar{t} \longrightarrow \text{HbW}\bar{b} \\
\begin{array}{l} \downarrow \searrow \bar{c}s \\ \downarrow \longrightarrow c\bar{s} \end{array} & \begin{array}{l} \downarrow \longrightarrow c\bar{s} \end{array}
\end{array}$$

The decay on the left is a six-quark final state that produces multiple jets. This mode does not contribute to either channel because of the absence of leptons and \cancel{E}_T in the events. In the decay on the right, only one W^\pm boson is available for producing high- P_T leptons. As a result, this mode has a reduced efficiency for passing the selection criteria of the lepton+jets channel, and almost no efficiency for passing the requirements of the dilepton channel. A similar deficit of events results if $H^\pm \rightarrow \tau\nu$, where the following decay modes will be prevalent.

$$\begin{array}{cc}
\bar{t}\bar{t} \longrightarrow \text{HbH}\bar{b} & \bar{t}\bar{t} \longrightarrow \text{HbW}\bar{b} \\
\begin{array}{l} \downarrow \searrow \bar{\tau}\nu \\ \downarrow \longrightarrow \tau\bar{\nu} \end{array} & \begin{array}{l} \downarrow \longrightarrow \tau\bar{\nu} \end{array}
\end{array}$$

The transverse momentum (P_T) of electrons and muons in these events typically will be much lower than those found in SM decays. This is due to the fact that in these events, electrons and muons will frequently originate from three-body tau decays, as compared to the direct decays $W^\pm \rightarrow e\nu, \mu\nu$ in SM $t\bar{t}$ events.

In summary, the charged Higgs scenario predicts a deficit of top dilepton and lepton+jets events. The theoretical value of $\sigma_{t\bar{t}}$ is used to calculate the expected number of events in each of these channels, assuming efficiencies calculated for a given point in parameter space ($M_{\text{top}}, M_{H^\pm}, \tan\beta$). Figure 1.3 shows the expected number of top dilepton events as a function of $\tan\beta$, calculated for the measured top mass and $M_{H^\pm} = 120 \text{ GeV}/c^2$. Also shown is the observed number of events (9). At small and large values of $\tan\beta$, $\mathcal{B}(t \rightarrow H^\pm b)$ is large, and the expected number of events has a very small probability for fluctuating to the observed number of events or higher. Parameter space is excluded in regions where this probability dips below 5%.

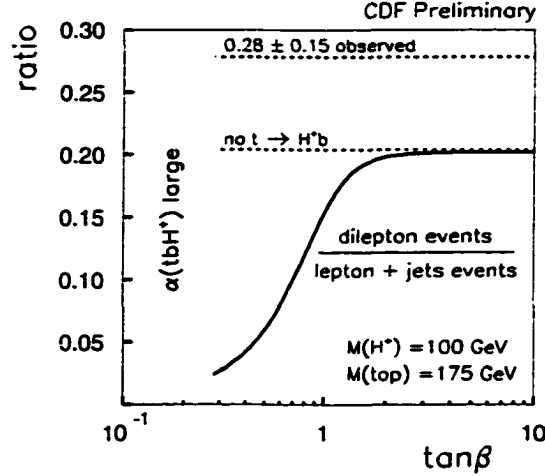


Figure 1.4: The predicted ratio of (dilepton / lepton+jets) events as a function of $\tan\beta$ for $M_{H^\pm} = 120 \text{ GeV}/c^2$. As $\tan\beta \rightarrow 0$, $\mathcal{B}(t \rightarrow H^\pm b \rightarrow csb) \rightarrow 1$, and a small ratio is predicted. The observed ratio is in agreement with the SM prediction.

1.4.2 Relative Rate Method

The method just described compares the absolute number of events predicted within the charged Higgs scenario to the observed number of events. An absolute value for $\sigma_{t\bar{t}}$ must be assumed. However, this is not true if charged Higgs is excluded by comparing the predicted balance of events in the two channels to the observed balance.

Fig. 1.4 plots the ratio of (dilepton / lepton+jets) efficiencies as a function of $\tan\beta$, for $M_{H^\pm} = 100 \text{ GeV}/c^2$. Also shown is the observed ratio, which is consistent with the SM prediction. Near $\tan\beta \approx 0$, $\mathcal{B}(t \rightarrow H^\pm b \rightarrow csb)$ is large, and the ratio is predicted to be much smaller than the SM value. This occurs because events with just one $H^+ \rightarrow c\bar{s}$ decay can contribute to the lepton+jets channel, but are invisible to the dilepton channel.

1.5 Thesis Overview

In this analysis, I set limits based on a calculation of the total expected number of events in each of two top decay channels. The expected number of events in a channel is given by

$$N_{\text{exp}} = N_{\text{bkg}} + \epsilon_{t\bar{t}} \sigma_{t\bar{t}} \int \mathcal{L} dt \quad (1.3)$$

where the first term, N_{bkg} , is the mean number of background events from non- $t\bar{t}$ processes, and the second term is the number of $t\bar{t}$ signal events. This second term is the product of the efficiency for $t\bar{t}$ events to pass the selection criteria of the channel, the $t\bar{t}$ cross section, and the time integral of the initial flux of proton and antiproton particles in collision, called the luminosity.

This thesis is organized as follows. In Chapter 2, I present the two-Higgs-doublet model, derive the couplings of the H^\pm to fermions, and describe how the top quark and H^\pm branching fractions depend on M_{H^\pm} and $\tan\beta$. Also, some special properties of the H^\pm are discussed. In Chapter 3, I describe the CDF detector, the luminosity measurement, and the selection criteria that are implemented in hardware and software in order to identify $t\bar{t}$ events, and collect a sample of events from which the analysis begins. Chapter 4 defines the selection criteria for the top dilepton and lepton+jets channels, and summarizes the non- $t\bar{t}$ background contribution N_{bkg} to these channels. In order to obtain the efficiency $\epsilon_{t\bar{t}}$ for $t\bar{t}$ events with H^\pm decays to pass the selection criteria of each channel, special Monte Carlo modeling of the signal was performed, and this is described in Chapter 5. The $t\bar{t}$ efficiencies and an explanation of their overall behavior are given in Chapter 6. Chapter 7 discusses the details of combining the two channels in order to set limits on H^\pm production using the absolute rate method outline above. Chapter 8 describes the limits obtained using the relative rate method, also outlined above. I conclude in Chapter 9, where I also discuss ideas for future charged Higgs searches.

Chapter 2

Theoretical and Experimental Framework

In the previous chapter, I introduced the predictive power of gauge invariance, which prescribes the form of the interaction between gauge bosons and matter. In this chapter, I quickly review the standard model (SM), and present the Higgs mechanism, which generates masses for the fermions and the gauge bosons. Following this, the two-Higgs-doublet extension to the SM is presented. Emphasis is placed on the differences between the two models, and also on the couplings of the charged Higgs boson to fermions. The branching fractions of the top quark and the H^\pm are specified, and some special properties of the decay $t \rightarrow H^\pm b$ are discussed. Next, I review the physics of top quark pair production, and present top quark measurements at the Tevatron. Finally, I review limits established from other searches for the H^\pm .

2.1 The Unbroken $SU(2)_L \times U(1)_Y$ Model

Associated with the group $SU(2)$ are three generators $\{T_i\}$, which form a vector in abstract “isospin” space. An $SU(2)$ gauge model is a close candidate for weak interaction theory, since the triplet of gauge fields $\{W_\mu^a\}$ associated with these generators could give rise to charged and neutral bosons, W^\pm and W^0 , to transmit the weak force [24]. For example, weak interaction phenomenology tells us that by the emission of a W^- , a left-handed electron can be transformed into a neutrino.

Similarly, a left-handed down-type quark can be transformed into a left-handed up-type quark. These pairs of particles form the following left-handed weak isospin $SU(2)_L$ doublets, where the prime denotes weak interaction eigenstates for quarks, which are different from the mass eigenstates,

$$\ell_{L1} = \begin{pmatrix} \nu \\ e^- \end{pmatrix}_L \quad q'_{L1} = \begin{pmatrix} u' \\ d' \end{pmatrix}_L . \quad (2.1)$$

Remember that the left- and right-handed components of a wavefunction u are

$$u_L = \frac{1}{2}(1 - \gamma^5)u \quad u_R = \frac{1}{2}(1 + \gamma^5)u . \quad (2.2)$$

To complete the $SU(2)_L$ symmetry, the neutral gauge boson W^0 would also couple to left-handed fermions exclusively, just like the W^\pm . However, the weak neutral current is observed to couple both to right- and left-handed fermions.

Glashow [25] was the first to realize that there exists an additional gauge symmetry with couplings to the right-handed fermions, which acts independently of the weak isospin symmetry $SU(2)_L$. This symmetry is called $U(1)_Y$, and the generator Y of this group commutes with the weak isospin generators, $[T, Y] = 0$. The resulting symmetry transformation is called $SU(2)_L \times U(1)_Y$. The quantum number Y is termed the “weak hypercharge”, related to charge and weak isospin through

$$Q = T^3 + \frac{Y}{2} . \quad (2.3)$$

By incorporating the electric charge Q , the $SU(2)_L$ symmetry can be preserved since the electromagnetic current has couplings both to right and left-handed fermions. Thus, left-handed fermions transform non-trivially under both $SU(2)_L$ and $U(1)_Y$. In contrast, right-handed fermions are $SU(2)$ singlets, and only transform under $U(1)_Y$. Table 2.1 lists the weak isospin and hypercharge quantum numbers, of doublets and singlets in the $SU(2)_L \times U(1)_Y$ model.

Quantum Numbers for the $SU(2)_L \times U(1)_Y$ Singlets and Doublets

doublet or singlet	T	Y	term in Lagrangian
$\ell_{Ln} = \begin{pmatrix} \nu_n \\ e_n^- \end{pmatrix}_L$	$\frac{1}{2}$	-1	$\bar{\ell}_{Ln} \gamma_\mu \left(\partial_\mu - \frac{ig}{2} \vec{\tau} \cdot \vec{W}_\mu + \frac{ig'}{2} B_\mu \right) \ell_{Ln}$
e_{Rn}^-	0	-2	$\bar{e}_{Rn} \gamma_\mu (\partial_\mu + ig' B_\mu) e_{Rn}$
$q'_{Ln} = \begin{pmatrix} u'_n \\ d'_n \end{pmatrix}_L$	$\frac{1}{2}$	$\frac{1}{3}$	$\bar{q}'_{Ln} \gamma_\mu \left(\partial_\mu - \frac{ig}{2} \vec{\tau} \cdot \vec{W}_\mu - \frac{ig'}{6} B_\mu \right) q_{Ln}$
u'_{Rn}	0	$\frac{4}{3}$	$\bar{u}'_{Rn} \gamma_\mu (\partial_\mu - \frac{2ig'}{3} B_\mu) u'_{Rn}$
d'_{Rn}	0	$-\frac{2}{3}$	$\bar{d}'_{Rn} \gamma_\mu (\partial_\mu + \frac{ig'}{3} B_\mu) d'_{Rn}$

Table 2.1: Listed are $SU(2)_L \times U(1)_Y$ doublets and singlets. The index n denotes the generation. The prime (') denotes the fact that the quarks are weak eigenstates, but not mass (= strong) eigenstates. For the terms in the Lagrangian, the eigenvalues for the operators Y and \mathbf{T} have been substituted.

The standard model consists of a gauge field B_μ for the $U(1)_Y$ symmetry, which couples to right- and left-handed leptons with a coupling strength set to $g'/2$. There is also a triplet of gauge fields \mathbf{W}_μ for $SU(2)_L$, which couple to left-handed fermions with a coupling strength g . This means that in the Dirac Lagrangian for a fermion singlet or doublet ψ ,

$$\mathcal{L} = \bar{\psi}(i\gamma^\mu \partial_\mu - m)\psi \quad (2.4)$$

the $U(1)$ gauge invariance is achieved with the substitution $\partial_\mu \rightarrow \partial_\mu - i\frac{g'}{2}YB_\mu$, while the $SU(2)$ gauge invariance requires the substitution $\partial_\mu \rightarrow \partial_\mu - i\frac{g}{2}\tau_a W_\mu^a$, where $\{\tau_a\}$ are the Pauli matrices. Also, the fermion mass term $-m\bar{\psi}\psi$ must be removed, since it is not gauge invariant. Fermion (and gauge field) masses must be generated from the process of spontaneous symmetry breaking and the Higgs

mechanism, described in the next section. Table 2.1 gives the gauge invariant terms in the Lagrangian corresponding to the $SU(2)_L$ doublets and $U(1)_Y$ singlets.

2.2 Hidden Symmetries and the Higgs Mechanism

Until now we have only considered the symmetry properties of the Lagrangian. However, as we stated in the introduction, the symmetry properties of a perturbative quantum field theory also require specification of the symmetry for the vacuum state [6]. Even if the Lagrangian of a system is invariant under a symmetry operation, the ground state of that system may not respect the symmetry. This is an example of spontaneous symmetry breaking, and the symmetry that is no longer apparent in the ground state is called a “broken” or “hidden” symmetry.

As an example of this¹ consider a complex scalar field $\phi = \frac{1}{\sqrt{2}}(\phi_1 + i\phi_2)$, subject to the following potential,

$$V(\phi) = \frac{\mu^2}{2}\phi^*\phi + \frac{\lambda}{4}(\phi^*\phi)^2. \quad (2.5)$$

The potential $V(\phi)$ is shown in Fig. 2.1 for the two cases ($\lambda > 0$, $\mu^2 > 0$) and ($\lambda > 0$, $\mu^2 < 0$). Note that in both cases there is rotational invariance around the vertical axis.

For the first case, where $\mu^2 > 0$, the ground state corresponds to $\phi = 0$. This state shares the rotational invariance of the Lagrangian. For the second case, where $\mu^2 < 0$, the ground state corresponds to the circle of minima of the potential in the (ϕ_1, ϕ_2) plane of radius v , where $v^2 = -\mu^2/\lambda$. To identify the particle spectrum associated with this potential, we must use perturbation theory and calculate fluctuations about the ground state energy. This forces us to choose *a particular point* among the degenerate ground states at radius v . Any particular

¹This discussion closely follows the treatment given in Refs. [5, 10].

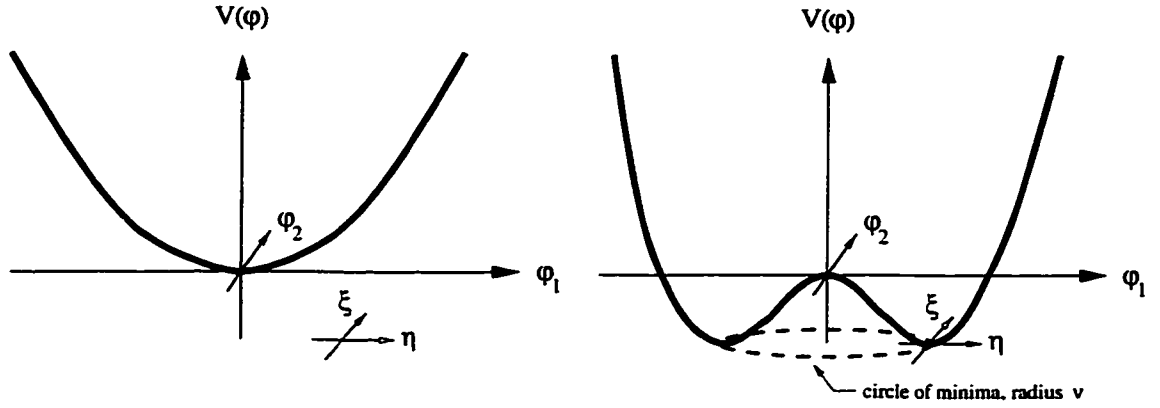


Figure 2.1: The potential energy curve $V(\phi) = \frac{\mu^2}{2}\phi^*\phi + \frac{\lambda}{4}(\phi^*\phi)^2$ for two cases. On the left, $(\lambda > 0, \mu^2 > 0)$, while on the right $(\lambda > 0, \mu^2 < 0)$. The ground state at $(\phi_1, \phi_2) = (v, 0)$ does not share the rotational symmetry of the potential, resulting in a “broken symmetry”. This potential is the standard model potential if we set ϕ_3 and ϕ_4 to zero in Eq. 2.8. This figure is adopted from Fig. 14.5 in Ref. [10].

minimum will not possess the rotational symmetry of the Lagrangian. This is a result of the fact that there is a non-zero “vacuum expectation value” of $|\phi| = v$ in the vacuum state.

Expanding \mathcal{L} about the minimum energy point $\phi_1 = v, \phi_2 = 0$, in terms of the fields shown in Fig. 2.1, $\phi = v + \eta + i\xi$, we find that the field η has a kinetic energy term and a mass term, while the field ξ only has a kinetic energy term. The mass term corresponds to radial oscillations in the η direction against the restoring force of the potential [10]. The potential is flat in the tangent ξ direction, and this corresponds to a massless mode. This is an example of the Goldstone theorem, which states that if a spontaneously broken symmetry is a continuous global symmetry, then one massless scalar field must appear for each group generator that has been broken. Mathematically, a generator \mathcal{G} will be unbroken only if it leaves

the vacuum state invariant [5],

$$e^{ia\mathcal{G}}\langle\phi\rangle_0 = \langle\phi\rangle_0 \quad \Rightarrow \quad \mathcal{G}\langle\phi\rangle_0 = 0 . \quad (2.6)$$

In our simple example, the generator of the group transformations is just the rotation matrix, which does *not* leave the vacuum state $\frac{1}{\sqrt{2}}(v, 0)$ invariant. The massless field ξ is the Goldstone boson associated with this broken generator.

The Goldstone theorem seems to prevent the use of spontaneous symmetry breaking to generate masses for bosons. The caveat is that the Goldstone theorem does not apply to local gauge field theories [26]. In fact, if a continuous local gauge theory is spontaneously broken, no massless Goldstone bosons appear. Instead, the “would-be” Goldstone bosons (corresponding to the broken generators) acquire mass without spoiling the gauge invariance of the original Lagrangian. This is called the Higgs mechanism.

As an example of this, suppose we form a locally $U(1)$ gauge invariant Lagrangian with an associated massless gauge field A_μ , and the same potential shown in Fig. 2.1. After symmetry breaking (and being careful to choose a gauge in which the particle spectrum is clear, see Ref. [10]), there will be a massive vector boson A_μ and a massive scalar boson h , called a Higgs boson. The “would-be” Goldstone boson is absent, and this degree of freedom has been turned into a mass for the A_μ field. Thus, the Higgs mechanism is really the result of an interplay between local gauge invariance and spontaneous symmetry breaking.

2.3 The Minimal Standard Model

Here I briefly describe the broken $SU(2) \times U(1)$ model of electroweak interactions, in the presence of a complex scalar field, and a potential energy for this field. The SM relations that have particular relevance to the two-Higgs-doublet model are

emphasized. These include the structure of the Higgs sector, the masses of the W^\pm and Z^0 bosons, and the coupling of the Higgs field to fermions, called Yukawa couplings.

2.3.1 The Higgs Sector

In the SM, the fermions and gauge bosons become massive through the spontaneous breakdown of the $SU(2) \times U(1)$ symmetry. In 1967, Weinberg [27] realized that this can be achieved if there exists a scalar field, subject to a spontaneously-broken potential energy. He introduced the only kind of gauge-invariant field whose vacuum expectation values could give the electron a mass, a spin zero $SU(2)$ doublet with $Y = 1$,

$$\phi = \begin{pmatrix} \phi^+ \\ \phi^0 \end{pmatrix} = \frac{1}{2} \begin{pmatrix} \phi_1 + i\phi_2 \\ \phi_3 + i\phi_4 \end{pmatrix} . \quad (2.7)$$

The potential energy for this field has the form that was considered earlier, Eq. 2.5,

$$\begin{aligned} \mathcal{L}_{\text{scalar}} &= (\mathcal{D}_\mu \phi)^\dagger (\mathcal{D}^\mu \phi) - V(\phi) \\ &= \left| \left(\partial_\mu \phi - \frac{ig}{2} \tau \cdot \mathbf{W}_\mu \phi - \frac{ig'}{2} B_\mu \phi \right) \right|^2 - \frac{\mu^2}{2} \phi^* \phi - \frac{\lambda}{4} (\phi^* \phi)^2 . \end{aligned} \quad (2.8)$$

Although this potential was first proposed by Goldstone [28] in analogy with the Bardeen model of a superconductor, it turns out to be the most general, gauge invariant and renormalizable (not higher than order four in the fields) potential for a scalar field [29].

2.3.2 The Gauge Boson Mass Spectrum

We must choose a vacuum expectation value for ϕ that leaves the vacuum invariant under $U(1)_Q$ transformations so that there is no (would-be) Goldstone boson

associated with the photon, and it remains massless. This occurs for the choice

$$\langle\phi\rangle_0 = \frac{1}{\sqrt{2}} \begin{pmatrix} 0 \\ v \end{pmatrix} \quad (2.9)$$

since the generator Q satisfies $Q\langle\phi\rangle_0 = (T_3 + \frac{Y}{2})\langle\phi\rangle_0 = 0$ (see Eq. 2.6). It can be verified that the other $SU(2) \times U(1)$ generators T^1 , T^2 , T^3 , and Y are broken.

Before symmetry breaking, then, we have four degrees of freedom in the Higgs doublet, and four massless gauge fields $B_\mu, \{W_\mu^i\}$ associated with the generators $Y, \{T^i\}$. These four generators will be broken, but Q , which is a combination of B_μ and W_μ^3 (Eq. 2.3) will not be broken. Thus, after symmetry breaking, we expect a massless boson to remain associated with one combination of B_μ and W_μ^3 , a massive boson corresponding to the orthogonal combination of B_μ and W_μ^3 , and two other massive bosons associated with the fields W_μ^1 and W_μ^2 . The fourth degree of freedom in the scalar Higgs doublet appears as a massive scalar boson, called the Higgs boson.

In order to expand about the particular vacuum $\langle\phi\rangle_0$, we can substitute the expression

$$\phi = \frac{1}{\sqrt{2}} \begin{pmatrix} 0 \\ v + \eta(x) \end{pmatrix} \quad (2.10)$$

This is not obvious, since one would think that the most general excitation above the vacuum would contain non-zero terms for ϕ_1, ϕ_2 and ϕ_4 given in Eq. 2.7. However, since the $SU(2)$ symmetry is local, we may perform a different isospin rotation at each point in space, reducing ϕ to the form given above [29, 10]. We will see that this argument does not apply to the two-Higgs-doublet model.

Substituting Eq. 2.10 into the Lagrangian of Eq. 2.8, and keeping only the lowest order terms without including interacting terms, the scalar Lagrangian gives us

$$\mathcal{L}_{\text{scalar}} = \frac{v^2\lambda}{8}\eta^2 + \frac{1}{2}(\partial_\mu\eta)^2 + \frac{g^2v^2}{4}W_\mu^+W^{\mu-} + \frac{v^2}{8}[(g^2 + g'^2)Z_\mu^2 + 0A_\mu^2] \quad (2.11)$$

This spectrum shows the presence of a scalar field η with a mass $\frac{v\sqrt{\lambda}}{2}$, charged W^\pm fields with mass $\frac{1}{2}vg$, a massive neutral vector field Z_μ with mass $\frac{1}{2}v\sqrt{g^2 + g'^2}$, and a massless A_μ field, corresponding to the photon. The vacuum expectation value v is $\frac{M_W}{2g} \approx 246$ GeV. As expected, the A_μ and Z_μ are linear combinations of the gauge fields B^μ and W_3^μ , while the charged W^\pm fields are linear combinations of the gauge fields W_μ^1 and W_μ^2 , $W^\pm = (W_\mu^1 \pm iW_\mu^2)/\sqrt{2}$. It is predicted that ρ , which measures the relative strength of the weak neutral and charged current reactions, is 1:

$$\rho = \frac{M_W^2}{M_Z^2 \cos^2 \theta_W} = 1. \quad (2.12)$$

2.3.3 Yukawa Couplings - Masses for the Fermions

Masses for the fermions arise from interactions with the scalar Higgs field, and have to be explicitly added. These so-called Yukawa couplings are the most general couplings of the scalar field ϕ to the fermions, subject to gauge invariance under $SU(2)_L \times U(1)_Y$ transformations. For the leptons and the “down-type” quarks, the couplings have the form

$$\bar{\ell}_{Lm} \phi e_{Rm} + \text{hermitian conjugate (H.C.)}, \quad \bar{q}'_{Lm} \phi d'_{Rn} + \text{H.C.} \quad (2.13)$$

The notation in these equations is the same as in Section 2.1. The subscripts m and n denote generations - for example, $(d'_{L1}, d'_{L2}, d'_{L3})$ denotes the down-type quarks (d'_L, s'_L, b'_L) . In this expression, lepton-number violating interactions are absent, but the quark eigenstates can couple across generations. Terms of the form $\bar{q}'_{mL} \phi u'_{nL}$, which one might think are required to generate masses for the up-type quarks, are forbidden because they violate $U(1)_Y$ invariance (the total Y is not zero) [30]. Instead, one must use the charge conjugate doublet $\tilde{\phi}$ with $Y = -1$, where $\tilde{\phi} = i\tau^2 \phi^\dagger$ [10, 30]. Thus the total Yukawa interaction has three components, for coupling of the Higgs field ϕ to leptons, to down-type quarks, and to up-type

quarks,

$$\mathcal{L}_{\text{Yukawa}} = \sum_m^3 \Gamma_m^\ell \bar{\ell}_{Lm} \phi e_{Rm} + \sum_{m,n=1}^3 \Gamma_{mn}^d \bar{q}'_{Lm} \phi d'_{Rn} + \sum_{m,n=1}^3 \Gamma_{mn}^u \bar{q}'_{Lm} \tilde{\phi} u'_{Rn} + H.C. \quad (2.14)$$

Fermion masses are predicted as a result of symmetry breaking. This is best illustrated by looking at the first term in the above expression, corresponding to the lepton coupling to the Higgs field. Upon the substitution $\phi = (0, v + \eta)/\sqrt{2}$, the $m = 1$ term (corresponding to electrons) becomes

$$\mathcal{L}_{\text{Yukawa-electron}} = m_e \bar{e}e + \frac{m_e}{v} \bar{e}e\eta, \quad m_e = \frac{\Gamma_e^\ell v}{\sqrt{2}} \quad (2.15)$$

which contains a mass term, and a Higgs coupling term proportional to the Higgs field η . Since Γ_e^ℓ is arbitrary, the electron mass is not predicted. However, the Higgs boson couples to fermion pairs with a strength proportional to the fermion mass,

$$\text{Higgs} - \text{fermion coupling} = \frac{m_f}{v} = \frac{g}{2M_W} m_f \quad (2.16)$$

A similar relation also holds for quarks, but the treatment is tricky, since the coupling is cross-generational. The complete derivation is given in Appendix B. As an example, taking just the last term in Eq. 2.14, corresponding to Higgs couplings to up-type quarks, we substitute $\tilde{\phi} = (v + \eta, 0)/\sqrt{2}$ [30],

$$\begin{aligned} \mathcal{L}_{\text{Yukawa}} &= \sum_{m,n=1}^3 \Gamma_{mn}^u (\bar{u}'_{Lm}, \bar{d}'_{Lm}) \frac{1}{\sqrt{2}} \begin{pmatrix} v + \eta \\ 0 \end{pmatrix} u'_{Rn} + H.C. \\ &= \bar{u}'_L (M^u + h^u \eta) u'_R + H.C. \end{aligned} \quad (2.17)$$

The summation has been replaced by matrix multiplication, in the second step, where $u'_L = (u', c', t')_L$, and $u'_R = (u', c', t')_R$. Also, the 3×3 up-quark mass matrix M^u , and coupling matrix h^u (proportional to the Higgs field η) have been introduced,

$$M_{mn}^u = \Gamma_{mn}^u \frac{v}{\sqrt{2}} \quad \text{and} \quad h_{mn}^u = \frac{1}{v} M_{mn}^u. \quad (2.18)$$

Notice that the coupling matrix h^u (essentially the Yukawa coupling matrix Γ_{mn}^u) is proportional to the mass matrix M^u . Hence, it is made diagonal by the same transformation that diagonalizes the mass matrix [30]. This means that the couplings of the Higgs boson are diagonal in flavor. In the two-Higgs-doublet model we find that these results are *not* true, and additional symmetries must be imposed to suppress flavor changing neutral currents (FCNCs).

2.4 The Two-Higgs-Doublet Extension to the SM

There is no reason why there should exist only one complex doublet of Higgs fields. As we stated in the introduction, in many extensions to the SM, such as supersymmetry, there exists an extended sector of two Higgs doublets,

$$\Phi_1 = \frac{1}{\sqrt{2}} \begin{pmatrix} \Phi_1^+ \\ \Phi_1^0 \end{pmatrix}, \quad \Phi_2 = \frac{1}{\sqrt{2}} v_2 \begin{pmatrix} \Phi_2^+ \\ \Phi_2^0 \end{pmatrix} \quad (2.19)$$

These models contain five Higgs bosons, with two charged scalars, and three neutral bosons. In this section we describe the two-Higgs-doublet potential, the spectrum of physical states, and the strength and form of the H^\pm couplings to fermions.

2.4.1 The Higgs Sector

In the two-Higgs-doublet model, the Higgs potential and the pattern of symmetry breaking are much more complicated than in the minimal SM. One of the principle requirements is that the vacuum state should conserve charge. In Section 2.3.2, we found that for a single Higgs doublet, one can always perform an $SU(2) \times U(1)$ rotation such that the vacuum expectation value of the Higgs field only has a real and neutral component. This can be achieved for one of the doublets in the two-doublet model, while in general the other one will have real and complex

components [30],

$$\langle \Phi_1 \rangle_0 = \frac{1}{\sqrt{2}} \begin{pmatrix} 0 \\ v_1 \end{pmatrix}, \quad \langle \Phi_2 \rangle_0 = \frac{1}{\sqrt{2}} v_2 \begin{pmatrix} e^{i\rho} \sin \alpha \\ e^{i\sigma} \cos \alpha \end{pmatrix}. \quad (2.20)$$

If $\alpha \neq 0$, then the electric charge operator will not leave the vacuum state invariant, $Q\langle \Phi_2 \rangle_0 = \frac{1}{2}(\tau_3 + Y)\langle \phi \rangle_0 \neq 0$, and charge conservation will be violated. In general, the quantities ρ , σ and α will depend in a complicated way on the values of the parameters of the potential [31, 32, 30]. The parameters should always be chosen so that electric charge is conserved.

The two-Higgs-doublet potential is a superposition of all the possible $SU(2)$ -invariant terms, which don't exceed dimension four so that the theory is renormalizable [31, 29, 32]. In addition, it is customary to impose invariance under the symmetry $\Phi_1 \rightarrow -\Phi_1$, which is done for simplification [11, 33, 34]. In addition to conserving charge, the potential must remain bounded from below. For spontaneous symmetry breaking it must achieve a nonzero vacuum expectation value for at least one of the two doublets. These constraints are clearly satisfied for the potential [11, 33, 34]

$$\begin{aligned} V(\Phi_1, \Phi_2) = & \lambda_1(\Phi_1^\dagger \Phi_1 - v_1^2)^2 + \lambda_2(\Phi_2^\dagger \Phi_2 - v_2^2)^2 \\ & + \lambda_3 \left[(\Phi_1^\dagger \Phi_1 - v_1^2) + (\Phi_2^\dagger \Phi_2 - v_2^2) \right]^2 \\ & + \lambda_4 \left[(\Phi_1^\dagger \Phi_1)(\Phi_2^\dagger \Phi_2) - (\Phi_1^\dagger \Phi_2)(\Phi_2^\dagger \Phi_1) \right] \\ & + \lambda_5 \left[\text{Re}(\Phi_1^\dagger \Phi_2) - v_1 v_2 \cos \xi \right] \\ & + \lambda_6 \left[\text{Im}(\Phi_1^\dagger \Phi_2) - v_1 v_2 \sin \xi \right]. \end{aligned} \quad (2.21)$$

The λ_i are all real by hermeticity. If we also assume that they are non-negative, then by inspection, the minimum of the potential ($V = 0$) is

$$\langle \Phi_1 \rangle = \begin{pmatrix} 0 \\ v_1 \end{pmatrix}, \quad \langle \Phi_2 \rangle = \begin{pmatrix} 0 \\ v_2 e^{i\xi} \end{pmatrix} \quad (2.22)$$

The fact that $V(0,0) > 0$ indicates that the symmetry is spontaneously broken. Since the CP operator transforms $\Phi \rightarrow \Phi^*$ [35], there will be CP violation in the Higgs sector if $\sin\xi \neq 0$. However, we expect $\sin\xi \approx 0$, since CP violation is generally a small effect. It should be noted that in supersymmetric models, $\lambda_5 = \lambda_6$ so that the last two terms of this potential can be combined and the phase ξ can be rotated away [11]. Thus we assume that $\xi = 0$.

2.4.2 Gauge Boson mass spectrum

With two doublets of complex fields, there will be eight degrees of freedom in the Higgs fields before symmetry breaking. Since this is four more than exists in the minimal SM, we expect a total of five physical Higgs bosons as a result of spontaneous symmetry breaking, rather than just one.

In the SM, there is a single term in the Lagrangian corresponding to the kinetic energy of the Higgs doublet, $(\mathcal{D}_\mu\phi)^\dagger(\mathcal{D}^\mu\phi)$ (Eq. 2.8). With two Higgs doublets, there will be two kinetic energy terms. As a result, the W^\pm and Z^0 bosons “get” their masses from both expectation values; their masses are given by the minimal SM expressions with v replaced by $\sqrt{2(v_1^2 + v_2^2)}$ (see Section 2.3.2),

$$2(v_1^2 + v_2^2) = v^2 = (246 \text{ GeV})^2. \quad (2.23)$$

This implies that the parameter ρ , which measures the relative strength of the weak charged and neutral currents (Eq. 2.12), is still predicted to be its SM value of 1. In this respect, the two-Higgs-doublet model is a very natural extension of the SM.

The potential energy term in the Lagrangian must be treated separately from the kinetic energy terms. To begin with, it is convenient to break up the Higgs

doublets into a real fields $\{\phi_i\}$, where $i = 1-8$,

$$\Phi_1 = \begin{pmatrix} \Phi_1^+ \\ \Phi_1^0 \end{pmatrix} = \begin{pmatrix} \phi_1 + i\phi_2 \\ \phi_3 + i\phi_4 \end{pmatrix}, \quad \Phi_2 = \begin{pmatrix} \Phi_2^+ \\ \Phi_2^0 \end{pmatrix} = \begin{pmatrix} \phi_5 + i\phi_6 \\ \phi_7 + i\phi_8 \end{pmatrix} \quad (2.24)$$

Since mass terms in the Lagrangian are of the form $\frac{1}{2}m^2\phi^2$, we can construct the mass matrix M from

$$M_{ij}^2 = \frac{1}{2} \frac{\partial^2 V}{\partial \phi_i \partial \phi_j} \quad (2.25)$$

This is an 8×8 matrix, but when $\xi = 0$, it separates into a series of 2×2 matrices [34]. The mass matrix for the charged Higgs boson corresponds to the indices $i = 1, 2, 5$ and 6 according to expression 2.24, and is composed of two identical 2×2 matrices of the form

$$\lambda_4 \begin{pmatrix} v_2^2 & -v_1 v_2 \\ -v_1 v_2 & v_1^2 \end{pmatrix} \quad (2.26)$$

The non-zero eigenvalue and its associated eigenvector give

$$m_{H^\pm}^2 = \lambda_4(v_1^2 + v_2^2) \quad (2.27)$$

$$H^\pm = -\Phi_1^\pm \sin\beta + \Phi_2^\pm \cos\beta \quad \text{with } \beta = \tan^{-1} \left(\frac{v_2}{v_1} \right) \quad (2.28)$$

Thus we see that β is the angle that rotates the charged scalar (and pseudoscalar, see below) fields into their mass eigenstates. The parameter $\tan\beta$ plays a crucial role in the phenomenology of the charged Higgs boson.

Due to the CP-invariance of the potential, the real and imaginary parts of the neutral scalar fields decouple [11, 33, 34]. In the imaginary CP-odd sector, there exists a pseudoscalar A^0 ,

$$A^0 = \sqrt{2}(-\text{Im}\Phi_1^0 \sin\beta + \text{Im}\Phi_2^0 \cos\beta) \quad (2.29)$$

$$m_{A^0}^2 = \lambda_6(v_1^2 + v_2^2). \quad (2.30)$$

The CP-even sector contains two physical Higgs scalars

$$H^0 = \sqrt{2} [(\text{Re}\phi_1^0 - v_1) \cos \alpha + (\text{Re}\phi_2^0 - v_2) \sin \alpha] \quad (2.31)$$

$$h^0 = \sqrt{2} [-(\text{Re}\phi_1^0 - v_1) \sin \alpha + (\text{Re}\phi_2^0 - v_2) \cos \alpha] \quad (2.32)$$

where the corresponding masses and mixing angle α are complicated functions of the parameters of the potential [11]. In summary, our Higgs doublets may be written in terms of the physical boson states [34]

$$\Phi_1 = \begin{pmatrix} -H^+ \sin \beta \\ v_1 + \sqrt{\frac{1}{2}}(H^0 \cos \alpha - h^0 \sin \alpha - iA^0 \sin \beta) \end{pmatrix} \quad (2.33)$$

$$\Phi_2 = \begin{pmatrix} H^+ \cos \beta \\ v_2 + \sqrt{\frac{1}{2}}(H^0 \sin \alpha + h^0 \cos \alpha + iA^0 \cos \beta) \end{pmatrix} \quad (2.34)$$

2.4.3 The Yukawa Couplings of H^\pm to Fermions

The general two-Higgs-doublet model predicts tree-level flavor-changing neutral currents (FCNCs). This can be seen from the most general couplings between the Higgs fields and fermions. Mass terms for the down-type quarks have the form

$$\begin{aligned} \mathcal{L}_{\text{Yuk}} &= \Gamma_{mn}^1 q'_{Lm} \Phi_1 d'_{Rn} + \Gamma_{mn}^2 q'_{Lm} \Phi_2 d'_{Rn} + H.C. \\ &= \Gamma_{mn}^1 d'_{Lm} v_1 d'_{Rn} + \Gamma_{mn}^2 d'_{Lm} v_2 d'_{Rn} + H.C. \end{aligned} \quad (2.35)$$

where in the second expression, the vacuum expectation values of the fields Φ_1 and Φ_2 have been substituted. As with the SM couplings (see Appendix B), before combining the first two terms in the expression with their hermitian conjugates, the following mass matrix must be diagonalized,

$$M_{mn}^D = \Gamma_{mn}^1 v_1 + \Gamma_{mn}^2 v_2 \quad (2.36)$$

We found that in the SM, where there is only one doublet, then diagonalization of M^D automatically diagonalizes the Yukawa coupling matrix Γ^D , so that the

resulting Higgs interactions are flavor diagonal (see Section 2.3.3). However, with two Higgs doublets, diagonalizing M^D does not necessarily diagonalize the coupling matrices Γ^1 and Γ^2 [31]. The resulting interactions are not flavor diagonal - for example, they can lead to tree-level $\bar{d}\phi s$ couplings [31].

The FCNCs can be eliminated by restricting the couplings of Higgs bosons to fermions. There are at least four distinct ways of doing this. Models of type I have all the fermions couple to one doublet only. Models of type II have up-type quarks couple to one doublet, and down-type quarks and charged leptons couple to the other doublet. Both of these models satisfy a theorem by Glashow and Weinberg, which states that tree-level FCNCs mediated by Higgs bosons will be absent if all fermions of a given electric charge couple to no more than one Higgs doublet [11]. There are other models (type III and IV) that violate this theorem, and require fine tuning to avoid experimental bounds [11]. They will not be discussed here.

Forcing invariance of the Yukawa coupling terms under the following discrete symmetries will force the Model I or Model II couplings [31],

$$(\text{Model I}) \quad \Phi_2 \rightarrow -\Phi_2, \quad (\text{Model II}) \quad \Phi_2 \rightarrow -\Phi_2, \quad d'_{Rn} \rightarrow -d'_{Rn} \quad (2.37)$$

Since these symmetries do not seem to correspond to any physical symmetry, imposing them is essentially fine-tuning the model. In this sense, the two-Higgs-doublet extension to the SM is very unnatural.

However, supersymmetric models require Model II couplings, which arise very naturally in the theory [11, 12, 36]. No arbitrary discrete symmetries such as those in Eq. 2.37 are needed. For this reason, we choose to be motivated by supersymmetry, and only treat Type II couplings in this thesis.

Thus we assume that one doublet, Φ_2 , gives mass to up-type quarks, and the

other, Φ_1 , gives mass to down-type quarks and charged leptons. Thus we have

$$\mathcal{L}_{\text{Yukawa}} = \sum_{m=1}^3 \Gamma_{Lm}^{\ell} \bar{\ell}_m \Phi_1 e_{Rm} + \sum_{m,n=1}^3 \Gamma_{mn}^d \bar{q}'_{Lm} \Phi_1 d'_{Rn} + \sum_{m,n=1}^3 \Gamma_{mn}^d \bar{q}'_{Lm} \tilde{\Phi}_2 u'_{Ln} + H.C. \quad (2.38)$$

A more general coupling would have these terms, as well as the corresponding terms with Φ_1 exchanged with Φ_2 . The Yukawa couplings of the H^{\pm} to fermions are found by substituting the physical Higgs states given in Eqs. 2.33 and 2.34 for Φ_1 and Φ_2 . I analyze these couplings in Appendix B, and give the results here. The H^+ coupling to a charged lepton and a neutrino $e_i \nu_i$, or a quark-antiquark pair $\bar{u}_i d_i$, are given by the terms in the Lagrangian that are proportional to $e_i \nu_i H^+$ and $\bar{u}_i d_i H^+$, respectively.

$$\mathcal{L}_{e_i \nu_i H^+} = -\frac{g \tan \beta}{2\sqrt{2}M_W} m_{ei} \nu_i (1 + \gamma^5) e_i H^+ \quad (2.39)$$

$$\mathcal{L}_{\bar{u}_i d_i H^+} = -\frac{g \{V_{CKM}\}_{ij}}{2\sqrt{2}M_W} \bar{u}_i [(1 - \gamma^5) m_i^u \cot \beta + (1 + \gamma^5) m_j^d \tan \beta] d_j H^+ \quad (2.40)$$

Similarly to the SM Higgs boson, the charged Higgs boson couples in proportion to the fermion mass. In contrast, the factors $\tan \beta$ or $\cot \beta$ also appear, which arise from the rotation of the charged Higgs fields into mass eigenstates given by Eqs. 2.26 and 2.28. The tbH^+ Yukawa coupling is summarized in Fig. 2.2. Note that at low $\tan \beta$, H^{\pm} primarily couples to up-type quarks, while at large $\tan \beta$, H^{\pm} couples to down-type quarks (and also charged leptons, which is not shown).

2.5 Properties of the Top Quark Decay $t \rightarrow H^{\pm} b$

As I described in the introduction, I search for top quark decays to a charged Higgs boson. It is the Yukawa couplings of the H^{\pm} to fermions that determines the branching fractions for the top quark and H^{\pm} . As indicated in Fig. 2.2, these couplings become arbitrarily large in the limit of small and large $\tan \beta$. This

tbH^+ coupling

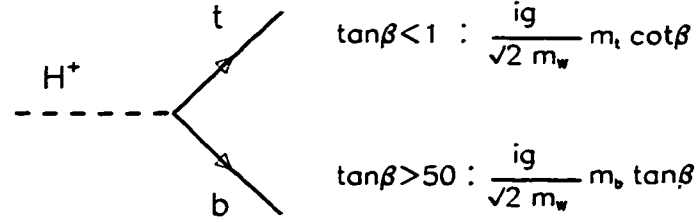


Figure 2.2: The tbH^+ Yukawa coupling at small and large values of $\tan\beta$.

divergent behavior results in a limited range of $\tan\beta$ in which perturbation theory can be applied, and large widths for the top quark and H^\pm .

2.5.1 Decays of the Top Quark and the H^\pm

The Higgs couples preferentially to the heaviest fermions. However, in a high energy proton-antiproton ($p\bar{p}$) collision, it is only the lightest valence quarks that carry a significant fraction of the parent hadrons' momentum, and are able to produce a hard scattering event. For this reason, the rate at which H^\pm can be directly produced in $p\bar{p}$ collisions at the Tevatron is extremely small [37].

However, the two Tevatron experiments currently hold the world's only sample of top quark events. The large top quark mass of $M_{\text{top}} = 175 \text{ GeV}/c^2$ will result in a large tbH^+ Yukawa coupling, as long as $\tan\beta$ is also small or large. Thus, at the Tevatron, if $M_{H^\pm} \lesssim M_{\text{top}} - M_b$, the primary mechanism for charged Higgs production is through the top decay $t \rightarrow H^\pm b$, which will compete with the SM decay $t \rightarrow W^\pm b$. The parameters M_{top} , M_{H^\pm} and $\tan\beta$ determine the dominant decay modes both for the top quark and the charged Higgs boson, which are summarized below.

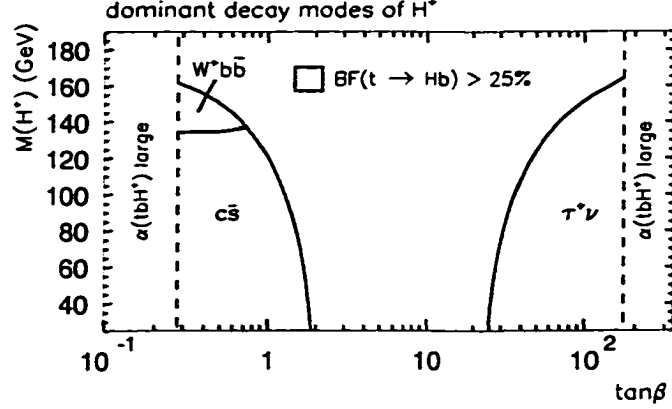


Figure 2.3: Regions in the M_{H^\pm} vs. $\tan\beta$ plane for which $\mathcal{B}(t \rightarrow H^\pm b) > 25\%$, and the dominant decay mode of H^\pm in these regions, assuming $M_{\text{top}} = 175 \text{ GeV}/c^2$.

• Top decay modes :

1. $t \rightarrow W^+ b$
2. $t \rightarrow H^+ b$

• H^+ decay modes :

1. $H^+ \rightarrow c\bar{s}$
2. $H^+ \rightarrow \tau^+ \nu$
3. $H^+ \rightarrow t^* \bar{b} \rightarrow W^+ b\bar{b}$

Later, I will demonstrate that CDF is sensitive to top quark branching fractions $\mathcal{B}(t \rightarrow H^\pm b)$ of 25% or larger. Fig. 2.3 shows the corresponding regions in the M_{H^\pm} vs. $\tan\beta$ plane for the measured top mass of $175 \text{ GeV}/c^2$, and the dominant decay modes of H^\pm in these regions. Until recently it was believed that an H^\pm produced from a top quark decay would itself decay into either the light quark pair cs or the tau-neutrino pair $\tau\nu$ [38, 11], depending on the value of $\tan\beta$. The cs decay mode dominates at small values of $\tan\beta < 1$, while the $\tau\nu$ decay mode dominates for larger values ($\tan\beta > 5$). Recently, however, it has been recognized [39] that the decay $H^+ \rightarrow t^* \bar{b} \rightarrow W^+ b\bar{b}$ may occur with the exchange of a virtual top quark. At small values of $\tan\beta$ this decay is enhanced due to a large Yukawa coupling that is

proportional to $M_{\text{top}} \cot \beta$, but suppressed due to the off-mass-shell top propagator. As long $M_{H^\pm} \gtrsim 135 \text{ GeV}/c^2$ so that the t^* does not have to be far off its mass shell of $175 \text{ GeV}/c^2$, this decay mode will dominate at low values of $\tan \beta$.

2.5.2 The Perturbative Range of $\tan \beta$

Fig. 2.3 also shows regions in the M_{H^\pm} - $\tan \beta$ plane for which the tbH^+ coupling becomes too large to be treated perturbatively. At $\tan \beta \ll 1$ and $\tan \beta \gg 1$, the tbH^+ couplings (Fig. 2.2) become arbitrarily large. This means that the perturbative treatment used to calculate physical quantities such as top quark width [11, 38] loses its predictive power.

A criteria exists for determining where the couplings are no longer perturbative [38, 40]. We can make an analogy with QED, in which the coupling strength between an electron and a photon is e , and the fine structure constant is $\alpha = e^2/4\pi$. For perturbation theory to work, $\alpha \leq 1$. If we require $\alpha \leq 1$ for the tbH^+ Yukawa couplings shown in Fig. 2.2, we derive the following relations:

$$\frac{g^2 m_{\text{top}}^2 \cot^2 \beta}{2M_W^2} \frac{1}{4\pi} \leq 1 \quad , \quad \frac{g^2 m_b^2 \tan^2 \beta}{2M_W^2} \frac{1}{4\pi} \leq 1 \quad (2.41)$$

This leads to the requirement that $\tan \beta$ satisfies

$$0.28 \leq \tan \beta \leq 170 \quad , \quad (2.42)$$

where a b -quark mass $m_b(\mu = M_{\text{top}})$ of $3.64 \text{ GeV}/c^2$ has been used, calculated at a renormalization scale of the top mass [38] (see Appendix A for details). Clearly there is no sharp boundary between values of the coupling that are small enough so that perturbation theory works, and those values for which it breaks down. The matter is further complicated by the fact that there can be large positive or negative electroweak corrections to the Yukawa couplings in the minimal supersymmetric model (MSSM) [41], which can effectively alter the perturbative boundaries. For

this reason, we address the entire range defined by Eq. 2.42, with the realization that near the boundaries, our modeling may be unphysical. It should be noted that within this perturbative range for the tbH^+ coupling, the $\tau^+\nu H^+$ and $c\bar{s}H^+$ couplings are also perturbative by a safe margin.

2.5.3 Large Top Quark and H^\pm Widths

Large Yukawa couplings near the edges of the perturbative region result in top quark and H^\pm widths that can exceed several GeV. The H^\pm width Γ_H is largest at high values of $\tan\beta$, where the H^\pm couples to the τ lepton,

$$\Gamma_H = \frac{g^2 m_\tau^2 \tan^2 \beta M_{H^\pm}}{32\pi m_W^2}. \quad (2.43)$$

This is shown as a function of $\tan\beta$ for several values of M_{H^\pm} in Fig. 2.4. Notice that since Γ_H is proportional to $M_{H^\pm} \tan^2 \beta$, it can exceed 10 GeV for high $\tan\beta$ and M_{H^\pm} close to M_{top} . For these near-threshold top quark decays, the large Γ_H results in a spread-out distribution of M_{H^\pm} around its nominal value. Furthermore, this mass distribution will not be symmetric, since the low-mass tail will be phase-space enhanced. Under these circumstances, the calculation of the partial width $\Gamma(t \rightarrow H^\pm b)$ is meaningless, since it assumes a particular value of M_{H^\pm} . Rather, it is correct to treat the H^\pm as a propagator, and calculate the three-body decay partial width $\Gamma(t \rightarrow H^\pm b \rightarrow \tau \nu b)$. This calculation has been performed by myself, and is shown in Appendix D. Monte Carlo modeling of a large Γ_H is detailed in Chapter 5.

To further complicate matters, the top quark width Γ_{top} can also be large. This is shown alongside Γ_H in Fig. 2.4. In the perturbative region, the total top quark width can exceed 15 GeV, which should be compared with the SM partial width $\Gamma(t \rightarrow W^\pm b) = 1.4$ GeV. The Γ_{top} is largest for a large mass difference $M_{\text{top}} - M_{H^\pm}$, for which the most phase space exists for the daughter particles H^\pm and b . At large

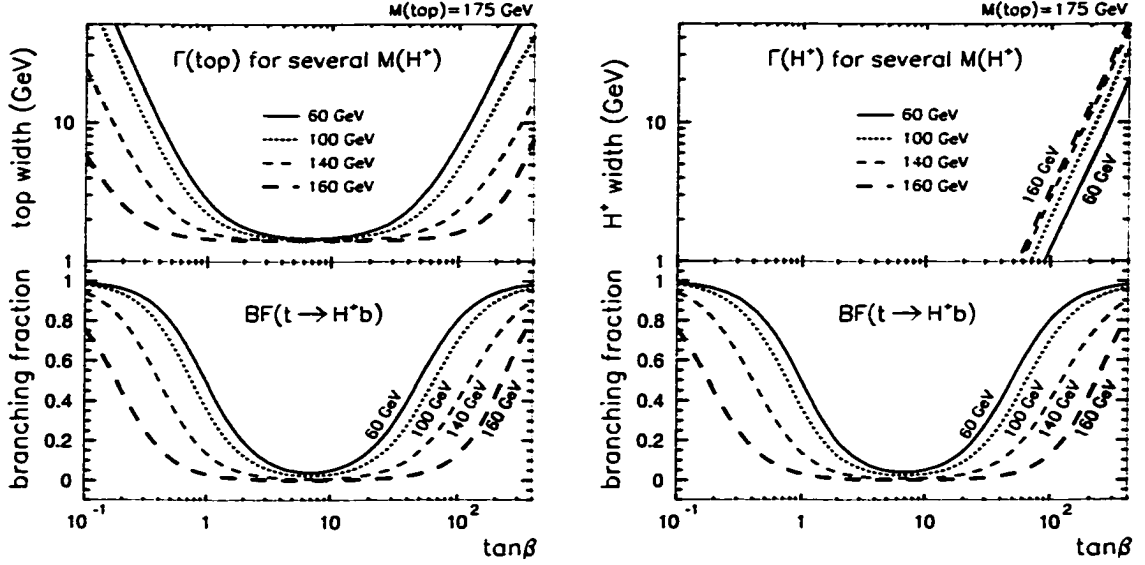


Figure 2.4: The width of the top quark and the H^\pm as a function of $\tan\beta$. The shaded regions correspond to $\tan\beta < 0.28$ and $\tan\beta > 170$, which are approximate regions where the tbH^+ coupling is no longer perturbative and the expressions used to calculate the top width are invalid.

values of $\tan\beta$, where Γ_H is also large, the top quark width is the sum of the partial widths $\Gamma_{\text{top}} = \Gamma_{t \rightarrow Wb} + \Gamma_{t \rightarrow \tau\nu b}$.

In this analysis, we model the top width with a Breit-Wigner resonance. In Chapter 5.4, we discuss a limitation of MC simulations where Γ_{top} is extremely large. For this reason, we limit the scope of this analysis to regions where $\Gamma_{\text{top}} \leq 15 \text{ GeV}$.

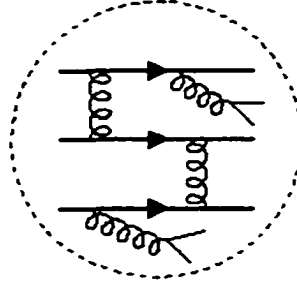


Figure 2.5: The currently accepted view of the proton, containing three valence quarks (uud) and a sea of gluons and quark-antiquark pairs. This figure is adopted from Fig. 9.7 in Ref. [10].

2.6 Top Quark Production

At the Tevatron, the $t\bar{t}$ final state is produced in proton-antiproton ($p\bar{p}$) collisions, through a hard scattering process between the quarks and gluons. It is not immediately obvious that one can use perturbative QCD to calculate the rate of $t\bar{t}$ production, since the proton itself is a complex object. Figure 2.5 represents the currently accepted view of the proton, which contains three valence quarks (uud), and a sea of gluons and quark-antiquark pairs. The quarks continually radiate and reabsorb gluons, which themselves may radiate quark-antiquark pairs or combine with other gluons. Generally these interactions occur at small momentum transfers Q , and are not calculable using perturbative QCD. These are also known as long-distance interactions, since their low Q^2 is characteristic of a long wavelength. In contrast, the production mechanism that produces the heavy top-antitop ($t\bar{t}$) pair is a high-momentum transfer (short-distance) interaction, which should be perturbatively calculable.

It is the factorization theorem that justifies the separation of long-distance, non-perturbative effects from the short-distance, perturbative hard scattering [42].

The cross section for a hard scattering process initiated by two hadrons is given by [17, 43]

$$\sigma(s) = \sum_{i,j} \int dx_1 dx_2 f_i(x_1, \mu^2) f_j(x_2, \mu^2) \hat{\sigma}_{ij}(\hat{s}, m_Q, \alpha_s(\mu)), \quad (2.44)$$

where the sum is carried over the initial parton states, and the integrations are performed over the two parton momentum fractions x_i . The terms in Eq. 2.44 have the following meanings.

- $f_i(x_i, \mu^2)$ is known as a parton distribution function (PDF), which gives the probability distribution for finding a parton of species i within the proton, with fraction x_i of the proton momentum P_i .
- $\hat{\sigma}_{ij}$ is the short-distance cross section for the scattering of partons of types i and j , which is perturbatively calculable.
- μ is the renormalization scale. There is no rigorous prescription for choosing its value, but usually it is set to the characteristic energy scale of the hard scattering².
- $\alpha_s(Q^2)$ is the strong running coupling constant. It decreases with increasing Q^2 , and is therefore small in short-distance interactions.
- \hat{s} is the square of the center-of-mass energy in the $i - j$ parton system, and is related to the $p\bar{p}$ center-of-mass energy \sqrt{s} by $\hat{s} = x_1 x_2 s$.
- m_Q is the mass of the heavy quark.

The hard-scattering cross section $\hat{\sigma}_{ij}$, when it is perturbatively calculated, contains contributions that occur on a time scale that is long compared to that of the

²Here we are not making a distinction between renormalization scale and factorization scale. They are set equal, as in most cross section calculations [17].

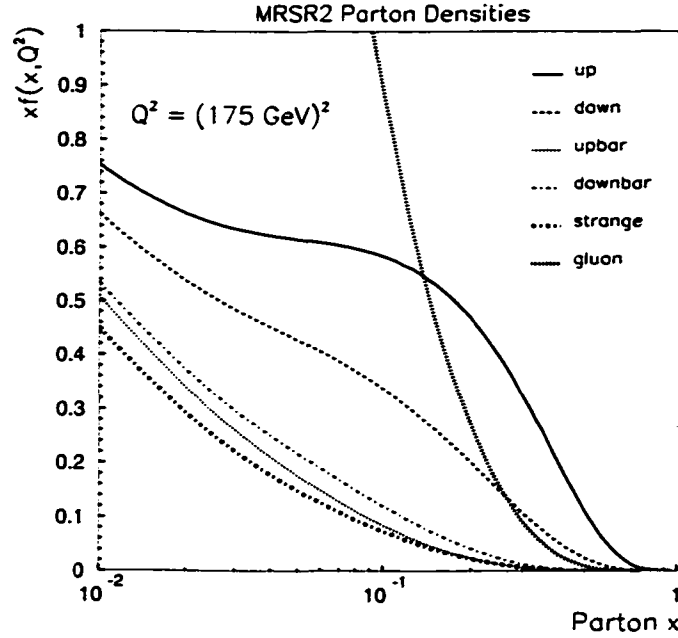


Figure 2.6: The parton densities $xf(x, Q^2 = M_{\text{top}}^2)$ for quarks and gluons, from the MRSR2 [44] set. The up and down quark curves are the sum of valence quarks, which contribute predominantly at $x \approx \frac{1}{3}$, and sea quarks, which increase as x decreases due to the increased probability for gluons to split into $q\bar{q}$ pairs. The gluon distribution dominates at $x < 0.15$.

hard scattering. These pieces are factored out and absorbed into the description of the incoming hadrons [43]. Thus, $\hat{\sigma}_{ij}$ does not depend on the type of incoming hadron. Roughly speaking, any propagator that is off-shell by μ^2 or more will contribute to $\hat{\sigma}_{ij}$, while below this scale, it gets grouped into the PDFs [42]. As a result, the PDFs depend on μ . Parton distributions for the MRSR2 set [44], derived from a global analysis, are shown in Fig. 2.6, for $Q^2 = M_{\text{top}}^2$.

The leading-order diagrams $\mathcal{O}(\alpha_s^2)$ for $t\bar{t}$ production are given in Fig. 2.7. Calculations of the cross section through next-to-leading order (NLO), $\mathcal{O}(\alpha_s^3)$ have been performed. In addition, the NLO result has been corrected for initial-state

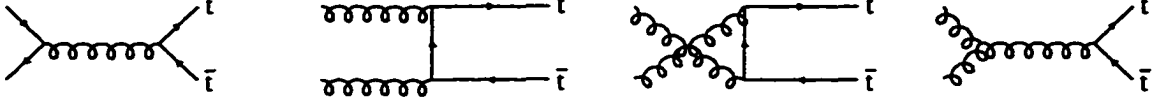


Figure 2.7: The leading order (α_s^2) diagrams for $t\bar{t}$ production in $p\bar{p}$ collisions. The first diagram represents $q\bar{q}$ annihilation, and the remaining three are gluon-gluon fusion diagrams. The total $t\bar{t}$ cross section contains only about a 10% contribution from gluon-gluon fusion.

$t\bar{t}$ Cross Sections calculated for $M_{\text{top}} = 175 \text{ GeV}/c^2$

$\sigma_{t\bar{t}}$	accuracy of calculation	Reference
$5.06^{+0.13}_{-0.36}$	NLO + NLL(gluon)	Bonciani, Catani, Mangano, Nason [17]
$5.52^{+0.07}_{-0.42}$	NLO + LL(gluon)	Berger, Contopanagos [18]
$4.95^{+0.70}_{-0.40}$	NLO + LL(gluon)	Laenen, Smith, van Neerven [19]

Table 2.2: Three theoretical calculations of $\sigma_{t\bar{t}}$, where the central value is calculated assuming $M_{\text{top}} = 175 \text{ GeV}/c^2$, and a renormalization scale $\mu = M_{\text{top}}$. For each calculation, the uncertainty results from changing μ from $M_{\text{top}}/2$ to $2M_{\text{top}}$.

soft gluon radiation to all orders in the coupling strength. This has been done to a level of accuracy called the leading-log (LL) level [18, 19], and to another, more accurate level called the next-to-leading-log (NLL) level [17]. These cross sections are shown in Table 2.2.

Finally, I should mention that with a theoretical width of at least 1.4 GeV [45], the top quark lifetime is about 10 times smaller than the typical time scale for hadronization. As a result, the top quark decays like a free quark, since there is not enough time for it to fragment and form a hadron.

2.7 Tevatron Top Quark Results

In Chapter 1, I introduced the dilepton and lepton+jets decay channels, and gave the results of the CDF counting experiments in each of these modes. In this section, I review these modes in a little more detail, since they are used in this analysis. Next, I review the top quark results obtained by the CDF and DØ collaborations over the past few years. The results are divided up into $t\bar{t}$ cross section measurements, top mass measurements, and kinematics of top events.

2.7.1 The Dilepton and Lepton+Jets Decay Modes

The dilepton and lepton+jets decay channels are optimized for the selection of events consistent with the SM decay $t\bar{t} \rightarrow WbW\bar{b}$. The dilepton channel selection criteria are used to identify $t\bar{t}$ events with two leptonic W^\pm decays, requiring two high- P_T electrons or muons, \cancel{E}_T from the undetected neutrinos, and two jets from hadronization of the two b quarks. The lepton+jets channel selection criteria are used to identify $t\bar{t}$ events with one leptonic and one hadronic W^\pm decay, requiring a high- P_T electron or muon, \cancel{E}_T from the undetected neutrino, and three or more jets from the b -quarks and the $W^\pm \rightarrow q\bar{q}'$ decay. This search uses both the lepton+jets and dilepton decay topologies.

The background in the dilepton channel comes from W^+W^- production, $Z^0 \rightarrow \tau\tau$, Drell-Yan production, and lepton misidentification in events with one real lepton. In the dilepton mode it is sufficient to make various kinematic and topological cuts to suppress the non- $t\bar{t}$ backgrounds [46, 23]. In the lepton+jets mode this is not the case. The background comes primarily from QCD production of W^\pm bosons produced with multiple jets. This background rate is roughly four times larger than the rate expected from $t\bar{t}$ production [47]. To reduce this background, the lepton+jets mode relies on the identification of at least one of the two b quarks

among the decay products of a $t\bar{t}$ event. More specifically, we rely on the fact that the b quark produced at the primary vertex of an event will immediately (within $\approx 10^{-23}$ s) hadronize to a B -hadron, which has a long lifetime ($c\tau = 470 \mu\text{m}$). We use the CDF silicon vertex detector (SVX) to locate decay vertices of B hadrons that are separated from the primary vertex of an event by as much as several mm, as a result of this long lifetime. The b -quarks identified this way are called “SVX tags”. By requiring one SVX tag in each event, the $t\bar{t}$ content of the lepton+jets sample is predicted to increase from 20% to 75% [47, 22]. Another technique for identifying b quarks, which is not used in this analysis, is to search for additional electrons and muons resulting from semileptonic decays of B hadrons. These are called “soft lepton tags” (SLTs), because typically the leptons have a much lower momentum than the primary leptons in the event from W^\pm decay.

In addition to these channels, there are two other decay modes that have been observed. The first of these is a class of dilepton events that contain one electron or muon, and a tau lepton identified through its hadronic decay mode [48]. The signal/background ratio for these “tau dilepton” events is much lower than that for e - e , e - μ and μ - μ dilepton events, primarily due to the relatively high rate at which generic QCD jets can fake the signature of a hadronically-decaying tau lepton. Tau dilepton events are not used in this analysis, since we want to maintain a high signal/background ratio. In addition, the H^\pm limits from this analysis will be better if $H^\pm \rightarrow \tau\nu$ decays are invisible to our $t\bar{t}$ selection criteria. The second class of events are found in the “all-hadronic” decay channel, which is optimized for $t\bar{t}$ events in which both W^\pm bosons decay to a light quark pair [15, 49]. Again, this decay channel is not used in this analysis.

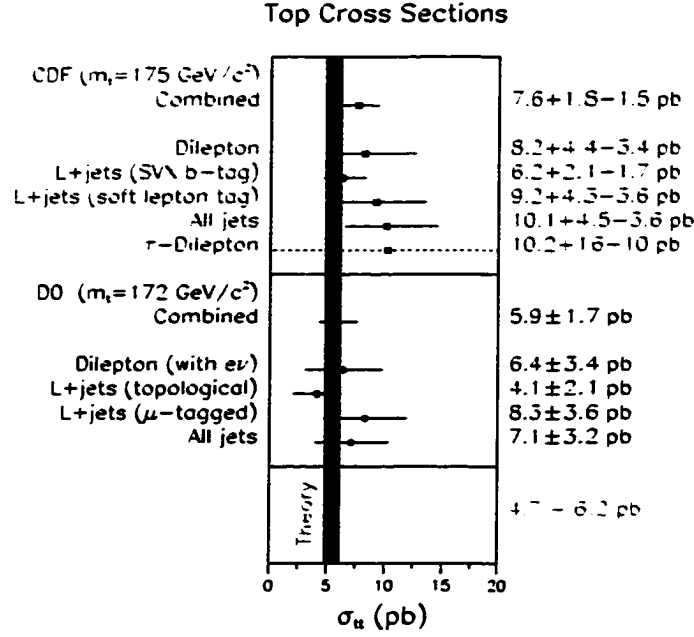


Figure 2.8: The values of $\sigma_{t\bar{t}}$ measured by the CDF and DØ Collaborations, in all the different decay channels observed. This figure is taken from Ref. [50].

2.7.2 Cross Section Measurements

Fig. 2.8 summarizes the cross-section measurements at the Tevatron, which are all consistent with one another. The combined CDF result is $\sigma_{t\bar{t}} = 7.6^{+1.8}_{-1.5}$ pb [22], while DØ finds $\sigma_{t\bar{t}} = 5.9 \pm 1.6$ pb [49]. Both of these numbers are consistent with the theoretical value of $\sigma_{t\bar{t}} \approx 5.0$ pb, discussed in Section 2.6.

It should be noted that all of these measurements assume only SM $t\bar{t}$ decays. This assumption is used when the cross section is calculated from the number of signal events observed in a particular decay channel. One must divide by the efficiency ϵ for $t\bar{t}$ events to pass the selection criteria of that channel, which is calculated assuming a $WbW\bar{b}$ final state.

$$\sigma_{t\bar{t}} = \frac{N_{\text{bkg}} - N_{\text{obs}}}{\epsilon \mathcal{L}} \quad (2.45)$$

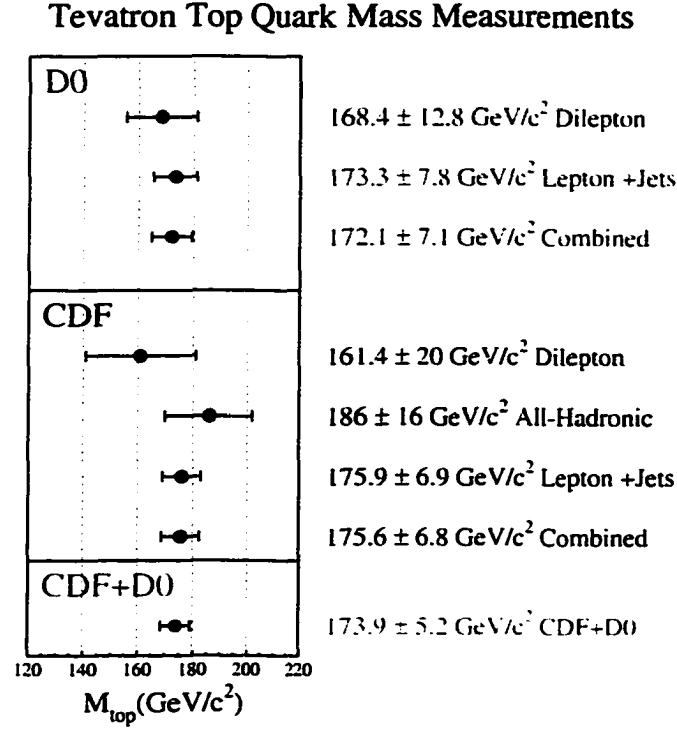


Figure 2.9: The values of M_{top} measured by the CDF and DØ Collaborations, corresponding to different decay channels. This figure is taken from Ref. [51].

If the two-Higgs-doublet model is correct, then there is a good chance that we are currently *underestimating* $\sigma_{t\bar{t}}$, since ϵ is much smaller than the SM value for much of the parameter space in the M_{H^\pm} - $\tan\beta$ plane. However, this seems unlikely, since the measured values of $\sigma_{t\bar{t}}$, calculated using SM efficiencies, are in agreement with the theoretical value of $\sigma_{t\bar{t}}$.

2.7.3 Top Mass Measurements

The top quark measurements at the Tevatron are all consistent with one another. Fig. 2.9 shows these measurements. The best number is the combined CDF and DØ result, which gives $173.9 \pm 3.6(\text{stat.}) \pm 3.8(\text{syst.}) \text{ GeV}/c^2$ [51].

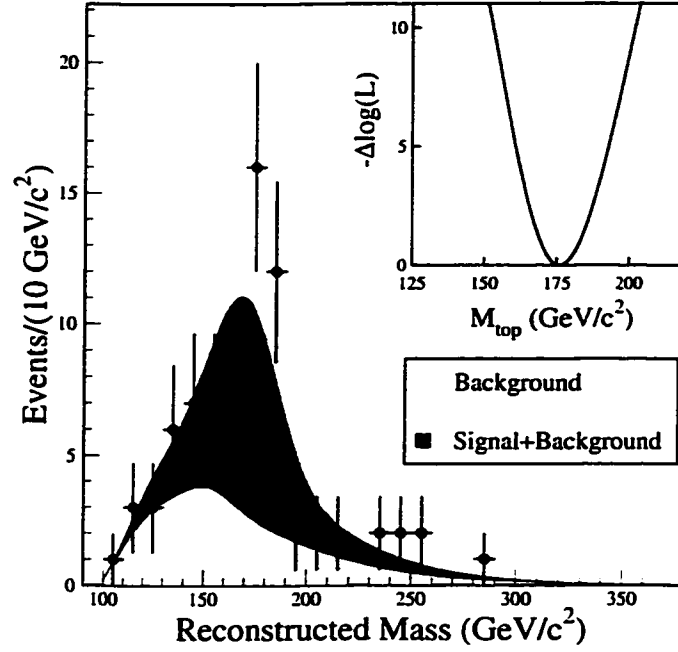


Figure 2.10: The top mass measured by CDF using the lepton+jets sample. This figure is taken from Ref. [52].

These mass measurements assume only SM top quark decays. For example, the best single mass measurement is made by CDF using lepton+jets events [52]. The events are divided into four orthogonal subsamples, depending upon whether they contain one SVX b -quark tag, two SVX tags, no SVX tags but an SLT tag, or no b -quark tags. The events are fit to the hypothesis of $t\bar{t}$ production followed by the following decays :

$$\begin{aligned}
 p\bar{p} &\rightarrow t\bar{t} + X \\
 t &\rightarrow W^+ b \rightarrow \ell^+ \nu_\ell b \quad (\text{or } q\bar{q}' b) \\
 \bar{t} &\rightarrow W^- \bar{b} \rightarrow q\bar{q}' \bar{b} \quad (\text{or } \ell^- \nu_\ell \bar{b})
 \end{aligned}$$

In this fit, the four most energetic jets in the event are matched to the four partons, consistent with tagging information, and a χ^2 minimization technique.

Fig. 2.10 shows the top mass distribution measured in the data, along with the expected mass distribution from $t\bar{t}$ events, and non- $t\bar{t}$ background events. While there is good agreement between the MC-predicted mass distribution and the one observed in data, the width of the data distribution is narrower than the MC distribution. Studies considering the outcome of many “trial experiments” indicate that there exists an 11% probability for obtaining a statistical uncertainty as small as the measured one [52]. Reasons for this have been explored in Ref. [53]. It is found that SM $t\bar{t}$ events, in which jet assignments are not correctly matched to the partons, tend to broaden the mass distribution. This can occur if one of the four most energetic jets in the event originates from initial or final state gluon radiation, and not one of the partons. Thus the data suggest that there may be more gluon radiation in the MC than there should be.

Given that incorrect jet-parton matching in a SM $t\bar{t}$ event results in a broadening of the mass distribution, it seems obvious that $t\bar{t}$ decays to topologies other than $WbW\bar{b}$ would also result in an equivalent, if not more dramatic, broadening of the top mass distribution. However, this has *not* been studied. Thus we conclude our discussion of the top mass results by stating that the observed mass distribution is consistent with only SM $t\bar{t}$ decays.

2.7.4 Kinematics of Events

CDF has reconstructed both the leptonic and the hadronic W^\pm decays in some $t\bar{t}$ events. Remember that lepton+jets events are primarily produced when one W^\pm decays leptonically and the other one decays hadronically, resulting in a $\ell\nu_\ell q\bar{q}'b\bar{b}$ final state. The transverse mass of the W^\pm may be reconstructed from the transverse momentum of the lepton and neutrino (E_T) in such events [46]. CDF has also observed hadronic W^\pm decays in these events, measuring $M_W =$

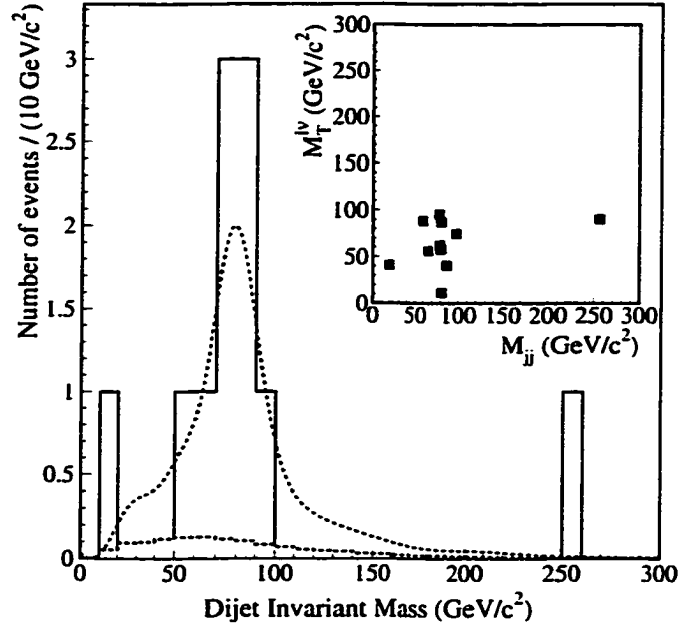


Figure 2.11: The dijet mass spectrum of the two untagged jets in double b -tagged lepton+jets events. The shaded curve shows the expected distribution from QCD $W^\pm + \text{jets}$ background, while the dashed curve shows the expected contribution from SM $t\bar{t}$ production plus background. The inset plots the transverse mass formed by the lepton and \cancel{E}_T for these events.

$77.2 \pm 3.5(\text{stat.}) \pm 2.9(\text{syst.}) \text{ GeV}/c^2$ with a peak significance of 3.3σ [54]. One method used to isolate this signal identifies both of the b quarks and the leptonic W^\pm decay in $W^\pm + 4 \text{ jets}$ events [54]. The hadronic W^\pm mass may be reconstructed from the dijet mass of the two remaining untagged jets. Fig. 2.11 shows this dijet mass for these double-tagged events. Eight events are observed in a mass window of 60-100 GeV/c^2 , while only 1.3 events are expected from non- $t\bar{t}$ background. The inset plot shows the transverse mass of the lepton and \cancel{E}_T for these events. The two reconstructed W^\pm peaks in these events give strong evidence

in favor of a $WbW\bar{b}$ final state. Both CDF and DØ have provided additional evidence that top quark kinematic distributions in data agree with MC predictions, assuming only SM $t\bar{t}$ decays [47, 55].

2.8 Existing Limits for H^\pm Production

There are many existing limits on H^\pm production, which are derived from studying both low and high-energy processes. Direct searches have been performed by experiments working at the energy frontier, including the CDF and DØ experiments at the Tevatron, and the ALEPH, DELPHI, L3, and OPAL experiments at LEP2. Remarkably, precision measurements of low-energy processes that are sensitive to H^\pm contributions also provide limits, which sometimes overlap and exceed the ones obtained by the high energy collider experiments. However, while the direct searches usually set limits that are essentially model independent, the indirect limits inferred from low-energy processes tend to be quite model dependent.

2.8.1 Direct Searches at the Tevatron and LEP2

The H^\pm will be produced predominantly through top quark decays at the Tevatron. In addition to the search described in this thesis, CDF has performed a direct search [56] for $t\bar{t}$ decays to $WbH\bar{b}$ and $HbH\bar{b}$ final states, where the H^\pm subsequently decays to $\tau\nu$. The expected event topologies are $Wb\tau\nu\bar{b}$ and $\tau\nu b\tau\nu\bar{b}$. Two event selection criteria are employed. The first requires at least one tau lepton and significant \cancel{E}_T , presumably from a $H^\pm \rightarrow \tau\nu$ decay; at least two jets from the b quarks; and one other lepton or jet. A second set of selection criteria is designed for events where the b jets have insufficient energy and are “lost”, which will happen if M_{H^\pm} is close to M_{top} and little energy is available to the b quarks. This second set of selection criteria requires just two τ leptons and significant \cancel{E}_T .

In this search, tau leptons are identified through their hadronic decays. A total of 7.3 ± 2.2 events are expected from non- $t\bar{t}$ background sources, while 7 candidate events are observed in the data. Charged Higgs masses as large as $137 \text{ GeV}/c^2$ have been excluded in the limit of large $\tan\beta$, assuming that $\sigma_{t\bar{t}} = 5.0 \text{ pb}$. The excluded regions from this search will be shown in Chapter 7, alongside the limits from my search.

The DØ Collaboration has excluded parameter space in the two-Higgs-doublet model using a search almost identical to the one described in this thesis [57]. The DØ limits will be discussed in Chapter 7.

The four experiments at the Large Electron-Positron II (LEP2) collider have recorded data from e^+e^- collisions at center-of-mass energies approaching 200 GeV. In these collisions, charged Higgs bosons are produced in pairs via couplings to the Z^0 boson and the photon, $e^+e^- \rightarrow Z^0/\gamma \rightarrow H^+H^-$. For $\sqrt{s} = 183 \text{ GeV}$, the cross section for this process ranges from about 0.55 pb for $M_{H^\pm} = 50 \text{ GeV}/c^2$ to 0.1 pb for $M_{H^\pm} = 80 \text{ GeV}/c^2$ [58]. Each experiment has used several tens of pb of data collected at (or close to) this energy, combined with lower energy data, to exclude H^\pm production.

In this energy range, the H^\pm will decay to the light quark pair cs or the lepton pair $\tau\nu$, resulting in the final states $c\bar{s}c\bar{s}$, $cs\tau\nu$, and $\tau^+\nu\tau^-\bar{\nu}$. These decays are identical to W^\pm decays, resulting in an irreducible background from events in which W^\pm bosons are pair produced, $e^+e^- \rightarrow W^+W^-$. This background, in addition to the low expected signal rate, renders almost hopeless the discovery of H^\pm with $M_{H^\pm} \gtrsim M_{W^\pm}$ [62]. However, M_{H^\pm} as large as $72 \text{ GeV}/c^2$ have been excluded. Table 2.3 lists the most recent published limits from LEP2. These are among the most stringent and model-independent limits for H^\pm production.

LEP2 Limits on the Mass of the Charged Higgs Boson

Experiment	M_{H^\pm} lower bound	best limit	highest Energy	Reference
L3	57.5 GeV/ c^2	70 GeV/ c^2	183 GeV	[59]
OPAL	59.5 GeV/ c^2	72 GeV/ c^2	183 GeV	[58]
DELPHI	54.5 GeV/ c^2	60 GeV/ c^2	172 GeV	[60]
ALEPH	52.0 GeV/ c^2	57 GeV/ c^2	172 GeV	[61]

Table 2.3: The H^\pm limits at the 95% confidence level, from the four LEP2 experiments. Shown is the lower bound of M_{H^\pm} set by each experiment irrespective of the $\mathcal{B}(H^\pm \rightarrow cs)$, and also the best mass limit that holds over some small range of this branching fraction.

2.8.2 Indirect Searches using $b \rightarrow s\gamma$

As an alternative to direct searches performed at high energies, one may look for the effect of new particle production on decay modes that are rare or forbidden by the SM, but may be enhanced by the presence of new particles. Flavor changing neutral current (FCNC) processes are particularly well-suited for such searches. Not only are they absent at the tree level, but they are predicted to have branching fractions on the order of 10^{-4} . This is a detectable rate, and thus a sensitive probe of new physics.

Some of the best H^\pm limits come from studying B hadron decays to a photon and a strange hadron, $B \rightarrow X_s \gamma$. Within the SM, this decay is represented by the electromagnetic “penguin” loop diagrams shown in Fig. 2.12, in which the photon is radiated from either the W^\pm or one of the quarks. This process has been calculated to an accuracy of 10% within next-to-leading order QCD, $\mathcal{B}(B \rightarrow X_s \gamma) = (3.28 \pm .33) \times 10^{-4}$ in Ref. [63] and $(3.62 \pm .33) \times 10^{-4}$ in Ref. [64]. The measured world-average branching fraction for this B decay is $\mathcal{B}(B \rightarrow X_s \gamma) = (3.14 \pm 0.48) \times$

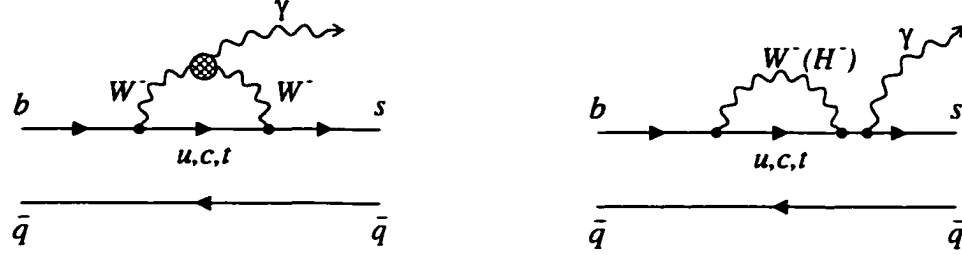


Figure 2.12: The decay $B \rightarrow X_s \gamma$ is represented by these “penguin” diagrams. In the charged Higgs scenario, an H^\pm constructively interferes with the W^\pm contribution, raising the branching fraction for this decay beyond the SM prediction.

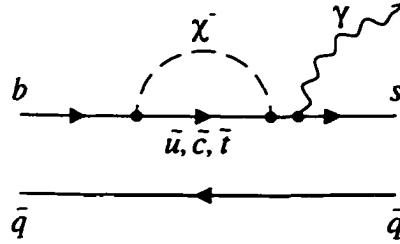


Figure 2.13: Within supersymmetry, diagrams containing a scalar top quark (\tilde{t}) and a chargino (χ^\pm) can interfere destructively with the diagrams above, reducing $\mathcal{B}(B \rightarrow X_s \gamma)$ to be in agreement with the SM prediction.

10^{-4} [65], in excellent agreement with these predictions. The measurement is dominated by the CLEO result [66], which is used to determine a 95% confidence limit (C.L.) range of $2.0 \times 10^{-4} < \mathcal{B}(B \rightarrow X_s \gamma) < 4.5 \times 10^{-4}$.

Within a two-Higgs-doublet extension to the SM, the H^\pm can be radiated by the b quark, along with the W^\pm , as indicated in Fig. 2.12. In the case of Model II Yukawa couplings, which are consistent with supersymmetry and the only couplings considered in this thesis, the charged Higgs contribution always interferes constructively with the W^\pm amplitude regardless of the value of $\tan\beta$ [64].

This increases the SM rate by more than factor of 2, for a large range of M_{H^\pm} - $\tan\beta$ values [64, 67]. This prediction provides stringent bounds on the two-Higgs-doublet model parameter space, since the CLEO measurement is consistent with the SM value. CLEO's original measurement established a 95% C.L. of $M_{H^\pm} > [244 + 63/(\tan\beta)^{1.3}] \text{ GeV}/c^2$ [68]. An analysis published in 1997 [67], which is only slightly outdated³ updated this lower bound of $M_{H^\pm} > 244 \text{ GeV}/c^2$ to $M_{H^\pm} > 300 \text{ GeV}/c^2$. At face value, this limit indicates that searching for H^\pm decays from a top quark with a mass of $175 \text{ GeV}/c^2$ is pointless

However, these limits can be substantially weakened from contributions from particles other than a W^\pm or H^\pm . For example, it has been shown [69, 70] that a scalar stop squark \tilde{t} and a chargino X^\pm , which are required by the minimal supersymmetric model, can enter into the loop (Fig. 2.13) and destructively interfere with the W^\pm and H^\pm amplitudes. These supersymmetric particles can even bring $\mathcal{B}(B \rightarrow X_s \gamma)$ *below* the SM prediction for some range of the parameter space [69, 70]. Thus, the limits from $b \rightarrow s \gamma$ can be circumvented, necessitating the need for a direct search. Still, the measurement of $\mathcal{B}(B \rightarrow X_s \gamma)$ is a powerful tool that can be used to limit the available parameter space for supersymmetry. For example, by choosing values for M_{H^\pm} and $\tan\beta$, upper bounds for the light chargino and scalar stop masses can be obtained [70].

2.8.3 Indirect Searches using Other Low-Energy Processes

Additional low energy constraints on the charged Higgs sector come from the measurement of rare semileptonic B decays. One of the best bounds comes from B hadron decays to a tau-neutrino pair $B \rightarrow \tau \nu$ (Fig. 2.14), which is helicity sup-

³For this analysis the 95% C.L. allowed range of $\mathcal{B}(B \rightarrow X_s \gamma)$ only extended to 4.2×10^{-4} according to CLEO [68], and the NLO theoretical result had about the same central value but errors 50% larger than the current theoretical value.

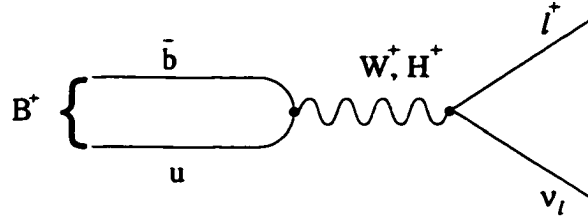


Figure 2.14: The decay $B \rightarrow \tau \nu$ ordinarily occurs via W^\pm exchange, but can be enhanced by the presence of the H^\pm .

pressed within the SM. The predicted branching fraction [71] for this decay is 10 times smaller than the 90% C.L. upper bound set by the L3 Collaboration, $\mathcal{B}(B \rightarrow \tau \nu) < (5.7 \times 10^{-4})$ [72]. In two-Higgs-doublet extensions to the SM, this branching fraction is enhanced by a factor of $(\tan^2 \beta \frac{m_l^2}{M_{H^\pm}^2} - 1)$ [71]. Using this fact, the L3 result translates into the limit $M_{H^\pm} > (2.63 \tan \beta) \text{ GeV}/c^2$ [72]. The effect of a supersymmetric spectrum of particles on this limit has not been analyzed, to my knowledge.

The inclusive decay $B \rightarrow X \tau \nu$ is another process that will be enhanced by H^\pm contributions to the W^\pm propagator. The branching fraction for this decay has been measured to be $\mathcal{B}(B \rightarrow X \tau \nu) = (2.69 \pm 0.44)\%$, which is determined almost solely by the ALEPH measurement [73]. This can be compared to the $\mathcal{B}(B \rightarrow X(e/\mu) \nu) = (10.43 \pm 0.24)\%$ [3]. The relative rate $\Gamma(B \rightarrow X \tau \nu)/\Gamma(B \rightarrow X e \nu)$ has been calculated assuming only a two-Higgs-doublet extension to the SM. This ratio is found to lie within 1σ of the experimental result at small and intermediate values of $\tan \beta$ [74]. However, at high values of $\tan \beta$, where the $\tau \nu H^+$ Yukawa coupling becomes large, the ratio is predicted to be much larger than the SM value. This fact is used to establish the 95% C.L. limit $M_{H^\pm} > (1.92 \tan \beta) \text{ GeV}/c^2$ [74].

Within supersymmetry, this limit seems to be very robust, since any additional

particles besides the W^\pm and H^\pm can only contribute to the rate for $B \rightarrow X\tau\nu$ through higher-order diagrams (and not at the “tree-level”) [75]. In Ref. [75] it is shown that one-loop effects from supersymmetric particles often result in a more restrictive bound than the one given above. However, in some cases the bound disappears altogether!

Two limits derived from semileptonic B decays have been presented, $M_{H^\pm} > (2.63 \tan\beta) \text{ GeV}/c^2$ from the decay $B \rightarrow \tau\nu$, and $M_{H^\pm} > (1.92 \tan\beta) \text{ GeV}/c^2$ from the decay $B \rightarrow X\tau\nu$. These two limits are very comparable to the limits obtained from considering the H^\pm contribution to semileptonic tau decays. The tau decay limits give 95% confidence limits in the range of $M_{H^\pm} > [(1.40 - 1.86) \tan\beta] \text{ GeV}/c^2$ [76, 77].

Limits on H^\pm can be obtained using electroweak properties at the Z^0 pole, as recorded by the LEP experiments. One of the most sensitive quantities is the Z^0 width into a $b\bar{b}$ pair, because of the presence of virtual top quarks that appear in higher-order vertex corrections to the tree-level diagram. The H^\pm tends to couple to these top quarks with a strength $m_t \cot\beta$. This results in a suppression of the Z^0 width into b -quark pairs at low values of $\tan\beta$ [78]. The observable that characterizes $Z^0 b\bar{b}$ couplings is the ratio $R_b = \Gamma(Z^0 \rightarrow b\bar{b})/\Gamma(Z^0 \rightarrow \text{hadrons})$. This ratio is presently measured to be 1.3σ higher than the SM prediction [3], constraining M_{H^\pm} and $\tan\beta$. Based on a value of 1994 value of R_b that was over 2σ higher than the SM expectation, the analysis in Ref. [78] found that at the 95% C.L., $\tan\beta > 1.0$ for $M_{H^\pm} \lesssim 300 \text{ GeV}/c^2$.

However, this analysis assumed only a two-Higgs-doublet extension to the minimal SM. As with the other searches, additional contributions from particles predicted by the minimal supersymmetric model, most notably a light scalar top and a light chargino, can enhance R_b [79, 80]. Using masses for these particles that were large enough to escape detection by the LEP2 and $D\bar{D}$ searches, Ref. [81]

finds that supersymmetry can accommodate a correction to R_b that easily covers the 0.6% discrepancy between the predicted and observed values of R_b .

Fig. 2.15 summarizes the H^\pm limits that are discussed in this section.

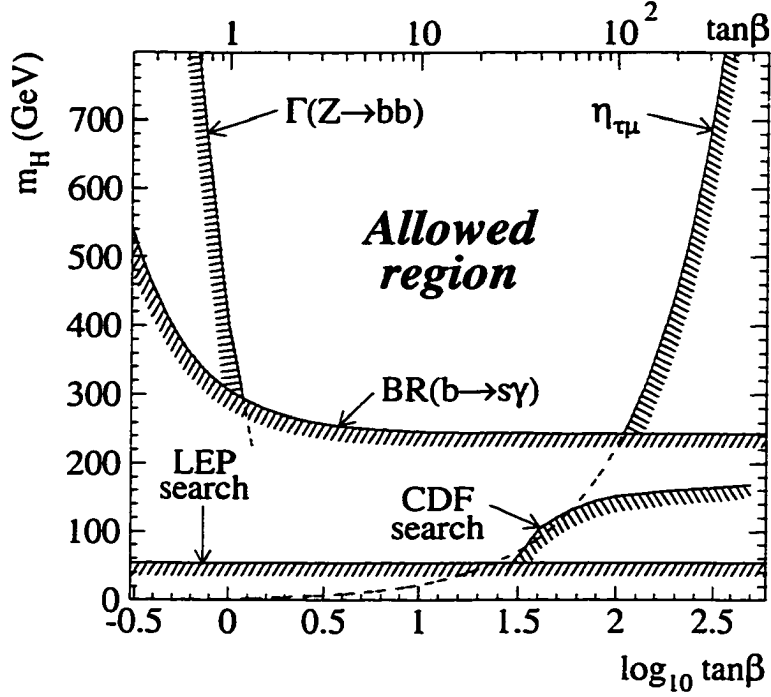


Figure 2.15: Existing 95% C.L. limits on H^\pm production. Only the CDF and LEP limits are based on direct searches. The rest of the limits are derived from indirect searches that assume a two-Higgs-doublet extension to the SM only. The limit $M_{H^\pm} > (1.86 \tan\beta) \text{ GeV}/c^2$ [76], labelled “ $\eta_{\tau\mu}$ ”, is derived from the branching fraction of taus to leptons. It is about as good as limits from the decays $B \rightarrow \tau\nu$ ($M_{H^\pm} > (2.63 \tan\beta) \text{ GeV}/c^2$ - 90% C.L.) [72] or $B \rightarrow X\tau\nu$ ($M_{H^\pm} > (1.92 \tan\beta) \text{ GeV}/c^2$) [74], which are not shown on the plot. Some of the limits are slightly outdated. The limit based on the measured value of $\mathcal{B}(B \rightarrow X_s\gamma)$ is the old CLEO limit $M_{H^\pm} > [244 + 63/(\tan\beta)^{1.3}] \text{ GeV}/c^2$ [68], but a more recent analysis raises this lower bound of $244 \text{ GeV}/c^2$ to over $300 \text{ GeV}/c^2$ [67]. The LEP searches now exclude $M_{H^\pm} < 59.5 \text{ GeV}/c^2$ [58], and the limit boundary is not flat, sometimes extending to $72 \text{ GeV}/c^2$ [58]. Finally, the limit based on R_b [78] uses a value that was over 2σ away from the SM prediction; it is now measured to be only a 1.3σ deviation [3]. This figure is taken from Ref. [76].

Chapter 3

The CDF Detector

The data used in this analysis were recorded by the Collider Detector at Fermilab (CDF) experiment. CDF is one of two large experiments situated on the beamline of the the highest-energy proton-antiproton ($p\bar{p}$) collider in the world, the Tevatron, located at Fermi National Accelerator Laboratory (Fermilab) in Batavia, Illinois. The CDF detector is centered on an interaction point where proton and antiproton beams collide head-on. It is composed of many subsystems that determine the trajectory, momentum, energy, charge and identity of particles that are produced in these collisions. This chapter begins with a description of the Tevatron, and the data used in this analysis that were recorded by CDF during a three year period. Next, the various CDF detector subsystems are described in some detail. The last portion of this chapter is devoted to explaining the selection criteria that are used to choose events for a data sample that becomes the starting point for the analysis described in later chapters.

3.1 The Tevatron

The Tevatron¹ is a 1 km radius superconducting synchrotron that performs the last of five separate stages of acceleration in order to produce beams of protons (p) and antiprotons (\bar{p}) that collide at a center-of-mass energy of 1800 GeV, or 1.8 TeV. The Fermilab Accelerator Complex, shown in Fig. 3.1, consists of five

¹The Tevatron is described in detail in Appendix C

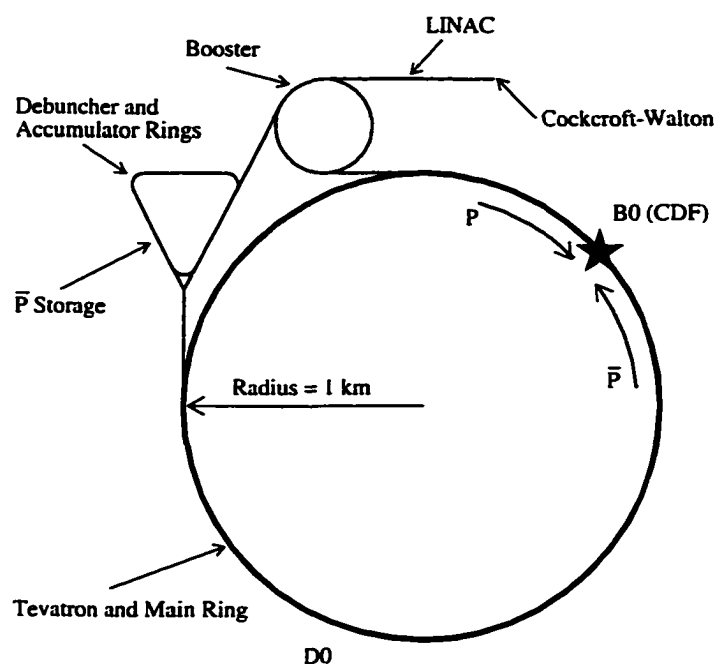


Figure 3.1: The Tevatron accelerator complex. Protons begin their journey in an ion source located in the Cockcroft-Walton accelerator. The Main Ring and the Tevatron lie on top of one another in the same tunnel.

accelerators (Cockcroft-Walton, Linac, Booster, Main Ring, and the Tevatron), as well as two storage rings (the antiproton Debuncher and Accumulator). Each accelerator in the chain boosts the energy of particles received, and passes them off to the next stage. Protons originate from a bottle of hydrogen gas, and then are passed through each of the accelerators, starting with the Cockcroft-Walton device. On the other hand, antiprotons are produced by colliding protons into a fixed target. They are separated from the debris, transferred to the Debuncher, and then are stacked in the Accumulator for several hours until a sufficient number have been collected to achieve high-rate interactions once they are injected into the Tevatron.

The Tevatron operates with six proton and six antiproton bunches circulating

in opposite directions within the same beam pipe. Each particle has an energy of 900 GeV, and the bunches are separated in time by about $3.5 \mu\text{s}$. A special pair of quadrupole magnets in the CDF experimental hall forces the two beams to collide at the center of the detector. At this interaction point, the beam spot size is made to be as small as possible in the transverse plane (measured to be $\sigma_{x,y} \approx 25 \mu\text{m}$ in Ref. [82]), in order to maximize the $p\bar{p}$ collision rate at this point. The longitudinal profile of the bunches is approximately Gaussian, having a width of 30 cm.

3.1.1 Luminosity

A fundamental property of a collider is the luminosity \mathcal{L} . The number of collisions per second dN/dt at the interaction region due to a physics process is

$$\frac{dN}{dt} = \sigma \times \mathcal{L} \quad (3.1)$$

where σ is the physics process cross section in units of cm^2 , and \mathcal{L} is the instantaneous luminosity of the colliding beams, measured in units of collisions/ cm^2/s . The luminosity can be approximated by the simplified equation [83]

$$\mathcal{L} = \frac{f B N_{\bar{p}} N_p}{4\pi \sigma_{x,y}^2} \quad (3.2)$$

where f is the revolution frequency of each bunch (47.7 kHz), B is the number of bunches in each beam (6), $N_{p,\bar{p}}$ are the number of proton and antiprotons in a bunch ($N_p \approx 150 \times 10^9$, $N_{\bar{p}} \approx 50 \times 10^9$), and $\sigma_{x,y}$ is the rms transverse size of the proton and antiproton beams ($\approx 25 \mu\text{m}$). This formula is simplified in part because it ignores dependence upon the longitudinal profile of a real beam [83].

The data used in this analysis were collected between 1992 and 1995, over the course of two periods called Run 1A and Run 1B. Table 3.1 shows the typical, best, and time-integrated values for the luminosity over the course of each of these

Luminosity Summary

	Run 1A	Run 1B
period of operation	Aug. 1992 - May 1993	Jan. 1994 - Jul. 1995
average luminosity	$0.54 \times 10^{31} \text{ cm}^{-2}\text{s}^{-1}$	$1.6 \times 10^{31} \text{ cm}^{-2}\text{s}^{-1}$
best luminosity	$0.92 \times 10^{31} \text{ cm}^{-2}\text{s}^{-1}$	$2.8 \times 10^{31} \text{ cm}^{-2}\text{s}^{-1}$
time integrated luminosity	$19.3 \pm 0.7 \text{ pb}^{-1}$	$90.1 \pm 7.2 \text{ pb}^{-1}$

Table 3.1: The luminosity from Run 1A and Run 1B. Remember $1 \text{ pb} = 10^{-24} \text{ cm}^2$.

two periods. The analysis described in this thesis uses data corresponding to the total time integrated luminosity of

$$\mathcal{L} = 109.4 \pm 7.2 \text{ pb}^{-1} . \quad (3.3)$$

3.2 An Overview of the CDF Detector

The CDF detector is designed to study many facets of the physics of $p\bar{p}$ collisions. It is designed with as much solid angle coverage as possible, and has approximate azimuthal and front-back symmetry. Fig. 3.2 shows a three-dimensional view of the detector, while Fig. 3.3 shows one quadrant of a side view. The Tevatron beam is contained within a pipe running through the detector, and focused at the interaction point at the center of the detector by the “low- β ” focusing quadrupole magnets embedded within the forward and backward steel toroids. Outside the beam pipe, and surrounding the interaction point, are three complementary tracking detectors that record the trajectory of charged particles in three dimensions. The momentum of a charged track is proportional to its radius of curvature in the 1.4 T axial magnetic field, which is generated by a superconducting solenoid of radius 1.5 m and length 4.8 m that surrounds the three tracking detectors. Just

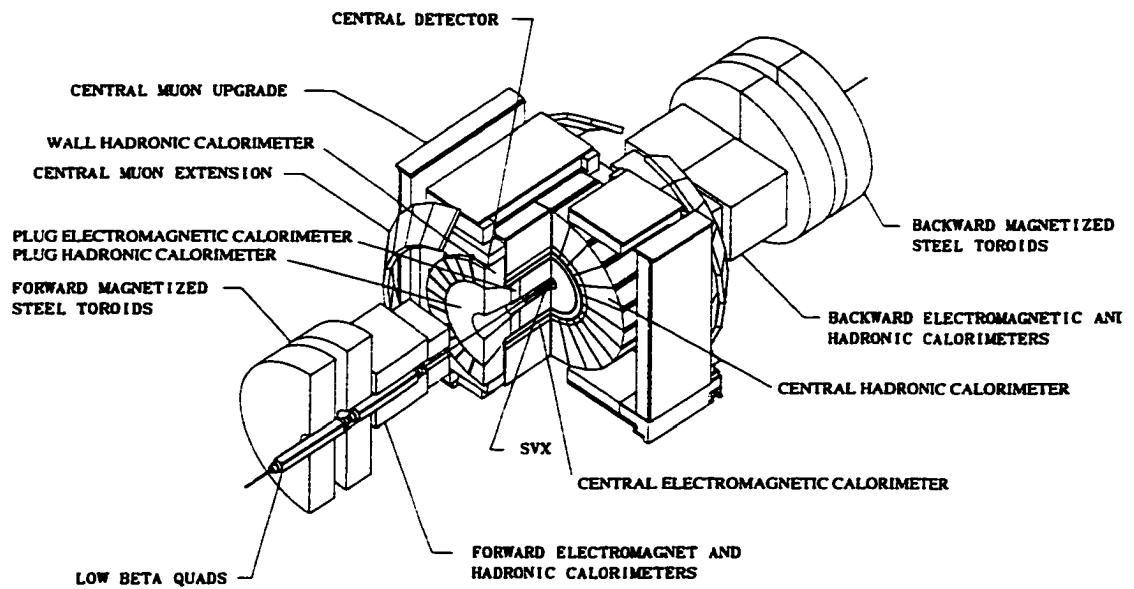


Figure 3.2: A three-dimensional view of the CDF detector.

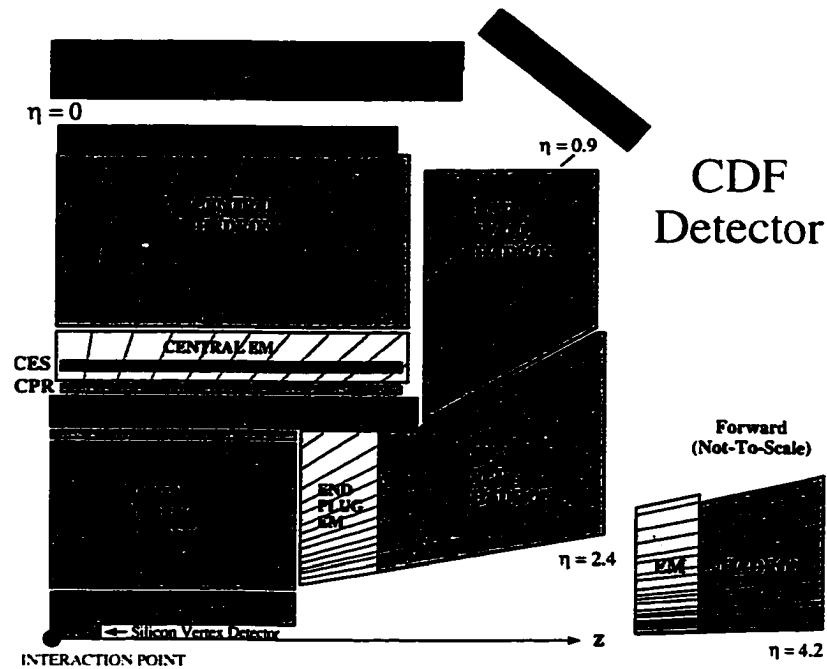


Figure 3.3: A side view of one quadrant of the CDF detector, showing the calorimeter segmentation in intervals of $\Delta\eta = 0.1$.

outside this solenoid lie the central calorimeters, which record the energy both of charged and neutral particles. Calorimeters also exist in the forward and backward regions of the detector. The calorimeters act as filters for the muons, which usually radiate very little energy (less than 1 GeV) as they pass through to the muon chambers, located outside the calorimeters. Neutrinos escape detection by CDF, but their presence can be inferred by an imbalance of energy in a plane transverse to the beam.

3.2.1 The CDF Coordinate System

The origin of CDF is the center of the detector, also the nominal interaction point for $p\bar{p}$ collisions. The proton beam direction defines the \hat{z} direction. Looking into the $+\hat{z}$ direction, onto the plane transverse to the beam, the 9 o'clock vertical position defines the \hat{x} direction, and the 12 o'clock position defines the \hat{y} direction. The magnetic field is in the $-\hat{z}$ direction, $\vec{B} = -1.4\hat{z}$ T. In polar coordinates, which are frequently used, the polar angle θ is measured from the $+\hat{z}$ direction, the azimuthal angle ϕ is measured in an anti-clockwise direction from the $+\hat{x}$ direction, and the radial distance r is measured from the center of the beamline. Often we speak of momentum transverse to the beam, in the $r - \phi$ plane, which is related to the total momentum through the relation $P_T = P \sin\theta$.

Rather than use the polar angle θ , it is more natural to use rapidity y , defined as

$$y = \frac{1}{2} \ln \left(\frac{E + p_z c}{E - p_z c} \right) \quad (3.4)$$

Under boosts along the z -axis, to an inertial frame moving with velocity β , the rapidity transforms as $y \rightarrow y + \tanh^{-1}\beta$. Thus the shape of a particle distribution in y , dN/dy , is invariant under these transformations. For highly relativistic particles

($p \gg mc$), the rapidity is well approximated by pseudorapidity η ,

$$\eta = -\ln \left(\tan \frac{\theta}{2} \right) \quad (3.5)$$

which is used at CDF for detector segmentation, and specification of particle position. Two types of pseudorapidity are used: η_{det} , or just η , denotes detector pseudorapidity measured from the nominal interaction point at the center of the detector, whereas η_{evt} measures the pseudorapidity of the decay products from the z -vertex of the $p\bar{p}$ collision in a particular event, which can occur at any point along the beam axis.

3.3 The Tracking System

The purpose of the tracking system is to measure the three-dimensional trajectory of charged particles, so that particles that decay close to the beam can be reconstructed, and their charge and momentum can be determined through their curvature in the magnetic field. In $t\bar{t}$ events, B -mesons are identified by their displaced vertex, which can appear several mm from the primary interaction point. For this purpose, the tracking detector must have excellent spatial resolution very close to the interaction point. However, good momentum resolution requires a large volume detector in order to measure the large radius of curvature of high- P_T tracks in the plane transverse to the beam (r - ϕ plane). Finally, in order to determine the direction of jets associated with calorimeter clusters, it is also necessary to know the trajectories of charged particles in the r - z plane.

To meet these requirements, CDF employs three complementary tracking systems. The Silicon Vertex Detector (SVX) lies just outside the beampipe, and measures the impact parameter of a charged track with an error of several tens of microns. Outside the SVX is the Vertex Drift Chamber (VTX), which performs a

precise measurement of the track in the r - z plane. Finally, surrounding the SVX and VTX is the Central Tracking Chamber (CTC), which has a large volume and measures tracks in the plane transverse to the beam with a high degree of precision. These three detectors are described below in more detail.

3.3.1 Silicon Vertex Detector (SVX)

The SVX is designed for precise track reconstruction very close to the interaction point. It surrounds the beampipe with four concentric 12-sided polygons, composed of silicon microstrip detectors. The outer radius of the beampipe is at $r = 1.9$ cm, and the four surrounding polygons have radii $r = 3.0$ cm, 4.2 cm, 6.8 cm, and 7.9 cm. There are two barrels, one on either side of $z = 0$ and spanning the region $|z| < 25$ cm and $|\eta| < 2.0$. Fig. 3.4 illustrates the geometry of one of the barrels. Given the longitudinal beam spread of ± 30 cm, the SVX $p\bar{p}$ interaction acceptance is 67%.

Each of the 12 sides of one layer of the SVX is called a ladder. Fig 3.4 reveals that a ladder is comprised of three silicon wafers bonded end-to-end, to reduce the number of channels that are read out. Each wafer contains rows of microstrips aligned along the z direction, and separated by either $55\ \mu\text{m}$ (outer layer) or $60\ \mu\text{m}$ (inner three layers). Fig 3.4 shows a magnified cross sectional view of the strips, which are made of a heavily doped p -type (p^+) semiconductor. Relative to the p^+ , a large positive bias voltage is applied to the n -type semiconductor via the n^+ contact. This results in a deep depletion region absent of charge carriers that extends into the n region, and has an electric field much like a parallel-plate capacitor. A charged particle will collide with the semiconductor lattice and excite valence electrons into the conduction band, creating electron-hole pairs that are swept toward the p^+ and n^+ electrodes. Charge is collected and integrated to give

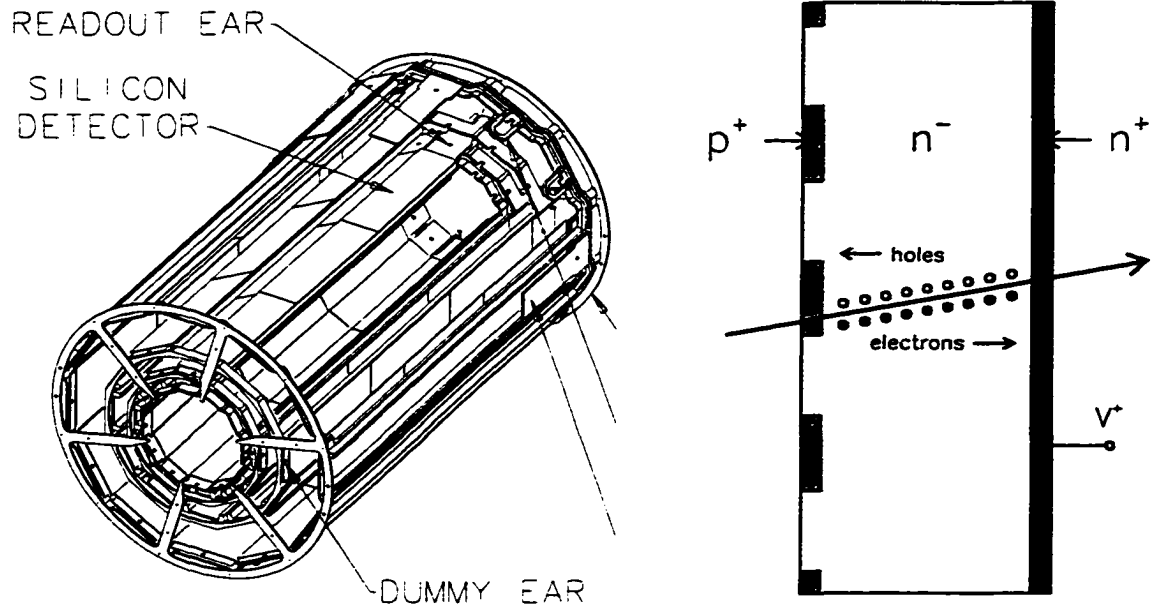


Figure 3.4: On the left is a one of two barrels of the SVX detector. Three silicon wafers are placed end-to-end on a ladder, and contain microstrips separated by 55 or 60 μm . A closeup of the microstrips is shown on the left, and the motion of electrons and holes is indicated.

a voltage pulse proportional to the amount of charge liberated. Although the strips are placed at least 55 μm apart, the position of the particle in the transverse plane can be determined to a higher degree of accuracy, by using the charge-weighted centroid of several adjacent strips that collect charge, called a cluster. It is the centroids of the clusters that are used to fit SVX tracks.

Due to its close proximity to the interaction point, and fine granularity (46,080 channels total), the SVX determines the impact parameter of an isolated track in the plane transverse to the beam with a resolution of $(13 + 40/P_T)$ μm , where P_T is expressed in units of GeV/c [84, 85]. The constant term is due to the inherent spatial resolution of the detector, while the momentum dependence arises due to

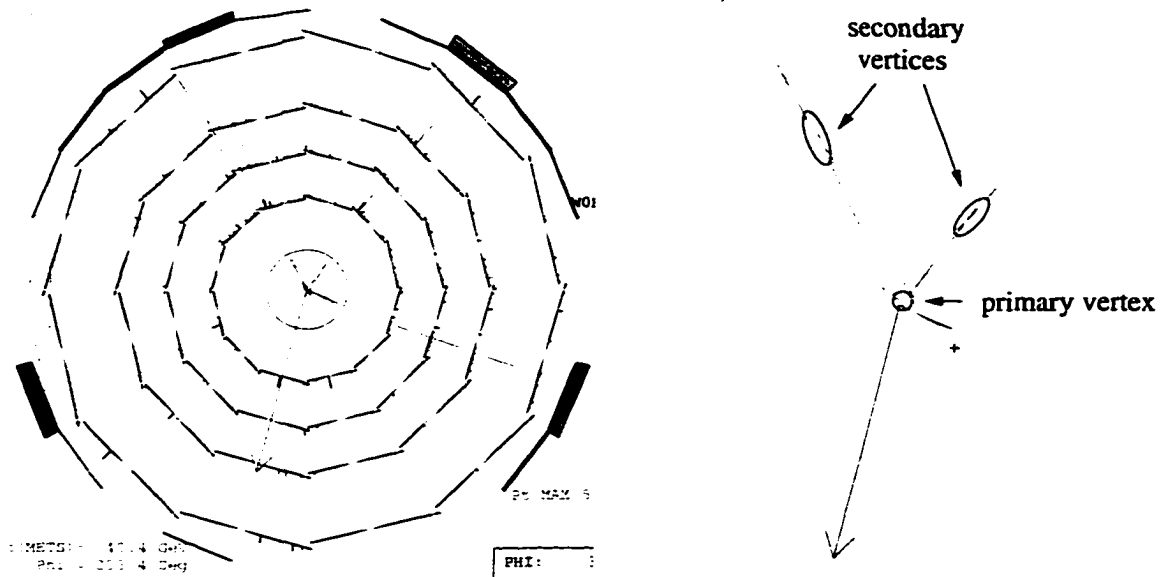


Figure 3.5: The SVX detector display for a top lepton+jets event, showing reconstructed tracks in a plane transverse to the beam line. Shown on the left are the 4 layers of the detector, along with a view of calorimeter energy deposited in ϕ , proportional to the height of towers along the circumference of the outer circle. The arrow shows the direction of missing energy. On the left is a magnified view of the beam line area, showing only tracks with $P_T > 2$ GeV/ c for clarity.

multiple scattering. The left plot of Fig. 3.5 shows a beam-line view of the SVX detector for a very unique top candidate event (Run 67824, Event 281883). The event contains one very straight track at 8 o'clock that points to an electromagnetic cluster in the calorimeter, indicating a high- P_T electron. The event also contains three distinct jets, at 1, 4 and 11 o'clock positions. The right plot of Fig. 3.5 shows a magnified view of tracks reconstructed in the beampipe region. Although the tracks associated with the electron and the jet at the 4 o'clock position originate from a common primary vertex, the other two jets contain tracks with significant impact parameters with respect to this primary vertex. Each bundle of displaced

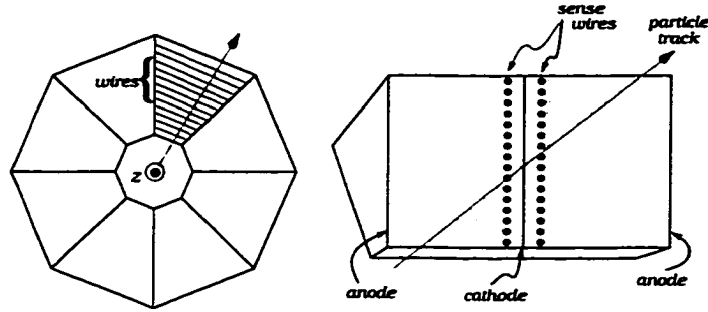


Figure 3.6: A schematic showing one segment of the VTX, and the location of the sense wires in one of the octants. Each octant contains either 24 or 16 sense wires, depending on whether it is shortened to make room for the SVX.

tracks crosses at a secondary vertex located several mm from the primary vertex, indicating the presence of a B -meson decay.

3.3.2 Vertex Drift Chamber (VTX)

The VTX is a drift chamber filled with argon/ethane gas that surrounds and supports the SVX, and provides tracking in the r - z plane. It determines the z coordinate of the primary vertex with a resolution of about 1 mm. It also provides the only forward/backward tracking at small angles $\theta < 10^\circ$ from the beamline, for particles that are directed towards the forward/backward calorimeters.

The VTX lies between a radius $8 < r < 22$ cm, and covers a pseudorapidity range $|\eta| < 3.3$, corresponding to $|z| < 150$ cm. It is comprised of 28 octagonal modules stacked end-to-end, where each module is comprised of eight wedges. A wedge, shown in Fig. 3.6, contains two drift regions 5 cm long, with sense wires strung in the azimuthal direction. These drift regions are filled with argon/ethane gas. An electric field is established between the anode planes at either end of the chamber, and the cathode plane in the middle of the chamber. When a charged

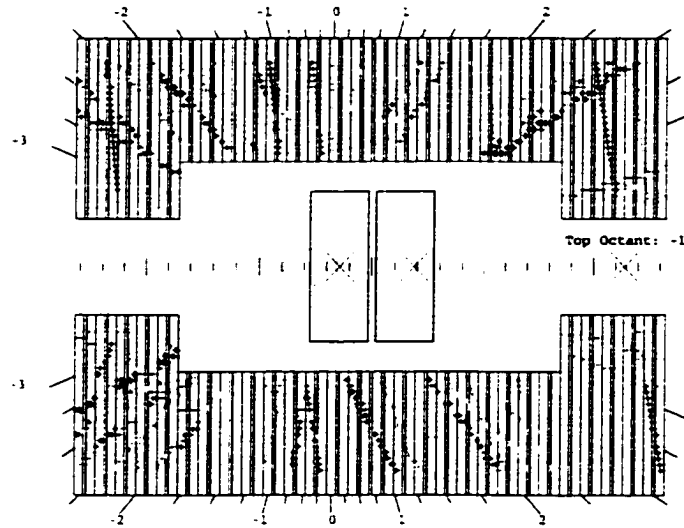


Figure 3.7: A VTX event display for a top dilepton event, showing drift hit positions reconstructed from drift times. The VTX is composed of 28 modules stacked together; the inner 18 modules are shortened to make room for the SVX, which is indicated by the two inner rectangles. The hits in all eight octants of the detector are displayed, so this is not a true “slice in ϕ ” side view.

track passes through the chamber, it ionizes the gas, producing a trail of electrons and positive ions. The positive ions drift at a constant velocity towards the cathode. Near the sense wire, the ions are accelerated by the $1/r$ electric field, creating an avalanche of ionization that deposits charge on the wire and can be detected. The drift times observed at the wire reveal the z position of the track and its angle with respect to the beam axis, while the position of the wire gives radial information.

Fig 3.7 is a VTX event display for a top dilepton candidate, showing the drift hits reconstructed from drift times in the VTX. Segments are formed from these drift hits. These segments are then used to determine vertex positions in z , which are shown as crosses along the beam axis. The vertices are ranked according to

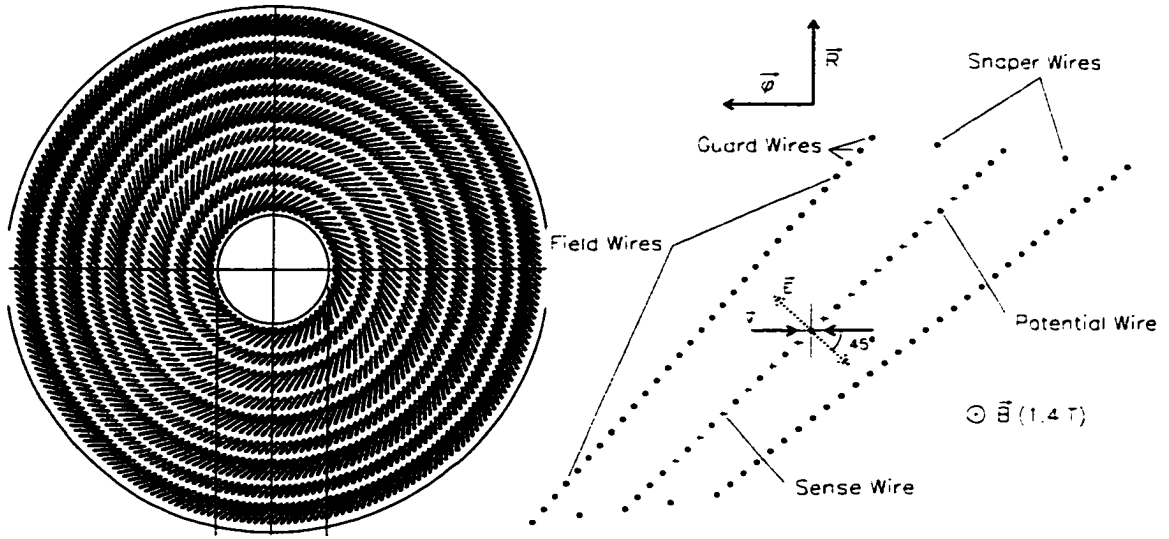


Figure 3.8: The CTC endplate, and one of the CTC cells, showing the drift velocity direction.

criteria such as the number of segments and total number of hits that project back to them [86]. The two larger crosses indicate candidates for the primary vertex of the event.

3.3.3 Central Tracking Chamber (CTC)

The CTC is a 3.2 m long cylindrical drift chamber extending between $r = 0.31$ and 1.32 m, surrounding the VTX and SVX, and providing tracking for $|\eta| < 1.1$. Its operation is similar to that of the VTX, except here the sense wires have a positive voltage, and attract electrons. The position of the wire gives r information about the track, and the distance between the track and the wire is inferred from the arrival time of the signal.

An endview of the CTC is shown in Fig 3.8. There are 84 layers of $40 \mu\text{m}$ diameter wires arranged into 9 superlayers. The bulk of the pattern recognition is done in the $r - \phi$ plane, but good pattern recognition in the $r - z$ plane is also

important. Therefore five of the nine superlayers contain 12 layers of *axial* sense wires arranged parallel to the beam, while four of the superlayers contain 6 layers of *stereo* sense wires with a tilt of $+3^\circ$ or -3° with respect to the beam axis. The superlayers are further divided into *cells*, also shown in Fig. 3.8. The maximum drift distance across a cell is 40 mm, corresponding to about $0.8 \mu\text{s}$ of drift time, which is shorter than the bunch crossing time of $3.5 \mu\text{s}$ in the Tevatron. Two planes of stainless steel wires called field wires define and shape the electric field in each cell. Together, the axial and stereo layers measure the trajectory of a track with a resolution of about $200 \mu\text{m}$ in the $r - \phi$ plane, and about 4 mm in the $r - z$ plane.

The cells are tilted at 45° with respect to the radial direction for three primary reasons [87]. Most importantly, the tilt lessens the demands of tracking reconstruction to determine what is known as a “left-right” ambiguity. When a track passes a row of sense wires, the distribution of drift times collected will not reveal whether the track passed the row on the right or the left side. When the rows of sense wires are tilted, this ambiguity is easily resolved because the ghost track defined by the improper assignment is rotated with respect to the true track direction by a large angle, and will not point back at the primary vertex [87]. Secondly, the tilt guarantees that every high- P_T radial track will pass close to at least one sense wire in every superlayer, allowing fast recognition by the trigger (see Section 3.7.2). Finally, this tilt compensates for the angle between the electric field and the drift velocity in the chamber, called the Lorentz angle, which is nonzero due to the crossed $\vec{E} \times \vec{B}$ fields present. With the drift velocity perpendicular to the radial direction, any nonlinear time-to-distance relationship at the edges of the cell is minimized².

²This also ensures that ionization electrons deposited uniformly along a high- P_T trajectory will all reach a sense wire in the shortest possible time window, maximizing the signal/noise ratio for the readout electronics.

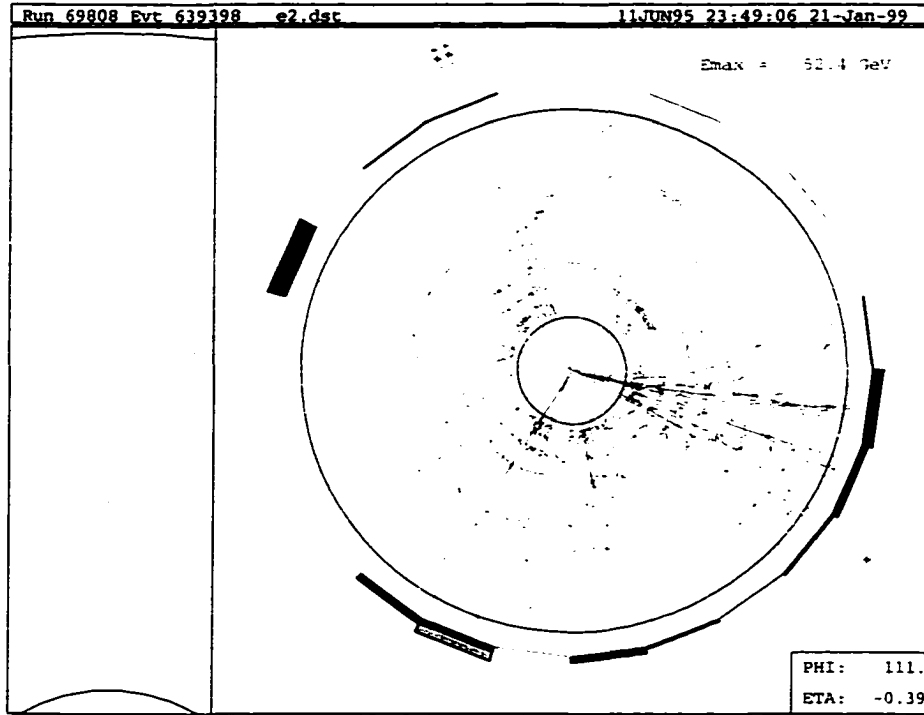


Figure 3.9: A CTC event display showing a top $e\text{-}\mu$ dilepton event. The electron track is at 10 o'clock, and points to an EM calorimeter cluster, while the muon track at 11 o'clock leaves very little calorimeter energy. There are also three jets in the event. The side window is a magnified view of the area in the box surrounding the muon track, showing the location of sense wires and "hits".

The CTC event display for a top dilepton event is shown in Fig. 3.9. Sense wire hits are indicated by dots, making the inner superlayers visible due to the high occupancy of low-momentum tracks in this region, which do not escape the CTC ($P_T < 0.275 \text{ GeV}/c$). There are two high- P_T tracks at 10 and 11 o'clock, which appear as straight lines because momentum is proportional to the radius of curvature R ,

$$P_T = 0.3BR, \quad (3.6)$$

where B is in Tesla, C is in m^{-1} , P_T is in GeV/c . The track at 10 o'clock points to an electromagnetic calorimeter cluster, indicating that it is an electron, while the track at 11 o'clock has deposited very little energy in the calorimeter, indicating it is a muon. The side window shows a magnified region of the area within the rectangular box surrounding the track at 11 o'clock. Using drift times, track segments are reconstructed on both sides of each row of sense wires, forming "X" patterns. The incorrectly assigned segments do not point back to the interaction point.

3.3.4 Track Reconstruction

Track reconstruction begins in the CTC, by fitting the hits within each axial superlayer with the arc of a helix. Track candidates are found first in the $r - \phi$ plane by linking these segments together. The VTX is used to determine a seed z -position of each track, which is then input to an algorithm that uses the CTC stereo sense wire information to reconstruct the track in three dimensions. Each track then is projected back into the SVX, where matching clusters are assigned to it, and the combined CTC-SVX hits are refit. The momentum resolution of the CTC is $0.002 P_T \oplus 0.0066$ for CTC tracks, where P_T is in GeV/c , and \oplus denotes adding the resolution term in quadrature with the constant term. The resolution improves to $0.0009 P_T \oplus 0.0066$ for tracks reconstructed both in the CTC and SVX.

3.4 Calorimeters and Jet Identification

Calorimeters are placed just outside the tracking chambers and the solenoid in order to measure the energy both of charged and neutral particles. They are the largest and most massive of the detector elements, because they have sufficient density and thickness to intercept an incident particle and cause it to deposit all

Summary of Calorimeter Properties

Detector	η -coverage	Energy resolution	Thickness
Central EM	$ \eta < 1.1$	$13.7\%/\sqrt{E_T} \oplus 2\%$	$18 X_0$
Central HAD	$ \eta < 0.9$	$50\%/\sqrt{E_T} \oplus 3\%$	$4.5\lambda_0$
Endwall HAD	$0.7 < \eta < 1.3$	$75\%/\sqrt{E} \oplus 4\%$	$4.5\lambda_0$
Plug EM	$1.1 < \eta < 2.4$	$22\%/\sqrt{E} \oplus 2\%$	$18 - 21 X_0$
Plug HAD	$1.3 < \eta < 2.4$	$106\%/\sqrt{E} \oplus 6\%$	$5.7\lambda_0$
Forward EM	$2.2 < \eta < 4.2$	$26\%/\sqrt{E} \oplus 2\%$	$25 X_0$
Forward HAD	$2.4 < \eta < 4.2$	$137\%/\sqrt{E} \oplus 3\%$	$7.7\lambda_0$

Table 3.2: Summary of the CDF calorimeter properties. Thickness is given in radiation lengths (X_0) for EM calorimeters, and absorption lengths (λ_0) for HAD calorimeters.

its energy by subsequent cascade, or “shower”, of increasingly lower energy particles [88]. A very small fraction of this energy is detected in the form of scintillation light or ionization charge, proportional to the incident particle’s energy. CDF uses *sampling* calorimeters, so named because they use a sandwich structure that interleaves an active medium with the passive absorber material in order to sample the energy loss at different depths of the shower.

The calorimeters are split into electromagnetic (EM) and hadronic (HA or HAD) elements, and are separated into three main detector regions defined by their pseudorapidity coverage, as shown in the side view of the detector, Fig 3.3. For this analysis the most important of these regions is the central region $|\eta| < 1$, where the Central Electromagnetic (CEM), Central Hadronic (CHA), and Wall Hadron (WHA) calorimeters are located. In this analysis, the CEM is used to measure the energy of electrons, photons and the electromagnetic components of jets, and helps

identify these particles as well as muons. The CHA and WHA measure the hadronic components of jets, and assist in the identification of electrons, photons and muons. The Plug region ($1.1 < \eta < 2.4$) contains the PEM and PHA calorimeters. These, as well as the central calorimeters, are used to identify jets and measure their energies in this analysis. Finally, forward and backward region calorimeters FEM and FHA extend coverage to $\eta < 4.2$. The energy measured by these calorimeters is not used to identify jets, but does contribute a measurement of transverse energy in an event, which can be used to infer missing energy as a result of high- P_T neutrinos that escape detection. Properties of the calorimeters are summarized in Table 3.2. Below, I describe the central calorimeters (CEM, CHA, and WHA) in detail.

3.4.1 The Central Electromagnetic Calorimeter (CEM)

The electromagnetic calorimeters exploit the phenomena of cascade showers, which are produced by highly energetic electrons, positrons and photons. In any medium, an electron (or positron) with an energy larger than several tens of MeV loses energy primarily by radiating photons, a process referred to as bremsstrahlung. These photons, in turn, lose energy by producing electron-positron pairs, which subsequently radiate secondary photons. The number of particles in the resulting shower increases exponentially with depth in the medium. The process continues until the average energy of particles in the shower is about 10 MeV, and electrons begin to lose energy primarily by ionization, and further radiation is not possible. At this point, called “shower maximum”, the shower contains the maximum number of charged particles. Roughly speaking, the number of particles at any given depth in the shower is proportional to the incident particle energy E_0 . Since fluctuations in the numbers of particles are governed by Poisson statistics, the

energy resolution for sampling calorimeters is proportional to $1/\sqrt{E_0^3}$.

The distance scale for the longitudinal development of the shower is called the radiation length X_0 , which is the thickness of the medium that reduces the mean energy of a beam of electrons by a factor e . It is proportional to the mass number A of the medium, and inversely proportional to the square of the atomic number Z . The electromagnetic calorimeter uses lead, a high- Z material, in order to minimize X_0 and keep the electromagnetic shower contained in as small a volume as possible. Shower maximum occurs at a depth that increases logarithmically with primary energy E_0 , $(3.9 + \ln E_0) X_0$. Up to shower maximum, typically more than 90% of the energy is contained in a cone of radius of $1X_0$ [89].

The CEM (along with the CHA) is composed of 48 wedge-shaped modules that surround the solenoid in $\Delta\phi = 15^\circ$ segments. A wedge is divided into 10 towers, where each tower subtends $\Delta\eta = 0.1$, and points back to the nominal interaction point, as shown in Fig. 3.10. Tower 0 intercepts particles ejected at 90° to the direction of the beam, and Tower 9 intercepts particles at 45° . Fig. 3.11 shows a schematic of one wedge, emphasizing its CEM elements. The active volume is comprised of 30 layers of 0.32 cm thick lead plates, alternating with 31 0.5 cm thick plastic scintillator plates, to achieve a total radiation thickness of $18X_0$. The solenoid contributes another $0.86X_0$ (at $\eta=0$). Light from each scintillator layer in a tower is collected with two wavelength shifters at each of the two wedge boundaries in ϕ , and transferred to two photomultiplier tubes via light pipes.

Embedded in the CEM, at the average shower maximum depth for 10 GeV electrons ($5.9 X_0$), is the Central Electromagnetic Strip chamber (CES) [90]. This gas proportional chamber contains both strips and wires, and is located next to

³Large fluctuations in the number of showers actually greatly exceed what is expected from Poisson statistics, because fluctuations in the first few radiation lengths result in an amplification in the later stages of the shower. See Ref. [89].

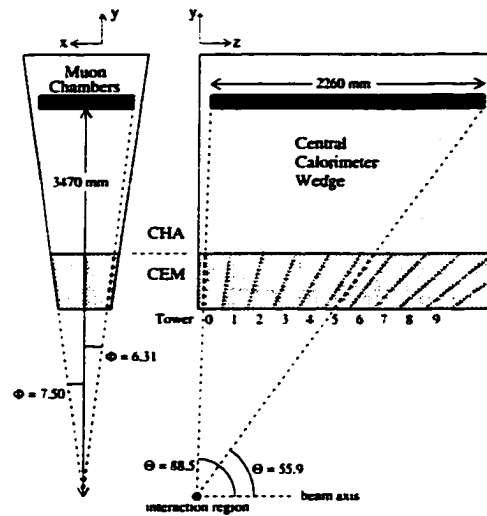


Figure 3.10: The geometry of a calorimeter wedge, showing the ten projective towers for the CEM, the division between the CEM and CHA, and the placement of the CMU muon modules.

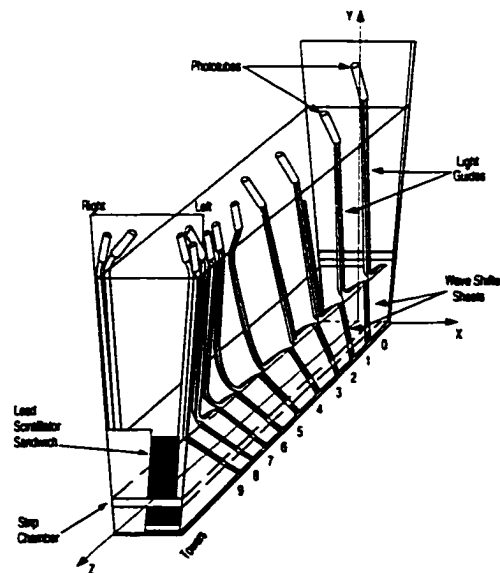


Figure 3.11: A calorimeter wedge, with the CEM light collection system and the CES strip chamber indicated.

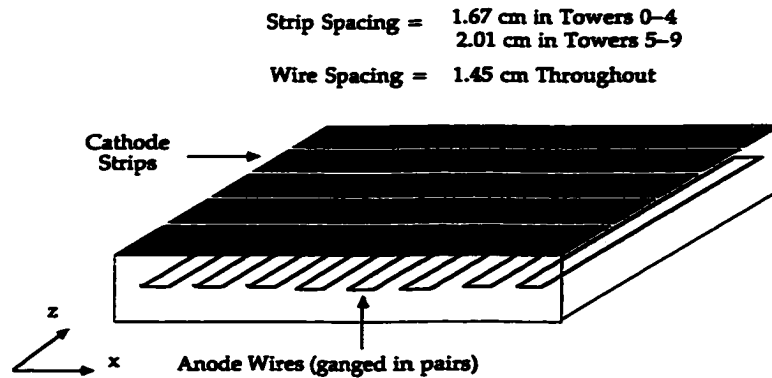


Figure 3.12: A schematic of the CES.

the eighth lead layer. It is used to determine the shower position, and the transverse development at shower maximum, by measuring the charge deposition on orthogonal strips and wires. Fig. 3.12 shows the orientation and spacing of the strips and wires. These measure a shower profile in the η and ϕ directions, each with a position resolution of about ± 2 mm, independent of the incident particle's energy. The CES is used to distinguish shower shapes due to electrons from those due to hadrons, which tend to initiate showers at a further longitudinal depth into the calorimeter.

The CEM was calibrated with exposure to 50 GeV electrons at a test beam setup [91]. It was cross-calibrated at the same time with a permanently attached movable ^{137}Cs source, which is guided on a rope pulley system passing near the shower maximum. This source has been used to periodically calibrate the detector after assembly and throughout the data taking runs. In addition to the ^{137}Cs source, Xenon and LED flasher systems are employed to calibrate the CEM. By using the source to inject electrons into the calorimeter, the Xenon flasher to inject light into the waveshifter, and the LEDs to inject light into the phototube, each of these light-collection elements can be monitored for radiation damage or change

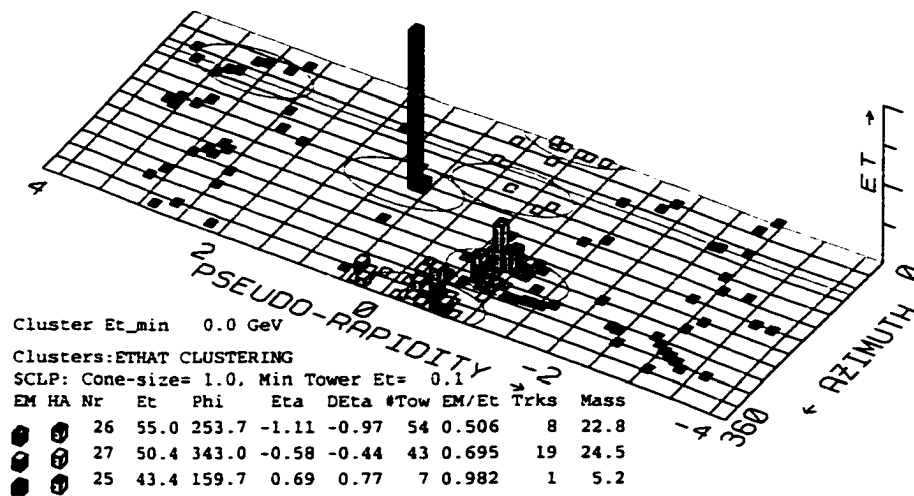


Figure 3.13: The distribution of transverse energy deposited in the calorimeters by the dilepton event shown in Fig. 3.9.

due to aging or exposure to the magnetic field [92]. During Run 1, source runs were performed about once a year, while flasher systems were used almost daily.

Fig. 3.13 shows the distribution of transverse energy deposited in the calorimeters for the dilepton event shown in Fig. 3.9. The segmentation of the plot in $\eta - \phi$ space is identical to that of the calorimeters, and the height of each block is proportional to the transverse energy recorded by the corresponding calorimeter tower. The EM (dark) and HAD (light) deposits are shown separately. The electron candidate deposits almost all of its energy in one tower. There are three other clusters in the central region due to jets, corresponding to the collimated groups of charged tracks visible in the CTC display, Fig. 3.9.

3.4.2 The Central Hadronic Calorimeters (CHA and WHA)

The sampling calorimeters used to detect showers initiated by hadrons are similar in construction to the electromagnetic calorimeters. However, the physical

processes that cause the propagation of a hadronic shower are considerably different from those responsible for an electromagnetic shower. A hadron shower results from an inelastic nuclear collision with the production of secondary hadrons, which themselves interact inelastically, and so on. Although the bulk of incident energy appears eventually in the form of ionization, roughly 30% of the energy is lost by the breakup of nuclei, nuclear excitation, and the production of neutrons [93]. The scale for the longitudinal development is set by the nuclear absorption length λ , which is proportional to the atomic mass A and inversely proportional to the nuclear absorption cross section σ_{abs} , which results in a total dependence of $A^{0.3}$. Since $\lambda > X_0$ for the same material, hadron calorimeters tend to be larger than electromagnetic calorimeters. To contain the shower in as small a volume as possible, it may appear that small- A materials are optimal. However, radiation length has the units of [length][density], and after dividing out density, it turns out that a given thickness of lead or iron will offer the same λ . Iron is chosen for CDF primarily because it is less expensive and less dense.

The Central Hadron (CHA) and Wall Hadron (WHA) calorimeters lie outside the CEM, and are shown in Fig. 3.3. Each tower in the CEM is matched by a hadronic calorimeter tower that lies along the same slice of η , and there is even some overlap between the CHA and WHA. The CHA is constructed of 32 layers of 2.5 cm thick steel absorber alternating with 1.0 cm thick plastic scintillator. The WHA is constructed from 15 layers of 5.1 cm thick steel absorber, alternating with 1.0 cm thick plastic scintillator. The extra thickness of the WHA steel layers is to account for the fact that for a given E_T , the total energy in this calorimeter has on average about $\sqrt{2}$ times more total energy than the CHA [94]. This calorimeter has a calibration system somewhat similar to the one described for the CEM, in Section 3.4.1.

3.4.3 Jet Identification

At CDF, jets are identified as localized deposits of energy in the calorimeter, using a fixed-cone jet clustering algorithm [95]. The parameters used in clustering are transverse energy, $E_T = E \sin \theta$, and the metric in η - ϕ space, $R = \sqrt{\Delta\eta^2 + \Delta\phi^2}$. The algorithm begins by identifying seed towers above a threshold of 1 GeV. For the purpose of finding seed towers only, towers in the plug and forward calorimeters are grouped together in sets of three in ϕ , so that they have the same central segmentation as the central region ($\Delta\phi = 15^\circ$). Preclusters are formed from groups of unbroken, adjacent seed towers that must decrease in E_T about some central seed tower, and have a maximum size of 7×7 seed towers. Clusters are formed by determining the E_T -weighted centroid of a precluster, and forming a cone of radius R about this centroid; this analysis uses a cone size $R = 0.4$. All towers (no ganging) that lie within this cone and have $E_T > 0.1$ GeV are used to calculate a new centroid for the cluster. This is repeated until the clusters remain unchanged. In an event with multiple jets, sometimes two clusters can overlap. If this happens, then an overlap fraction is computed as the sum of E_T of the common towers, divided by the E_T of the smaller cluster. If this overlap fraction is larger than 0.75, then the towers are combined. Otherwise, each tower in the overlap region is assigned to the centroid of the cluster closest in $\eta - \phi$ space. The resulting clusters are interpreted as jets and the following variables are defined:

$$E = \sum_{i=1}^N E_i, \quad (3.7)$$

$$P_x = \sum_{i=1}^N E_i \sin \theta_i \cos \phi_i, \quad (3.8)$$

$$P_y = \sum_{i=1}^N E_i \sin \theta_i \sin \phi_i, \quad (3.9)$$

$$P_z = \sum_{i=1}^N E_i \cos \theta_i, \quad (3.10)$$

where the sum is over towers, θ_i and ϕ_i are computed at the center of each tower, E is the total energy of the jet, and the momentum components determine the jet axis.

3.4.4 Jet Energy Corrections

The raw transverse energy of a jet is almost always a low estimate of the corresponding parton energy for several reasons: (1) the absolute calorimeter response to low-energy charged hadrons is nonlinear, so the P_T recorded for a jet with many particles will be lower on average than the sum of the separate responses from these particles [95, 96]; (2) there exists cracks between calorimeter wedges and towers, allowing particles to escape the active volume of the calorimeter [96]; (3) hadronization particles appear outside the cone radius of 0.4; (4) the collection of relatively low- P_T particles arising from interactions between spectator partons, called the “underlying event”, can contribute a small amount of additional energy to the jet cone [96]; (5) muons and neutrinos in the jet fail to deposit energy in the calorimeter [46, 53].

In this analysis, jets in dilepton events undergo an *absolute* energy correction to compensate for the absolute energy response, item (1), and also a *relative* energy correction to correct for non-uniformity in calorimeter response as a function of η , item (2). These two corrections are the most important of the 5 items listed above. Very briefly, the absolute jet energy correction [96] is derived by first tuning the jet fragmentation in Monte Carlo event generation plus detector simulation to behave the same way as observed in the CTC, using variables such as charged-particle multiplicity. Then, the correction is taken as the ratio, of the sum of the P_T of

all generated particles lying in a cone around the jet axis, to the response in the calorimeter, for these MC events [95]. This ratio is parameterized as a function of jet E_T , and typically corrects a jet in the central region by $+(10-15)\%$ [96]. Once the absolute response in the central calorimeter is understood, the response is then extended into other region of the detector. This is done using a jet balancing technique in dijet events, where one jet lies in the central region, and the other jet is the “probe” jet, located in another part of the detector. A systematic \vec{P}_T imbalance in the calorimeter indicates an energy scale difference between the central region and the probe region, from which the relative jet correction may be determined [96]. This correction depends on jet η and P_T , and can correct a jet energy by as much as 30% [97]. Typically, the systematic uncertainty on a jet energy measurement is a few percent [98].

3.4.5 Missing Energy (\cancel{E}_T) Measurement

In a $p\bar{p}$ collision, particles with significant longitudinal momentum but little transverse momentum, such as hadronization products from spectator quarks, can escape down the beampipe. Therefore it is not the total detected energy and momentum that we expect to balance, but the *transverse* energy and momentum. Neutrinos do not interact with our detector, but their presence can be inferred by an imbalance of energy in a plane transverse to the beam, called *missing transverse energy*, denoted \cancel{E}_T . It can also be a result of detector resolution effects, and particles passing through uninstrumented regions, such as calorimeter cracks. The \cancel{E}_T is defined to be the negative of the vector sum of transverse energy in all calorimeter towers with $|\eta| < 3.6$. To be included in the sum, individual tower energies must exceed detector-dependent energy thresholds that range from 100 MeV in the central region, to 800 MeV in other calorimeters. For events with muon candidates,

the vector sum of the calorimeter transverse energy is corrected by vectorially subtracting the energy deposited by the muon, and then adding the P_T of its track as measured by the tracking chamber. The E_T resolution is approximately $\sigma(E_T) \approx 0.7\sqrt{\sum E_T}$ [46, 99].

3.5 Muon Chambers

Since muons do not feel the strong force, and do not radiate significantly in matter, they only lose energy in the calorimeters through ionization. Therefore the muon chambers are placed outside the central calorimeters, which act as electron, photon and hadron absorbers. The muon detection system in the central portion of the detector is divided up into three major subsystems, the Central Muon (CMU) detector, the Central Muon Upgrade (CMP), and the Central Muon Extension (CMX), which are shown in Figs. 3.2 and 3.3. All of these detectors are comprised of proportional drift chambers filled with argon/ethane gas in order to measure the trajectories of charged particle tracks.

The Central Muon (CMU) detection system is comprised of four layers of drift chambers, which are placed close to the outside of each calorimeter wedge at a radius of about 3.5 m from the beam axis, as shown in Fig. 3.10. Each of these modules consists of a 4×4 array of rectangular aluminum drift cells, shown in Fig. 3.14. The cells have a cross section of about 6×3 cm, and run most of the length of the calorimeter wedge, parallel to the beam axis. A positive potential applied between a $50 \mu\text{m}$ diameter resistive stainless steel wire strung through the center of each cell and the conducting walls produces a uniform time-to-distance relationship throughout the cell for ionization electrons.

A charged track with significant transverse momentum will pass through four layers of drift cells, called a tower, as shown in Fig. 3.14. Two of the four sense

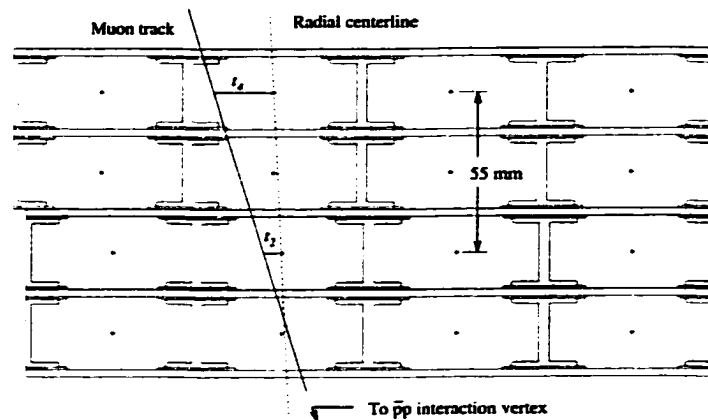


Figure 3.14: A CMU module consists of four layers of drift cells. A track with sufficiently high transverse momentum passes through a CMU tower, consisting of four cells.

wires in a tower, from alternating layers, lie on a radial line passing through the interaction point. In order to resolve the ambiguity as to which side of the sense wires in ϕ a charged track passes, the remaining two wires in a tower lie on a radial line offset from the first by 2 mm in azimuth, measured at the midpoint of the chamber [100]. Tracks are reconstructed in the $r - \phi$ plane with a resolution of 0.25 mm, by using the difference in arrival times of the drift electrons in each cell, as pictured in Fig. 3.14. A muon *stub* is formed if a track is measured in at least 3 of the 4 layers in a muon tower. If this stub matches a CTC track, then this track is classified as a muon candidate.

It is desirable to reduce the number of electronics channels, and to enable readout of the chambers to occur at one end of the detector only (near $\eta = \pm 0.6$). To achieve this, the alternating drift cells in a tower share the same wire, which loops around the $\eta = 0$ end of the chambers. Both ends of each common sense wire are read out. In order to measure a track's z position, charge division is used; the charge deposited at each end of the wire is inversely proportional to

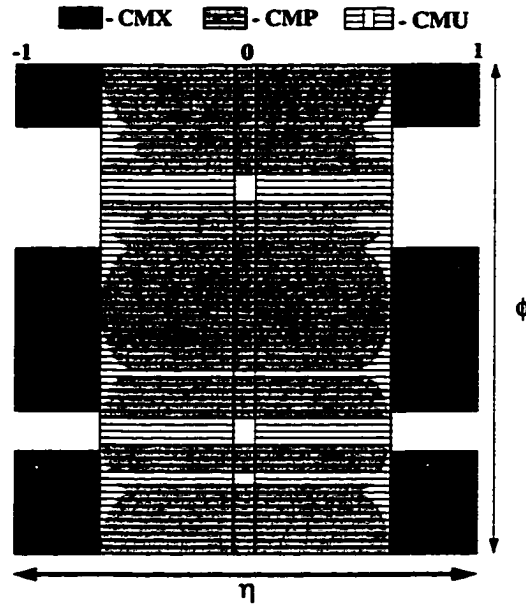


Figure 3.15: The coverage in $\eta - \phi$ space of the three different muon systems.

to the impedance, and hence the length of wire, between the track position and the readout for that end [100, 89]. This method yields a z measurement with a resolution of 1.2 mm.

The calorimeters in front of the muon chambers present an average of 5.4 interaction lengths to particles before they reach the CMU. Despite this, there still exists a *punch-through* probability for a pion to pass through all this material without interacting, and leave a track in the muon chambers. This probability ranges from 0.1-0.4% for pion energies in the range of 15-50 GeV [100], which is a significant source of background for CMU muon identification.

In order to reduce this background, 60 cm (2.4 interaction lengths) of steel have been placed beyond the CMU system as shielding for an additional four layers of axially-aligned drift chambers similar to those in the CMU. This detector system, called the Central Muon Upgrade (CMP), has a box shape that covers 63% of the

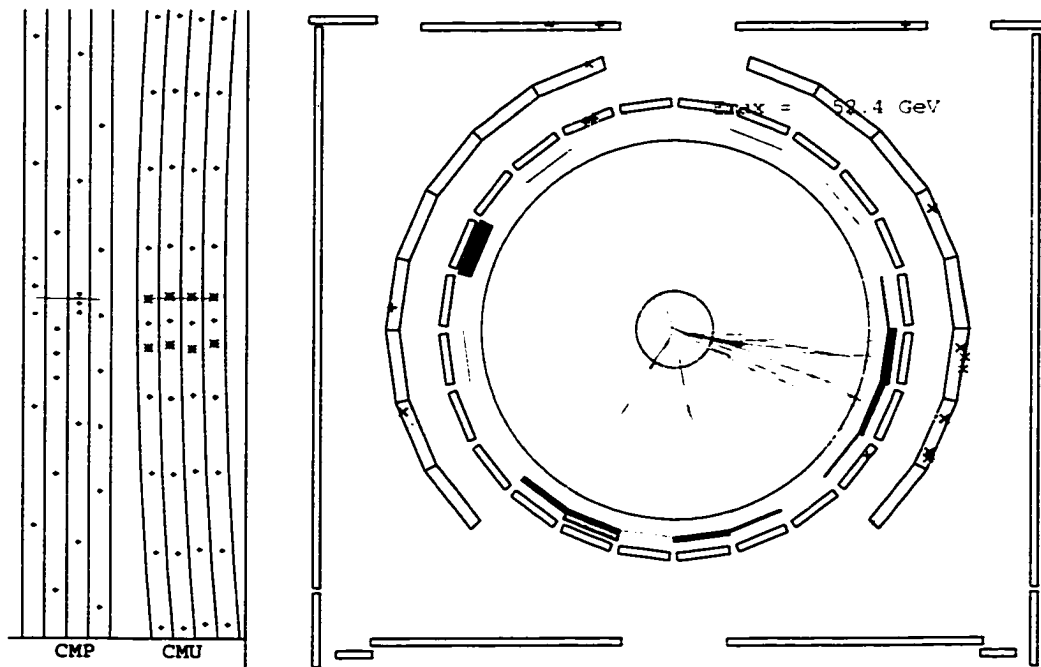


Figure 3.16: A top dilepton candidate, as viewed in many of the detector systems including the CMU, CMP and CMX (outer three) detectors. The muon candidate at 11 o'clock produces hits in the CMU and CMP, which are shown on a magnified view in the side window

region $|\eta| < 0.6$. The combined CMU-CMP system has 53% coverage.

Finally, the coverage of the CMU and CMP is extended to $|\eta| < 1.0$ through the addition of four free-standing conical arches (see Fig. 3.2), which hold four layers of drift chambers for muon detection, sandwiched between scintillator counters for triggering. The drift chambers are similar to the ones found in the CMU and CMP, only shorter (1.8 m long). This system, called the Central Muon Extension (CMX), covers approximately 71% of the solid angle for the range $0.6 < |\eta| < 1.0$. Fig. 3.15 shows the coverage in $\eta - \phi$ space for each of the central muon detectors.

An event display that shows a beam-line view of the CTC, the calorimeters, and all three muon systems is shown in Fig. 3.16. The event is the top dilepton candidate that is also shown in Figs. 3.9 and 3.13. The CMU is placed just outside the CTC, and is represented by the circle of thin rectangles with small gaps between them. Outside the CMU is the CMX, which is represented by the two arches (although in reality more area of the CMX is visible, since the detector is tilted by about 45° with respect to the beam axis). Finally, the box-shaped CMP is the furthest detector from the beam pipe at CDF. In line with the muon track at 11 o'clock are muon hits both in the CMU and the CMP. A closeup of the region where the track extrapolates to the muon chambers is shown in the side window, where hits in all four layers of each of the detectors are visible.

3.6 Beam-Beam Counters and Luminosity

Two Beam-Beam Counters (BBCs) are placed in the forward and backward regions of the detector at $3.2 \leq |\eta| \leq 5.9$ in order to monitor the $p\bar{p}$ interaction rate and determine the luminosity. The detectors, which are located at $z = \pm 5.8$ m, consist of planes of scintillation counters arranged in a rectangle surrounding the beam pipe, in the $r - \phi$ plane (Fig. 3.17). Each covers an area of more than 1 m^2 . Coincident hits in both counters coordinated with the beam crossing are evidence that a beam-beam interaction has occurred.

The rate of coincident hits in the BBC, R_{BBC} , is related to the instantaneous luminosity through the following simplified equation,

$$R_{\text{BBC}} = \sigma_{p\bar{p},\text{BBC}} \mathcal{L} \quad (3.11)$$

where $\sigma_{p\bar{p},\text{BBC}}$ is the total $p\bar{p}$ cross section visible to the beam-beam counters. This

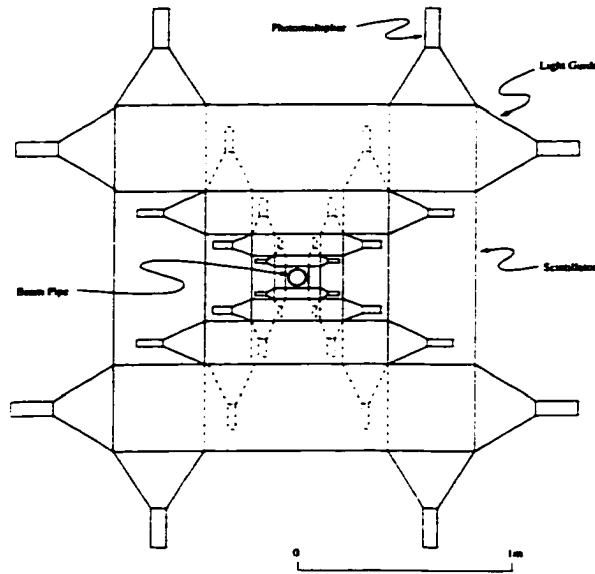


Figure 3.17: One of the BBC counters.

was experimentally calculated [101] to be about 51 mb, from the expression

$$\sigma_{p\bar{p},\text{BBC}} = \sigma_{p\bar{p}} \frac{R_{\text{BBC}}}{R_{p\bar{p}}} \quad (3.12)$$

where $\sigma_{p\bar{p}}$ is the total $p\bar{p}$ cross section, R_{BBC} is defined above, and $R_{p\bar{p}}$ is the total $p\bar{p}$ interaction rate. The quantity $\sigma_{p\bar{p}}$ that appears in the above equation could not be calculated within perturbative QCD, so it had to be measured. Such a measurement seems to require the luminosity, the very quantity we are trying to determine. However, the optical theorem can be used to derive an expression for $\sigma_{p\bar{p}}$ that is independent of the luminosity, but involves $p\bar{p}$ elastic and inelastic scattering rates that have been experimentally determined at CDF [102]. For a concise but complete summary of the CDF luminosity measurement, see Ref. [103].

Eq. 3.11 is oversimplified because it is only accurate when the average number of interactions per beam crossing is much less than 1. When the luminosity is high enough so that the mean number of interactions per crossing ≈ 1 , the probability of getting two or more interactions in the same crossing is high. Under these

conditions, Eq. 3.11 underestimates the luminosity, and has to be corrected [104]. A much smaller ($< 1\%$) correction is performed for accidental coincidences due to sources such as beam-gas collisions [105].

3.7 Trigger and Data Acquisition Systems

The CDF detector elements I have described contain over 150,000 individual channels of electronics. Readout of all of these channels by the CDF data acquisition system (DAQ) requires a significant amount of time (a few ms), and occupies a significant amount of disk storage space (about 150 kB per event). During Run I, $p\bar{p}$ bunch crossings occurred every $3.5 \mu\text{s}$ in the center of the detector, corresponding to an event rate of 286 kHz. Clearly, the DAQ does not have time to read out every event, and even if were able to keep up, it would produce an unmanageable data rate of over 40 GB/s. CDF can only record data to permanent storage media (such as 8 mm tape) at a maximum rate of a few events per second.

Fortunately, even though the DAQ has to contend with a few hundred thousand events per second, only a small fraction of them are “interesting”. At the operational luminosity of $10^{31} \text{ cm}^{-2}\text{s}^{-1}$, a total $p\bar{p}$ cross section of about 80 mb [102] results in an average of 2.8 $p\bar{p}$ interactions per bunch crossing. Most are due to elastic $p\bar{p}$ scattering, or diffractive scattering such as $p\bar{p} \rightarrow pX$, called *minimum bias* events, which almost never produce high- P_T end-products. Events that are considered interesting to most CDF analyses, such as the top analyses, tend to produce high- P_T particles and have tiny cross sections. For example, a $t\bar{t}$ event is expected to be produced about once every $5\frac{1}{2}$ hours, a rate that is more than 11 orders of magnitude smaller than the beam crossing rate.

Sets of selection criteria designed to identify the most interesting events, called *triggers*, are implemented in hardware and software in order to filter the data.

CDF employs a three-tier trigger system, where each increasing level examines fewer events using a more sophisticated and time consuming analysis than the previous level. The design philosophy of the system is to filter most of the data with the first two triggers very quickly, using mostly fast hardware components. Only when an event satisfies the Level 1 and Level 2 triggers, will the DAQ perform the digitization and readout of all the detector components (which takes about 3 ms). This information is then transferred to the Level 3 trigger, implemented as software running on a commercial system.

3.7.1 Level 1 Trigger

The Level 1 trigger uses fast analog outputs from the calorimeter and muon chamber electronics. These signals are processed to determine if there exists a calorimeter cluster with energy exceeding a given threshold, a muon with P_T over some threshold, or some combination of these event characteristics. Table 3.3 shows the ten Level 1 triggers used during the Run 1B data-taking period at CDF.

There are three Level 1 triggers that employ calorimeter information only. The Level 1 (and also Level 2) trigger uses *trigger towers* for the calorimetry, which span a width of $\Delta\phi = 15^\circ$ and $\Delta\eta = 0.2$; this corresponds to two physical towers in η and one (three) in ϕ for the central (plug and forward) regions. One trigger requires a single calorimeter tower with a programmable threshold; typical values used in the central region were $E_T > 8$ GeV for the CEM, and $E_T > 12$ GeV in the CHA. Another trigger requires a lower threshold, $E_T > 4$ GeV, but is “prescaled” so that it is accepted only one out of 40 times. Finally, a dielectron trigger requires two EM towers above 4 GeV as the signature of two electrons.

There are seven triggers that employ muon information, some of which also use calorimeter information. The Level 1 trigger uses muon trigger towers, which

Level 1 Triggers

Calorimeter tower above threshold: CEM: 8 GeV,CHA: 12 GeV,PEM: 11 GeV
Calorimeter tower above threshold : $E_T > 4$ GeV, prescaled.
Two electrons with $P_T > 4$ GeV.
Muon in CMU and CMP, $P_T > 6$ GeV/ c , hadron TDC req. if no CMP seg.
Muon in CMX, $P_T > 10$ GeV/ c , matching hadron tower TDC required.
Muon in CMU and CMP, $P_T > 3.3$ GeV/ c , matching hadron TDC required.
Two CMU or CMX muons, $p_T > 3.3$ GeV/ c .
CEM tower with $E > 4$ GeV and a CMU or CMX muon with $P_T > 3.3$ GeV/ c .
Single Forward Muon (FMU) detector muon, $P_T > 7.5$ GeV/ c , rate limited.
Two FMU muons, $P_T > 7.5$ GeV/ c , rate limited.

Table 3.3: Summary of the ten Level 1 triggers.

are comprised of four overlapping muon chambers aligned along the radial direction, as shown in Fig. 3.14. A P_T measurement is made by exploiting the fact that tracks pass the chambers at an angle with respect to the radial direction, producing different arrival times of drift electrons on the wires. The muon trigger requires coincidence hits on either of two pairs of these wires within a time window determined by the DAQ; increasing the time window allows for acceptance of larger angle, lower- P_T tracks.

The Level 1 trigger examines every event, making a trigger decision within the time between beam crossings (3.5 μ s), and is therefore deadtimeless. It accepts 1-2% of events, outputting to the Level 2 system a rate of a few kHz (the exact value is determined by the trigger thresholds set by the DAQ). If Level 1 accepts the event, then the event is passed on to Level 2, which takes about 30 μ s to process it. This results in deadtime because there is no buffering of events performed in

the Level 2 trigger system.

3.7.2 Level 2 Trigger

Similarly to Level 1, the Level 2 trigger is mostly implemented in custom-built hardware and uses fast analog outputs from the readout electronics. In addition to using muon and calorimeter information, the Level 2 trigger also reconstructs tracks. With about 40 different triggers, it has more programmable hardware (including two DEC Alpha processors in Run 1B), and can reconstruct more details of an event than the Level 1 trigger. It makes decisions based on reconstructed jet clusters, the total transverse energy, the missing energy, two-dimensional tracks in the $r - \phi$ plane, and matching of these tracks to muon stubs and calorimeter clusters.

The Level 2 trigger identifies calorimeter clusters using a simple algorithm that looks for trigger towers with $E_T > 3$ GeV, and then adds adjacent trigger towers over a shoulder threshold of 1 GeV to the cluster. The ratio of electromagnetic to total energy is used to distinguish electromagnetic from hadronic clusters.

The Central Fast Tracker (CFT) performs track reconstruction in the $r - \phi$ plane using only axial layers of the CTC. It takes advantage of the fact that a high- P_T (approximately radial) track will cross very close to at least one sense wire in each CTC superlayer, due to the 45° slant of sense wire rows from the radial direction. This generates a series of hits with small drift times, called “prompt” hits. For every prompt hit in the outer CTC superlayer (superlayer 8), the CFT scans 32 “roads” of hit patterns that a track from the origin of the detector might generate. These are divided into eight P_T bins and two azimuth bins for each sign of curvature, in order to cover the entire momentum range above 2.5 GeV/ c [106]. If an acceptable hit-pattern match is found with a road search, a Level 2 trigger

is issued, usually about $2.5 \mu\text{s}$ after the beam crossing. Delayed hits, arriving 500–600 ns after the beam crossing, are processed on a second pass through the data, and are used to verify high- P_T tracks found while processing prompt hits. The CFT finishes generating a track list after about $8 \mu\text{s}$. The CFT track momentum resolution is about 3.5%, which can be compared with the offline reconstruction accuracy of 0.2%.

The top analyses use 15 of approximately 40 Level 2 triggers. Two are electron triggers, while the rest are muon triggers. A central electromagnetic (CEM) cluster is an electron candidate if it has $E_T > 16 \text{ GeV}$, and matches a CFT track with $P_T > 12 \text{ GeV}$. This requirement is only about 90% efficient for electrons with $E_T > 20 \text{ GeV}$. Because electrons will be produced from W^\pm decay, and accompanied by a high- P_T neutrino in a $t\bar{t}$ event, an additional trigger requires a CEM cluster with $E_T > 16 \text{ GeV}$, and $\cancel{E}_T > 20 \text{ GeV}$. Together, the Level 1 and 2 are about 100% efficient for triggering on electrons that have $E_T > 20 \text{ GeV}$ and are within the geometric acceptance of the CEM.

The triggers for CMU central muons are given in Table 3.4. A Level 2 muon trigger is satisfied if a CFT track with $P_T > 12 \text{ GeV}/c$ matches to within $\Delta\phi = 5^\circ$ of a Level 1 muon stub. Regions instrumented with both CMU and CMP chambers must record muon stubs in both, while regions with CMU coverage but no CMP overlap will contain only one muon stub. Some of the muon triggers are prescaled in order to reduce the Level 2 accept rate to a manageable level. In order to retain good trigger efficiency for top events containing a muon and multiple jets, additional triggers require both a muon and a Level 2 calorimeter cluster with $E_T > 15 \text{ GeV}$. Finally, since high- P_T muons are expected from the decay $W^\pm \rightarrow \mu\nu$ in a top event, other triggers require jet activity along with \cancel{E}_T , presumably from an undetected neutrino, for events in which the muon is undetected by the muon chambers.

Level 2 CMU and CMU-CMP Triggers

Trigger	prescale?
CMU muon + matching CFT track with $P_T > 12 \text{ GeV}/c$	Yes
CMU-CMP muon + CFT track $P_T > 12 \text{ GeV}/c$	No
CMU muon + CFT track $P_T > 12 \text{ GeV}/c$; 1 jet $E_T > 15 \text{ GeV}$	No
CMU-CMP muon + CFT track $P_T > 12 \text{ GeV}/c$; 1 jet $E_T > 15 \text{ GeV}$	No
CMU-CMP muon + CFT track $P_T > 7.5 \text{ GeV}/c$; 1 jet $E_T > 15 \text{ GeV}$	Yes
$E_T > 35 \text{ GeV}$, two jets not forward, $E_T > 3 \text{ GeV}$	No
$E_T > 35 \text{ GeV}$, one jet in CEM or CHA, $E_T > 3 \text{ GeV}$	No

Table 3.4: Summary of Level 2 triggers for CMU and CMU-CMP muons used in the Run 1B top analyses.

The Level 2 trigger incurs deadtime over its $\approx 30 \mu\text{s}$ of decision making time. If Level 2 accepts the event, a signal is sent to the detector electronics to digitize the event, and the DAQ subsequently reads out all the channels. This takes about 3 ms, accounting for another few percent of deadtime. The Level 2 accept rate was limited to 40-55 Hz for Run 1B, governed mainly by the electronics readout times, and the processing power available in the Level 3 system [107].

Before discussing the Level 3 trigger system, I will discuss the data acquisition system at CDF, which is responsible for coordinating the trigger systems, and readout of the detector electronics.

3.7.3 Data Acquisition

The CDF data acquisition (DAQ) system coordinates data flow along two separate paths. The first of these is the control of fast analog outputs from a subset of the detector systems into the Level 1 and Level 2 hardware trigger systems. The second

involves the readout of digitized detector signals into the Level 3 trigger system. Fig. 3.18 shows the essential elements of the DAQ for Run 1B.

The hardware trigger system is composed of the Level 1 and Level 2 subsystems, and FRED (Front-End Readout and Decision Board). Analog outputs that are split off from the front-end electronics are fed to the Level 1 and Level 2 trigger hardware crates. Trigger bits from these crates are sent to FRED, which contains the logic for making the final trigger decisions. FRED also serves as the interface between the analog trigger system, and the rest of the DAQ.

It is the Trigger Supervisor (TS) that coordinates the analog and fully-digitized data paths. On a beam crossing, the TS, which is synchronized with the Master Clock, signals all the detector components to start sampling the event. For calorimeter systems this may mean activating charge integrator circuits, while tracking systems may activate time-to-digital converters. On a Level 1 accept, FRED signals the TS, and the TS then instructs the front end electronics to hold the data for the event, during the 30 μ s period in which the Level 2 decision is being made. If the Level 2 trigger is satisfied, FRED signals the TS, and the TS issues a “digitize event” control signal to all of the electronics. The TS also signals readout controllers to access the digitized data.

The front-end electronics are located in 60 FASTBUS and 129 RABBIT crates mounted on the detector in the collision hall. These crates are read out with FASTBUS Readout Controllers (FRCs), which are microprocessors running Vx-Works, a UNIX-compatible operating system. These FRCs, in turn, are read out with six VME-based Scanner CPUs (SCPU) over a custom bus, which transfer the data to the Level 3 system via a high-bandwidth commercial network called Ultranet. After the FRCs have read out the front-end electronics, the TS frees the front-end electronics for more data taking. By this time the TS has also notified the Scanner Manager (SM) of a new event. The SM synchronizes the data flow

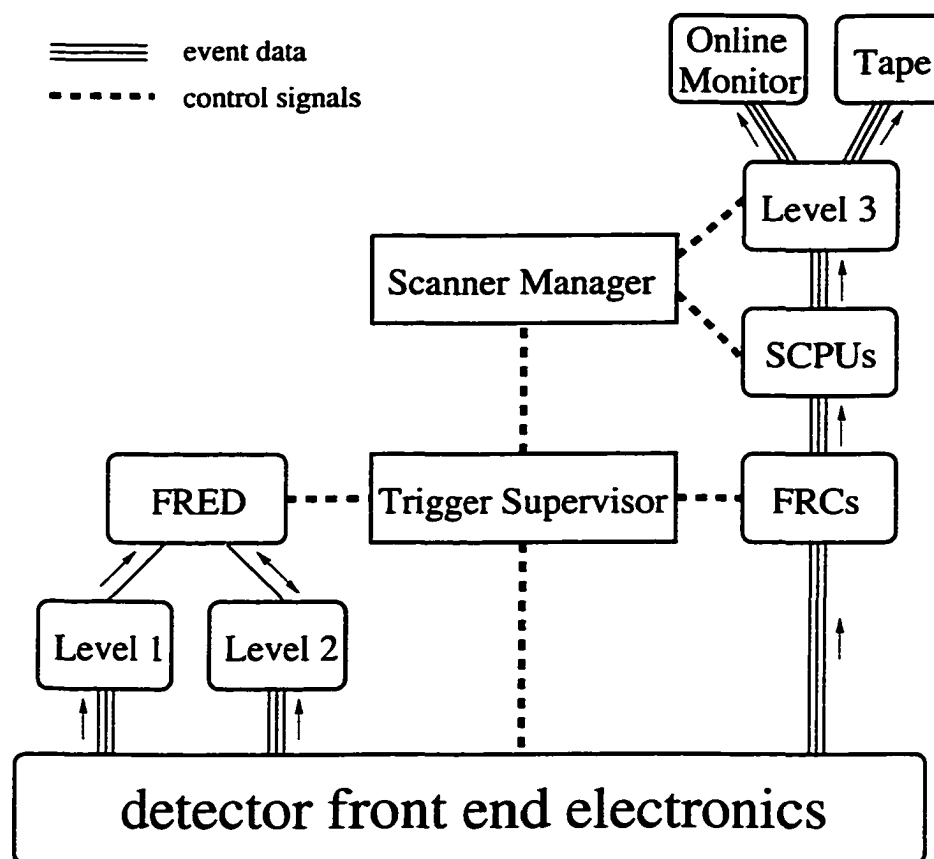


Figure 3.18: A simplified block diagram of the Run 1B data acquisition system.

between the SCPUs and Level 3, by storing a list of free Level 3 input buffers that can be written to, and assigning one to the SCPUs.

3.7.4 Level 3 Trigger and Raw Top Data Samples

The Run 1B Level 3 trigger system [107] runs on multiprocessor Silicon Graphics Unix machines running the IRIX operating system. There are four Challenge series systems with at least eight R4400 CPUs each, and four Power Server series systems with eight R3000 processors each. Each of these systems is logically divided into receiver, reformatter, reconstruction, and dispatcher processes. The

receiver process monitors the input buffer, and passes the buffer to the reformatter once all the event fragments are received. Here, the event is reformatted into the CDF standard YBOS structure, which is a long one-dimensional array composed of data from all of the separate detector banks linked end-to-end. The event is then reconstructed, using most of the same FORTRAN analysis software that is used for offline reconstruction, with some modifications to increase speed. For example, three-dimensional track reconstruction is performed using VTX and CTC information but no SVX information. Also, only one pass is made through the tracking data, whereas the offline code employs an additional, separate algorithm.

Once an event is reconstructed, a trigger decision can be made on each of approximately 70 Level 3 triggers. The top analyses use seven of these triggers, given in Table 3.5, to select events with at least one high- P_T lepton.

The first of two electron triggers selects events containing a cluster with $E_T > 18$ GeV, and an associated track with $P_T > 13$ GeV. The track and the cluster must match well, $\Delta X < 3$ cm and $\Delta Z < 5$ cm, and the cluster must be predominantly electromagnetic with a ratio of HAD/EM energy less than 1/8. Two other cuts are made, which will be discussed in the next chapter. The second electron trigger is designed to identify high- P_T electrons that may not pass the tight cuts of the first trigger. It requires $E_T > 50$ GeV and an associated track with $P_T > 25$ GeV.

Five triggers select muons from the three different muon detector systems. Muons passing through the CMX and CMP traverse more material, and are deflected more than CMU muons. Therefore CMX and CMP muons are required to match a $P_T > 18$ GeV track within $\Delta X < 10$ cm, while CMU muons must have $\Delta X < 5$ cm. In addition, since muons are expected to produce only a minimum ionizing signal in the calorimeters, less than 6 GeV of energy must reside in the hadronic calorimeter that the muon passes through.

Events that pass one of the Level 3 triggers are sent to *consumers*, which

Level 3 Triggers

MUONS	ELECTRONS
$P_T > 18 \text{ GeV}, E_{\text{HAD}} < 6 \text{ GeV},$ $\left[\Delta x _{\text{CMU}} < 5 \text{ cm} \right.$ <p style="text-align: center;">OR</p> $ \Delta x _{\text{CMP}} < 10 \text{ cm}$ <p style="text-align: center;">OR</p> $\left. \Delta x _{\text{CMX}} < 10 \text{ cm} \right]$	$E_T > 18 \text{ GeV}, P_T > 13 \text{ GeV},$ $\frac{E_{\text{HAD}}}{E_{\text{EM}}} < 0.125, L_{\text{shr}} < 0.2,$ $ \Delta x < 3 \text{ cm}, \Delta z < 5 \text{ cm},$ $\chi_{\text{strip}}^2 < 10$ <p style="text-align: center;">OR</p> $E_T > 50 \text{ GeV}, P_T > 25 \text{ GeV}$

Table 3.5: Run 1B Level 3 triggers used to create the top samples. There are actually five muon triggers, since the CMU muons are subdivided into three categories, depending on whether they *don't* match a CMP segment, they *do* match a CMP segment, or they are found where no CMP coverage exists.

temporarily store the data to files on disk, before writing them to 8 mm tape. The consumers also perform online monitoring of data quality and of detector subsystem performance, for use in diagnostics by the shift crew on duty in the CDF control room.

Events are organized into different files depending on the class of triggers they satisfy. Events satisfying triggers designed to identify high-priority topologies, such as those from W^\pm , Z^0 or $t\bar{t}$ events, are sent to Stream A. The majority of the remaining events go to Stream B, and low priority events go to Stream C.

The inclusive lepton sample that is used as a starting point for this analysis is made by running over all the Stream A tapes, and selecting events that satisfy the seven Level 3 triggers listed in Table 3.5. These Run 1B samples contain about 750,000 electrons and 570,000 muons. The next chapter describes the additional identification requirements that are enforced in order to select $t\bar{t}$ candidate events.

Chapter 4

Selection Criteria, SM Efficiencies, and Non- $t\bar{t}$ Backgrounds

The last chapter described the triggers that identify $t\bar{t}$ dilepton and lepton+jets decay topologies. These triggers select events “online”, during the data-taking period. In this chapter, I summarize the complete set of “offline” selection criteria used to identify candidate events in each channel, applied in a detailed analysis performed after the events have been written to tape. I give the efficiencies for SM $t\bar{t}$ events to satisfy these sets of selection criteria. In order to preserve good signal acceptance, the cuts used to identify candidate events permit contributions from sources other than $t\bar{t}$ production. Sources of background are identified, and the event rate from each source is calculated.

It should be emphasized that almost none of the results presented in this chapter are my own. Most of this work was done by the other members of the Top Group at CDF, in order to discover the top quark and measure its properties. The results in this chapter form a framework that is used as a starting point for my analysis.

4.1 The High- P_T Electron and Muon Samples

The last chapter described the Run 1B inclusive high- P_T lepton sample, created by running over all the Stream A data tapes, and selecting events that satisfy at least one of the seven Level 3 triggers listed in Table 3.5. This inclusive lepton sample

contains about 750,000 electrons and 570,000 muons. From this sample, and a similar Run 1A sample, a second inclusive sample is made with much tighter identification cuts for electrons and muons. This second inclusive lepton sample [108], which is described in the next two sections, is used as a starting point for the top analyses. The Run 1B portion of this second sample contains about 130,000 electron events and 90,000 muon events [108], while the Run 1A portion of the sample contains a little less than one-fifth as many events [46].

4.1.1 Electron Identification

This analysis considers electron (and positron) candidates in the central electromagnetic calorimeter ($|\eta| < 1.0$) only. Electron candidates consist of a high- P_T CTC track that extrapolates to a deposition of energy in the electromagnetic calorimeter. The energy, which is usually almost entirely contained in a single calorimeter tower, must be consistent with the momentum of the track measured by the CTC. Requirements on the position of the shower, measured by the CES strip chamber, ensure that the electron candidate is not near calorimeter boundaries, so that its shower is contained within the active volume of the detector. These are called *fiducial* requirements (or “cuts”), and require that the electron be located at least 3.2 cm away from a wedge boundary in ϕ , and 9 cm from the transverse plane at $z = 0$, to avoid the gap between the two cylindrical halves of the central calorimeters. The fiducial volume covers 84% of the solid angle in the region $|\eta| < 1.0$ [46].

One of the largest backgrounds to physics signals in the high- E_T inclusive electron sample is due to real electrons from photons that interact in the detector and convert to electron-positron pairs. Prior to conversion removal, roughly 30–40% of the sample contains conversions (before isolation cuts are applied to the

leptons, or E_T is required) [109]. These are removed by searching for oppositely-charged tracks that can be paired with an electron candidate, passing closely in both the $r-\phi$ plane (within 0.3 cm) and the $r-z$ plane ($\Delta\cot\theta < 0.06$). Conversion candidates must also have a vertex located where most of the material in the detector lies, $-20 \text{ cm} < r < 50 \text{ cm}$ [109]. If the P_T of the paired conversion candidate is too low, the track may not be reconstructed. To identify conversions of this type, electron candidates with fewer than 20% of the expected hits in the VTX are identified as coming from a conversion. The efficiency for conversion removal is about 90%, while only removing a few percent of high- P_T leptons from W^\pm boson decays [109].

A variety of selection variables are used to identify high- P_T electron and positron candidates, and discriminate against charged hadrons and muons. Electrons from W^\pm decays are expected to have significant transverse momentum; we require $E_T > 20 \text{ GeV}$ for the cluster. The momentum P of the track associated with the cluster may be mismeasured due to photon radiation, but a crude energy-momentum match is still required; the E/P ratio cannot be much greater than 1. Also, the ratio of hadronic energy to electromagnetic energy in the calorimeter cluster, $E_{\text{HAD}}/E_{\text{EM}}$, should be small. Two variables compare the shape of the energy distribution of electron candidates in the calorimeter with test-beam electrons. One variable is L_{shower} , the lateral distribution of energy in CEM towers adjacent to the one containing most of the energy deposition [110]. The other is χ_{strip}^2 , a χ^2 fit of the CES lateral shower profile to a shape derived from the test-beam electrons. There are track quality cuts, too. The z position of the lepton track must lie within 5 cm of the primary event vertex. In addition, the distance between the extrapolated track and the CES shower position must be small; this is measured with Δx in the $r-\phi$ plane and Δz in the $r-z$ plane. Finally, electrons and muons from W^\pm decays are usually isolated from other particles. The particle activity

Electron Candidate Selection Criteria

variable	tight cuts	Loose cuts - 2nd lepton
		of a dilepton pair only.
E_T	$> 20 \text{ GeV}$	$> 20 \text{ GeV}$
E/P	< 1.8	< 4.0
$E_{\text{HAD}}/E_{\text{EM}}$	< 0.05	$0.055 + \frac{0.045 E}{100}$
L_{shower}	< 0.2	< 0.2
$ \Delta x $	$< 1.5 \text{ cm}$	$< 1.5 \text{ cm}$
$ \Delta z $	$< 3.0 \text{ cm}$	$< 3.0 \text{ cm}$
z-vertex match	$< 5.0 \text{ cm}$	$< 5.0 \text{ cm}$
χ^2_{strip}	< 10	-
$I_{\text{cal}}, I_{\text{trk}}$	lepton+jets event: $I_{\text{cal}} < 0.1$ dilepton: 1 lepton with $I_{\text{cal}} < 0.1, I_{\text{trk}} < 0.1$	

Table 4.1: The selection cuts for central electrons. A dilepton event must have one electron or muon candidate passing “tight” selection criteria, and another that passes “tight” or “loose” cuts. The lepton candidate in an electron+jets event must pass the “tight” cuts.

around a lepton candidate can be measured quantitatively using calorimeter I_{cal} and tracking I_{trk} isolation variables, essentially the fractional energy and momentum appearing in the immediate neighborhood of the lepton, respectively. They are defined as

$$I_{\text{trk}} = \frac{P_T^{0.4}}{P_T}, \quad I_{\text{cal}} = \frac{E_T^{0.4}}{E_T} \text{ (electrons)}, \quad \frac{E_T^{0.4}}{P_T} \text{ (muons)} \quad (4.1)$$

where the $E_T^{0.4}$ is the sum of transverse energy inside a cone of radius $\Delta R = \sqrt{(\Delta\phi)^2 + (\Delta\eta)^2} = 0.4$, centered on the lepton, but excluding the transverse energy deposited by the lepton, and $P_T^{0.4}$ is the sum of the P_T of the tracks within this

cone, excluding the lepton track.

The electron identification cuts are given in Table 4.1. There are two classes of cuts, with different degrees of purity. The lepton+jets analysis requires the stringent “tight” cuts for identification of the single lepton in the event. In the dilepton channel, it is expected that the second lepton in the event may not be as cleanly identified as the first one. Thus, for the dilepton channel, one lepton must satisfy “tight” cuts, while the other is permitted to satisfy the “loose” criteria.

Using $Z^0 \rightarrow e^+e^-$ decays, it is determined that the efficiency for *fiducial* electrons with $E_T > 20$ GeV to pass all the requirements in Table 4.1, excluding the isolation cuts, is about 82% for the “tight” cuts, and 89% for the “loose” cuts [111]. These efficiencies are known as electron identification efficiencies.

4.1.2 Muon Identification

In the muon+jets search, we identify muons in the central region ($|\eta| < 1.0$) of the detector by requiring a match between a CTC track and a muon segment in one of the central muon chambers (CMU, CMP, or CMX). For the dilepton search, we also include muon candidates in regions of the detector not covered by muon chambers, but where a well-reconstructed track extrapolates through the center of a calorimeter tower, leaving an amount of energy that is consistent with a minimum ionizing particle. For this reason, these muon candidates are called Central Minimum Ionizing (CMI) muons. They do not cause triggers, but are present in events that are triggered another way.

CMI muons must satisfy a fiducial requirement for passing through the active volume of the calorimeter, which is similar to the one made for electrons. They can be found in the region $1.0 < |\eta| < 1.2$, which is not instrumented by muon chambers, and the area $|\eta| < 1.0$ in regions of missed muon chamber coverage (see

Fig. 3.15). CMI muons are similar to loose electron candidates, since they are considered to be loose by dilepton standards, and are not used in the lepton+jets search.

Just as photon conversions present a sizable background to the inclusive electron sample, cosmic ray muons lead to fake dimuon events. Cosmic ray muons can pass close to the beam line, creating the appearance of back-to-back tracks. These tracks are out of time as measured by the hadron calorimeter TDCs, since they don't originate at a vertex along the beam axis. A cosmic ray filter removes events by rejecting muons pairs that are separated by $\Delta\phi \approx 180^\circ$. TDC timing information is also used [111].

A variety of selection variables are used to identify high- P_T muon candidates, and discriminate against charged hadrons. Muons from W^\pm decay have significant transverse momentum; we require $P_T > 20 \text{ GeV}/c$. In addition, the energies deposited in the electromagnetic calorimeter E_{EM} and the hadronic calorimeter E_{HAD} should be consistent with a minimum ionizing particle - not more than a few GeV, but not zero, either. Several track quality cuts are imposed. The impact parameter, the distance of closest approach between the reconstructed muon track and the beam axis in the $r - \phi$ plane, should be less than 3 mm, indicating that the muon originated from the primary vertex. In addition, the distance between the muon segment and the extrapolated track in the $r - \phi$ plane $|\Delta x|$ should be small. Muons from W^\pm decay will usually be isolated from other particles. This isolation can be measured with I_{cal} and I_{trk} , calorimeter and track isolation variables, defined in Eq. 4.1. Finally, because CMIs do not have muon chamber hits, more stringent tracking and isolation requirements are imposed to reduce the rate of objects faking a CMI. A candidate must have I_{cal} and I_{trk} less than 0.1, and an associated track with a minimum number of superlayer hits in the CTC.

Using $Z^0 \rightarrow \mu^+ \mu^-$ decays, it is determined that the efficiency for *fiducial* muons

Muon Candidate Selection Criteria

variable	tight cuts	CMI “loose” muon.
	central muon only	Dilepton channel only.
$P_T \cdot c$	$> 20 \text{ GeV}$	$> 20 \text{ GeV}$
E_{EM}	$< 2 \text{ GeV}$	$< 2 \text{ GeV}$
E_{HAD}	$< 6 \text{ GeV}$	$< 6 \text{ GeV}$
$E_{\text{EM}} + E_{\text{HAD}}$	$> 0.1 \text{ GeV}$	$> 0.1 \text{ GeV}$
impact parameter d_0	$< 3 \text{ mm}$	$< 3 \text{ mm}$
z-vertex match	$< 5 \text{ cm}$	$< 5 \text{ cm}$
$ \Delta x _{\text{CMU}}$	$< 2 \text{ cm}$	-
$ \Delta x _{\text{CMP, CMX}}$	$< 5 \text{ cm}$	-
#axial, stereo, tot. SL	-	$\geq 3, \geq 2, \geq 6$
$I_{\text{cal}}, I_{\text{trk}}$	lepton+jets event: $I_{\text{cal}} < 0.1$ dilepton: 1 tight lepton w/ $I_{\text{cal}} < 0.1, I_{\text{trk}} < 0.1$ a CMI must have $I_{\text{cal}} < 0.1, I_{\text{trk}} < 0.1$	

Table 4.2: The selection cuts for muons. A dilepton event must have one electron or muon candidate passing “tight” selection criteria, and another that passes “tight” or “loose” cuts. The muon in a muon+jets event must pass the “tight” cuts.

with $P_T > 20 \text{ GeV}$, to pass the requirements in Table 4.2 excluding the isolation cuts, is about 92% regardless of the type of muon [111]. This is known as the muon identification efficiency.

4.2 The Lepton+Jets Channel

Lepton+jets events are expected to contain a leptonic W^\pm decay to $e\nu$ or $\mu\nu$, a hadronic W^\pm decay to $q\bar{q}'$, and two b -quarks. Lepton+jets events must have an electron or muon that passes the “tight” identification cuts outlined in the previous section. Leptons from W^\pm decay are usually isolated. To discriminate against jets and leptons from $b\bar{b}$ production that tend to be less isolated, the lepton is required to have calorimeter isolation $I_{\text{cal}} < 0.1$. A neutrino in the event should result in significant \cancel{E}_T , so we require $\cancel{E}_T > 20$ GeV, where the \cancel{E}_T is corrected for the presence of muons, as described in Section 3.4.5. This helps reduce backgrounds from misidentified leptons in QCD events, and semileptonic decays in $b\bar{b}$ events. The Z^0 boson decays are removed by rejecting e^+e^- or $\mu^+\mu^-$ pairs with an invariant mass in the Z^0 mass window ($75 \text{ GeV} < M_{\ell\bar{\ell}} < 105 \text{ GeV}$). Since the “second leg” of these Z^0 decays may not be identified as cleanly as the first leg, the selection criteria for this second lepton is much looser than the criteria for the primary lepton in the event. Finally, three jets ($N_{\text{jet}} \geq 3$) with $E_T > 15$ GeV and $|\eta| < 2.4$ are required from the four quarks in the event. While in principle, one might expect to observe one jet for each quark in the final state of a $t\bar{t}$ decay, in practice this is not the case because jets might coalesce, be lost down the beam line, or fail the 15 GeV calorimeter threshold requirement [46]. Jet clustering is done with a cone of radius 0.4 in η - ϕ space, as discussed in Section 3.4.3. The jet energies are the raw jet energies, uncorrected for non-uniformities in calorimeter response or the absolute value of the jet energy scale.

After applying these selection criteria, the resulting sample has a signal-to-background ratio of one-to-four [47]. As I stated in Chapter 2, additional background rejection is provided by requiring the presence of a b -flavored hadron in the events. We use the CDF silicon vertex detector (SVX) to locate decay vertices of

B hadrons that are separated from the primary vertex of an event by several mm, as a result of their long lifetime of $c\tau = 470 \mu m$. The jets with displaced vertices are said to contain “SVX tags”, and the tagging algorithm is called SECVTX. I require the lepton+jets events in this analysis to have at least one SVX tag.

Before using the SECVTX algorithm to locate secondary vertices in an event, the primary vertex of the event must be determined. In the following sections, I describe both the primary vertex finder, and SECVTX.

4.2.1 The Primary Vertex

The offline reconstruction of the primary vertex begins with track segments in the VTX, as described in Section 3.3.2. These segments are used to determine vertex positions in z , along the beam axis. Typically, there will be more than one $p\bar{p}$ interaction per event, resulting in several vertex positions. These vertices are ranked into classes according to the number of track segments that project back to each vertex, the total number of drift hits in these segments, and the forward-backward asymmetry of these segments [86]. The vertex with the highest class relative to the others is identified as a primary vertex, but other vertices passing predetermined selection criteria are also classified as primary vertices.

In Run 1B, the SVX and the beam were not aligned; the beam slope was typically $6 \mu m/cm$ in x and $-3 \mu m/cm$ in y [112]. With multiple vertices, this offset causes tracks emanating from one vertex to appear displaced from other vertices separated in z by many cm. Thus, all tracks associated with an event vertex are required to extrapolate to within $z = 5$ cm of that vertex. The primary vertex is chosen to be the one with the greatest total transverse momentum of associated tracks [46, 113]. It coincides with the primary high- P_T lepton z -vertex in most lepton+jets events [46, 114].

To form a seed vertex, the z -value of the primary vertex is combined with the run-averaged position of the beam in the x - y plane. The run-averaged position of the beam is determined using SVX tracks from all the events in the run (many tens of thousands of events), and is known to a resolution of $\sigma_{x,y} \approx 25 \mu m$ [112]. Starting with an event's seed vertex, an iterative procedure determines the primary vertex, from a weighted fit of the SVX tracks in the event, with corrections for the detector offset and slope. The first iteration of the fit uses all quality SVX tracks in the event (tracks with $P_T > 0.4 \text{ GeV}/c$, ≥ 3 SVX hit layers, $|d_0| < 2.0 \text{ cm}$), to determine a new vertex. The track with the highest residual is removed at the end of each iteration, until there are no tracks contributing more than a set amount to the vertex χ^2 [115]. The uncertainty of the primary vertex in the transverse coordinates ranges from 6-36 μm , depending on the number of tracks and the event topology [46].

4.2.2 SECVTX - the Displaced Vertex Tagging Algorithm

The SECVTX algorithm [116] searches for displaced vertices associated with jets. A jet is considered “taggable” if it has $E_T > 15 \text{ GeV}$, $|\eta| < 2$, and at least two SVX tracks. The algorithm makes two passes through all the SVX tracks associated with a jet. The first pass requires three tracks of somewhat loose quality to form a secondary vertex. If no such vertex is found, then a second pass is made, requiring two tracks satisfying tighter cuts to form a displaced vertex. The criteria for tracks to be considered for each of these fits are shown in Table 4.3.

In the first pass of the SECVTX algorithm, a set of candidate tracks is obtained using the loose track selection criteria listed under “pass 1” in Table 4.3. The tracks are ranked according to their P_T , impact parameter significance d_0 / σ_{d_0} , and number of good clusters on the track [117]. The two highest-quality tracks are

SECVTX Criteria for Track Quality, Good Hits, and Vertex Quality

pass 1 (3 SVX trks)	pass 2 (2 SVX trks)	good cluster cuts	final vertex cuts
$d_0 / \sigma_{d_0} > 2.5$	$d_0 / \sigma_{d_0} > 3.0$		
<u>2-hit tracks</u>	<u>3-hit tracks</u>	≤ 3 strips	$ L_{xy} < 2.5$ cm
$P_T > 1.5$ GeV/ c	$P_T > 1.0$ GeV/ c	no noisy strips	$ L_{xy} / \sigma_{L_{xy}} \geq 3$
#good cluster = 2	#good cluster ≥ 2	no dead strips	no K_s^0 or Λ^0
<u>3,4-hit tracks</u>	<u>4-hit tracks</u>	not shared	
$P_T > 0.5$ GeV/ c	$P_T > 1.0$ GeV/ c		
#good cluster ≥ 1	#good cluster ≥ 1		

Table 4.3: The SVX track quality cuts used by the SECVTX algorithm. An “ n -hit” track means n of the four SVX layers registered hits from the track. Also given are the requirements for a good SVX cluster, and the final cuts imposed on the displaced vertex.

constrained to come from a single vertex, which is then used as a seed to test other tracks for association. One of these two seed tracks must have $P_T > 2.0$ GeV. All of the remaining tracks are looped over in search of additional tracks that have a impact parameter significance of less than 3, relative to the seed vertex. If at least one such track is found, the algorithm performs a full three-dimensional fit, simultaneously constraining all the attached tracks to originate from a common vertex. If no such third track is found, then other tracks pairs are tried as seeds. If all track pairs have been used as seeds unsuccessfully, then a second pass is performed.

In the second pass, all the SVX tracks that satisfy the tight quality cuts in column two of Table 4.3 are fit to a common three-dimensional vertex. Any track contributing $\chi^2 > 50$ to the vertex fit is discarded, and the vertex is refit. This

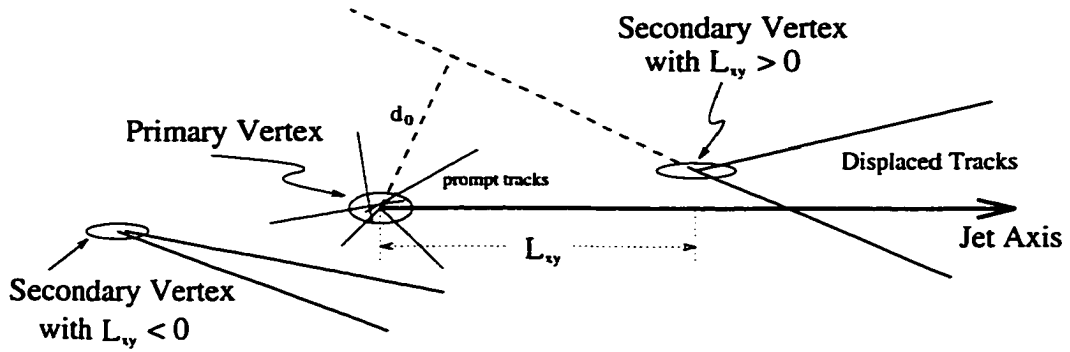


Figure 4.1: An illustration of two SVX tags. One has a positive decay length L_{xy} , and another has a negative L_{xy} .

procedure is repeated until no further tracks are removed. A secondary vertex is found if two displaced tracks remain, and one has $P_T > 2.0$ GeV.

If a candidate displaced vertex is found, then the two-dimensional decay length L_{xy} is calculated, defined as the distance along the jet axis between the primary and secondary vertices in the plane transverse to the beam, as shown in Fig. 4.1. This quantity is positive if it lies on the same side of the primary vertex as the jet, and negative otherwise. Finally, some quality cuts are required of a secondary vertex in order for it to be declared an SVX tag. The decay length significance $|L_{xy}| / \sigma_{L_{xy}}$ must be larger than 3.0, and the decay length must reside inside the beampipe, $|L_{xy}| < 2.5$ cm. Finally, the decay cannot be consistent with decays from K_s^0 or Λ^0 particles [116, 117].

4.2.3 Lepton+jets Selection Efficiency for $t\bar{t} \rightarrow WbW\bar{b}$

In this section, I give the efficiency for SM $t\bar{t}$ events to pass the selection criteria of the lepton+jets channel. This efficiency is mostly determined from Monte Carlo $t\bar{t}$ event generators, combined with a detailed simulation of the CDF detector. I also explain the cross checks and corrections to this efficiency that are made,

based on the behavior of other high- P_T processes that are observed. I include a brief discussion of the systematic uncertainties, which are due to limitations in determining the efficiency.

The $t\bar{t}$ efficiency for passing the selection criteria of the lepton+jets channel can be written as [118]

$$\epsilon_{t\bar{t},SVX} = \frac{1}{\mathcal{L}_{tot}} A_{t\bar{t}} (\epsilon_{trig,1A} \cdot \epsilon_{tag,1A} \cdot \mathcal{L}_{1A} + \epsilon_{trig,1B} \cdot \epsilon_{tag,1B} \cdot \mathcal{L}_{1B}) . \quad (4.2)$$

Here, $A_{t\bar{t}}$ is the efficiency for all selection criteria other than the trigger and tagging requirements, and is common to Run 1A and Run 1B. The trigger efficiency ϵ_{trig} and tagging efficiency ϵ_{tag} are run-dependent quantities, since the trigger system and the SVX detector changed significantly between Run 1A and Run 1B. They must be combined separately for each run using the proper luminosity weighting. The luminosity has been measured separately in Run 1A ($\mathcal{L}_{1A} = 19.3 \pm 0.7 \text{ pb}^{-1}$) and Run 1B ($\mathcal{L}_{1B} = 90.1 \pm 7.2 \text{ pb}^{-1}$). The factor \mathcal{L}_{tot} is their sum, $\mathcal{L}_{tot} = 109.4 \text{ pb}^{-1}$. The individual factors that are given in Eq. 4.2 are listed in Table 4.4, and are described in more detail below.

$A_{t\bar{t}}$: This is the efficiency for $t\bar{t}$ events to pass all the selection criteria except for trigger and b -tagging requirements. Table 4.4 shows that the efficiency for having an isolated lepton in an event is about 14%. This number takes into account the branching fraction of 30% for $t\bar{t}$ to decay into $(qq'b)(e/\mu\nu\bar{b})$, the $t\bar{t}$ final state that contributes most heavily to the lepton+jets sample. Not all of these events will become part of the lepton+jets sample, since only a fraction of them are found in the geometric and kinematic acceptance of the detector. Monte Carlo generators tell us that about 85% of the leptons from W^\pm decays have $P_T > 20 \text{ GeV}/c$, and about 75% are in the region $|\eta| < 1.1$ [111]. Further reduction of efficiency is due to application of the lepton fiducial cuts, photon conversion removal cuts, cosmic ray removal cuts, Z^0 removal cuts, lepton identification cuts, and the lepton isolation

SM Efficiency for Lepton+Jets Selection Cuts

category	Run 1A	Run 1B
isolated e/μ	$(13.7 \pm 0.5)\%$	
$E_T > 20 \text{ GeV}$	$(88 \pm 2)\%$	
$N_{\text{jet}} \geq 3$	$(85 \pm 2)\%$	
Total $A_{t\bar{t}}$	$(10.3 \pm 0.4)\%$	
trigger	$(84.1 \pm 7.6)\%$	$(92.0 \pm 8.0)\%$
tag	$(33 \pm 10)\%$	$(40.2 \pm 3.2)\%$
trig-tag	$(35.4 \pm 4.6)\%$	
total	$(3.65 \pm 0.62)\%$	

Table 4.4: The SM efficiencies for $t\bar{t}$ decays to satisfy the lepton+jets selection cuts. The error on $A_{t\bar{t}}$ is due to uncertainties associated with lepton identification efficiencies, the z -vertex cut efficiency, and limited Monte Carlo statistics. The error on the trigger-tagging term contains an 11% error from combining trigger and tagging systematics, along with the 7% luminosity error. The error on the total efficiency is due to all the systematic effects listed in Table 4.5.

requirement. The efficiency for each of these successive cuts ranges between 80-95%, for SM $t\bar{t}$ events. Finally, other $t\bar{t}$ decay topologies besides $(qq'b)(e/\mu\nu\bar{b})$ contribute to the lepton+jets sample, particularly those containing tau leptons.

The $A_{t\bar{t}}$ is the raw efficiency derived from simulated Monte Carlo samples of events, and corrected for two effects, which the simulation may not model well. The first of these is the lepton identification efficiencies, which were discussed in Sections 4.1.1 and 4.1.2. These efficiencies have been measured in the data, using electrons and muons from Z^0 decays. They are found to be smaller than the corresponding detector simulation efficiencies by 5-9%, depending on the type of

Systematic Errors for the SM $t\bar{t}$ Efficiency

category	SVX channel	Dilepton channel
lepton ID ϵ	3%	7%
trigger ϵ	8%	2%(trig. only)
SVX b -tag ϵ	8%	-
jet energy scale	5%	3%
ISR/FSR	8%	3%
Luminosity	7%	
z -vertex res. effect	2%	2%
Total	17%	11%

Table 4.5: Systematic errors in each channel for the product $\epsilon\mathcal{L}$.

lepton [111]. The second effect is the z -vertex distribution, also which is measured from the data [119]. The total value of $A_{t\bar{t}}$ for SM $t\bar{t}$ events is shown in Table 4.4. The associated error is due to systematic uncertainties associated with the lepton identification efficiencies and the z -vertex cut efficiency: these errors are listed in Table 4.5.

ϵ_{trig} : This is the Level 1 \times Level 2 \times Level 3 trigger efficiency for $t\bar{t}$ events, which differs between Run 1A and Run 1B as shown in Table 4.4. Both numbers are relatively high, and have systematic uncertainties of 9% [46, 120, 121, 122].

ϵ_{tag} : This is the efficiency for finding at least one SVX b -tagged jet in a SM $t\bar{t}$ event. The tagging efficiencies of $(33 \pm 10)\%$ for Run 1A, and $(40.2 \pm 3.2)\%$ for Run 1B, take into account the fact that only 67% of $t\bar{t}$ events lie within the geometrical acceptance of the SVX detector. These tagging efficiencies are found to differ between data and Monte Carlo events. One of the primary reasons for this disagreement is due to the fact that the Monte Carlo typically overestimates

the efficiency for reconstructing a track within the core of a jet by about 10% [123].

Traditionally, tagging efficiencies have been measured in the inclusive lepton sample, which is enriched in $b\bar{b}$ events [46, 124, 116, 125]. These efficiencies are then compared with predictions for a similar sample of Monte Carlo $b\bar{b}$ events, to obtain a correction ratio that is applied to the b -tagging efficiency for Monte Carlo $t\bar{t}$ events. However, it has been pointed out [126] that these studies have inadequate statistics in the high- E_T region $E_T \gtrsim 50$ GeV, which is the energy range for the majority of the jets from $t\bar{t}$ decays. For this reason, the tagging efficiency is currently calculated from Monte Carlo events, using the measured efficiency for reconstructing tracks within the core of a jet [124, 123]. This method is subject to change.

The trigger \times tagging efficiencies for Run 1A and Run 1B are shown in Table 4.4. The combined Run 1A + 1B $\epsilon_{trig} \cdot \epsilon_{tag}$ efficiency has a 11% error from combining the trigger uncertainties and b -tagging efficiency uncertainties given above. A separate 7% error is due to the Run 1A and Run 1B luminosity measurements.

The total efficiency for $t\bar{t} \rightarrow WbW\bar{b}$ to pass the selection criteria of the lepton+jets channel is measured to be $(3.65 \pm 0.62)\%$, where the quoted error is due to all the systematic errors listed in Table 4.5. This number agrees with the efficiency quoted in [118].

One source of error, that has not been discussed yet, arises due to uncertainty in the energy of jets measured by the calorimeter. This error is about 3% [98] for jets that have been corrected for detector and reconstruction effects, described previously in Section 3.4.4. Among these, the most important corrections are for non-linear calorimeter response and the absolute energy response. These corrections are applied to the jets in dilepton events. However, only the raw uncorrected jet energy is used for lepton+jets events. The systematic uncertainty for the raw jet energy is conservatively estimated to be 10% [127]. This is the value used

throughout this analysis for jets found in both dilepton and lepton+jets events. To measure the systematic error that is associated with the jet energy scale uncertainty, I systematically vary the E_T of the jets in a top Monte Carlo sample by $\pm 10\%$. Jets that correspond to high- P_T electrons are not varied. The \cancel{E}_T is recalculated according to the shifted energies. The $\pm 10\%$ variation gives a $\pm 5\%$ change in efficiency for SM $t\bar{t}$ decays, due to shifts in the efficiencies of the \cancel{E}_T and jet-multiplicity cuts.

Another source of uncertainty arises from modeling initial and final-state radiation (ISR and FSR) of photons and gluons, in $t\bar{t}$ Monte Carlo events. I take a conservative approach, and determine the difference in efficiency between the extreme cases when there is no initial state radiation (-3%) and no final state radiation ($+13\%$). I take half of this 16% difference as a systematic error. This approach is slightly different from the approach used by CDF to measure $\sigma_{t\bar{t}}$ [22], in which the effects of initial and final state radiation are added in quadrature.

4.2.4 Non- $t\bar{t}$ Backgrounds in the Lepton+Jets Sample

To determine backgrounds for the lepton+jets channel, the composition of the W^\pm +jets sample is determined in terms of the production mechanism for the lepton. Contributions are expected from W^\pm +jets events, Z^0 +jets events, W^+W^- and $W^\pm Z^0$ events, events with only a single top quark, and QCD events (including $b\bar{b}$ events and multijet events where a hadron fakes the signature of a lepton) [128]. These background sources, and estimates for the backgrounds as a function of jet multiplicity, are given in Table 4.6. Below, I briefly describe how these backgrounds are determined. The strategy is first to determine the number of W^\pm and Z^0 events present in the sample.

Lepton+Jets Backgrounds : $109 \pm 7 \text{ pb}^{-1}$

	$W^\pm + 1 \text{ jet}$	$W^\pm + 2 \text{ jets}$	$W^\pm + 3 \text{ jets}$	$W^\pm + \geq 4 \text{ jets}$
evts before tagging	10,716	1,663	254	70
$Wb\bar{b}, Wc\bar{c}$	19.3 ± 6.7	9.7 ± 2.4	2.3 ± 0.6	0.85 ± 0.24
Wc	17.8 ± 5.1	4.8 ± 1.3	0.8 ± 0.2	0.22 ± 0.06
$Zb\bar{b}, Zc\bar{c}, Zc$	2.4 ± 1.0	1.2 ± 0.5	0.3 ± 0.1	0.12 ± 0.05
QCD (non- W)	7.7 ± 3.0	4.0 ± 1.5	1.4 ± 0.5	0.77 ± 0.33
Fake tags	20.9 ± 6.3	7.2 ± 2.1	1.7 ± 0.5	0.63 ± 0.22
single top	1.3 ± 0.4	2.8 ± 0.7	1.0 ± 0.4	0.29 ± 0.14
Uncorrected Total	71 ± 11	31 ± 4	7.7 ± 1.1	2.9 ± 0.5
Corrected Total	71 ± 11	31 ± 4	7.2 ± 1.1	2.0 ± 0.4
expected $t\bar{t}$ events	0.64 ± 0.19	4.4 ± 1.4	8.6 ± 2.3	11.4 ± 3.0
observed events	70	45	18	16

Table 4.6: The mean number of non- $t\bar{t}$ background events expected in each jet multiplicity bin of the lepton+jets channel, taken from Ref. [22]. Also given is the expected number of $t\bar{t}$ events, assuming only SM decays and $\sigma_{t\bar{t}} = 5.0 \text{ pb}$.

In most QCD multijet events, the \cancel{E}_T is usually small, arising from jet energy mismeasurement and low- P_T neutrinos. Furthermore, leptons that come from heavy quark decays rarely will be isolated. Therefore, only a small fraction of QCD events should have large \cancel{E}_T and isolated leptons, enabling them to appear in the signal region. To estimate the QCD background, it is assumed that \cancel{E}_T and lepton isolation in a QCD event are independent variables. For lepton+jets events with low- \cancel{E}_T , the ratio of isolated to non-isolated lepton events forms a rejection factor, which is then applied to the number of non-isolated leptons with high- \cancel{E}_T . This determines the number of QCD events N_{QCD} in the signal region [129, 110].

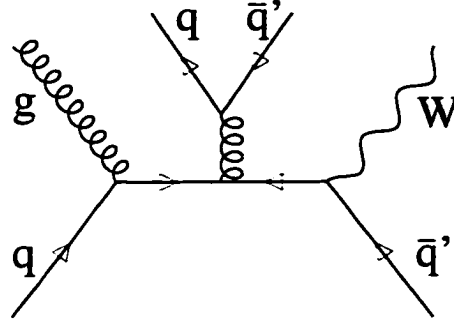


Figure 4.2: An example of a higher-order diagram for $Wb\bar{b}$ production.

Absolute predictions are made for the single top, W^+W^- , $W^\pm Z^0$, and $Z^0 \rightarrow \tau\tau$ contributions to the backgrounds, using efficiencies derived from simulated Monte Carlo samples of events. For the first three of these processes, event rates are calculated using the corresponding NLO theoretical cross sections, while the expected rate for $Z^0 \rightarrow \tau\tau$ events is given by the measured cross section times branching fraction $\sigma B(Z^0 \rightarrow e^+e^-)$ [101].

From the initial sample of W^\pm + jets events, we subtract off the mean number of QCD, single top, W^+W^- , $W^\pm Z^0$, and $Z^0 \rightarrow \tau\tau$ background events, to determine the number of W^\pm and Z^0 events in each jet-multiplicity bin. This number forms the numerator in the following equation, for the number of W^\pm + jets events in the sample,

$$N_W = \frac{N_{data} - N_{QCD} - N_{WW} - N_{WZ} - N_{Z \rightarrow \tau\tau}}{1 + \frac{N_W}{N_Z}}. \quad (4.3)$$

where we have also introduced the ratio of Z^0/W^\pm events $\frac{N_Z}{N_W}$, found to be about 1/20 for electron events, and 1/10 for muon events, independent of the jet multiplicity in the event [128].

One of the most important backgrounds after tagging is W^\pm production in association with jets containing b or c quarks, such as the $Wb\bar{b}$ topology shown

in Fig. 4.2. To calculate backgrounds containing $Wb\bar{b}$, $Wc\bar{c}$ and Wc final states, HERWIG and VECBOS Monte Carlo programs are used in conjunction with detector simulation, to predict the rate for each of these final states, relative to the total rate for W^\pm production, for each jet multiplicity [130]. These fractions are applied to the total number of observed W^\pm +jets events, to find the absolute number of expected events. Backgrounds from $Zb\bar{b}$, $Zc\bar{c}$, and Zc final states are calculated in a similar way, but also using the ratio $\frac{N_Z}{N_W}$ [128].

Fake tags can occur from reconstruction errors in light quark jets. To determine this background, we assume that for this source, the distribution of reconstructed transverse decay length L_{xy} is symmetric about zero [22]. The negative L_{xy} distribution in generic jet data is parameterized as a function of jet E_T , η , and the number of SVX tracks in a jet. This parameterization is then applied to all the jets in the W^\pm + jets data events, prior to tagging, to find the expected number of mistagged events.

4.2.5 The Background for the Charged Higgs Analysis

The backgrounds that are calculated as a fraction of the observed number of W^\pm +jets events do not take into account the fact that $t\bar{t}$ contributes to these samples. This is clearly incorrect - for example, we know that about 25% of the untagged W^\pm + ≥ 3 jet events are expected to be $t\bar{t}$ events, assuming only SM decays. To take this into account, an iterative correction, to account for the $t\bar{t}$ content of the W^\pm + jets events, is applied to those backgrounds that are calculated as a fraction of the observed number of these events [46, 22]. The background calculated before this iterative correction is called the “uncorrected” background (10.6 ± 1.6 events), while the background calculated afterwards is called the “corrected” background (9.2 ± 1.5 events).

In this analysis, I use the uncorrected background described above. This is done because the corrected background is performed under the assumption that $t \rightarrow W^\pm b$ 100% of the time, and I am removing this assumption. Furthermore, the portion of the uncorrected background due to single top production (1.29 events) is scaled by $[1.0 - \mathcal{B}(t \rightarrow H^\pm b \rightarrow csb)]$. This is done because single top is not expected to contribute to the lepton+jets channel if it decays to an all-hadronic final state. Thus, for parameter space in which $\mathcal{B}(t \rightarrow H^\pm b \rightarrow csb) = 0$, the background used is the uncorrected background of 10.6 ± 1.6 events.

In Table 4.6, the observed numbers of events in the $W^\pm + 3 \text{ jet}$ and $W^\pm + \geq 4 \text{ jet}$ bins are far above the non- $t\bar{t}$ background estimates. However, the sum of the non- $t\bar{t}$ background estimate, and the expected signal contribution from $t\bar{t}$ (assuming $\sigma_{t\bar{t}} = 5.0 \text{ pb}$), is close to the observed number of events in each of these bins. The observed number of events is a little higher than the mean number of expected (background + signal) events, resulting in the measurement $\sigma_{t\bar{t}} = 6.2^{+2.1}_{-1.7} \text{ pb}$ [22] in the lepton+jets channel. This is slightly above, but still consistent with, the theoretical value of 5 pb.

4.3 The Dilepton Channel

Dilepton events are expected to contain two W^\pm decays to $e\nu$ or $\mu\nu$, and two b -quarks. We require two high- E_T , oppositely-charged electrons or muons to be found in the central region of the detector. At least one of these leptons must satisfy the “tight” selection criteria given in Tables 4.1 and 4.2. The other lepton in the event is allowed to pass these “tight” cuts, *or* satisfy the more relaxed criteria for a “loose” electron or a CMI muon candidate. At least one lepton must simultaneously satisfy “tight” cuts and be well isolated, both from nearby calorimeter activity ($I_{\text{cal}} < 0.1$) and other tracks ($I_{\text{trk}} < 0.1$). Events from $Z^0 \rightarrow$

$\ell^+\ell^-$ decays are rejected by requiring the invariant mass for e^+e^- and $\mu^+\mu^-$ events to lie outside the Z^0 mass range $75 \text{ GeV}/c^2 < M_{\ell\ell} < 105 \text{ GeV}/c^2$. Also required are two jets with $E_T > 10 \text{ GeV}$ in the range $|\eta| < 2.0$, presumably from the two b -quarks in the event. Finally, the signature of the two neutrinos is missing transverse energy \cancel{E}_T .

The requirements for the \cancel{E}_T are essential for reducing the background from non- $t\bar{t}$ processes in the dilepton channel. Before requirements are made on the \cancel{E}_T , non- $t\bar{t}$ backgrounds are expected from Drell-Yan events, $Z^0 \rightarrow \tau\tau$ events, $b\bar{b}$ events, and events with one real lepton from a W^\pm decay and one misidentified lepton. “Drell-Yan” refers to the process $q\bar{q} \rightarrow \gamma/Z^0 \rightarrow \ell^+\ell^-$. This process contributes events to the dilepton channel if jets are produced in association with the lepton pair, and the invariant mass of the lepton pair is mismeasured or appears in the continuum outside of the Z^0 peak. Drell-Yan events and $b\bar{b}$ events do not produce high- P_T neutrinos, but \cancel{E}_T can arise from jet energy mismeasurement. To reduce these backgrounds, and the background from $Z^0 \rightarrow \tau\tau$, we require $\cancel{E}_T > 25 \text{ GeV}$.

In addition, we also place a cut on the \cancel{E}_T direction. Nonuniformities in the calorimeter response cause large non-Gaussian fluctuations in the corrected jet energies. It is found that most Drell-Yan events with large \cancel{E}_T near or above the 25 GeV threshold contain a jet with corrected energy that has fluctuated below (rather than above) the true parton energy [46]. To eliminate such events, where the \cancel{E}_T is nearly aligned with the jet direction, we require $\cancel{E}_T > 50 \text{ GeV}$ for those events in which 20° or less in azimuth exists between the \cancel{E}_T and the closest jet. A similar cut rejects events if the \cancel{E}_T points along the direction of one of the leptons, $\Delta\phi(\cancel{E}_T, \ell) < 20^\circ$. This cut reduces background from events in which mismeasurement occurs for a muon’s momentum or an electron’s energy. The azimuthal angle between the \cancel{E}_T and the closest lepton or jet is shown as a function of the \cancel{E}_T in Fig. 4.3, for $Z^0 + \text{jets}$ data events. The same plot is shown in

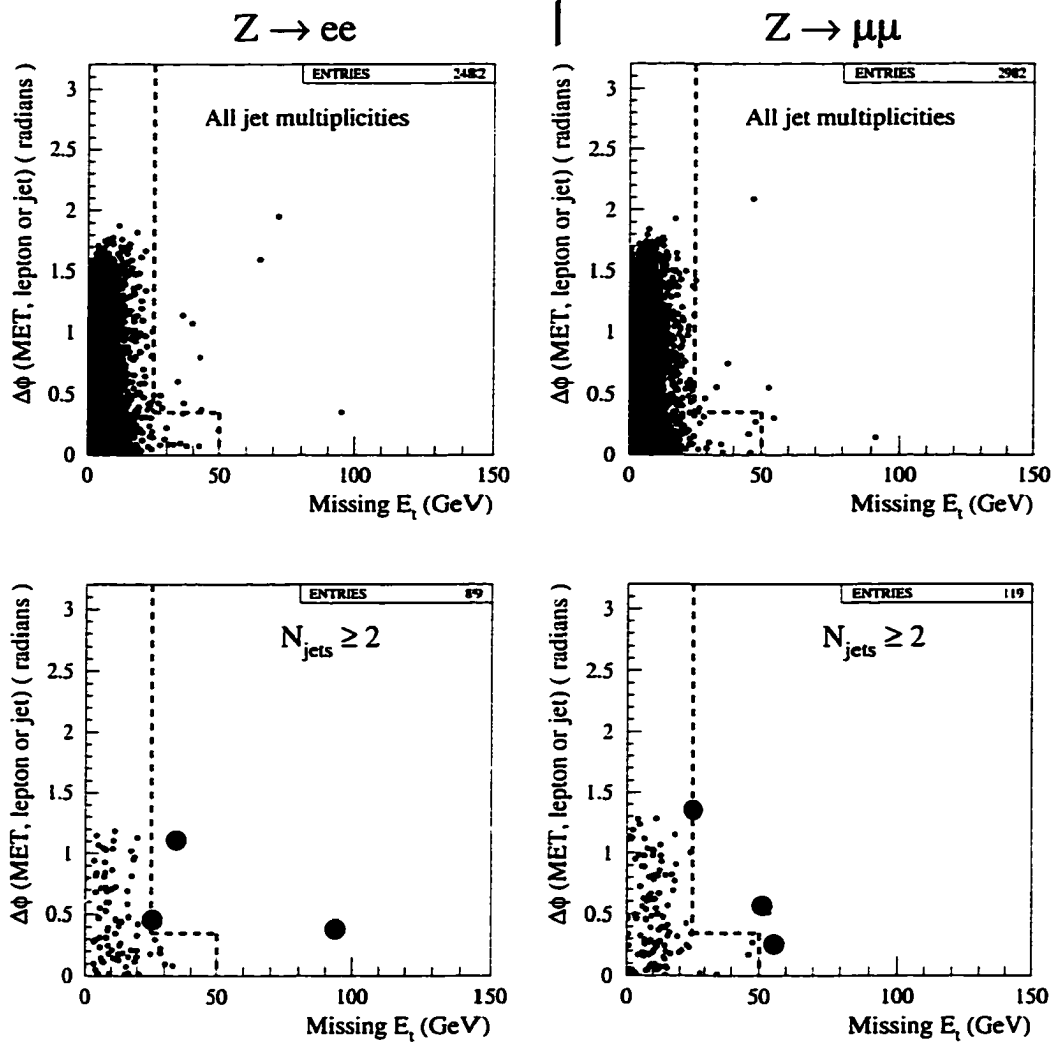


Figure 4.3: The azimuthal angle between the \cancel{E}_T and the closest lepton or jet, versus the \cancel{E}_T , for $Z^0 \rightarrow e^+e^-$ (left) and $Z^0 \rightarrow \mu^+\mu^-$ (right) data events. The events in the top plots have no jet requirements, and are dominated by $Z^0 + 0$ jets events. The events in the bottom plots must have at least two jets. This figure is taken from Ref. [111]. The $t\bar{t}$ signal is found to be spread out over a large portion of these plots - see Fig. 4.4.

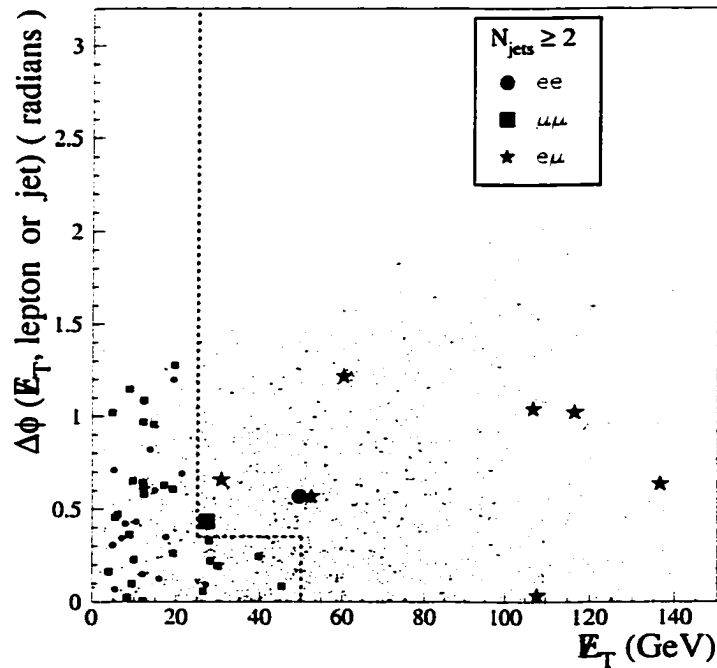


Figure 4.4: The azimuthal angle between the \vec{E}_T and the closest lepton or jet, versus the \vec{E}_T , for data events passing all the dilepton selection cuts except for the \vec{E}_T cuts. The 9 candidate dilepton events are marked. The small dots are $t\bar{t}$ Monte Carlo events. This figure is taken from Ref. [23].

Fig. 4.4 for data events that pass all the selection criteria of the dilepton channel, except for the \vec{E}_T cuts. Also shown is the expected \vec{E}_T distribution for SM $t\bar{t}$ events.

Since the \vec{E}_T is used for a sensitive topological cut, it is calculated taking into account high- P_T muons and jet energy corrections. These jet energy corrections include an *absolute* energy correction to compensate for the absolute energy response of the calorimeter, and also a *relative* energy correction to correct for non-uniformity in calorimeter response as a function of η . These corrections are discussed in Section 3.4.4.

SM Efficiency for Dilepton Selection Cuts

selection cut	efficiency
two e or μ	$(1.21 \pm 0.02)\%$
\cancel{E}_T cuts	$(75.5 \pm 1.5)\%$
2-jet cut	$(84.4 \pm 1.4)\%$
trigger	$(99 \pm 1)\%$
Total:	$(0.74 \pm 0.08)\%$

Table 4.7: The SM efficiencies for $t\bar{t}$ decays to satisfy the dilepton selection cuts. The error on each of the quantities is due to MC statistics, except for the total, which has an 11% uncertainty due to all the systematic effects listed in Table 4.5. These efficiencies come from Refs. [111, 131].

4.3.1 Dilepton Selection Efficiency for $t\bar{t} \rightarrow WbW\bar{b}$

Table 4.7 contains the efficiencies for dilepton selection cuts. The efficiency for finding two opposite-sign electrons or muons is only about 1.2%. This number includes the $t\bar{t}$ branching fraction of about 5% to the final state $(\ell\nu_\ell b)(\ell\nu_\ell \bar{b})$. Assuming only SM decays, it is this $t\bar{t}$ topology that contributes most of the $t\bar{t}$ events (84%) to the dilepton sample [111]. However, not all these events end up in the dilepton sample. Only 85% of the leptons from W^\pm decays have $P_T > 20$ GeV/ c , and about 75% are found in the central region of the detector [111]. Further reduction in the efficiency is caused by fiducial cuts, photon conversion or cosmic ray removal cuts, Z^0 removal cuts, the *two* lepton identification cuts, and lepton isolation cuts. Each of these successive cuts has an efficiency ranging between 80-95% for SM $t\bar{t}$ events (see Table 4.7) [111]. The total SM $t\bar{t}$ efficiency is found to be $(0.74 \pm 0.08)\%$ [131]. The error on this efficiency is due to all the effects

listed in Table 4.5. The dominant systematic error is associated with lepton identification efficiencies (7%), which are not modeled well in Monte Carlo events (see Section 4.2.3).

The total SM $t\bar{t}$ efficiency in the dilepton channel (0.74%) is the average efficiency calculated using ISAJET, PYTHIA and HERWIG generators, along with a simulation of the CDF detector [111]. It is the number used in the top cross section PRL [22]. However, in this analysis I only use the PYTHIA generator, which gives an efficiency of 0.71% [131, 132]. To account for the fact that PYTHIA seems to be underestimating $t\bar{t}$ efficiency in the dilepton channel relative to the average of all the MC generators, I inflate all PYTHIA-returned dilepton channel efficiencies by a factor of $(0.74/0.71) = 1.04$ when the limits for this analysis are computed.

4.3.2 Non- $t\bar{t}$ Backgrounds in the Dilepton Sample

There are a variety of SM processes that resemble $t\bar{t}$ decays to two leptons, \cancel{E}_T , and two jets. These backgrounds are listed in Table 4.8, and include Drell-Yan production, $Z^0 \rightarrow \tau\tau$ decays, $W^\pm + \text{jets}$ events where one of the jets fakes a lepton, diboson production, and a variety of other sources.

As I stated before, most of the Drell-Yan events are eliminated by the \cancel{E}_T and the invariant mass cuts. The remaining Drell-Yan background is calculated from the observed number of events inside the Z^0 mass window, and passing all the dilepton selection requirements except for the invariant mass cut. This number is scaled by the expected ratio of Drell-Yan events in the continuum to those inside the Z^0 mass window [111], calculated from a Monte Carlo sample of events. This background gets a minute correction of 0.1 events, due to the contribution of $t\bar{t}$ to the Z^0 mass window, which has to be subtracted in order to get the expected background from Drell-Yan processes alone [111].

Dilepton Backgrounds : $109 \pm 7 \text{ pb}^{-1}$

background source	Expected events
Drell-Yan	0.70 ± 0.20
$Z^0 \rightarrow \tau\tau$	0.59 ± 0.14
W^\pm +jets, fake lepton	0.37 ± 0.23
WW	0.36 ± 0.11
$\mu\mu$ evt, mismeasured μ track	0.3 ± 0.3
$b\bar{b}$	0.05 ± 0.03
radiative Z , $Wb\bar{b}$, WZ , ZZ	0.1 ± 0.1
Uncorrected Total	2.5 ± 0.5 events
Corrected Total	2.4 ± 0.5 events
expected $t\bar{t}$ events	(4.0 ± 0.4) events
observed events	9 events

Table 4.8: The mean number of non- $t\bar{t}$ background events expected in the dilepton channel, taken from Ref. [23]. Also given is the expected number of $t\bar{t}$ events assuming only SM decays, and $\sigma_{t\bar{t}} = 5.0 \text{ pb}$. The observed number of dilepton events is consistent with the sum of background events and expected signal events.

The background from $Z^0 \rightarrow \tau\tau$ is estimated by using the event rate given by the CDF-measured cross section times branching fraction, $\sigma B(Z^0 \rightarrow e^+e^-) = 0.231 \pm 0.012 \text{ nb}$ [101], and also by calculating the efficiency for these events to pass the dilepton selection criteria, determined from a sample of Monte Carlo events. Similarly, the diboson background from W^+W^- , $W^\pm Z^0$, and Z^+Z^- events is calculated from Monte Carlo events [111], using event rates given by the NLO cross sections for these processes (typically several pb).

Dilepton events are expected from $W^\pm + \geq 3 \text{ jet}$ events, where the W^\pm decays

leptonically, and a hadron from one of the jets fakes the signature of an electron or a muon. This can occur if a charged hadron doesn't shower in the calorimeters, and "punches through" to the muon chambers, faking a muon segment. Also, jets containing a large fraction of photons or π_0 's can create mostly-electromagnetic clusters. The background for these fakes is calculated by determining the probability of a jet to fake a lepton signature, and then applying this probability to all of the "fakeable" jets in the $W^\pm + \geq 3$ jet sample [133].

Finally, it appears that a small fraction of $\mu\mu$ events, presumably from Z^0 decays, will contain a muon track that is poorly reconstructed. Misconstraining the track to the beam position results in a mismeasurement of the \cancel{E}_T in the event [134]. The background for these events is small, but non-negligible.

In Table 4.8, the observed number of events is far above the non- $t\bar{t}$ background estimate. However, the sum of the non- $t\bar{t}$ background, and the expected signal contribution from $t\bar{t}$ (assuming $\sigma_{t\bar{t}} = 5.0$ pb), is close to the observed number of events. The observed number of events is slightly higher than the mean number of expected (background + signal) events, resulting in a measurement $\sigma_{t\bar{t}} = 8.2^{+4.4}_{-3.4}$ pb [23] in the dilepton channel. This is slightly above, but still consistent with, the theoretical value of 5 pb.

Chapter 5

Modeling $t\bar{t}$ Events with H^\pm Decays

In the last chapter, I described the efficiencies for SM $t\bar{t}$ events to pass the selection criteria of the dilepton and lepton+jets channels. These efficiencies are derived from modeling the physics of $t\bar{t}$ production and decay with Monte Carlo event generators, and then passing these events through a simulation of the CDF detector. I also discussed some of the limitations in the modeling of the detector response, based on the behavior of other high- P_T processes observed in the data. For example, from the measured detector response to electrons and muons from Z^0 decays, we know that our detector simulation overestimates lepton identification efficiencies by 5-9% [111]. Also, the efficiency for reconstructing tracks within the core of a jet is measured in data to be about 10% lower than the efficiency in the CDF detector simulation [123]. As a result, to achieve the correct SVX B -tagging efficiency, tracking efficiency in the simulated Monte Carlo events must be degraded.

In this chapter, I describe the unique Monte Carlo modeling performed for this analysis, to simulate the physical production and decay of $t\bar{t}$ events containing charged Higgs decays. This level of simulation, where mass distributions, kinematics of events, and branching fractions are determined, is called the *generator* level. I rely on the CDF detector simulation to determine the detector response to these events once they are generated.

To model the signal from $t \rightarrow H^\pm b$ decays, I rely on versions 5.7 and 6.1 of the PYTHIA [135] Monte Carlo program. However, modifications to this program

are necessary for three reasons. First, I need to simulate the recently-recognized three-body decay mode $H^\pm \rightarrow W^\pm b\bar{b}$. Second, I need to model a large width for the H^\pm (Γ_H), which occurs at large $\tan\beta$. This results in H^\pm mass distributions that significantly deviate from the symmetric Breit-Wigner distributions often used within PYTHIA to model resonances. Finally, it is important to understand the limitations of modeling a large top quark width Γ_{top} , which occurs for low M_{H^\pm} at the boundaries of the perturbative range of $\tan\beta$. In the following sections, I describe the modeling that takes into account these effects.

5.1 $H^\pm \rightarrow c\bar{s}$

This decay mode is included in versions 5.7 and 6.1 of PYTHIA. It is prevalent at small values of $\tan\beta$, where Γ_H is less than 1 GeV. For this reason, Breit-Wigner resonances are adequate for describing the H^\pm mass distribution, and either version of PYTHIA may be used to calculate efficiencies.

5.2 $H^\pm \rightarrow W^\pm b\bar{b}$

The three-body H^\pm decay mode was recognized in 1997 by Roy, Wudka, and Ma [39]. In their paper, these authors calculate the spin-averaged matrix element-squared $|\mathcal{M}|^2$ for $H^\pm \rightarrow W^\pm b\bar{b}$, and use it to calculate the partial width for this process. In addition, they also predict the kinematics of $t\bar{t}$ events containing this three-body decay.

The partial width for the decay $H^\pm \rightarrow W^\pm b\bar{b}$ [39] has the form [136]

$$\frac{d\Gamma_{H \rightarrow Wb\bar{b}}}{dm_{12}^2 m_{23}^2} = \frac{1}{(2\pi)^3 32 M_{H^\pm}^3} |\mathcal{M}|^2 \quad (5.1)$$

where m_{12}^2 and m_{23}^2 are the square of the four-momentum transferred to the \bar{b} and

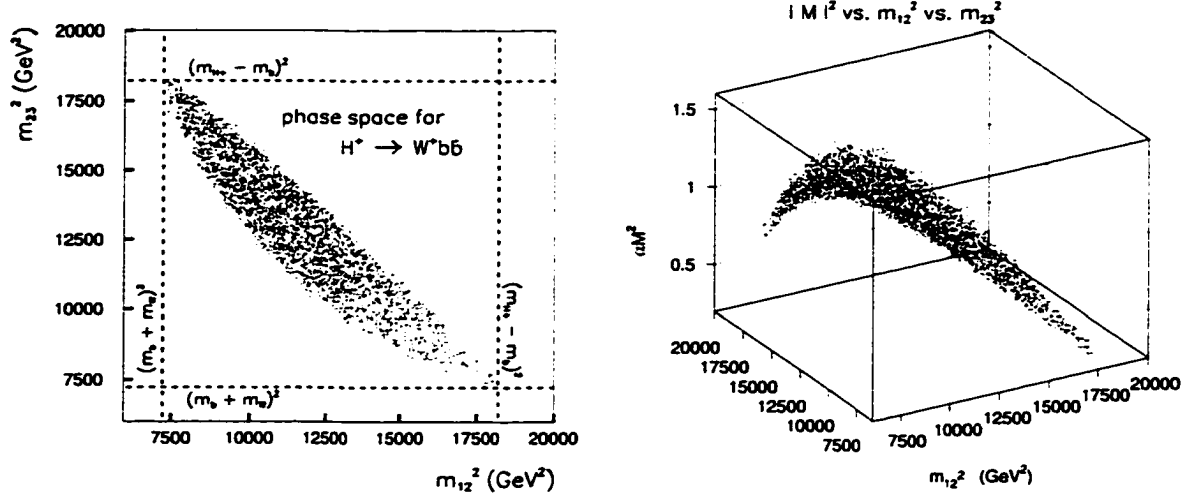


Figure 5.1: On the left is the $H^\pm \rightarrow W^\pm b \bar{b}$ phase space (Dalitz plot) in the m_{23}^2 vs. m_{12}^2 plane, for $M_{H^\pm} = 140 \text{ GeV}/c^2$. The phase space is defined with points generated in a MC simulation. The density of the points is non-uniform because the phase space is weighted by the matrix element squared $\langle |\mathcal{M}|^2 \rangle$, which is shown on the right, multiplied by a constant α .

b quarks, respectively,

$$m_{12}^2 = (p_{H^\pm} - p_b)^2 \quad (5.2)$$

$$m_{23}^2 = (p_{H^\pm} - p_{\bar{b}})^2 \quad (5.3)$$

$$m_{13}^2 = M_{H^\pm}^2 + m_b^2 + m_b^2 + m_W^2 - m_{12}^2 - m_{23}^2 \quad (5.4)$$

The $|\mathcal{M}|^2$ is a function of these variables. Fig. 5.1 shows the phase space in the m_{23}^2 vs. m_{12}^2 plane for $M_{H^\pm} = 140 \text{ GeV}/c^2$. It also shows the dependence of $|\mathcal{M}|^2$ on this phase space. The boundary is specified by the masses of the daughter particles $W^\pm b \bar{b}$.

Unfortunately, the three-body decay $H^\pm \rightarrow W^\pm b \bar{b}$ is not available in the default

$t\bar{t} \rightarrow (Hb)(W\bar{b}) \rightarrow (Wb\bar{b}b)(W\bar{b})$ Monte Carlo, $M_{H^\pm}=140 \text{ GeV}/c^2$

Monte Carlo source	number of b -quarks with $P_T > 20 \text{ GeV}/c, \eta < 2.0$				
	0	1	2	3	4
custom PYTHIA v6.1	0.21%	4.8%	27.7%	49.7%	17.6%
Roy, Wudka, Ma [39]	0.2%	4.7%	25.6%	50.6%	18.9%
$t\bar{t} \rightarrow WbW\bar{b}$ comparison	0.5%	13.3%	86.2%	-	-

Table 5.1: A comparison of the multiplicity of b -quarks that pass a set of kinematic cuts, for Monte Carlo $t\bar{t} \rightarrow WbH\bar{b}$ decays. Predictions are shown for my implementation, the one in Ref. [39], and also for SM decays.

PYTHIA v5.7 or v6.1 programs. However, PYTHIA is flexible and allows the addition of new decay modes for a particle. The decay $H^\pm \rightarrow W^\pm b\bar{b}$ has been defined in my custom version of PYTHIA by specifying its daughter particles in the decay table database file called PYDATA (ordering: W^\pm, b, \bar{b}). In addition, I have exploited the generic three-body decay routine called PYTBODY, which by default generates decays that uniformly populate the available phase space. I altered this program to weight the phase space by Roy, Wudka and Ma's matrix element $|\mathcal{M}|^2$ [39].

I have performed several cross checks of this implementation of the decay $H^\pm \rightarrow W^\pm b\bar{b}$ into PYTHIA. I find that the total width $\Gamma_{H^\pm \rightarrow Wb\bar{b}}$, calculated by integrating the matrix element $|\mathcal{M}|^2$ over the available phase space for the decay, yields the correct branching fractions predicted by Roy, Wudka and Ma [39]. This demonstrates that I am calculating the phase space, and implementing the author's value of $|\mathcal{M}|^2$ correctly. In addition, for $t\bar{t} \rightarrow WbH\bar{b}$ events where $H^\pm \rightarrow W^\pm b\bar{b}$, Roy, Wudka and Ma have calculated the multiplicity of b -quarks that would both

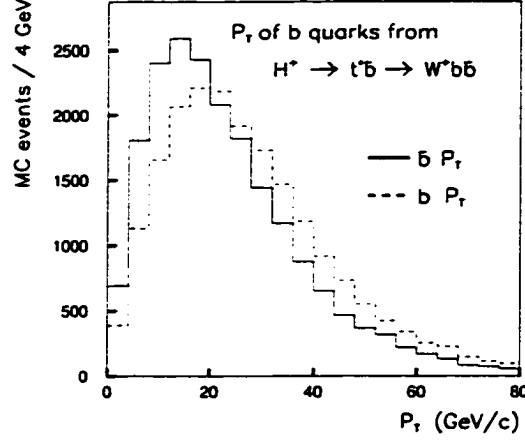


Figure 5.2: The P_T spectrum of the b - and \bar{b} -quarks from the three-body decay $H^+ \rightarrow W^+ b \bar{b}$, where $M_{H^\pm} = 140 \text{ GeV}/c^2$.

lie within the geometric acceptance of the CDF detector ($|\eta| < 2.0$), and be energetic enough ($P_T > 20 \text{ GeV}/c$), to be tagged by the SVX. Their results, along with the results from my simulation, are shown in Table 5.1, for $M_{H^\pm} = 140 \text{ GeV}/c^2$. There is good agreement between the two sets of predictions. Note that the presence of at least one $H^\pm \rightarrow W^\pm b \bar{b}$ decay in a $t\bar{t}$ event results in a significant fraction of events with three or four b -quarks satisfying the P_T and η cuts, while SM decays usually have two such b -quarks.

As an additional check, I have compared the P_T spectrum of the b - and \bar{b} -quarks from the H^+ decay with the authors' predictions. In the decay $H^+ \rightarrow t^* \bar{b} \rightarrow W^+ b \bar{b}$, the P_T spectrum of the b -quark should be harder than that of the \bar{b} , since the b comes from a virtual top quark, which “wants” to be as close to M_{top} as possible. The P_T spectrums are compared for $M_{\text{top}} = 175 \text{ GeV}/c^2$ and $M_{H^\pm} = 140 \text{ GeV}/c^2$

in Fig. 5.2. The b -quark P_T spectrum is indeed harder. For the means of these distributions, I find $\langle P_T(\bar{b}) \rangle = 23.6 \text{ GeV}/c$ and $\langle P_T(b) \rangle = 28.2 \text{ GeV}/c$, while D.P. Roy finds [137] $\langle P_T(\bar{b}) \rangle = 24 \text{ GeV}/c$ and $\langle P_T(b) \rangle = 30 \text{ GeV}/c$.

Finally, I have verified that the P_T spectrum of leptons from W^\pm 's, where the W^\pm is produced in the decay $H^\pm \rightarrow W^\pm b\bar{b}$, is not significantly different from the corresponding distribution for SM top decays, in agreement with the predictions of Refs. [39, 138].

It should be noted that the the matrix element squared $|\mathcal{M}|^2$ is not a strong function of the phase space variables, as shown in Fig. 5.1. When I substitute my “custom” three-body decay routine for the default PYTHIA routine, in which all points in the available phase space are weighted equally, then the kinematics of the events (b -quark energies and lepton P_T spectrum) do not change much.

It is worth mentioning that the radiation of gluons from the b -quarks is probably not modeled properly in my implementation of the decay $H^\pm \rightarrow W^\pm b\bar{b}$. A parton typically radiates gluons, which often carry a significant fraction of the parton's momentum. PYTHIA models this radiation “showering” in such a way that it assigns an effective mass for the parton only after the shower has occurred. As a result, energy and momentum balancing must be performed to conserve these quantities. For example, in the top quark decay $t \rightarrow W^\pm b$, the b -quark showers in the center-of-mass of the top quark, and *then* it is assigned an effective mass. The momentum of the W^\pm , opposite to the b -quark momentum, must subsequently be adjusted, since otherwise it is not possible to conserve both energy and momentum for the $W^\pm b$ system.

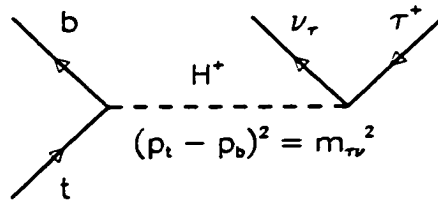
For the three body decay $H^\pm \rightarrow W^\pm b\bar{b}$, this momentum balancing only takes place between two of the particles. In my implementation of PYTHIA, the showering routine (PYSHOW) transforms to the center of mass of the $b\bar{b}$ system, performs the gluon showering for both quarks, assigns masses to them, performs momentum

balancing, and then transforms back to the lab system. One would like to perform this balancing in the center-of-mass of the H^\pm system, in such a way that the W^\pm would absorb some of the necessary momentum shifting. Unfortunately, with three final products, there is no unique recipe for sharing momentum shifts when a parton is assigned an effective mass by the shower [139].

Perhaps a better solution for modeling the radiation in the $H^\pm \rightarrow W^\pm b\bar{b}$ decay would be to treat it as a two-step process. The showering for the decay $H^\pm \rightarrow tb$ could take place, followed by the shower of the b -quark in the decay $t \rightarrow W^\pm b$. However, since the top quark is so short-lived, this separation of the radiation is probably not safe, which means that currently, there may be no simple and fully-accurate solutions to this problem [139].

5.3 $H^\pm \rightarrow \tau^\pm \nu$: Modeling Large Γ_H

At small and intermediate values of $\tan\beta$, the partial width for $H^\pm \rightarrow \tau\nu$ is less than 1 GeV, and the H^\pm resonance has a Breit-Wigner shape. However, at large values of $\tan\beta$, Γ_H can be as large as 10 GeV, since it is proportional to $M_{H^\pm}\tan^2\beta$ (see Section 2.5.3). Under these circumstances, it is invalid to describe top quark decays to a charged Higgs boson as a two-step process that involves the sequential chain decays $t \rightarrow H^\pm b$ and $H^\pm \rightarrow \tau\nu$. Rather, one must take into account the spread-out H^\pm mass distribution by calculating the three-body decay rate $\Gamma_{t \rightarrow \tau\nu b} = \Gamma(t \rightarrow H^\pm b \rightarrow \tau\nu b)$, where the H^\pm is treated as a propagator.



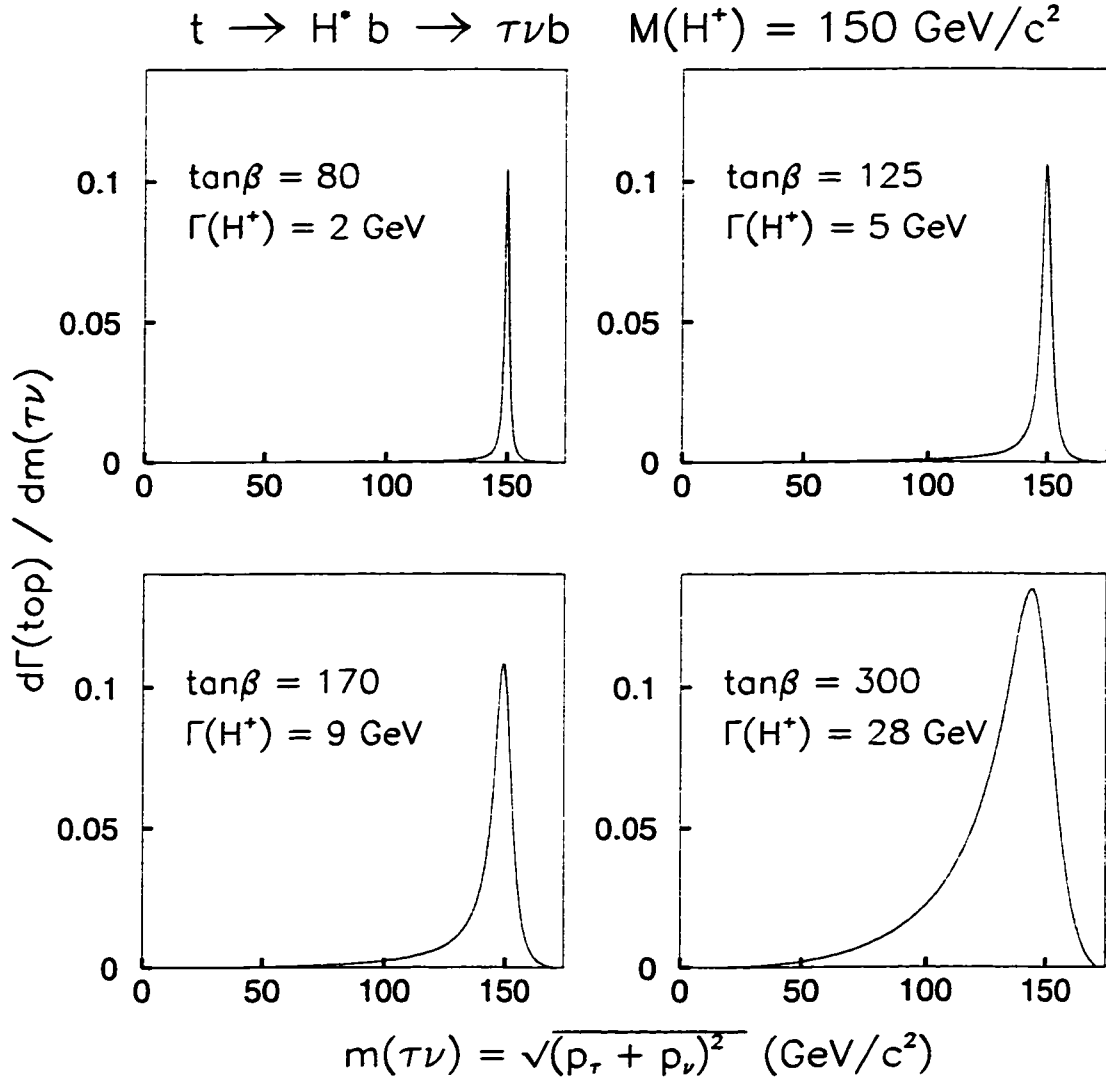


Figure 5.3: The expected distribution of $m_{\tau\nu}$ (effective H^\pm mass) from the decay $t \rightarrow \tau\nu b$, for $M_{H^\pm} = 150 \text{ GeV}/c^2$ and various values of $\tan\beta$. As Γ_H increases with $\tan\beta$, the mass distribution becomes skewed towards lower masses, where more phase space exists for the top quark decay products.

In this decay, the invariant mass between the tau and the neutrino pair $m_{\tau\nu}$ is the effective M_{H^\pm} of the event. I have calculated the decay rate for this diagram in Appendix D. The expected distribution of $m_{\tau\nu}$ is found from the differential rate $d\Gamma_{t \rightarrow \tau\nu b} / dm_{\tau\nu}$. This is given by Eq. D.20, and shown pictorially in Fig. 5.3 for $M_{H^\pm} = 150 \text{ GeV}/c^2$ and several values of $\tan\beta$. Note that a large Γ_H results in a $m_{\tau\nu}$ distribution that is asymmetric, and has a prominent tail at low $m_{\tau\nu}$. This tail is due to phase space enhancement. The decay rate for $t \rightarrow \tau\nu b$ is the product of a coupling factor, a propagator factor, and a phase space factor. Ordinarily, for a small Γ_H , $m_{\tau\nu}$ is constrained to be close to the nominal M_{H^\pm} , since a strong suppression from the propagator factor outweighs the increase in the phase space factor due to one of the daughter particles ($m_{\tau\nu}$) becoming lighter. For a larger Γ_H , this is no longer true, and $m_{\tau\nu}$ is distributed more widely.

To generate $t\bar{t}$ events containing $t \rightarrow \tau\nu b$ decays, where Γ_H is large, I do not use the PYTHIA machinery for three-body decays. Rather, I simulate the two-body decay $t \rightarrow H^\pm b$. To generate the proper H^\pm mass distribution, $m_{\tau\nu}$ is selected from the distribution $d\Gamma_{t \rightarrow \tau\nu b} / dm_{\tau\nu}$, described above. This is performed in the PYTHIA routine PY2ENT, which generates two-body decays. One advantage of using two-body decays is that I avoid the problems of modeling gluon radiation for a three-body decay, described in the previous section for $H^\pm \rightarrow W^\pm b\bar{b}$.

5.4 Modeling a Large Top Quark Width

At the extremes of small and large values of $\tan\beta$, the top quark width can be as large as 15 GeV - see Fig. 2.4. To understand whether it is possible to simulate such large top quark widths, I quickly review the way PYTHIA models $t\bar{t}$ production.

PYTHIA first models the top resonance by selecting t and \bar{t} masses from a Breit-Wigner distribution that has a width set equal to the top quark width. These

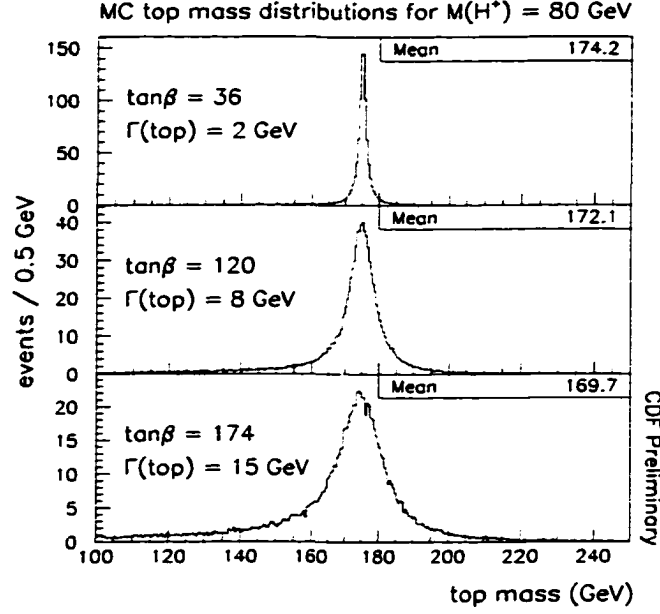


Figure 5.4: The top mass distribution for three different values of Γ_H , and $M_{H^\pm} = 80 \text{ GeV}/c^2$. This is from a simulation of $t\bar{t} \rightarrow Wb\tau\nu b$ events. The asymmetry is due to the increased probability for finding partons with smaller fractions of the proton momentum, which are able to produce top quarks with smaller masses.

masses determine the phase space for the decay, which in turn is sampled to find the kinematic variables \hat{s} and \hat{t} . These variables are used to calculate the short-range hard scattering $t\bar{t}$ cross section $\hat{\sigma}(\hat{s}, \hat{t}, M_{\text{top}})$. Next, the parton distributions in the proton and the antiproton are sampled, to determine the probability that they will provide partons with energies that will yield the selected \hat{s} and \hat{t} kinematic variables. The various probability weights from the above steps are combined to form a final weight, which decides whether or not the event survives. Through this procedure, the parton distribution functions deform the original Breit-Wigner mass distribution shape, to make it what it should be [139, 140]. Fig. 5.4 shows the predicted top mass distribution for the topology $t\bar{t} \rightarrow Wb\tau\nu b$, for $M_{H^\pm} =$

80 GeV/ c^2 and several values of Γ_{top} . As the top quark width increases, the distribution develops a long, low-mass tail. This occurs because the parton distribution functions favor the production of low-mass top quarks. A smaller M_{top} requires a lower value of the kinematic variable $\hat{s} = x_1 x_2 s$, where $s = E_{\text{cm}}^2$, the center-of-mass energy of the $p\bar{p}$ collision, and x_1 (x_2) is the fraction of momentum carried by the quark (antiquark) involved in the hard scattering. As I discussed in Chapter 2, low- x partons are much more abundant than high- x ones (see Fig. 2.6).

Thus, a large top quark width is modeled with a Breit-Wigner resonance in the hard scattering cross section, and gets distorted as the result of the parton distribution functions. The Γ_{top} is the sum of partial widths; $\Gamma_{\text{top}} = \Gamma_{t \rightarrow Wb} + \Gamma_{t \rightarrow Hb}$ at small values of $\tan\beta$, and $\Gamma_{\text{top}} = \Gamma_{t \rightarrow Wb} + \Gamma_{t \rightarrow \tau\nu b}$ at large values of $\tan\beta$, where Γ_H becomes larger than several GeV. I have written a routine that calculates $\Gamma_{t \rightarrow \tau\nu b}$ (see Appendix D). This routine is called within the PYTHIA routine PYWIDT in order to calculate the width of each top quark as a function of $\tan\beta$, M_{H^\pm} , and M_{top} , and determine its branching fraction. The dependence of this branching fraction on M_{top} is shown for $M_{H^\pm} = 140$ GeV/ c^2 and $\tan\beta = 150$ in Fig. 5.5. The plot demonstrates that even if M_{H^\pm} is larger than M_{top} , the top quark decay $t \rightarrow \tau\nu b$ can take place via the exchange of virtual H^\pm 's.

There is a technical problem that prevents the simulation of large top quark widths. The short-range cross section $\hat{\sigma}(\hat{s}, \hat{t}, M_{\text{top}})$ is calculated at a particular value of the top quark mass, but the t and \bar{t} masses in an event may be quite different if the top quark width is large. Ideally, one would like to treat both of the top quarks in an event as propagators, calculating, as an example, the matrix element for the $2 \rightarrow 4$ process $q\bar{q} \rightarrow t^*\bar{t}^* \rightarrow WbH\bar{b}$. However, this decay is not available in PYTHIA. Instead, I rely on the $2 \rightarrow 2$ process included in PYTHIA, and use the mean of the t and \bar{t} masses to calculate the cross section. This is a slight variation of the default PYTHIA v6.1 algorithm PYSIGH, which used only the

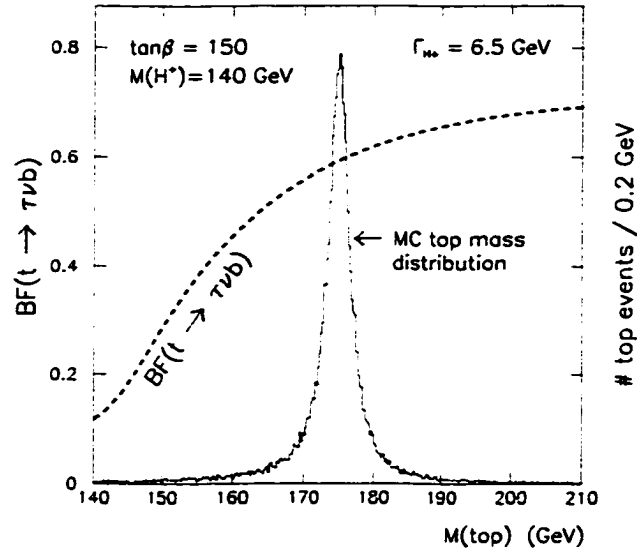


Figure 5.5: The dependence of $\mathcal{B}(t \rightarrow \tau \nu b)$ on M_{top} for $M_{H^\pm} = 140 \text{ GeV}/c^2$, and $\tan\beta = 150$. Superimposed is the top mass distribution. This demonstrates that $\mathcal{B}(t \rightarrow \tau \nu b)$ must be calculated as a function of M_{top} for each top quark that is decayed (twice per $t\bar{t}$ event). This plot also demonstrates that even if $M_{\text{top}} \leq M_{H^\pm}$, $\mathcal{B}(t \rightarrow \tau \nu b)$ can be significant due to the large Γ_H .

t mass¹. Since this treatment is an approximation that degrades with increasing top quark width, I do not attempt to model top quark widths larger than 15 GeV.

Finally, one may worry about the dependence of $\sigma_{t\bar{t}}$ on Γ_{top} , since I use the theoretical value of $\sigma_{t\bar{t}}$ to set limits, calculated assuming a top quark width of about 1.4 GeV. However, the cross section calculated and returned by PYTHIA is the same whether Γ_{top} is set to 2 GeV or 15 GeV in the simulation. An independent calculation by M. Mangano confirms that the $t\bar{t}$ cross section will not change significantly for top quark widths in this range [140].

¹This has been altered in subsequent releases of the v6.1 software, available from Ref. [141]

Chapter 6

Selection Criteria Efficiency for the Signal

In the last chapter, I discussed the Monte Carlo modeling of $t\bar{t}$ events with charged Higgs decays. In this chapter, I give the efficiencies for these events to pass the selection criteria of the dilepton and lepton+jets channels. These efficiencies are determined using the same method for SM $t\bar{t}$ decays, described in Chapter 4 - essentially by running the Monte Carlo events through a CDF detector simulation. I begin this chapter by specifying the $(M_{H^\pm}, \tan\beta)$ parameter space in which the large top quark and H^\pm widths are modeled. Next, I describe the efficiencies for all the separate $t\bar{t}$ decay topologies in the two-Higgs-doublet model, assuming narrow Γ_{top} and Γ_H . Following this, the effect of large widths is discussed. Finally, I plot the total $t\bar{t}$ efficiency in each channel as a function of $\tan\beta$ for several values of M_{H^\pm} , taking all the different $t\bar{t}$ decay modes into account.

6.1 Regions in which Large Widths are Simulated

Lets quickly review the width effects that we want to simulate, presented in the last chapter. First of all, the H^\pm width is less than 2 GeV, except for large $\tan\beta$ and M_{H^\pm} close to M_{top} ($M_{H^\pm} \gtrsim 140 \text{ GeV}/c^2$). For these near-threshold top quark decays, it is correct to model the wide asymmetric M_{H^\pm} distribution, derived from $d\Gamma_{t \rightarrow \tau \nu b}/dm_{\tau \nu}$, and presented in the last chapter (see Fig. 5.3). For the rest of the parameter space, where Γ_H is small, we rely on the standard PYTHIA simulation, which uses Breit-Wigner resonances to model the H^\pm widths.

Also, we wish to model large top quark widths. Remember that on the boundaries of the perturbative region of $\tan\beta$, the top quark width is no more than several GeV for $M_{H^\pm} \gtrsim 120 \text{ GeV}/c^2$, but can be as large as 15 GeV for $M_{H^\pm} \approx 80 \text{ GeV}/c^2$ (see Fig. 2.4). Fortunately, the LEP limits exclude $M_{H^\pm} \gtrsim 60 \text{ GeV}/c^2$, where Γ_{top} is even larger than 15 GeV. In this chapter, I will show that a top quark width of several GeV does not change $t\bar{t}$ efficiencies significantly, when M_{H^\pm} is far away from M_{top} . In addition, in the two chapters following this one, it will be shown that the top quark width only becomes larger than about 7 GeV deep into our excluded regions of parameter space, and not on the boundaries of the regions, where the limits are determined. Deep into the excluded regions, the limits are very strong anyway, due to a large $\mathcal{B}(t \rightarrow H^\pm b)$, and are not sensitive to small variations in the efficiency. For the reasons stated here, I do not bother to simulate a large top quark width for sufficiently small M_{H^\pm} .

Threshold effects become important as M_{H^\pm} gets close to M_{top} if the top width is equal to a few GeV. For this reason, this analysis does properly simulate the top quark width for the region where $\tan\beta$ is large, and $M_{H^\pm} \geq 140 \text{ GeV}/c^2$. Under these circumstances $\Gamma_{\text{top}} = \Gamma_{t \rightarrow \tau \nu b} + \Gamma_{t \rightarrow W b}$. To summarize, our efficiencies are derived using the following simulation:

- For the low- $\tan\beta$ region, and the high- $\tan\beta$ region where $M_{H^\pm} < 140 \text{ GeV}/c^2$, it is assumed that $\Gamma_H \approx 2 \text{ GeV}$, and $\Gamma_{\text{top}} \approx 1.5 \text{ GeV}$. The assumption for Γ_H is approximately correct. However, while Γ_{top} can be much larger than 1.5 GeV, this has no effect on the limits that are set, as described above.
- For the high- $\tan\beta$ region where $M_{H^\pm} \geq 140 \text{ GeV}/c^2$, I simulate both the correct Γ_{top} ($= \Gamma_{t \rightarrow \tau \nu b} + \Gamma_{t \rightarrow H b}$) and the large Γ_H , as described in the previous chapter.
- Low- $\tan\beta$ modeling of the correct top quark width for M_{H^\pm} close to M_{top} is

not necessary, since low- $\tan\beta$ limits cannot be set for $M_{H^\pm} > 140 \text{ GeV}/c^2$.

6.2 $t\bar{t}$ with $H^\pm \rightarrow cs$ or $\tau\nu$ Decays

In this Section, I give efficiencies in the top dilepton and lepton+jets channels for $t\bar{t}$ with $H^\pm \rightarrow cs$ and $H^\pm \rightarrow \tau\nu$ decays. The decay $H^\pm \rightarrow W^\pm b\bar{b}$ is discussed in the next section. These efficiencies are calculated assuming that the H^\pm width and the top quark width are less than about 2 GeV. As a guideline, the results from this section can be applied to all perturbative regions of parameter space except for $\tan\beta \gtrsim 100$, and $M_{H^\pm} \gtrsim 140 \text{ GeV}/c^2$, as discussed above. Also, regions where Γ_{top} is larger than about 7 GeV need special treatment.

Efficiencies for $WbH\bar{b}$ or $HbH\bar{b}$ final states, where $H^\pm \rightarrow cs$ or $H^\pm \rightarrow \tau\nu$, are shown as a function of M_{H^\pm} in Figure 6.1. The numerical values for these efficiencies are given in Tables E.1 and E.2 of Appendix E. The most important feature of these efficiencies is that they are all significantly lower than the SM efficiency, which is also shown on the plots. The reasons for this are described in Section 1.4.1. The all-hadronic decay mode $t\bar{t} \rightarrow HbH\bar{b} \rightarrow c\bar{s}b\bar{c}s\bar{b}$ is omitted from both plots, because it contributes a number of events that is small compared to the number of background events. In the dilepton channel, efficiencies for decay modes with $H^\pm \rightarrow cs$ decays are small, and are not shown.

The efficiencies for the decay modes in Fig. 6.1 tend to first increase with increasing M_{H^\pm} . Eventually the efficiencies decrease as the M_{H^\pm} is increased further. This behavior is due to competing effects. The momentum spectrum of electrons and muons, from the decay $H^\pm \rightarrow \tau^\pm \bar{\nu} \rightarrow (e \text{ or } \mu) \bar{\nu} \nu \bar{\nu}$, will be higher for a larger Higgs mass M_{H^\pm} . The P_T spectrum for such leptons is shown in Fig. 6.2, where a comparison is made for $M_{H^\pm} = 80 \text{ GeV}/c^2$ and $140 \text{ GeV}/c^2$. A larger M_{H^\pm} will

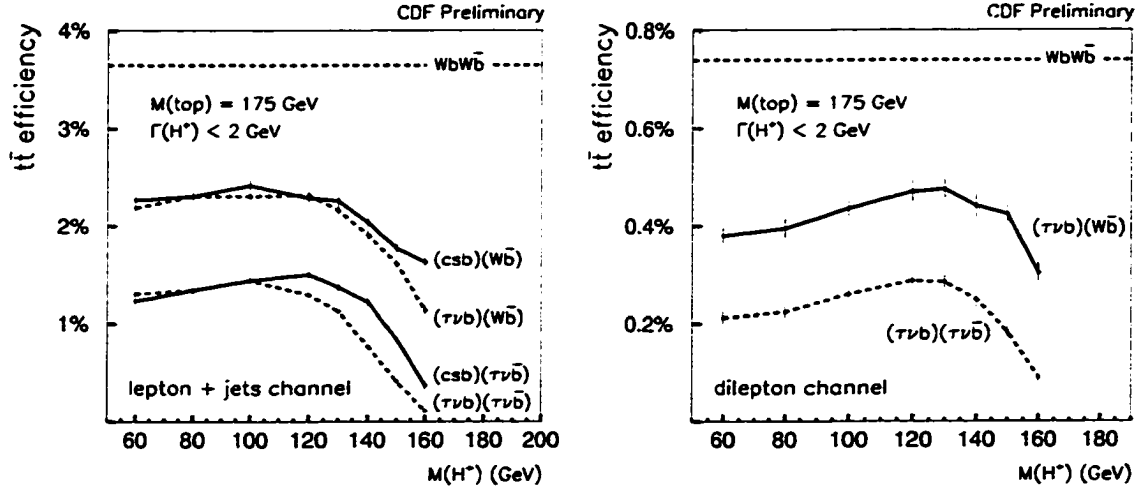


Figure 6.1: Efficiencies for $t\bar{t}$ topologies containing $H^\pm \rightarrow cs$ and $H^\pm \rightarrow \tau\nu$ decays to pass the selection criteria of the dilepton and lepton+jets channels. A narrow Γ_H is assumed. These efficiencies are significantly smaller than the SM value in each channel, which is also shown. The errors are due to MC statistics alone. The numerical values for these efficiencies are given in Tables E.1 and E.2 in Appendix E.

also produce higher- E_T jets from the decay $H^\pm \rightarrow cs$. The result from these effects is an initial increase in $t\bar{t}$ efficiency with increasing M_{H^\pm} . However, as M_{H^\pm} is increased for a fixed top mass, less energy becomes available to the b -quarks from the decay $t \rightarrow H^\pm b$, so the b -jet E_T spectrum becomes softer. In Fig. 6.3, I plot the transverse energy spectrum for jets from b -quarks in $t \rightarrow H^\pm b$ decays, for $M_{H^\pm} = 80 \text{ GeV}/c^2$ and $140 \text{ GeV}/c^2$. Note that the b -jet E_T spectrum is much softer for $M_{H^\pm} = 140 \text{ GeV}/c^2$, which results in a decreased efficiency for the formation of jets with $E_T \geq 15 \text{ GeV}$. Additional loss in efficiency comes from reduced tagging efficiency for lower- E_T jets.

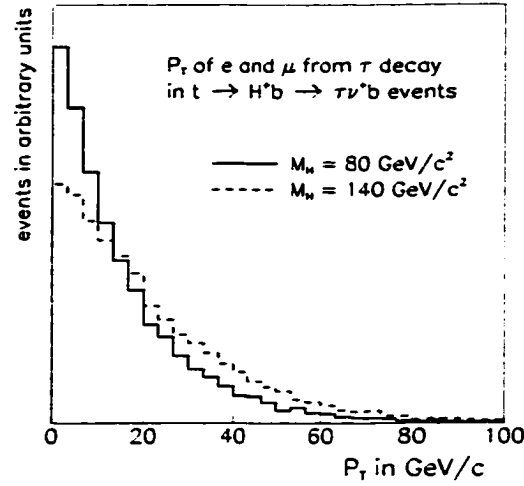


Figure 6.2: The P_T of electrons and muons from $H^+ \rightarrow \tau^+ \nu$ decay. For $M_{H^\pm} = 80 \text{ GeV}/c^2$, 28% of the electrons and muons have $P_T > 20 \text{ GeV}/c$, while for $M_{H^\pm} = 140 \text{ GeV}/c^2$, 41% of the leptons pass this requirement.

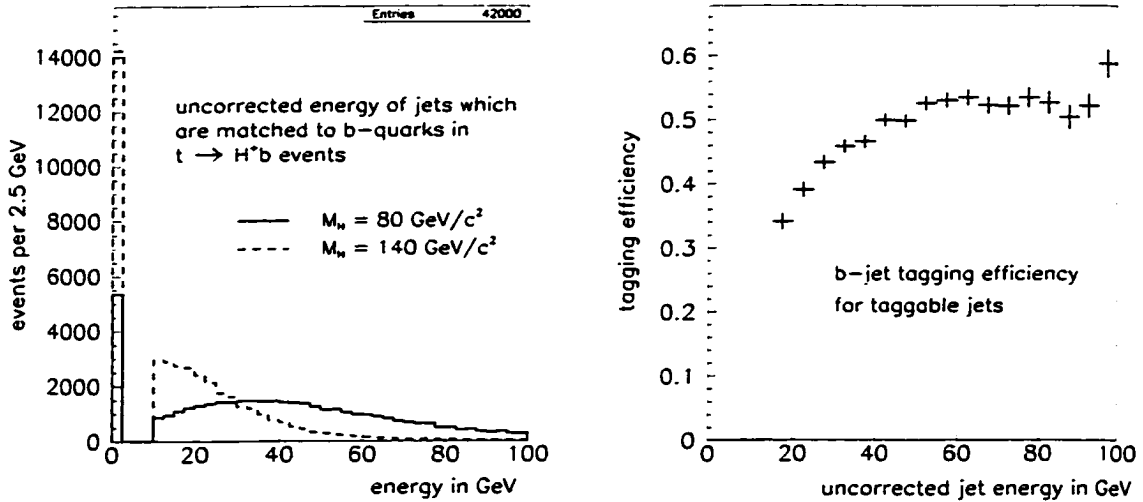


Figure 6.3: On the left is the E_T spectrum of jets arising from the hadronization of b -quarks from $t \rightarrow H^\pm b$ decay. Curves are shown for $M_{H^\pm} = 80$ and $140 \text{ GeV}/c^2$. The peak at 0 GeV is formed by b -quarks that fail to form 15 GeV jets in the calorimeter. On the right is the SVX b -tagging efficiency for jets with two SVX tracks, as a function of jet E_T .

Efficiency of Successive Selection Cuts in the Lepton+Jets Channel

$t\bar{t}$ decay	M_H	efficiency of successive SVX cuts for Run 1B					
		high- P_T e or μ	$\cancel{E}_T >$ 20 GeV	#jets ≥ 3	trig	tag	total
$W^+bH^-\bar{b}$ $H^- \rightarrow \bar{c}s$	80 GeV	$8.5 \pm .1\%$	89%	87%	92%	40%	$(2.42 \pm .06)\%$
	140 GeV	$8.7 \pm .1\%$	89%	83%	92%	36%	$(2.14 \pm .06)\%$
$W^+bH^-\bar{b}$ $H^- \rightarrow \tau\bar{\nu}$	80 GeV	$12.9 \pm .1\%$	89%	55%	93%	41%	$(2.42 \pm .04)\%$
	140 GeV	$14.2 \pm .1\%$	90%	45%	92%	38%	$(2.00 \pm .04)\%$
$H^+bH^-\bar{b}$ $(c\bar{s}b)(\tau^+\nu\bar{b})$	80 GeV	$4.9 \pm .1\%$	85%	86%	95%	41%	$(1.40 \pm .05)\%$
	140 GeV	$6.7 \pm .1\%$	87%	70%	93%	34%	$(1.28 \pm .05)\%$
$H^+bH^-\bar{b}$ $H^\pm \rightarrow \tau\nu$	80 GeV	$9.6 \pm .1\%$	87%	44%	93%	41%	$(1.40 \pm .04)\%$
	140 GeV	$13.9 \pm .1\%$	87%	20%	90%	37%	$(.81 \pm .03)\%$

Table 6.1: Efficiency of successive cuts in the lepton+jets channel, compared for $M_{H^\pm} = 80$ and $140 \text{ GeV}/c^2$, for several $t\bar{t}$ decay topologies. The total efficiencies are for Run 1B only.

To summarize, associated with a higher M_{H^\pm} is a higher acceptance for high- P_T leptons, reduced jet- E_T spectrums from b -quarks, and a decreased SVX b -tagging efficiency. To demonstrate these effects, I give the efficiency for *successive* selection criteria cuts in Tables 6.1 and 6.2, starting with the efficiency for the high- P_T lepton requirement. This is done for many of the $t\bar{t}$ topologies considered in this section, for $M_{H^\pm} = 80 \text{ GeV}/c^2$ and $140 \text{ GeV}/c^2$.

Efficiency of Successive Selection Cuts in the Dilepton Channel

$t\bar{t}$ decay	M_H	2 high- P_T e or μ	\cancel{E}_T cuts	# jets ≥ 2	trig	total
$W^+bH^-\bar{b}$	80 GeV	(.631 \pm .024)%	74%	83%	98%	(.380 \pm .021)%
$H^- \rightarrow \tau\bar{\nu}$	140 GeV	(.802 \pm .026)%	81%	68%	96%	(.424 \pm .030)%
$H^+bH^-\bar{b}$	80 GeV	(.374 \pm .020)%	69%	86%	98%	(.214 \pm .013)%
$H^\pm \rightarrow \tau\nu$	140 GeV	(.654 \pm .028)%	73%	53%	94%	(.238 \pm .014)%

Table 6.2: Efficiency of successive cuts in the dilepton channel, compared for $M_{H^\pm} = 80$ and 140 GeV/ c^2 , for several $t\bar{t}$ decay topologies. The first cut applied is the high- P_T lepton identification requirement, and all other cuts are applied in succession.

Finally, as a cross check, I calculate the efficiencies for $t\bar{t}$ topologies that are identical to the ones in this section, but have H^\pm bosons replaced by W^\pm bosons. This is done for $M_{H^\pm} = M_W = 80$ GeV/ c^2 only, and the results are shown in Appendix F.

6.2.1 Systematic Uncertainties

The efficiency for $t\bar{t}$ decays to pass the selection criteria of either channel will be afflicted by the same systematic errors that are associated with SM $t\bar{t}$ efficiencies. The systematics for lepton identification, the z-vertex cut, trigger efficiencies, and tagging efficiencies are assigned the same values as shown in Table 4.5 for SM $t\bar{t}$ decays. However, systematic errors due to the uncertainty in the jet energy scale and uncertainty in the modeling of initial and final state radiation are dependent upon M_{H^\pm} and the topology of the particular $t\bar{t}$ decay mode.

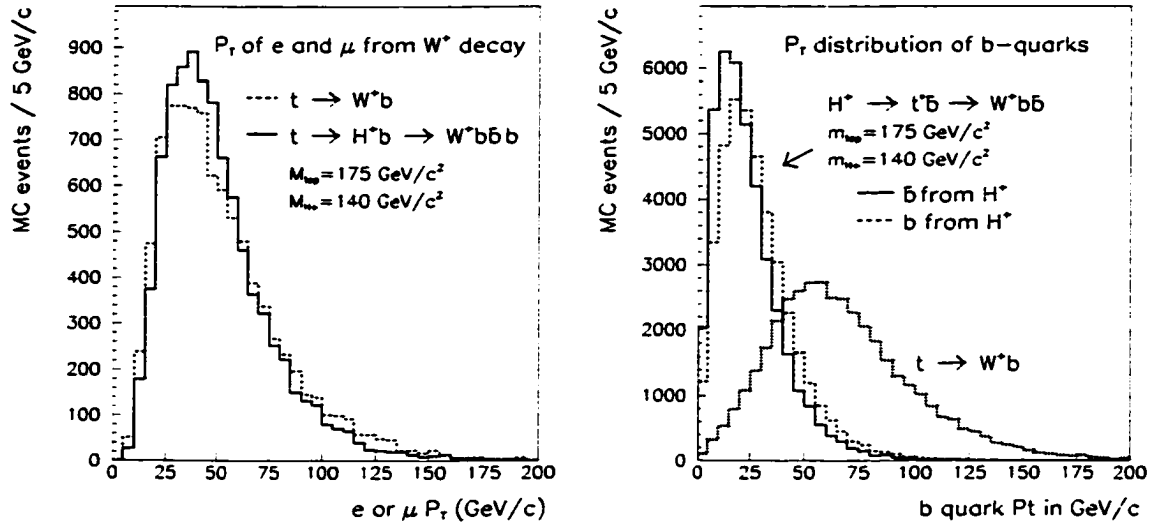


Figure 6.4: On the left is the P_T spectrum for leptons from W^\pm decay. One curve is for W^\pm 's from $t \rightarrow W^\pm b$, while the other curve is for W^\pm 's from $H^\pm \rightarrow W^\pm b \bar{b}$, where $M_{H^\pm} = 140 \text{ GeV}/c^2$. Shown on the right are P_T spectrums of b -quarks from $t \rightarrow W^\pm b$, and also from $H^\pm \rightarrow W^\pm b \bar{b}$, for $M_{H^\pm} = 140 \text{ GeV}/c^2$.

To understand this, consider the decay mode $t\bar{t} \rightarrow HbH\bar{b} \rightarrow \tau\nu b\tau\nu\bar{b}$. For this decay to contribute to the lepton+jets channel, one τ must decay to $e\nu\bar{\nu}$ or $\mu\nu\bar{\nu}$. Only two partons and a tau lepton are left to satisfy the 3-jet requirement. In contrast, most SM events are of the type $t\bar{t} \rightarrow WbW\bar{b} \rightarrow \ell\nu_\ell bqq'\bar{b}$, where four partons exist in order to satisfy the 3-jet requirement. Thus, the efficiency for the decay mode with two tau leptons will be more sensitive to initial and final-state radiation, which can give rise to extra jets in the event. This is what is observed: for SM decays, I find a 16% difference between the extremes of no initial state and no final state radiation in the lepton+jets channel, while for the $\tau\nu b\tau\nu\bar{b}$ final state, this shift ranges from 24-35%, depending on M_{H^\pm} . Shown in Table G.2 are the differences in $t\bar{t}$ efficiencies under the extremes of no initial state radiation, and no final state radiation, for all the $t\bar{t}$ decay modes discussed in this section.

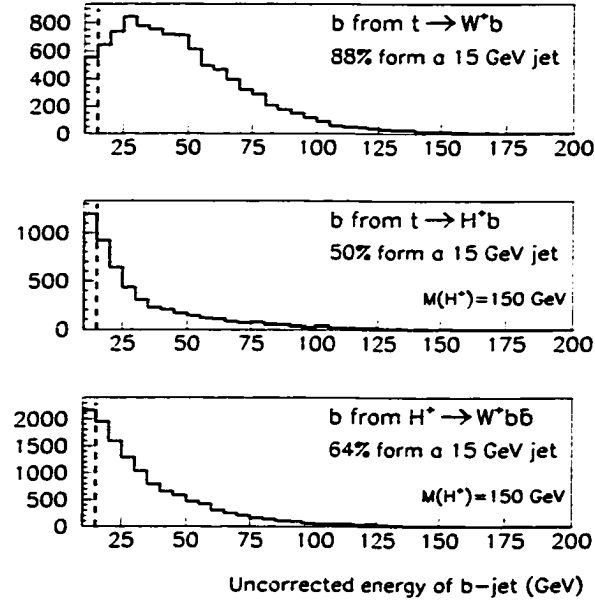


Figure 6.5: Uncorrected energy of jets with $E_T > 10$ GeV, that are matched to b -quarks, for the three different types of decays that generate b -quarks at low $\tan\beta$ and $M_{H^\pm} = 150$ GeV/ c^2 . Also given are the total efficiencies for a b -quark to produce a jet with $E_T > 15$ GeV.

Jet energy scale shifts also have a large effect on the efficiency for $t\bar{t}$ events with $H^\pm \rightarrow \tau\nu$ decays, since tau jets have a E_T spectrum that is steeply falling as it crosses the threshold of $E_T = 15$ GeV, unlike jets from partons. Shown in Table G.3 are the differences in $t\bar{t}$ efficiencies when all jet energies are systematically shifted from -10% to +10% of their nominal values. This is done for several decay modes and several charged Higgs masses.

6.3 $t\bar{t}$ with $H^\pm \rightarrow W^\pm b\bar{b}$ Decays

The $t\bar{t}$ events with one or two $H^\pm \rightarrow W^\pm b\bar{b}$ decays have the very unique final states $WbW\bar{b}\bar{b}$ and $Wb\bar{b}W\bar{b}\bar{b}$, respectively. The P_T spectrum of leptons found in these decays will be similar to those found in SM decays, since the W^\pm is non-relativistic in both cases. Fig. 6.4 compares these P_T spectrums, for $M_{H^\pm} = 140 \text{ GeV}/c^2$. Despite this similarity, on average, the b -quarks in $t\bar{t}$ events with $H^\pm \rightarrow W^\pm b\bar{b}$ decays will be less energetic than those found in SM decays. These spectrums are compared in Fig. 6.4. The E_T spectrums of jets produced by these b -quarks are shown in Fig. 6.5.

Its interesting to note that for $WbH\bar{b}$ and $HbH\bar{b}$ events, the jet multiplicity distribution for jets with $E_T > 15 \text{ GeV}$ is similar to that of SM predictions. Fig. 6.6 compares this distribution for SM $t\bar{t}$ events, and $t\bar{t}$ events that are generated assuming $M_{H^\pm} = 150 \text{ GeV}/c^2$, and $\mathcal{B}(t \rightarrow H^\pm b \rightarrow Wb\bar{b}) = 0.85$.

Fig. 6.7 shows the efficiencies for $t\bar{t}$ decay modes that contain one or two $H^\pm \rightarrow W^\pm b\bar{b}$ decays. Note that the two topologies with two W^\pm bosons and four or six b -quarks have lepton+jets channel efficiencies that exceed the SM value. This is due to increased b -tagging efficiency in these events. In the dilepton channel, although the events contain two W^\pm bosons, the multiple jets from b -quarks tend to result in fewer isolated leptons, and more events that fail the $\Delta\phi(\text{jet}, \cancel{E}_T) > 20^\circ$ requirement.

The systematic errors associated with the efficiency for $t\bar{t}$ events with $H^\pm \rightarrow W^\pm b\bar{b}$ decays are given in Appendix G. Table G.4 shows the total shifts in dilepton and lepton+jets efficiencies when all the jet energies in the events are shifted from -10% to +10% of their nominal values. Table G.5 shows shifts in the efficiencies between the extremes of no initial state radiation, and no final state radiation. These shifts are evaluated assuming $M_{H^\pm} = 130 \text{ GeV}/c^2$. Systematic errors are

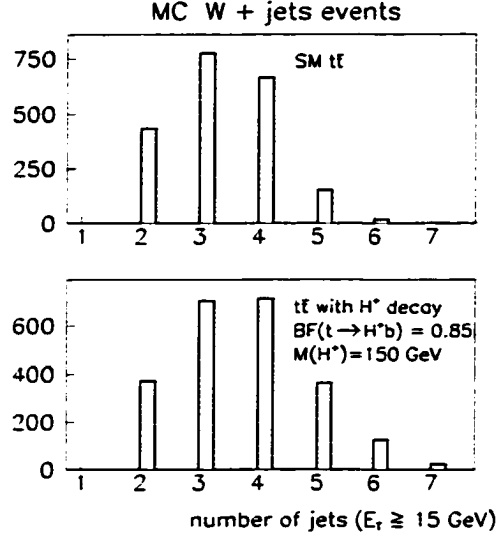


Figure 6.6: Jet multiplicity distribution for jets with $E_T > 15$ GeV. The top plots shows the distribution expected from SM $t\bar{t}$ decays. The bottom plot shows the distribution expected from the charged Higgs scenario, assuming that $M_{H^\pm} = 150$ GeV/ c^2 , and $\mathcal{B}(t \rightarrow H^\pm b \rightarrow W b b \bar{b}) = 0.85$.

assigned to be one-half of these shifts.

6.4 $t\bar{t}$ with a Large H^\pm Width

In Section 6.2, I described efficiencies for $t\bar{t}$ decay topologies that contain $H^\pm \rightarrow \tau\nu$ decays. These efficiencies are calculated for a relatively narrow H^\pm width, $\Gamma_H \lesssim 2$ GeV. In this section, I calculate the effect of a large Γ_H , in the range of 5–10 GeV. This is done using my custom version of PYTHIA described in Section 5.3. As I have already pointed out, large H^\pm widths only occur in the high- $\tan\beta$ region, for $M_{H^\pm} \gtrsim 140$ GeV/ c^2 . While reading this section, it is important to keep a mental picture of the effect of a large Γ_H , shown in Fig. 5.3 - the Higgs mass distribution becomes wide and asymmetric, and peaks at a value shifted downwards from the

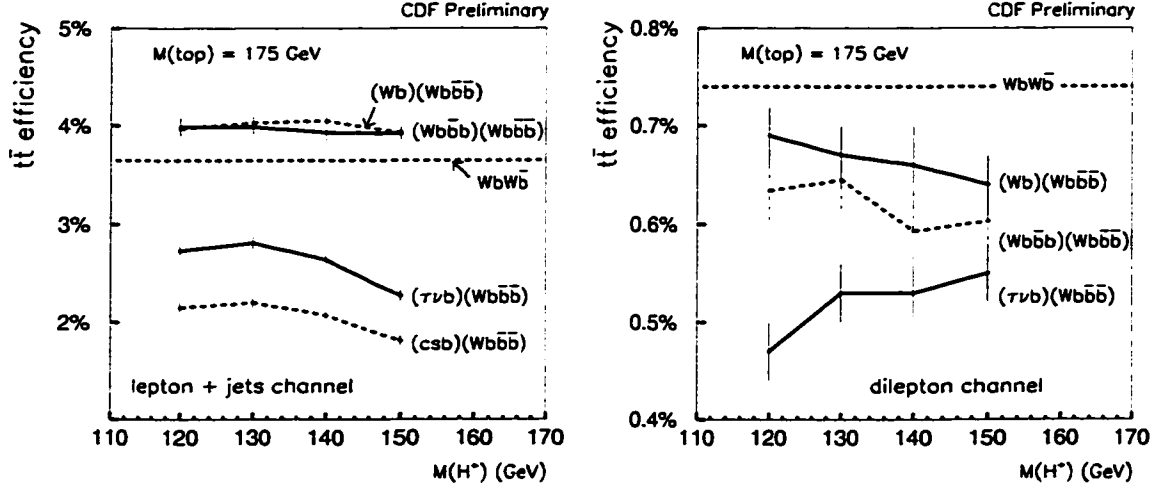


Figure 6.7: Efficiencies for $t\bar{t}$ topologies containing $H^\pm \rightarrow W^\pm b\bar{b}$ decays, to pass the selection criteria of the dilepton and lepton+jets channels. The SM value in each channel is also shown. The errors are due to MC statistics alone. The numerical values for these efficiencies are given in Tables E.3 and E.4 in Appendix E.

nominal value of M_{H^\pm} .

According to my earlier discussion, it is known that as the M_{H^\pm} distribution gets shifted toward lower masses, the $t\bar{t}$ efficiency increases (see Fig. 6.1). This is due to changes in the kinematics of the events - the P_T spectrum of leptons from tau decay becomes softer, but the b -jet E_T spectrum rapidly becomes harder. In Fig. 6.8, these distributions are shown for the $\tau\nu b\tau\nu\bar{b}$ final state, and compared for two different values of Γ_H , 2 GeV and 9 GeV. Between these two values of Γ_H , the lepton P_T spectrum changes only slightly, but the b -jet E_T spectrum changes significantly.

Fig. 6.9 shows efficiencies for the decay $t\bar{t} \rightarrow \tau\nu b\tau\nu\bar{b}$ as a function of $\tan\beta$, assuming $M_{H^\pm} = 150 \text{ GeV}/c^2$. The $t\bar{t}$ efficiency for this decay mode increases with

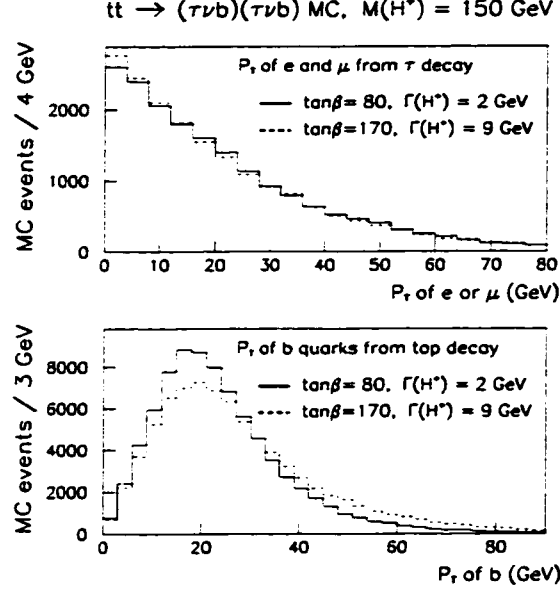


Figure 6.8: A comparison of lepton P_T (top plot) and b -jet E_T spectrums (bottom plot) for two different values of Γ_H , assuming $M_{H^\pm} = 150 \text{ GeV}/c^2$ and $t\bar{t} \rightarrow \tau\nu b\tau\nu\bar{b}$.

Γ_H . The greatest increase occurs in the lepton+jets channel, where the three-jet requirement is more marginally satisfied than the two-jet requirement of the dilepton channel, making it more sensitive to changes in the jet- E_T spectrum. (See Tables 6.1 and 6.2, and Ref. [111]). Also shown in Fig. 6.9 is the total $t\bar{t}$ efficiency in each channel, taking into account all the decay modes at high- $\tan\beta$. It is calculated in two ways: the correct way, by modeling the large Γ_H as a function of $\tan\beta$, and also the incorrect way, by assuming a narrow Γ_H ($\Gamma_H = 2 \text{ GeV}$). In the lepton+jets channel, the efficiency calculated for a narrow Γ_H underestimates the number of signal events by about 10% for $\tan\beta = 170$, near the perturbative boundary. It becomes a 30% effect at $\tan\beta = 300$.

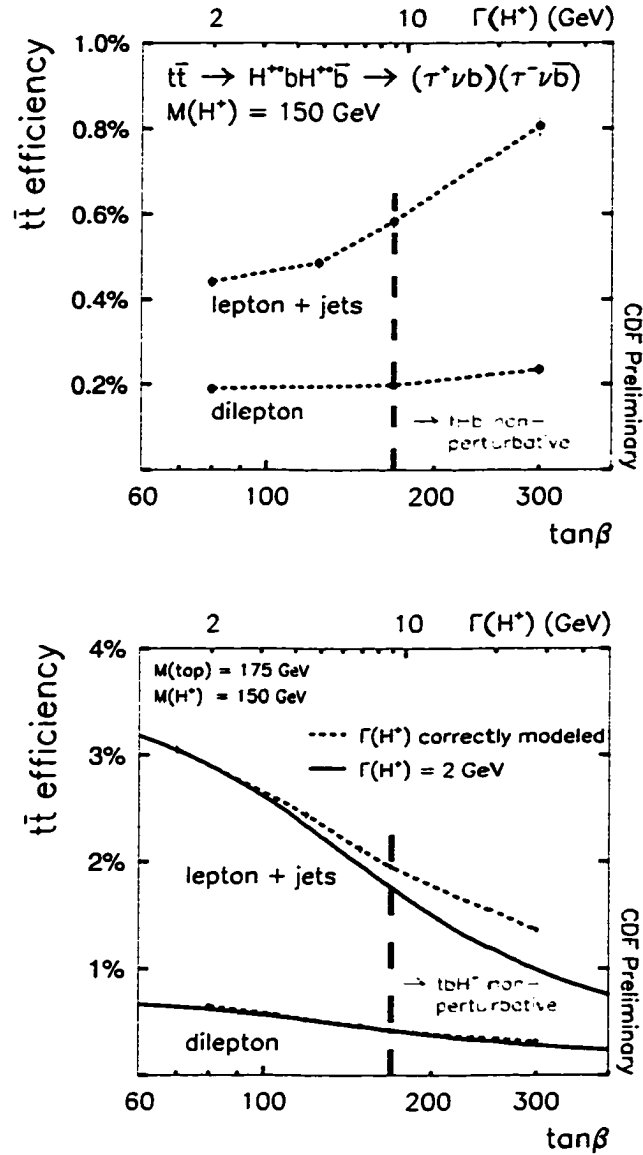


Figure 6.9: The top plot shows efficiencies for $t\bar{t} \rightarrow \tau \nu b \tau \nu \bar{b}$ with $M_{H^\pm} = 150$ GeV/ c^2 , as a function of $\tan\beta$ (lower horizontal axis) which determines Γ_H (upper horizontal axis). On the bottom plot, the total $t\bar{t}$ efficiency is shown in each channel, for all decay modes included.

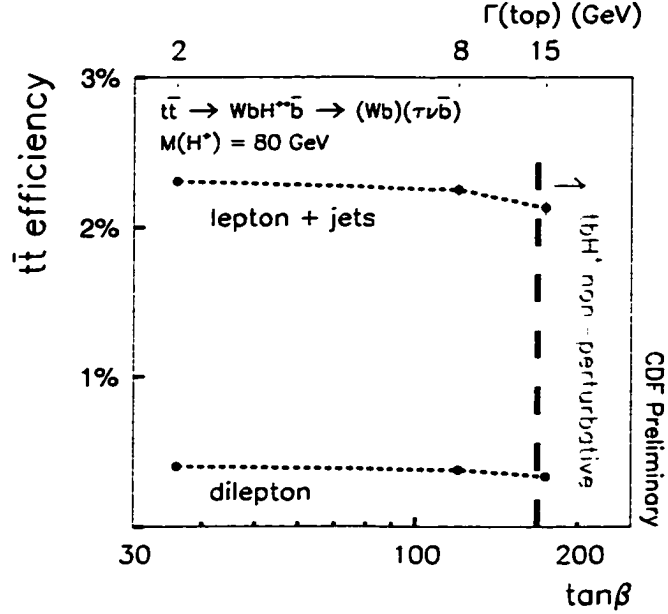


Figure 6.10: The $t\bar{t}$ efficiency for the decay mode $t\bar{t} \rightarrow (Wb)(\tau\nu b)$ and $M_{H^\pm} = 80 \text{ GeV}/c^2$, as a function of $\tan\beta$ (bottom horizontal axis) which determines Γ_{top} (upper horizontal axis). Although the efficiencies change slightly as Γ_{top} increases from 2 to 15 GeV, $\mathcal{B}(t \rightarrow \tau\nu b) > 80\%$ for $\Gamma_{\text{top}} > 5 \text{ GeV}$, and so the effect only becomes significant in regions where the limits are already strong.

6.5 $t\bar{t}$ with a Large Top Quark Width

Within the perturbative region of $\tan\beta$, Γ_{top} exceeds 5 GeV only for M_{H^\pm} at the low end of our range of sensitivity, $M_{H^\pm} \lesssim 120 \text{ GeV}/c^2$ (see Fig. 2.4). This range is far below the top mass of $175 \text{ GeV}/c^2$. Thus, we expect that the effects of a spread-out top quark mass distribution on the kinematics of a $t\bar{t}$ event should average out, as long as the top quark mass distribution remains symmetric about its mean. As an example, for SM $t\bar{t}$ decays, a change of $(+15, -15) \text{ GeV}/c^2$ in M_{top} from its measured value of $175 \text{ GeV}/c^2$ results in a change of $(+5, -7)\%$ in the

lepton+jets channel efficiency [118], and a similar level of linearity in the dilepton channel efficiency [111]. Decay topologies such as $WbH\bar{b}$ and $HbH\bar{b}$ display a similar amount of symmetry, as long as $M_{H^\pm} \lesssim 120 \text{ GeV}/c^2$.

However, a large top quark width will distort the M_{top} spectrum in such a way that it becomes asymmetric and shifted towards lower masses, so that the mean value of M_{top} decreases from its nominal value. This was discussed in Section 5.4, and the effect is shown in Fig. 5.4.

Such systematic shifts do not cause a large decrease in $t\bar{t}$ efficiency, except when Γ_{top} exceeds about 10 GeV. The $t\bar{t}$ efficiencies for the decay mode $t\bar{t} \rightarrow (Wb)(\tau\nu\bar{b})$ and $M_{H^\pm} = 80 \text{ GeV}/c^2$ are shown in Fig. 6.10 as a function of $\tan\beta$ and Γ_{top} . Although the efficiencies decrease as Γ_{top} increases from 2 to 15 GeV, $\mathcal{B}(t \rightarrow \tau\nu b)$ is already 80% for $\Gamma_{\text{top}} \approx 5 \text{ GeV}$, for which there is almost no change in efficiency. Thus, there is only a very slight change in efficiencies until we go deep into our excluded regions, where the confidence level of the limits is much higher than 95%.

Again, it is important to note that I do perform a detailed simulation of the large Γ_{top} (as well as large Γ_H) for $M_{H^\pm} \geq 130 \text{ GeV}/c^2$ and large values of $\tan\beta$. Such effects are important as M_{H^\pm} approaches M_{top} because $\mathcal{B}(t \rightarrow \tau\nu b)$ becomes a sensitive function of M_{top} , as shown in Fig. 5.5. Also, the $t\bar{t}$ efficiency is a very non-linear function of M_{top} for near-threshold $t\bar{t}$ decays.

Finally, I would like to justify my assertion that detailed simulation of the top quark and H^\pm widths is not necessary for $M_{H^\pm} \lesssim 130 \text{ GeV}/c^2$. Fig. 6.11 shows the total $t\bar{t}$ efficiency as a function of $\tan\beta$, for $M_{H^\pm} = 120 \text{ GeV}/c^2$. Within the perturbative region of $\tan\beta$, the efficiencies calculated either by properly simulating the widths, or assuming narrow widths, agree within statistical errors.

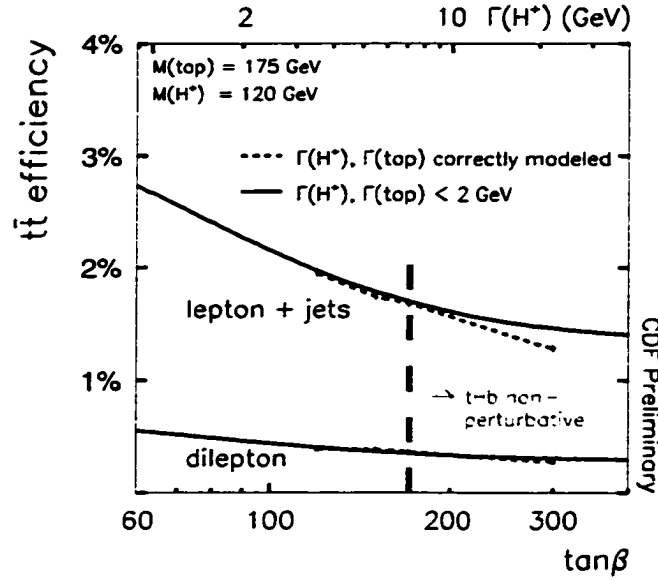


Figure 6.11: The total $t\bar{t}$ efficiency as a function of $\tan\beta$, for $M_{H^\pm} = 120 \text{ GeV}/c^2$. It is calculated by correctly modeling Γ_{top} and Γ_H , and also by assuming that these widths are narrow. For very large $\tan\beta$, Γ_{top} becomes large and drives the efficiency down.

6.6 The Total $t\bar{t}$ Efficiency - Dependence on M_{H^\pm} and $\tan\beta$

I calculate the total $t\bar{t}$ efficiency as a function of $\tan\beta$ using two different methods. The simplest method is used for the regions of $\tan\beta$ where the widths of the top quark and the H^\pm are both narrow. Under these circumstances, the efficiency for a given $t\bar{t}$ decay topology is independent of $\tan\beta$. The total $t\bar{t}$ efficiency is computed as a weighted sum of the separate efficiencies for the possible $t\bar{t}$ decay topologies. The weights in the sum are determined from the top quark and H^\pm branching fractions (given in Appendix A), which depend on $\tan\beta$.

However, at large values of $\tan\beta$ and $M_{H^\pm} \geq 140 \text{ GeV}/c^2$, the efficiency for a

given $t\bar{t}$ decay topology is $\tan\beta$ -dependent, since Γ_H and Γ_{top} are both functions of $\tan\beta$, and must be modeled properly. In this region, efficiencies are found by running Monte Carlo at discrete $(M_{H^\pm}, \tan\beta)$ points. To create a plot of efficiency as a function of $\tan\beta$ for fixed M_{H^\pm} , a smooth curve must be fit to several discrete points at the high- $\tan\beta$ region of the plot.

Fig. 6.12 shows the $t\bar{t}$ efficiency in each channel as a function of $\tan\beta$, for $M_{H^\pm} = 120 \text{ GeV}/c^2$. Also shown are the top quark and H^\pm branching fractions as a function of $\tan\beta$. The $\mathcal{B}(t \rightarrow H^\pm b)$ is significant at small- $\tan\beta$, where H^\pm decays predominantly to cs , and also at large- $\tan\beta$, where $H^\pm \rightarrow \tau\nu$. In the next chapter, I set limits based on the suppression of efficiency predicted in these regions.

The same set of plots is shown in Fig. 6.13, for $M_{H^\pm} = 150 \text{ GeV}/c^2$. At large $\tan\beta$, where $H^\pm \rightarrow \tau\nu$, there is still a suppression of efficiency in each channel. However, for low- $\tan\beta$, where $H^\pm \rightarrow W^\pm b\bar{b}$, the efficiencies are not significantly suppressed compared to SM predictions. For this reason, I am unable to set low- $\tan\beta$ limits for $M_{H^\pm} > 140 \text{ GeV}/c^2$.

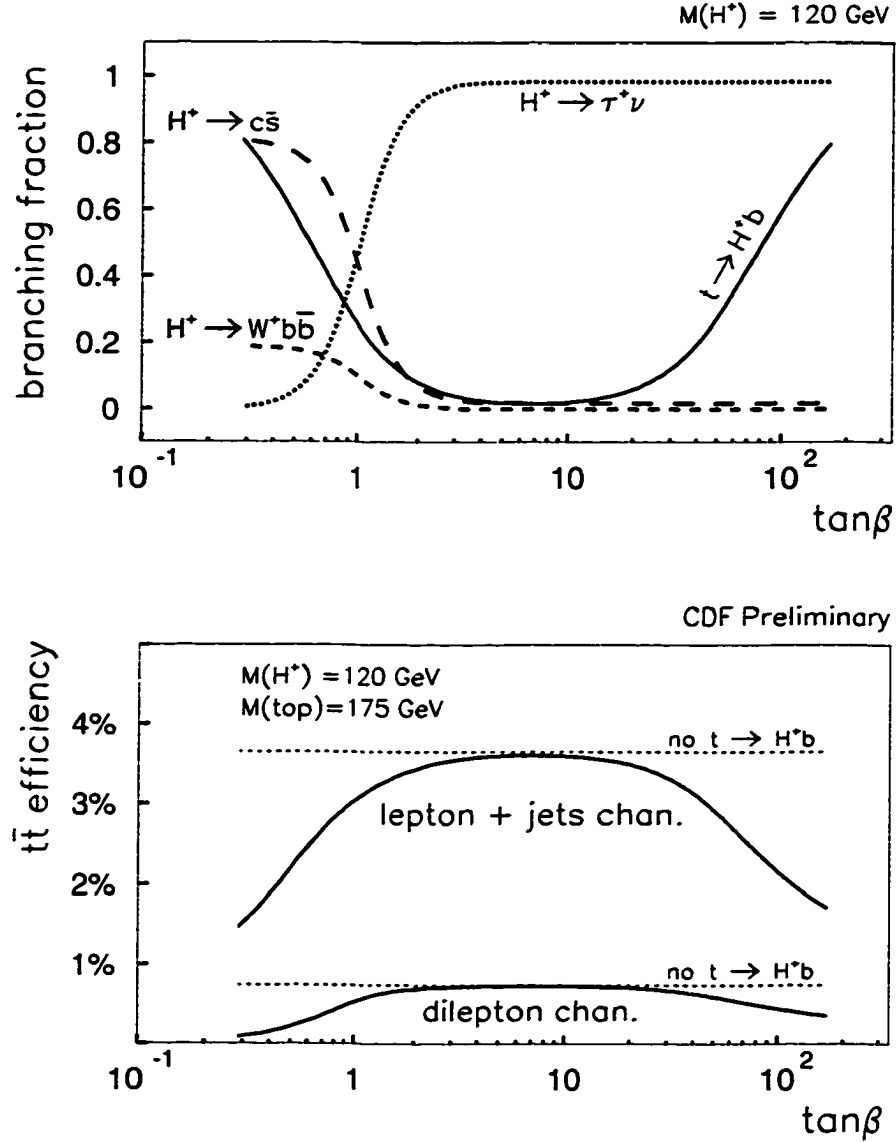


Figure 6.12: The top plot shows the branching fractions for the top quark and the charged Higgs boson as a function of $\tan\beta$, for $M_{H^\pm} = 120 \text{ GeV}/c^2$. Shown in the bottom plot is the $t\bar{t}$ efficiency in each channel. When $B(t \rightarrow H^\pm b) = 0$, the efficiency in each channel is its SM value (marked “no $t \rightarrow H^\pm b$ ”).

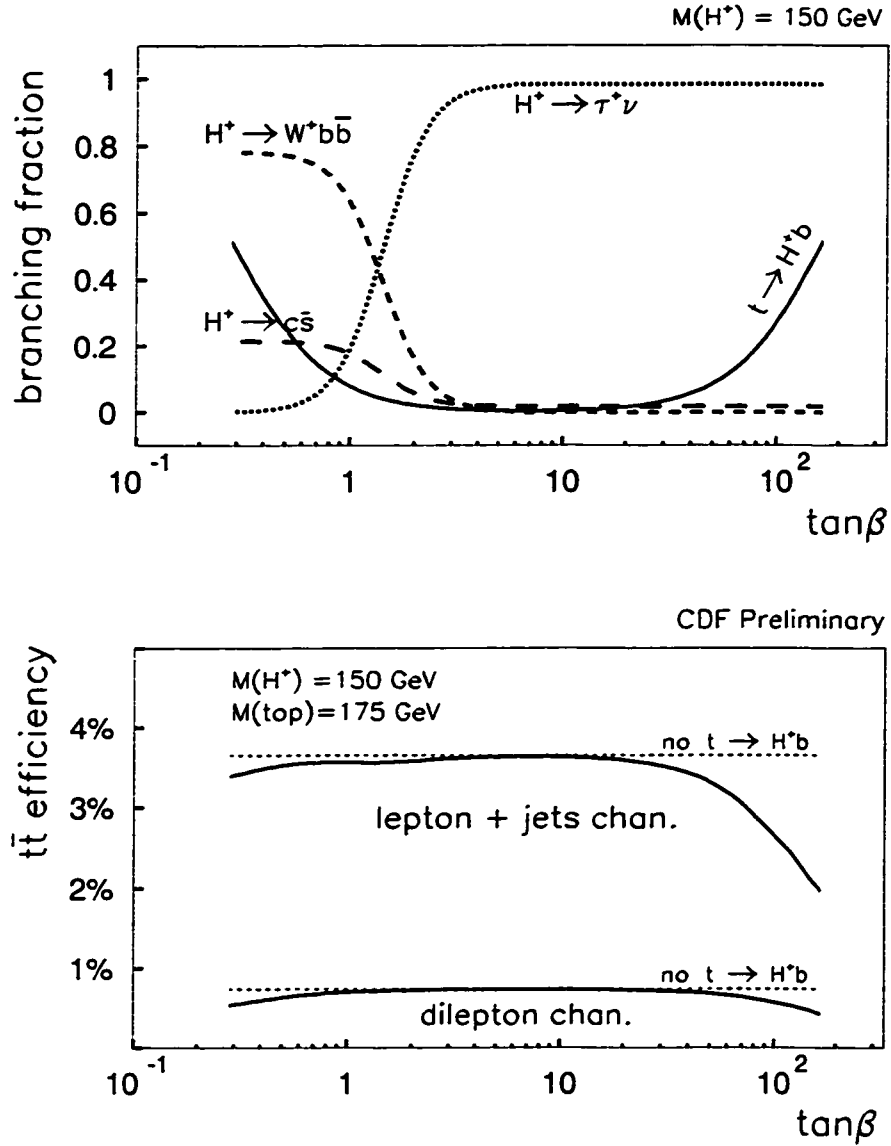


Figure 6.13: The top plot shows the branching fractions for the top quark and the charged Higgs boson, as a function of $\tan\beta$, for $M_{H^\pm} = 150 \text{ GeV}/c^2$. Shown in the bottom plot is the $t\bar{t}$ efficiency in each channel. When $\mathcal{B}(t \rightarrow H^\pm b) = 0$, the efficiency in each channel is its SM value (marked “no $t \rightarrow H^\pm b$ ”).

Chapter 7

Limits using the Absolute Rate of Events

In the last chapter, I determined the efficiencies for $t\bar{t}$ events with H^\pm decays to pass the selection criteria of the top dilepton and lepton+jets channels. Using these efficiencies $\epsilon_{t\bar{t}}$, the total number of expected events in each channel is calculated according to Eq. 1.3, which is repeated below,

$$N_{\text{exp}} = N_{\text{bkg}} + \epsilon_{t\bar{t}} \sigma_{t\bar{t}} \mathcal{L} . \quad (7.1)$$

Here, N_{bkg} is the expected number of background events from non- $t\bar{t}$ processes, $\sigma_{t\bar{t}}$ is the $t\bar{t}$ cross section, and \mathcal{L} is the luminosity. In Fig. 7.1, the mean number of events in each channel is plotted as a function of $\tan\beta$, for $M_{H^\pm} = 120 \text{ GeV}/c^2$. This is done for $\sigma_{t\bar{t}} = 5.0$ and 7.5 pb . At small and large values of $\tan\beta$, only an improbable upward statistical fluctuation in the number of expected events can account for the observed number of events in each channel. This fact is used to exclude these regions.

7.1 Assumptions

I make several assumptions in order to set limits using this method. First of all, the top mass is assumed to be the measured value of $175 \text{ GeV}/c^2$ [20, 21]. For simplicity, the statistical and systematic errors associated with this measured value are not taken into account.

The method used in this chapter also requires an assumption about the $t\bar{t}$ cross section. I use the theoretical value $\sigma_{t\bar{t}} = 5.0 \text{ pb}$ (see Table 2.2), because the

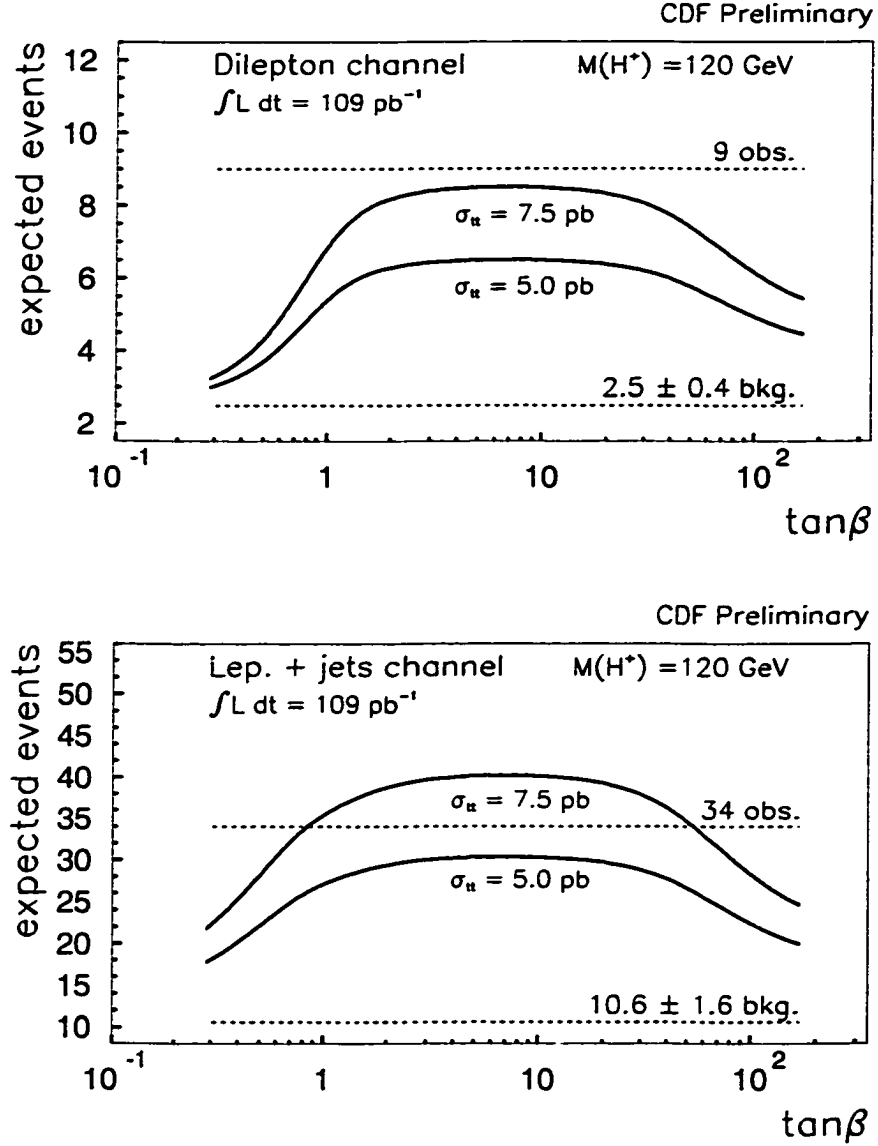


Figure 7.1: *Top plot:* the number of expected dilepton events as a function of $\tan\beta$, for $M_{H^\pm} = 120 \text{ GeV}/c^2$. Also shown are the observed number of events, and the number of non- $t\bar{t}$ background events. Near $\tan\beta = 7$, $\mathcal{B}(t \rightarrow H^\pm b) \approx 0$, and the efficiency equals its SM value. *Bottom plot:* the number of expected lepton+jets events vs. $\tan\beta$.

measured value is determined by assuming that the top quark only decays to $W^\pm b$ (see Section 2.7.2). I also present results for a value which is 50% higher, $\sigma_{t\bar{t}} = 7.5$ pb, to illustrate sensitivity to this value, and also to demonstrate the effect of an upward statistical fluctuation in the observed number of events. It should be noted that this value of 7.5 pb substantially exceeds the theoretical values that are in the range 4.9-5.5 pb, some of which have been calculated with a systematic error of less than 10% (see Table 2.2).

Finally, one of the most important assumptions in this search is the premise that only $t\bar{t}$ with charged Higgs decays, and other known SM backgrounds, contribute events to the top dilepton and lepton+jets channels. This assumption must be made since limits are established based on the fact that *too many* events are observed for the top quark to frequently decay to a charged Higgs boson. I discuss this assumption further in Chapter 9.

7.2 Methods for Combining the Channels

Since a deficit of events is predicted in each channel, it seems obvious that the best limit should be obtained by combining the channels, rather than using only the dilepton channel, or only the lepton+jets channel. However, this should be decided with a Monte Carlo simulation, rather than an examination of the data. I determine 95% C.L. limits for many representative points in $(M_{H^\pm}, \tan\beta)$ space, assuming that the top quark only decays to $W^\pm b$, and that the most probable number of events is observed in each channel. This is done for $\sigma_{t\bar{t}} = 5.0$ and 7.5 pb. In each simulation, the best limits are derived not from either channel alone, but from summing the dilepton and lepton+jets events.

Of course, there are other ways of combining the two channels. In this chapter, I give results for one other method. It is the approach used to determine the

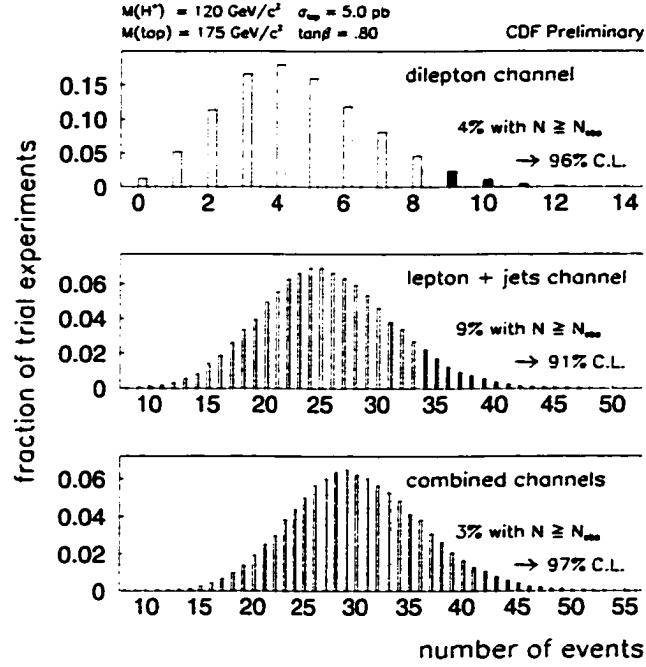


Figure 7.2: Distribution of dilepton events, lepton+jets events, and the sum of these events in many trial experiments for an assumed point in parameter space. The best limit is obtained with the sum of dilepton and lepton+jets events, rather than the results of either separate channel.

combined significance of the observed excess of top events above the background in multiple decay channels, at the time of the top quark discovery [13, 142]. This method is more complex, but gives similar limits to the first method. Below, the two methods are described in detail.

7.3 Method 1: Sum the Events from Each Channel

The simplest method for combining channels is to sum the dilepton and lepton+jets data samples, and treat them as a single counting experiment. I exclude values of $\tan\beta$, M_{H^\pm} and $\sigma_{t\bar{t}}$ if there is less than a 5% probability for finding a total

number of events at least as large as the observed number (9 dilepton events + 34 lepton events = 43 events). In other words, the 95% confidence limit means that if we could repeat our experiment countless times, and charged Higgs exists in the assumed parameter space, in less than 5% of the experiments would we see a sum of events equal to or larger than the observed number.

The probability for the expected number of events to fluctuate to the observed number of events or higher is calculated from a Poission distribution with a mean equal to the expected number of events,

$$N_{\text{exp,SUM}} = N_{\text{bkg,DIL}} + N_{\text{bkg,L+J}} + (\epsilon_{t\bar{t},DIL} + \epsilon_{t\bar{t},L+J}) \sigma_{t\bar{t}} \mathcal{L} . \quad (7.2)$$

However, this mean has a Gaussian-shaped systematic uncertainty associated with it, due to separate uncertainties associated with the number of background events in each channel ($N_{\text{bkg,DIL}}$ and $N_{\text{bkg,L+J}}$), the efficiency in each channel ($\epsilon_{t\bar{t},DIL}$ and $\epsilon_{t\bar{t},L+J}$), and the luminosity (\mathcal{L}).

There are at least two comparable ways to take into account this uncertainty on the mean. The simplest method is to mathematically convolute a Gaussian distribution with the Poission distribution, where the width of the Gaussian is set equal to the error on $N_{\text{exp,SUM}}$. Another method is to use a “trial-experiments” approach. In each of many trial experiments, the number of expected events is constructed from Eq. 7.2, by choosing each of the quantities that appear in this equation from a Gaussian distribution, centered on the mean value of the quantity, with a width equal to the associated error. Then, the total number of events is randomly chosen from a Poission distribution with this mean. The fraction of a large number of these trial experiments in which the sum of events is equal to the observed sum or more, determines the probability for the expected number of events to fluctuate to the observed number of events or higher.

While the two approaches described here give similar results, it is easier to

Sources of Systematic Error for the $t\bar{t}$ Efficiency

correlated between chan.	uncorrelated between chan.
lepton ID efficiency $\varepsilon_{\text{lep ID}}$	SVX b -tag efficiency ε_{tag}
jet energy scale $\varepsilon_{\text{jet E}}$	trigger efficiency $\varepsilon_{\text{trig}}$
initial/final state radiation $\varepsilon_{\text{ISR/FSR}}$	Monte Carlo statistics $\varepsilon_{\text{MCstat}}$
z -vertex resolution $\varepsilon_{\text{Z vtx}}$	

Table 7.1: Systematic uncertainties in the $t\bar{t}$ efficiency, separated into two categories, depending on whether they are correlated or uncorrelated between the dilepton and lepton+jets channels.

modify the trial-experiments approach to include the effect of correlated systematic errors, which is described in the next section.

7.3.1 Correlated Systematic Errors

Some of the errors associated with the $t\bar{t}$ efficiencies $\epsilon_{t\bar{t}, DIL}$ and $\epsilon_{t\bar{t}, L+J}$ will be statistically correlated between the two channels, since they arise from similar sources. Table 7.1 lists these errors, and designates the ones that are correlated. I assume 100% correlation. To take this into account, I use the trial-experiments approach described above, but I use more care in choosing the $t\bar{t}$ efficiencies. The efficiency in each separate channel is generated with a distribution that is Gaussian, and has a width equal to the quadrature sum of the individual errors associated with that channel. However, correlations between channels are correctly taken into account.

This is achieved as follows. In each trial experiment, six numbers $\sigma_1, \sigma_2, \sigma_3, \sigma_4, \sigma_5$ and σ_6 are chosen randomly from a Gaussian distribution centered at zero, of width $\sigma = 1$. Then, the central value of the efficiency in each channel is adjusted,

according to the following expressions

$$\epsilon_{t\bar{t}, DIL} \rightarrow \epsilon_{t\bar{t}, DIL} + \sigma_1 \epsilon_{\text{lep ID}} + \sigma_2 \epsilon_{\text{jet E}} + \sigma_3 \epsilon_{\text{ISR/FSR}} + \sigma_4 \epsilon_{Z \text{ vtx}} + \sigma_5 \epsilon_{\text{trig}} + \text{MC stat} \quad (7.3)$$

$$\epsilon_{t\bar{t}, L+J} \rightarrow \epsilon_{t\bar{t}, L+J} + \sigma_1 \epsilon'_{\text{lep ID}} + \sigma_2 \epsilon'_{\text{jet E}} + \sigma_3 \epsilon'_{\text{ISR/FSR}} + \sigma_4 \epsilon'_{Z \text{ vtx}} + \sigma_6 \epsilon'_{\text{trig+tag}} + \text{MC st} \quad (7.4)$$

The unprimed and primed errors correspond to dilepton and lepton+jets channel systematic errors, respectively (they are different sizes). Note that the first four errors in the first expression, and the corresponding errors in the second expression, are shifted by the same fractional magnitude, and in the same direction, since they are correlated. The last error, which is due to the quadrature sum of the trigger×tagging efficiency error and the Monte Carlo statistical error, is uncorrelated between channels.

The difference between limits calculated using the trial-experiments approach with correlated systematic errors, and an approach that ignores the correlated systematic errors, is very small. It is found that by ignoring the correlations, typically a 95% C.L. limit becomes degraded into a 94.5% C.L. limit! This is true because only some of the errors are correlated between channels. In addition, the limits are determined mostly by statistics, and not systematic errors.

Fig. 7.3 shows the expected number of events for $M_{H^\pm} = 120 \text{ GeV}/c^2$, and $150 \text{ GeV}/c^2$. Taking into account a typical systematic uncertainty of about 18% in the lepton+jets channel, and 12% in the dilepton channel, this analysis excludes parameter space at the 95% C.L. if 31.2 events or fewer are predicted. Thus, regions are excluded where the expected number of events dips below this “95% C.L.” line, at 31.2 events. The limits using this method are given in Table 7.2, for $\sigma_{t\bar{t}} = 5.0$ and 7.5 pb .

The disadvantage of this sum-of-events method is that the dilepton channel,

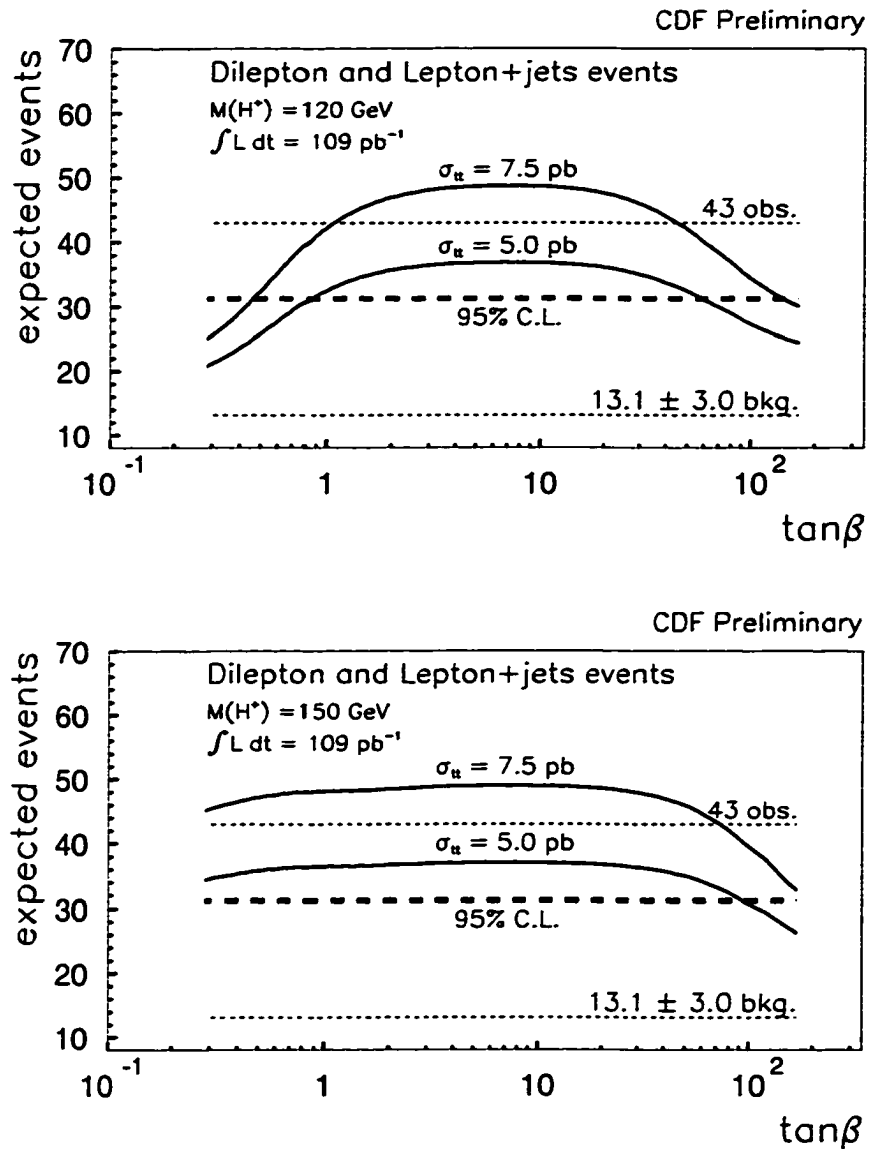


Figure 7.3: *Top plot:* the expected number of (dilepton + lepton+jets) events as a function of $\tan\beta$, for $M_{H^\pm} = 120 \text{ GeV}/c^2$. Also shown are the observed number of events, and the number of non- $t\bar{t}$ background events. Limits at the 95% C.L. or higher are set in regions where the expected number of events dips below the “95% C.L.” line. *Bottom plot:* Same plot as above, for $M_{H^\pm} = 150 \text{ GeV}/c^2$.

95% C.L. Limits Derived from the Absolute Rate of Events

M_{H^\pm} (GeV)	$\sigma_{t\bar{t}} = 5.0 \text{ pb}$				$\sigma_{t\bar{t}} = 7.5 \text{ pb}$			
	sum of evts		product of prob.		sum of evts		product of prob.	
	$\tan\beta$	$B(t \rightarrow Hb)$	$\tan\beta$	$B(t \rightarrow Hb)$	$\tan\beta$	$B(t \rightarrow Hb)$	$\tan\beta$	$B(t \rightarrow Hb)$
	>	<	>	<	>	<	>	<
60	1.50	30%	1.58	28%	.87	56%	.92	53%
80	1.30	31%	1.37	29%	.78	56%	.86	51%
100	1.11	31%	1.17	29%	.675	55%	.75	50%
120	.85	32%	.92	29%	.45	63%	.52	56%
130	.56	44%	.65	37%	.195	87%	.295	74%
140	.26	70%	.35	56%	-	-	-	-
	$\tan\beta$	$B(t \rightarrow Hb)$	$\tan\beta$	$B(t \rightarrow Hb)$	$\tan\beta$	$B(t \rightarrow Hb)$	$\tan\beta$	$B(t \rightarrow Hb)$
	<	<	<	<	<	<	<	<
60	33	31%	33	31%	77	71%	73	69%
80	39	34%	37	32%	95	75%	86	71%
100	47	35%	47	35%	125	79%	113	75%
120	61	36%	61	36%	155	77%	149	76%
130	67	32%			155	71%		
140	78	29%			170	65%		
150	95	25%			195	59%		
160	137	23%			243	55%		
165	169	23%			-	-		

Table 7.2: The 95% C.L. limits for the two methods of combining the dilepton and lepton+jets channels. Limits are shown for $\sigma_{t\bar{t}} = 5.0 \text{ pb}$ and 7.5 pb . The two methods exclude similar regions of parameter space, so I use the simpler “sum-of-events” method for combining the channels.

with the fewest events, may get “washed out” by the lepton+jets channel, which has a much larger number of events (but a similar signal/background ratio). This method is not wrong, but it may give a conservative limit. Thus, I investigate another method for combining the results of the dilepton and lepton+jets channels.

7.4 Method 2: Use a Product-of-Probabilities Approach

There is an alternative approach to combining the channels by summing the events. I employ a method [143] similar to the one used to determine the combined significance of the excess of $t\bar{t}$ events, above the non- $t\bar{t}$ background, observed in three different decay channels at the time of the top discovery [142, 13].

Using efficiencies calculated for the parameters M_{H^\pm} and $\tan\beta$, in each channel I compute the probability that the expected number of events fluctuates to the observed number of events or more. The product of these probabilities

$$\begin{aligned}
 P_{\text{obs}} &= (\text{probability of finding a number of dilepton events} \geq N_{\text{obs, DIL}}) \\
 &\times (\text{probability of finding a number of lepton + jets events} \geq N_{\text{obs, L+J}})
 \end{aligned}
 \tag{7.5}$$

is a measure of the probability of the configuration of 9 dilepton and 34 lepton+jets events. Limits are set by determining the probability of finding a product of probabilities P equal to or smaller than P_{obs} .

To do this, I perform many trial experiments. In each one, I generate a number of dilepton events N_{DIL} and a number of lepton+jets events $N_{\text{L+J}}$. These numbers are selected from Poission distributions, with the following means.

$$N_{\text{exp, DIL}} = N_{\text{bkg, DIL}} + \epsilon_{t\bar{t}, \text{DIL}} \sigma_{t\bar{t}} \mathcal{L} \tag{7.6}$$

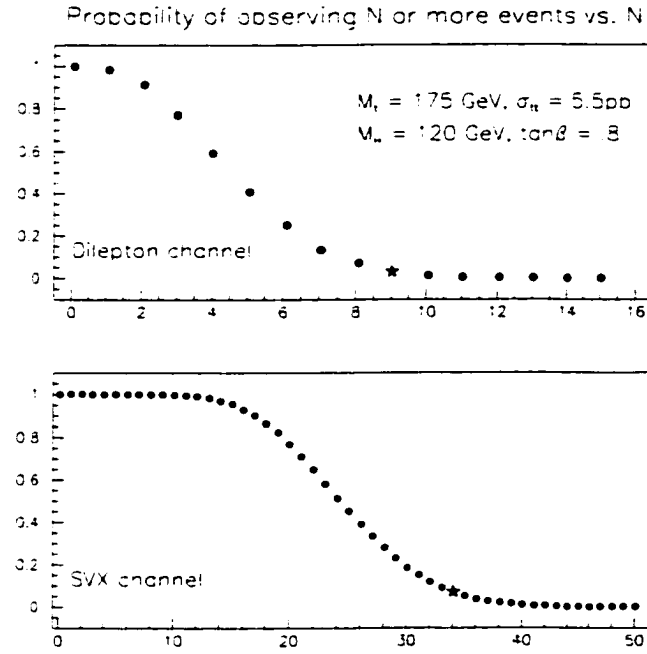


Figure 7.4: Probability for observing N or more events vs. N for the dilepton channel, and the lepton+jets channel (called the “SVX channel” on the bottom plot). These distributions are formed for the particular point in parameter space specified on the upper right. The stars indicate the values of probability observed in the data.

$$N_{\text{exp}, L+J} = N_{\text{bkg}, L+J} + \epsilon_{t\bar{t}, L+J} \sigma_{t\bar{t}} \mathcal{L} \quad (7.7)$$

This is done using the method described in the previous section, where the correlations for the errors on the efficiencies $\epsilon_{t\bar{t}, DIL}$ and $\epsilon_{t\bar{t}, L+J}$ are accounted for by using Eqs. 7.3 and 7.4.

In order to calculate the product-of-probabilities P in a trial experiment, via Eq. 7.5, we need to know the probability for observing N or more events in each channel. I use many trial experiments to construct these distributions. Examples are shown in Fig. 7.4. Then, these distributions are used by many additional trial

experiments that are run in order to determine P . I record the fraction of the trial experiments in which this product-of-probabilities P is smaller than the one observed in the data P_{obs} . If this fraction is less than 5%, then the particular combination of M_{H^\pm} , $\tan\beta$, and $\sigma_{t\bar{t}}$ is excluded at the 95% confidence limit or higher.

In Table 7.2 I list the 95% C.L. limits for the “product of probabilities” method. This is done for $\sigma_{t\bar{t}} = 5.0$ and 7.5 pb, and the results are shown side-by-side with the results of the sum-of-events method described in the previous section. Since the product-of-probabilities method is intended to be used as a cross check of the sum-of-events method, some of the limits derived using this approach have not been updated to include the effect of a large H^\pm width at high- $\tan\beta$, and hence do not appear in the table.

7.5 Results

The “product-of-probabilities” method excludes only slightly more parameter space than the simple “sum-of-events” method. For this reason, I use this simpler and better-understood “sum-of-events” approach to exclude charged Higgs bosons. The excluded regions from Table 7.2 are shown in the M_{H^\pm} vs. $\tan\beta$ plane in Fig. 7.5, and the M_{H^\pm} vs. $\mathcal{B}(t \rightarrow H^\pm b)$ plane in Fig. 7.6. The limits are shaded, and marked “ $\sigma_{t\bar{t}} = 5.0$ pb” and “ $\sigma_{t\bar{t}} = 7.5$ pb”. Limits for the region marked “ $\sigma_{t\bar{t}}$ -indep.” are set without assuming a value for $\sigma_{t\bar{t}}$, and are discussed in the next chapter. Also shown on the plots are the excluded regions from the direct search at CDF, for $t\bar{t}$ events containing $H^\pm \rightarrow \tau\nu$ decays [56, 107]. Finally, it should be noted that these are preliminary results, which will almost certainly change before a final manuscript summarizing the work done in this thesis is submitted to Physical Review Letters.

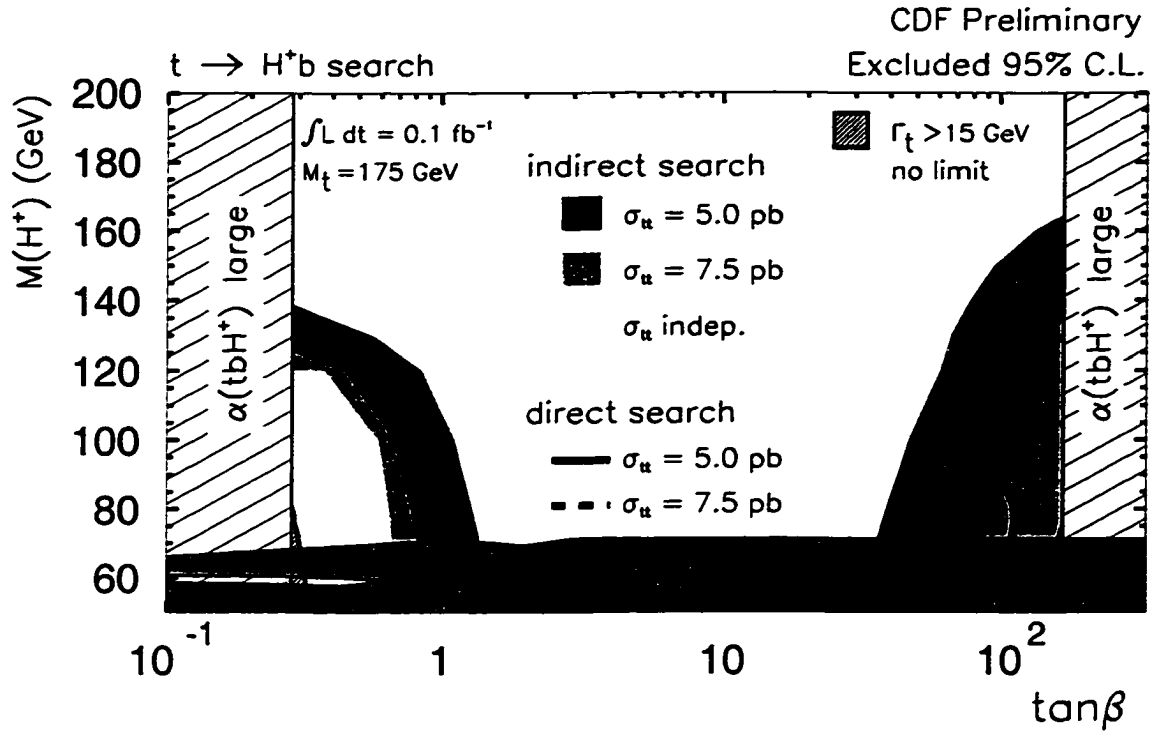


Figure 7.5: CDF excluded regions (95% C.L.) in the M_{H^\pm} vs. $\tan\beta$ plane. The solid regions are the limits from this search, while the lines are limits from the direct search for $t\bar{t}$ events with $H^\pm \rightarrow \tau\nu$ decays, performed by the Rutgers group at CDF. The cross-hatched regions are not addressed by these searches. The LEP2 limits are also shown.

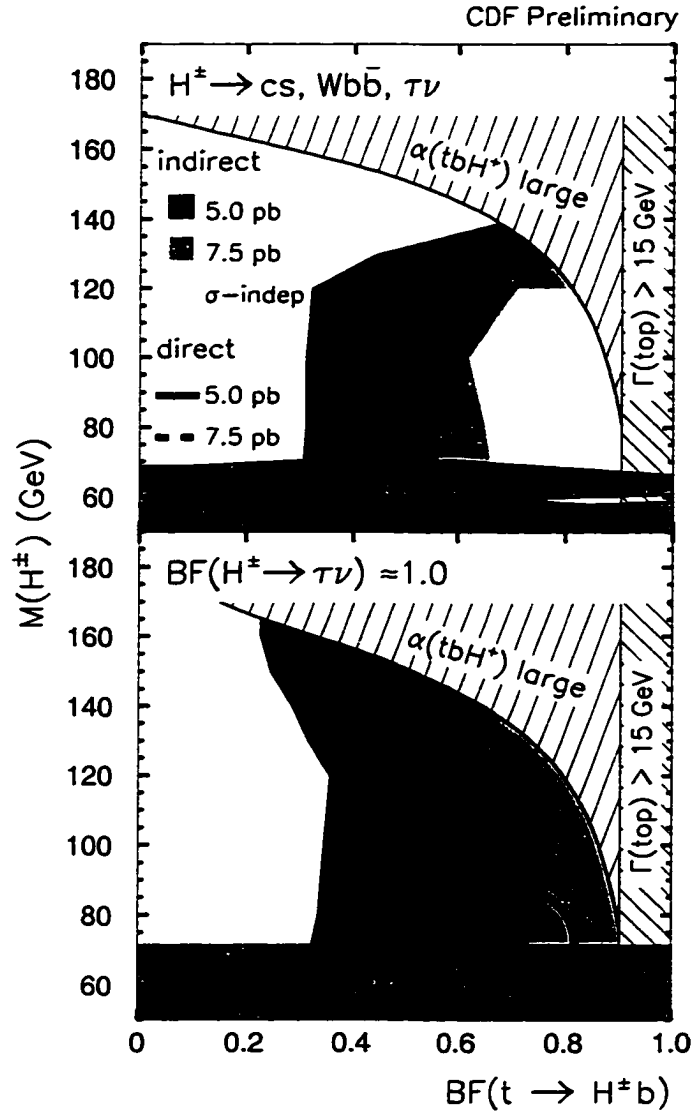


Figure 7.6: CDF excluded regions (95% C.L.) in the M_{H^\pm} vs. $\mathcal{B}(t \rightarrow H^\pm b)$ planes. The top plot corresponds to the low- $\tan\beta$ region, while the bottom plot corresponds to the high- $\tan\beta$ region. The solid regions are the limits from this search, while the lines are limits from the direct search for $t\bar{t}$ events with $H^\pm \rightarrow \tau\nu$ decays, performed by the Rutgers' group at CDF. The cross-hatched regions are not addressed by these searches. The LEP2 limits are also shown.

7.5.1 Features of the Limit Plots

Low- and high- $\tan\beta$ regions of parameter space are excluded where the observed number of $t\bar{t}$ events is significantly larger than the expected number. If $\sigma_{t\bar{t}}$ increases, then more $t\bar{t}$ events are expected for a given region of parameter space, and the limits become degraded. Thus, the limits corresponding to $\sigma_{t\bar{t}} = 5.0$ pb exclude more parameter space than the limits that are set assuming the value $\sigma_{t\bar{t}} = 7.5$ pb. This is in contrast to the limits from the direct H^\pm search at CDF, based on the observation of too few $t\bar{t}$ events with $H^\pm \rightarrow \tau\nu$ decays, which exclude more parameter space with an increasing $\sigma_{t\bar{t}}$. For this reason, the two methods are complementary; the high- $\tan\beta$ limits from this search are superior for $\sigma_{t\bar{t}} = 5.0$ pb, while the direct search limits are superior for $\sigma_{t\bar{t}} = 7.5$ pb. However, when comparing these two searches, one must remember that there are different assumptions made for each one. These assumptions will be discussed in Chapter 9.

At high- $\tan\beta$, the limits extend to $M_{H^\pm} = 165$ GeV/ c^2 . However, at low- $\tan\beta$, limits cannot be set for $M_{H^\pm} > 140$ GeV/ c^2 . In this region, the dominant charged Higgs boson decay mode is $H^\pm \rightarrow W^\pm b\bar{b}$. The $t\bar{t}$ events with this decay have efficiencies similar to the SM value, for passing the selection criteria of the dilepton and lepton+jets channels. As a result, no significant suppression of events is predicted in this region, as shown in Fig. 7.3.

The regions where the tbH^+ Yukawa coupling becomes non-perturbative, $\tan\beta < 0.28$ and $\tan\beta > 170$, are also marked. The boundaries for these regions form straight lines in the M_{H^\pm} vs. $\tan\beta$ plane. However, in the M_{H^\pm} vs. $\mathcal{B}(t \rightarrow H^\pm b)$ plane, the boundaries are curved lines that extend into the low- $\mathcal{B}(t \rightarrow H^\pm b)$ region for large M_{H^\pm} . This occurs because the partial width $\Gamma_{t \rightarrow Hb}$, which determines the branching fraction $\mathcal{B}(t \rightarrow H^\pm b)$, is composed of a coupling term and a phase-space term. The coupling remains constant, but the phase space decreases with

increasing M_{H^\pm} , resulting in a decreasing partial width $\Gamma_{t \rightarrow Hb}$.

In Section 5.4 I discussed a limitation with modeling a large top quark width ($\Gamma_{\text{top}} \gtrsim 15$ GeV). According to the excluded plot in the M_{H^\pm} vs. $B(t \rightarrow H^\pm b)$ plane, the region where $\Gamma_{\text{top}} > 15$ GeV is completely covered by the non-perturbative regions, and the LEP2 excluded regions, except for a small sliver of parameter space at $\tan\beta \approx 0.3$, between $M_{H^\pm} = 60$ and 80 GeV/ c^2 .

7.5.2 Comparison to the DØ Limits

Using an analysis similar to the one described in this chapter, the DØ collaboration uses its sample of 30 observed lepton+jets events to set $\sigma_{t\bar{t}}$ -dependent limits on charged Higgs production [144]. DØ sets 95% C.L. limits using a “frequentist approach” that is very similar to the method I use to establish limits. DØ also sets limits using a Bayesian approach that I do not subscribe to. The limits are shown in Fig. 7.7. By comparing these limits with those from CDF (Fig. 7.5), one can see that the two searches have similar sensitivity.

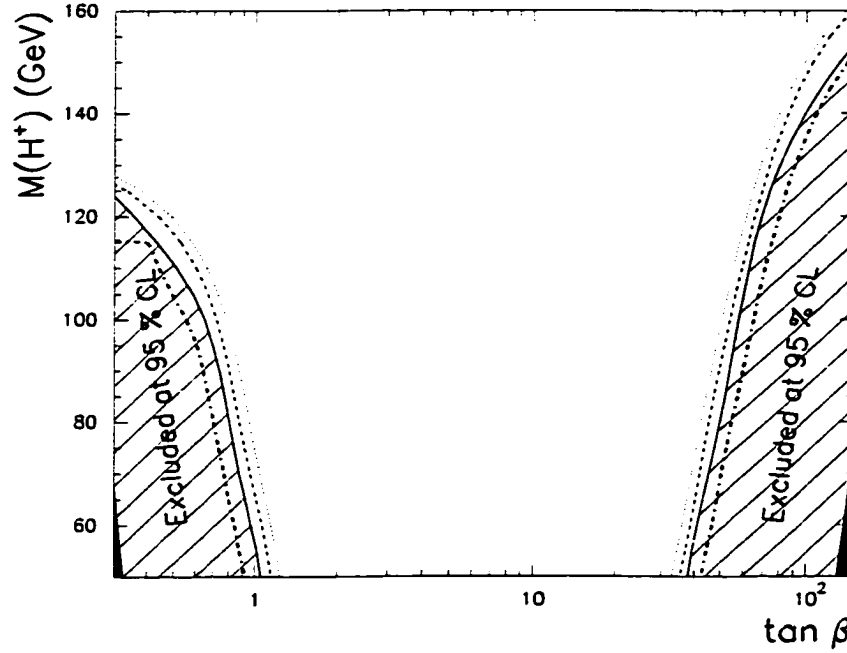


Figure 7.7: The DØ 95% C.L. excluded regions in the M_{H^\pm} vs. $\tan\beta$ plane, for the charged Higgs boson H^\pm , assuming that $M_{\text{top}} = 175 \text{ GeV}/c^2$. The thick dot-dashed lines inside the hatched area are the exclusion boundaries obtained by assuming $\sigma_{t\bar{t}} = 5.5 \text{ pb}$, using a method similar to mine. The other limits are obtained with a Bayesian approach, assuming $\sigma_{t\bar{t}} = 5.5 \text{ pb}$ (hatched areas), 5.0 pb (dashed lines), and 4.5 pb (dotted lines). No limits are set for the dark shaded regions, where the top quark width is larger than 15 GeV .

Chapter 8

Limits using the Relative Rate of Events

In the previous chapter, I exploit the fact that a deficit of dilepton events and lepton+jets events is predicted within the two-Higgs-doublet model. The two channels are combined, and limits are set in regions where the observed number of events can only be explained by an improbable statistical fluctuation. To set these limits, it is necessary to assume an absolute value for $\sigma_{t\bar{t}}$, in order to compute the expected number of events.

However, it is possible to exclude parameter space at small $\tan\beta$ without assuming a value for $\sigma_{t\bar{t}}$. To do this, I exploit another prediction of the two-Higgs-doublet model, that the dilepton event rate will be more severely suppressed than the lepton+jets event rate. This effect is most pronounced at low- $\tan\beta$, if $\mathcal{B}(t \rightarrow H^\pm b \rightarrow csb)$ is large, for the following reason. If $H^\pm \rightarrow cs$, then the $t\bar{t}$ final states $WbW\bar{b}$ and $WbH\bar{b}$ both produce isolated high- P_T leptons, and contribute to the lepton+jets channel. However, usually only $WbW\bar{b}$ can have two high- P_T leptons and contribute to the dilepton channel. The ratio R of $\frac{\text{dilepton events}}{\text{lepton+jets events}}$ can be written in terms of the efficiencies for these final states, and $\beta \equiv \mathcal{B}(t \rightarrow H^\pm b)$,

$$R \approx \frac{\epsilon_{WbW\bar{b}, \text{ dilepton}} (1 - \beta)^2}{\epsilon_{WbW\bar{b}, \text{ lep+jets}} (1 - \beta)^2 + \epsilon_{WbH\bar{b}, \text{ lep+jets}} \beta (1 - \beta)} . \quad (8.1)$$

As $\mathcal{B}(t \rightarrow H^\pm b)$ approaches 1, the ratio R becomes very small, $\lim_{\beta \rightarrow 1} R = 0$. In contrast, the ratio observed in the data is consistent with the SM value of 0.204. Fig. 8.1 shows the predicted ratio as a function of $\tan\beta$ for $M_{H^\pm} = 100 \text{ GeV}/c^2$, along with the SM ratio and the observed ratio.

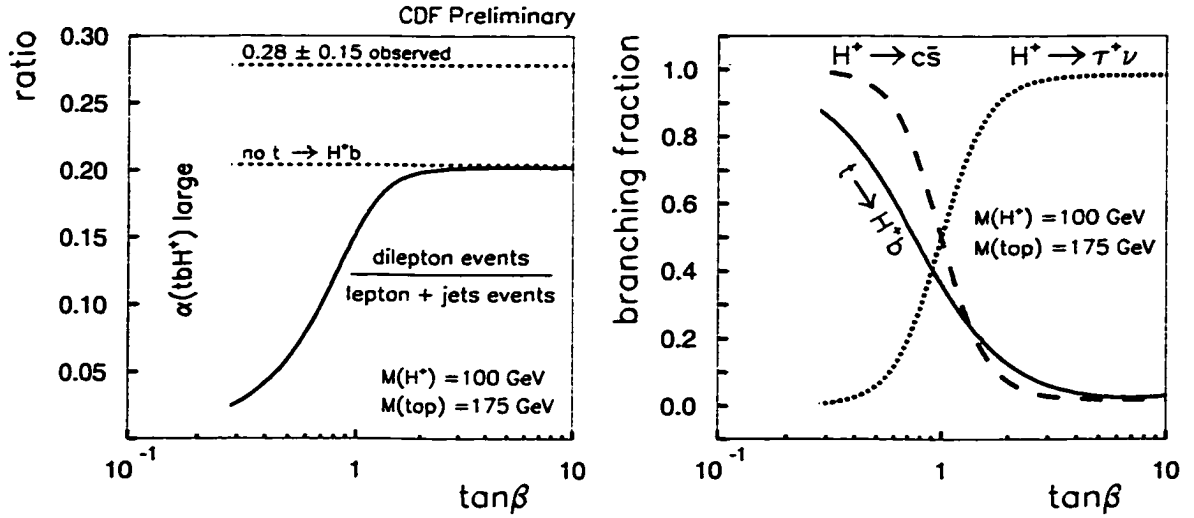


Figure 8.1: On the left is the predicted ratio of dilepton to lepton+jets events as a function of $\tan\beta$, for $M_{H^\pm} = 100 \text{ GeV}/c^2$. On the right is the branching fraction of the top quark and the H^\pm as a function of $\tan\beta$.

There are several ways to test whether the observation of 9 dilepton events is inconsistent with the observation of 34 lepton+jets events, assuming a particular combination of M_{H^\pm} and $\tan\beta$. The obvious method is to calculate the predicted ratio of dilepton to lepton+jets events,

$$R = \frac{N_{\text{exp, DIL}} - N_{\text{bkg, DIL}}}{N_{\text{exp, L+J}} - N_{\text{bkg, L+J}}} \quad (8.2)$$

and compare this to the observed ratio. Certainly the mean value for R can be calculated with an accuracy of 10-15%, limited by systematic errors. However, when only a small number of events are expected, a large range of values for this ratio will be predicted, since the numerator and denominator are subject to relatively large statistical fluctuations. To demonstrate this behavior, I calculate the expected distribution for the ratio, using a “trial-experiments” approach, as described in the previous chapter. In each of many trial experiments, I generate a number of dilepton events, a number of lepton+jets events, and the ratio R

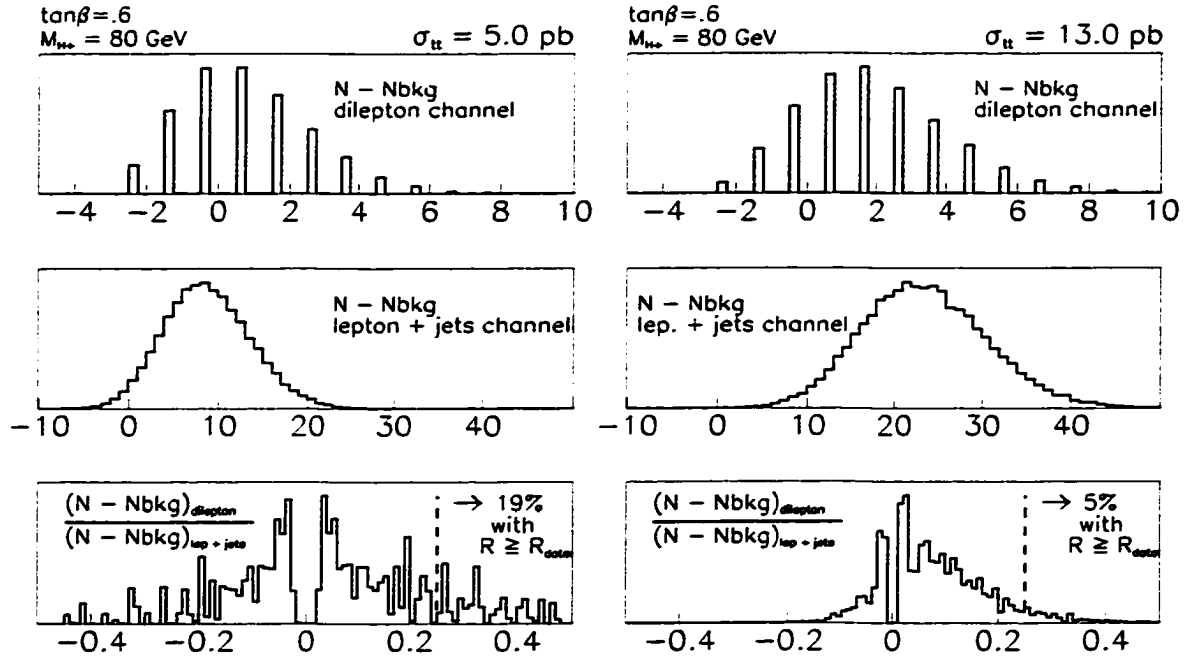


Figure 8.2: The number of dilepton events (top pair), lepton+jets events (middle pair), and the ratio of these events (bottom pair) in many trial experiments where $M_{H^\pm} = 80 \text{ GeV}/c^2$, and $\tan\beta = 0.62$. On the left, $\sigma_{t\bar{t}} = 5.0 \text{ pb}$, and on the right $\sigma_{t\bar{t}} = 13.0 \text{ pb}$. The larger cross section results in a narrower ratio distribution, due to a larger expected number of events, and smaller relative statistical fluctuations in the numerator and denominator. Parameter space can be excluded only for $\sigma_{t\bar{t}} \geq 13.0 \text{ pb}$, for which there is less than a 5% chance for observing a ratio as large as the one observed in the data. Thus “ $\sigma_{t\bar{t}}$ -independent” limits cannot be established just using the ratio.

according to Eq. 8.2.

Fig. 8.2 shows the results of this procedure, performed for $\tan\beta = 0.62$, $M_{H^\pm} = 80 \text{ GeV}/c^2$, and the two values $\sigma_{t\bar{t}} = 5.0 \text{ pb}$ and 13.0 pb . The distribution for the ratio is narrower for the higher $\sigma_{t\bar{t}}$, where the expected number of events N_{exp} in each channel is larger. This is due to smaller relative statistical fluctuations in the numerator and denominator, which scale as $\sqrt{N_{\text{exp}}}$. Fig. 8.2 indicates that the observed ratio is less than 5% likely if $\sigma_{t\bar{t}} = 13.0 \text{ pb}$ is assumed, but not if $\sigma_{t\bar{t}} = 5.0 \text{ pb}$. This demonstrates that it is not possible to exclude H^\pm in a “ $\sigma_{t\bar{t}}$ -independent” way, just by using the ratio of events.

It should be noted that a cross section of 5.0 pb is unlikely for this point in parameter space, since Fig. 8.2 indicates that there is less than a 5% probability for finding either the observed number of dilepton events (9) or the observed number of lepton+jets events (34). Just using the ratio, this information is lost.

A more effective method for excluding H^\pm is to use the absolute number of events observed in one channel, the lepton+jets channel, to measure $\sigma_{t\bar{t}}$, using efficiencies that correspond to a particular combination of M_{H^\pm} and $\tan\beta$. This $\sigma_{t\bar{t}}$ is used to calculate the expected distribution of dilepton events, which can be compared to the observed number. This procedure is outlined below, and explained in more detail in the following sections.

1. Assume values for M_{H^\pm} and $\tan\beta$.
2. Use the observed number of events in the lepton+jets channel to measure $\sigma_{t\bar{t}}$. This gives a probability distribution for finding the true value of $\sigma_{t\bar{t}}$.
3. Use this $\sigma_{t\bar{t}}$ distribution to predict the distribution for the number of events in the dilepton channel.
4. Since a deficit of dilepton events is predicted, exclude H^\pm where too few

dilepton events are predicted to account for the observed number of dilepton events.

8.1 Reconstructing $\sigma_{t\bar{t}}$

Two complementary approaches are used to reconstruct the $t\bar{t}$ cross section from our observed number of lepton+jets events. The primary method used is a trial-experiments approach. As a cross check, I also use a log-likelihood approach.

8.1.1 Trial-Experiments Method

In this approach, the value of $\sigma_{t\bar{t}}$ is swept in small steps (typically 0.15 pb) over a suitable range. For each value of $\sigma_{t\bar{t}}$, 10^4 trial experiments are simulated, where every trial experiment generates a number of dilepton events, and a number of lepton+jets events. This is done in exactly the same way that was discussed in Section 7.3.1. The fraction of the 10^4 trial experiments in which the observed number of lepton+jets events is generated may be plotted as a function of $\sigma_{t\bar{t}}$, to display the probability distribution for finding the true value of $\sigma_{t\bar{t}}$. This is done in Fig. 8.3, for $M_{H^\pm} = 80 \text{ GeV}/c^2$ and $\tan\beta = 0.62$.

Note that the measured value $\sigma_{t\bar{t}} = 13.2^{+4.5}_{-3.6} \text{ pb}$ shown in this figure, is much larger than the theoretical value of 5.0 pb. This larger value of $\sigma_{t\bar{t}}$ compensates for the suppressed lepton+jets channel efficiency in the assumed parameter space, in order to give an expected number of events consistent with the observed number of events. Using this logic, it is clear that the cross section should be even larger if it is measured in the dilepton channel. Although it is unnecessary for our analysis, this $\sigma_{t\bar{t}}$ is shown in Fig. 8.4.

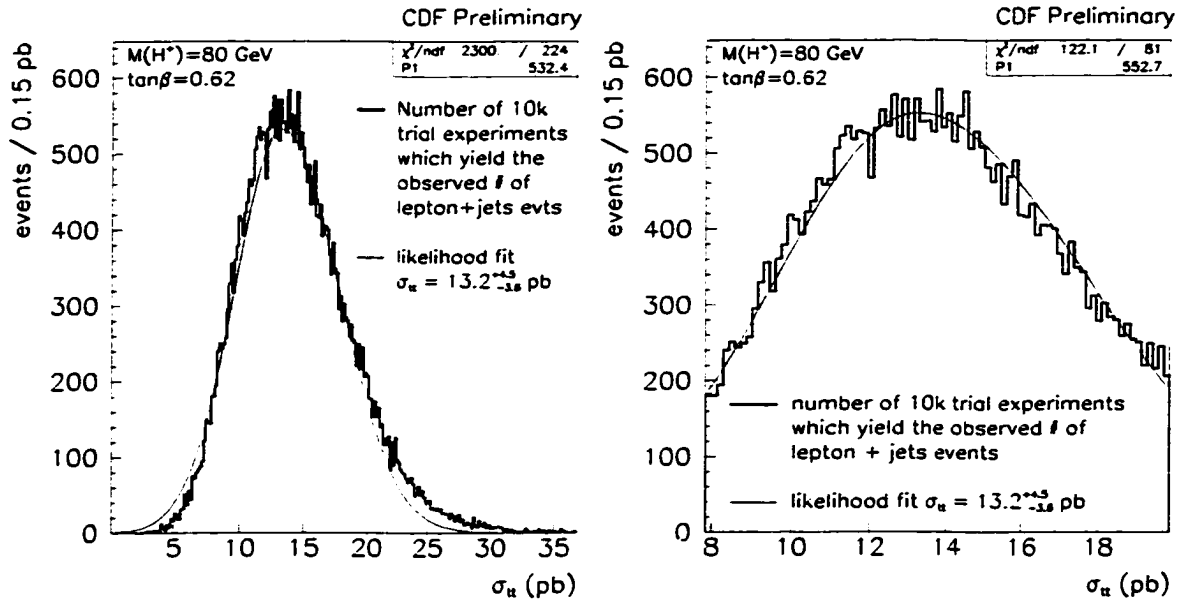


Figure 8.3: The $t\bar{t}$ cross section in the lepton+jets channel for $M_{H^\pm} = 80 \text{ GeV}/c^2$ and $\tan\beta = 0.62$. The two curves correspond to cross sections found using the trial-experiments approach, and also the log-likelihood approach. While the asymmetric Gaussian from the likelihood approach does not fit well to the trial-experiments distribution over the entire range of $\sigma_{t\bar{t}}$, shown on the left, the fit is good for the peak region ($13.2^{+1.5}_{-1.5} \text{ pb}$), shown on the right.

8.1.2 Log-Likelihood Approach

As a cross-check, a log-likelihood method should yield a consistent measurement of $\sigma_{t\bar{t}}$. The central value of $\sigma_{t\bar{t}}$ is found from

$$\sigma_{t\bar{t}} = \frac{N_{\text{obs}} - N_{\text{bkg}}}{\epsilon \mathcal{L}}. \quad (8.3)$$

The $\sigma_{t\bar{t}}$ distribution can be calculated from the following likelihood function,

$$L = G(\mathcal{L}, \sigma_{\mathcal{L}}) \cdot G(\epsilon, \sigma_{\epsilon}) \cdot G(N_{\text{bkg}}, \sigma_{N_{\text{bkg}}}) \cdot P(N_{\text{obs}}, N_{\text{bkg}} + \sigma_{t\bar{t}} \epsilon \mathcal{L}) \quad (8.4)$$

Here,

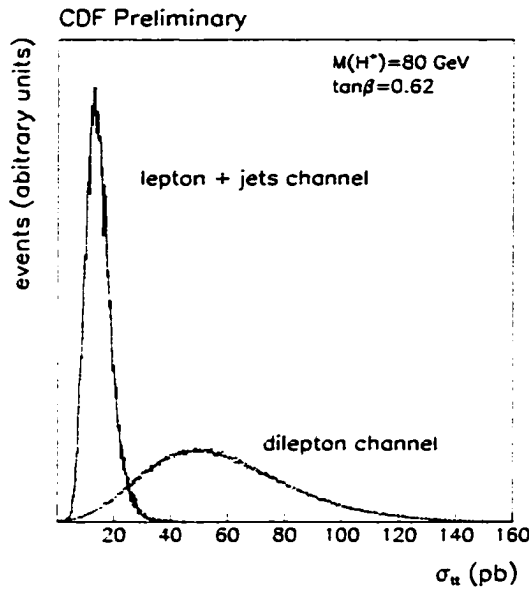


Figure 8.4: The $\sigma_{t\bar{t}}$ measured separately using the observed number of dilepton events, and the observed number of lepton+jets events, assuming that $M_{H^\pm} = 80 \text{ GeV}/c^2$ and $\tan\beta = 0.62$.

$G(\mu, \sigma)$ is a Gaussian distribution with mean μ and width σ

$P(N, \mu)$ is the Poisson probability for finding N events with mean μ

\mathcal{L} , $\sigma_{\mathcal{L}}$ is the luminosity and its error

ϵ , σ_{ϵ} is the $t\bar{t}$ efficiency in the lepton+jets channel, and its error

N_{bkg} , $\sigma_{N_{\text{bkg}}}$ is the mean number of background events, and its error

N_{obs} is the observed number of events

The $\pm 1\sigma$ errors for $\sigma_{t\bar{t}}$ correspond to the points where the negative logarithm of the likelihood function L changes from its minimum value by one-half, $\Delta(-\log L) = \frac{1}{2}$. Typically, the errors will not be symmetric, due to the Poisson term, and the resulting distribution is approximated by an asymmetric Gaussian distribution.

For our representative point $M_{H^\pm} = 80 \text{ GeV}/c^2$ and $\tan\beta = 0.62$, Fig 8.3 compares distributions for $\sigma_{t\bar{t}}$ obtained with the log-likelihood approach, and the trial-experiments approach. The fits are roughly the same. The asymmetric distribution from the log-likelihood approach is oversimplified, and does not fit the distribution from the trial-experiments method very well over the entire range of $\sigma_{t\bar{t}}$. However, in the peak region of $\sigma_{0-1.5\sigma_-}^{+1.5\sigma_+}$, the log-likelihood shape fits the distribution from the trial experiments rather well. Having served as an adequate cross-check, the distribution of $\sigma_{t\bar{t}}$ derived from the likelihood function will not be used any further.

8.2 Limits Using the Number of Dilepton Events

I calculate $\sigma_{t\bar{t}}$ with the trial-experiment method. Using this $\sigma_{t\bar{t}}$, and the $t\bar{t}$ efficiency in the dilepton channel calculated for the assumed values of M_{H^\pm} and $\tan\beta$, I determine the predicted distribution of dilepton events. The measured $\sigma_{t\bar{t}}$, and the predicted distribution for the number of dilepton events, are shown in Fig. 8.5 for $M_{H^\pm} = 80 \text{ GeV}/c^2$ and $\tan\beta = 0.62$. I exclude charged Higgs if the probability for finding a number of dilepton events equal to or greater than the observed number of events is less than 5%.

To determine the predicted distribution of dilepton events (shown in the lower plot of Fig. 8.5), I merely plot the number of dilepton events from all of the trial experiments in which the number of lepton+jets events is equal to the observed number (shown in the upper plot of Fig. 8.5). This technique takes into account the correlations between the dilepton and lepton+jets channel efficiencies, as well as the common luminosity factor, because pairs of numbers for dilepton events and lepton+jets events are generated with correlated systematic errors (see Section 7.3.1).

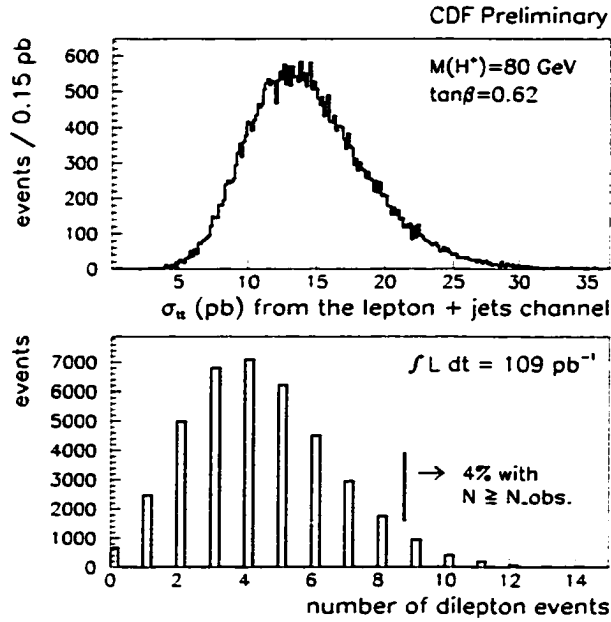


Figure 8.5: The top plot is the measured value of $\sigma_{t\bar{t}}$, assuming $M_{H^\pm} = 80 \text{ GeV}/c^2$ and $\tan\beta = 0.62$. Each entry in the top plot comes from a trial experiment in which the number of lepton+jets events is equal to the observed number (34). The number of dilepton events in each of these select trial experiments is shown on the bottom plot. The parameter space is excluded since there is less than a 5% probability for finding the observed number of dilepton events (9) or more.

8.3 Results

The 95% C.L. limits derived without assuming a value for $\sigma_{t\bar{t}}$ are shown in Table 8.1. The corresponding region of parameter space that is excluded at the 95% C.L. is displayed graphically in Figs. 7.5 and 7.6. It is the shaded region marked “ $\sigma_{t\bar{t}}$ -indep”. On the boundary of this region, a typical value of $\sigma_{t\bar{t}}$ measured in the lepton+jets channel is 14 pb. As a result, less parameter space is excluded with this approach than for the absolute rate method described in the previous chapter,

95% C.L. Limits Derived from the Relative Rate of Events

M_{H^\pm}	$\tan\beta >$	$\mathcal{B}(t \rightarrow H^+b) <$
60 GeV	.69	67%
80 GeV	.645	65%
100 GeV	.585	62%
120 GeV	.375	71%

Table 8.1: Limits derived from comparing the observed balance of dilepton and lepton+jets events, with the balance predicted within the two-Higgs-doublet model.

which establishes limits assuming $\sigma_{t\bar{t}} = 5.0$ pb and 7.5 pb.

Note that limits can only be established where $\mathcal{B}(H^\pm \rightarrow cs)$ is large, for $M_{H^\pm} \leq 120 \text{ GeV}/c^2$ at low- $\tan\beta$. For larger M_{H^\pm} , the decay $H^\pm \rightarrow W^\pm b\bar{b}$ becomes prevalent, and the ratio of (dilepton events / lepton+jets events) does not significantly deviate from the SM value.

Chapter 9

Conclusion

I begin this concluding chapter by summarizing the two methods used to set limits on top quark decays to a charged Higgs boson. I also specify the unique features of this analysis. Then, I explain how my limits compare to the other more stringent limits that have been obtained from the study of low-energy processes. To make such a comparison, it is important to consider the assumptions made about the effect of a richer particle spectrum that lies just beyond the detection capabilities of existing accelerators, such as the one predicted by supersymmetry. I will show that if such a spectrum were found to exist, it may force a reinterpretation of the limits presented here. Finally, I estimate the limits that could be set using the increased data set projected for the next Tevatron data-taking period, and present two additional methods for searching for $t \rightarrow H^\pm b$ decays.

9.1 Summary

One method for excluding H^\pm is to exploit the fact that a large $\mathcal{B}(t \rightarrow H^\pm b)$ results in rates for $t\bar{t}$ decays to dilepton final states and lepton+jets final states that are significantly smaller than the SM predictions for these rates. This is true if H^\pm decays predominantly to cs or $\tau\nu$. The data immediately indicate that such a large branching fraction for $t \rightarrow H^\pm b$ is unlikely, since the observed number of events in each channel is consistent with SM predictions. Assuming the theoretical value for $\sigma_{t\bar{t}}$, parameter space is excluded where the predicted number of events within

the two-Higgs-doublet model is significantly smaller than the observed number of events.

The second method relies on the fact that a large $\mathcal{B}(t \rightarrow H^\pm b \rightarrow csb)$ results in a ratio of dilepton events to lepton+jets events that is much smaller than the SM value. I test whether the observed number of dilepton events is consistent with the observed number of lepton+jets events, assuming a particular point in $M_{H^\pm}, \tan\beta$ parameter space. This is done by first measuring $\sigma_{t\bar{t}}$ using the observed number of lepton+jets events. This $\sigma_{t\bar{t}}$, in turn, is used to determine the probability for finding a number of dilepton events at least as large as the observed number. Since $\sigma_{t\bar{t}}$ is measured, it does not have to be assumed.

The analysis described in this thesis sets limits for M_{H^\pm} as high as 165 GeV/ c^2 . This is the highest M_{H^\pm} to be excluded with a search that is sensitive to direct decays of real charged Higgs bosons (as opposed to indirect searches sensitive to virtual H^\pm effects). This was the first analysis at the Tevatron to

- exclude charged Higgs bosons at low- $\tan\beta$, where $H^\pm \rightarrow cs$
- incorporate the $H^\pm \rightarrow W^\pm b\bar{b}$ decay mode into the search.
- exclude H^\pm without assuming a value for $\sigma_{t\bar{t}}$
- accurately model the large H^\pm width at high- $\tan\beta$

While the first two items are also achieved with the $D\bar{D}$ search, the last two items are unique features of my analysis.

9.2 Comparison to Indirect Searches

In Section 7.5.1, the features of the limit curves from this analysis were described. Also, these results were compared to limits from the other direct searches, performed at the Tevatron and LEP2. However, I have not yet made a comparison with the limits from indirect searches, using low-energy processes. This is done now.

The excluded regions of parameter space from this analysis are eclipsed by many of the limits from other low-energy processes, as discussed in Section 2.8, and summarized in Fig. 2.15. Most notably, the CLEO limit, based on measuring the rate for the decay $b \rightarrow s\gamma$, gives a 95% C.L. lower bound of at least $M_{H^\pm} > 300 \text{ GeV}/c^2$ [68, 67], independent of $\tan\beta$. This is almost twice as high as the largest excluded M_{H^\pm} in this analysis, $165 \text{ GeV}/c^2$.

Despite this, there are still at least two justifications for the search described in this thesis. First of all, my search is based on the absence of direct decays of the top quark to a real charged Higgs boson. Therefore, it is a more direct method than determining the effect of a virtual H^\pm contribution to a low-energy process, which involves a difficult calculation. Secondly, as discussed in Section 2.8, it is known that almost all the limits from low-energy processes, including the $b \rightarrow s\gamma$ limit, can be evaded if there exists a supersymmetric particle spectrum just out of the range of detection from present-day experiments. As an example, the $b \rightarrow s\gamma$ limit can be circumvented by supersymmetric particles that can destructively interfere with the W^\pm and H^\pm amplitudes, and alter the rate for the decay (see Section 2.8.2).

It is important to recognize that my analysis does not account for the existence of such a particle spectrum beyond the SM. In fact, the best limits from this analysis are based on the fact that the expected number of events within the charged Higgs scenario lies far below the observed number of events. In order

to set limits, I must assume that no other processes besides $t\bar{t}$ with H^\pm decay, and other known SM backgrounds, contribute significantly to the top dilepton or lepton+jets channels. If new particles were found to exist, then their impact on the $t\bar{t}$ decay channels used in this analysis would have to be evaluated. If these new processes contributed a significant number of events, then my limits would have to be reinterpreted. These comments also apply to the region at low- $\tan\beta$, excluded without assuming a value for $\sigma_{t\bar{t}}$. A source of dilepton events that has been overlooked means that this excluded region is too large.

In contrast, limits from the other direct searches, based on looking for an excess of events from H^\pm , are not weakened by extra contributions from processes that have not been accounted for. This is the primary advantage of the limits from the direct search performed by CDF, and also the LEP limits, over the limits presented in this thesis.

9.3 Effect of Radiative Corrections on the Limits

I have plotted excluded regions of parameter space in the M_{H^\pm} - $\tan\beta$ plane in Fig. 7.5, and the M_{H^\pm} - $\mathcal{B}(t \rightarrow H^\pm b)$ plane in Fig. 7.6. To determine $\mathcal{B}(t \rightarrow H^\pm b)$, I use partial widths that have been corrected for QCD effects, such as the exchange of a gluon between the charm and strange quarks in the decay $H^\pm \rightarrow cs$. These QCD-corrected widths are described in Ref. [38], and given in Appendix A. However, within the minimal supersymmetric extension to the SM (MSSM), the top quark partial width $\Gamma_{t \rightarrow Hb}$ can also undergo large electroweak corrections, due to the exchange of virtual supersymmetric particles [41]. These corrections are particularly large at high- $\tan\beta$, since the b -quark mass in the tbH^+ Yukawa coupling is sensitive to the electroweak effects. The corresponding correction to $\Gamma(t \rightarrow H^\pm b)$ can range from a few percent to over $\pm 100\%$, depending on $\tan\beta$, M_{H^\pm} , and the other

MSSM parameters [41]. The result is a large shift in $\mathcal{B}(t \rightarrow H^\pm b)$ for fixed values of M_{H^\pm} and $\tan\beta$. Since the limits have a strong dependence on $\mathcal{B}(t \rightarrow H^\pm b)$, large electroweak corrections will cause large changes to the limit curve in M_{H^\pm} - $\tan\beta$ plane.

In contrast, if $\mathcal{B}(t \rightarrow H^\pm b)$ is determined, changing $\tan\beta$ only changes the H^\pm width, assuming that $\tan\beta$ is large so that H^\pm decays to $\tau\nu$ almost 100% of the time. Since this change has a relatively small effect on $t\bar{t}$ efficiencies, the limit curves in the M_{H^\pm} - $\mathcal{B}(t \rightarrow H^\pm b)$ plane will still be quite accurate. If the size of the electroweak correction were known, the mapping between $\tan\beta$ and $\mathcal{B}(t \rightarrow H^\pm b)$ could be determined, and the excluded region in the M_{H^\pm} - $\mathcal{B}(t \rightarrow H^\pm b)$ plane could be used to reconstruct the excluded region in the M_{H^\pm} - $\tan\beta$ plane.

9.4 Prospects for Run II

The analysis described in this thesis is very effective for excluding large $\mathcal{B}(t \rightarrow H^\pm b)$, despite the limited size of the Run I samples of $t\bar{t}$ candidate events. However, the discovery potential is not unlimited with a larger sample of data, due to limitations from systematic errors. I illustrate this point with an extrapolation to the larger data set expected at CDF in Run II, to begin in the year 2000.

In Run II [145], 1 fb^{-1} of integrated luminosity is expected in each year of running. This corresponds to nine times the amount of data used for this analysis, per year. The upgraded CDF II detector is predicted to collect about 990 lepton+jets events (with an SVX b -tag), and 155 dilepton events [145] in the first two years of running, assuming only SM $t\bar{t}$ decays. The sum of events will have only a 3% statistical error. I will assume a systematic error of 8%, which is only about one-half of the systematic error in Run I, and consistent with the estimate given in the CDF II Technical Design Report, Ref. [145]. In addition, the theoretical

uncertainty on $\sigma_{t\bar{t}}$ is about 5% (see Table 2.2). Combining these errors, the total uncertainty on the expected number of dilepton + lepton+jets events is 10%. Therefore, the presence of a charged Higgs signal will be seen at the 3σ level, only if it results in a 30% reduction in the number of $t\bar{t}$ events in our samples. From the plots of efficiency as a function of $\tan\beta$, shown in Figs. 6.12 and 6.13, one can see that the region of intermediate $\tan\beta$, where $\mathcal{B}(t \rightarrow H^\pm b) \lesssim 0.2-0.3$, will be inaccessible still. If the H^\pm signal does not exist, then limits can be set for regions of parameter space where there is only a 5% chance for the expected number of events to fluctuate to the observed number of events or more. This will correspond to regions where a deficit of 1.64σ , or about 16%, is predicted, but not observed.

The relative rate method may give better results, since some systematic errors, such as luminosity or jet energy scale uncertainty will cancel in the ratio of dilepton to lepton+jets events. This has not been studied.

Better yet, with much more data, there is the prospect for performing direct searches. Certainly the direct search for $H^\pm \rightarrow \tau\nu$ decays in $t\bar{t}$ events, performed by CDF (see Section 2.8.1) will be improved. Some additional ideas for searching for H^\pm are given below.

9.5 Alternative Search Strategies

It is possible to use the kinematics of $t\bar{t}$ events to exclude H^\pm , rather than using just the results of counting experiments, as done in this thesis. I have attempted to perform a direct search for $t\bar{t}$ events that contain $H^\pm \rightarrow cs$ decays at low- $\tan\beta$. This is described below. A method for excluding charged Higgs at high- $\tan\beta$, based on the transverse mass reconstructed in lepton+jets events, is also described.

9.5.1 A Direct Search for $H^\pm \rightarrow cs$

If $\mathcal{B}(t \rightarrow H^\pm b)$ is large and $H^\pm \rightarrow cs$, then $t\bar{t}$ will frequently decay to the all-hadronic state $c\bar{s}b\bar{c}s\bar{b}$. Isolating a single charged Higgs boson in such a decay would be very difficult because of the irreducible backgrounds from QCD, and SM $t\bar{t}$ events. For this reason I look for $t\bar{t}$ events where one top quark decays to $H^\pm b$, and the other decays to $W^\pm b$ [146]. This approach is not useful for excluding the *very* low $\tan\beta$ region, where the $t \rightarrow W^\pm b$ decay mode is highly suppressed. However, that scenario is unlikely, given the results of the analysis described in this thesis. Thus, I look for the $WbH\bar{b}$ final state, where the W^\pm boson decays leptonically, yielding a signature of a high- P_T e or μ , \cancel{E}_T , and four jets.

$$\begin{array}{c}
 t\bar{t} \longrightarrow HbWb \\
 \qquad \qquad \qquad \downarrow \quad \searrow \\
 \qquad \qquad \qquad \quad \quad \quad lv \\
 \qquad \qquad \qquad \quad \quad \quad c\bar{s}
 \end{array}$$

If the two b -jets can be tagged in such an event, then M_{H^\pm} can be reconstructed from the two untagged jets, corresponding to the $c\bar{s}$ pair. Thus, I look for events that pass the lepton+jets selection criteria, have two b -tagged jets, and also contain two untagged jets. This search is only valid for M_{H^\pm} significantly far away from the W^\pm mass region of $80 \text{ GeV}/c^2$, where a strong signal exists from the SM decay $t\bar{t} \rightarrow WbW\bar{b}$.

This approach is an extension of the analysis that reconstructs the W^\pm mass in lepton+jets events [54], discussed in Section 2.7.4. The mass peak from that analysis is shown in Fig. 2.11. In the data, 10 double-tagged lepton+jets events are observed, with none contributing a dijet mass in the $100\text{-}200 \text{ GeV}/c^2$ range. I attempt to use this absence of events to exclude a heavy H^\pm .

I rely on three different tagging algorithms to identify b -jets in lepton+jets events. The first is the SECVTX algorithm, used throughout this thesis. The

second is to search for additional electrons and muons resulting from semileptonic decays of B hadrons. These are called “soft lepton tags” (SLTs), because typically the leptons have a much lower momentum than the primary leptons in the event from W^\pm decay. Finally, an algorithm is used to determine the probability that a jet originates from the primary vertex of the event, called the jet probability (JP) [46].

The dijet mass distributions for Monte Carlo lepton+jets events, with two b -tagged jets and two other jets, are shown in Fig. 9.1. Plotted is the mass peak expected from SM $t\bar{t}$ events, and the mass peak from $t\bar{t} \rightarrow WbH\bar{b}$ events, where $H^\pm \rightarrow cs$ and $M_{H^\pm} = 120 \text{ GeV}/c^2$. Events are darkened if both of the b -tagged jets originate from b -quark hadronization, and the two untagged jets correctly match those of W^\pm or H^\pm decay. It turns out that about 65-70% of the events, appearing in a mass window $40 \text{ GeV}/c^2$ wide and centered on the boson mass, have correctly identified b -quark jets and parton jets from W^\pm decay. The other events have mistags, or incorrect jet-parton matching due to effects such as gluon radiation.

Therefore, to search for a charged Higgs boson of mass M_{H^\pm} , one can count the number of events having a dijet mass in a $40 \text{ GeV}/c^2$ mass window centered at M_{H^\pm} . I estimate the expected number of events for $M_{H^\pm} = 120 \text{ GeV}/c^2$, by extrapolating the results for SM $t\bar{t}$ decays. In the SM, the branching fraction for $t\bar{t}$ to the lepton+jets final state $\ell\nu_\ell bq\bar{q}'\bar{b}$ is 30%. A fit to the observed dijet mass distribution, assuming contributions from SM $t\bar{t}$ and non- $t\bar{t}$ background events, finds about 6.5 SM $t\bar{t}$ events in the $40 \text{ GeV}/c^2$ mass window centered on the W^\pm mass [54]. In the two-Higgs-doublet model, the signal of interest is $t\bar{t} \rightarrow WbH\bar{b} \rightarrow \ell\nu_\ell bc\bar{s}\bar{b}$. The branching fraction for this decay depends on M_{H^\pm} and $\tan\beta$. For $M_{H^\pm} = 120 \text{ GeV}/c^2$, it never exceeds about 8%, and is larger than 5% only for the narrow range $0.26 < \tan\beta < 0.88$. Thus, assuming identical efficiencies for lepton+jets final states originating from a W^\pm or an H^\pm , the expected number of

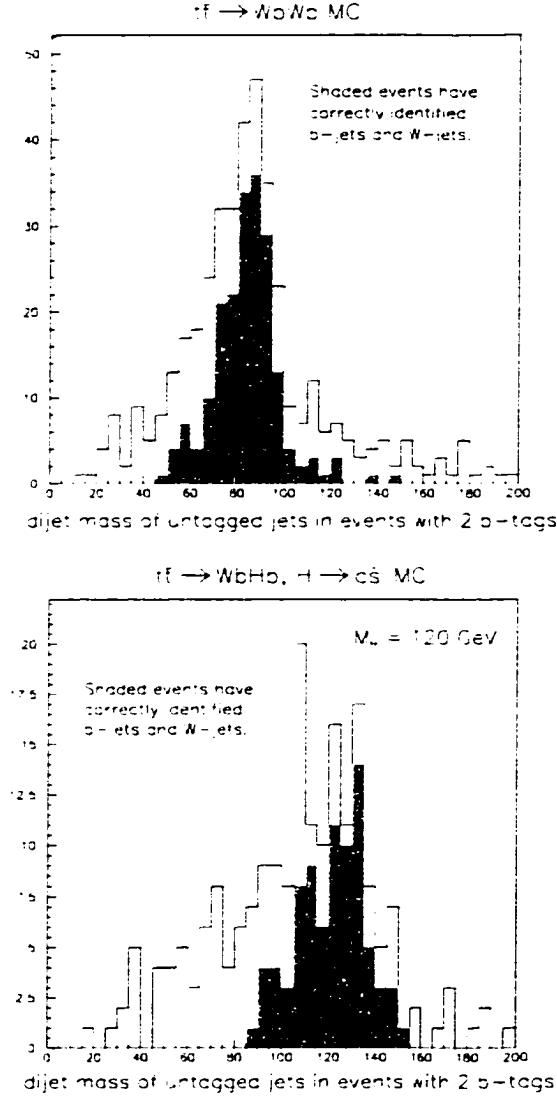


Figure 9.1: The dijet mass of the two jets without b -tags, in Monte Carlo $t\bar{t}$ events that pass the lepton+jets selection cuts, have two b -tags, and two other jets. In the top plot are SM $t\bar{t}$ events. The lower plot shows the mass peak from $t\bar{t} \rightarrow WbH\bar{b}$ events, for $M_{H^\pm} = 120 \text{ GeV}/c^2$. In all events, W^\pm is free to decay, but $H^\pm \rightarrow cs$. Events with the correct dijet *and* b -jet assignments are darkened.

signal events in the H^\pm -mass peak is about $(5\%/30\%) \times 6.5 = 1.1$ events for this narrow range of $\tan\beta$.

It is clear that in the present data set, not enough signal events are expected to set a limit. Even with ten times the data, the same procedure would predict an excess of events only for a small region of $\tan\beta$. In addition, this search method is only valid for $110 \text{ GeV}/c^2 \lesssim M_{H^\pm} \lesssim 130 \text{ GeV}/c^2$, away from $M_W = 80 \text{ GeV}/c^2$, and also below $M_{H^\pm} \approx 135 \text{ GeV}/c^2$, where $H^\pm \rightarrow W^\pm b\bar{b}$ becomes the dominant decay mode of H^\pm . Still, it is an interesting idea for Run II.

9.5.2 Transverse Mass in Lepton+Jets Events

Within the standard model, most of the events in the top lepton+jets channel should arise from $t\bar{t}$ decays in which one W^\pm boson decays to an $e\nu$ or $\mu\nu$, and the other decays to light quarks.

$$\begin{array}{c}
 t\bar{t} \longrightarrow WbWb \\
 \quad \quad \quad \swarrow \searrow \\
 \quad \quad \quad qq \\
 \quad \quad \quad \downarrow \\
 \quad \quad \quad l \bar{\nu}
 \end{array}$$

In these events, the missing transverse energy \cancel{E}_T corresponds to the energy of the neutrino from W^\pm decay. It is possible to reconstruct the transverse mass M_T of the W^\pm boson, using the transverse momentum vectors of the lepton and the \cancel{E}_T . The first plot in Fig. 9.2 shows this transverse mass distribution for events passing the lepton+jets criteria, both in the data and in SM $t\bar{t}$ Monte Carlo events.

Within the charged Higgs scenario, the lepton+jets channel will be populated with a significant fraction of $t\bar{t}$ events in which one top quark decays to Wb , and the other decays to Hb . If $H^\pm \rightarrow \tau\nu$, the missing energy will no longer correspond to a single neutrino.

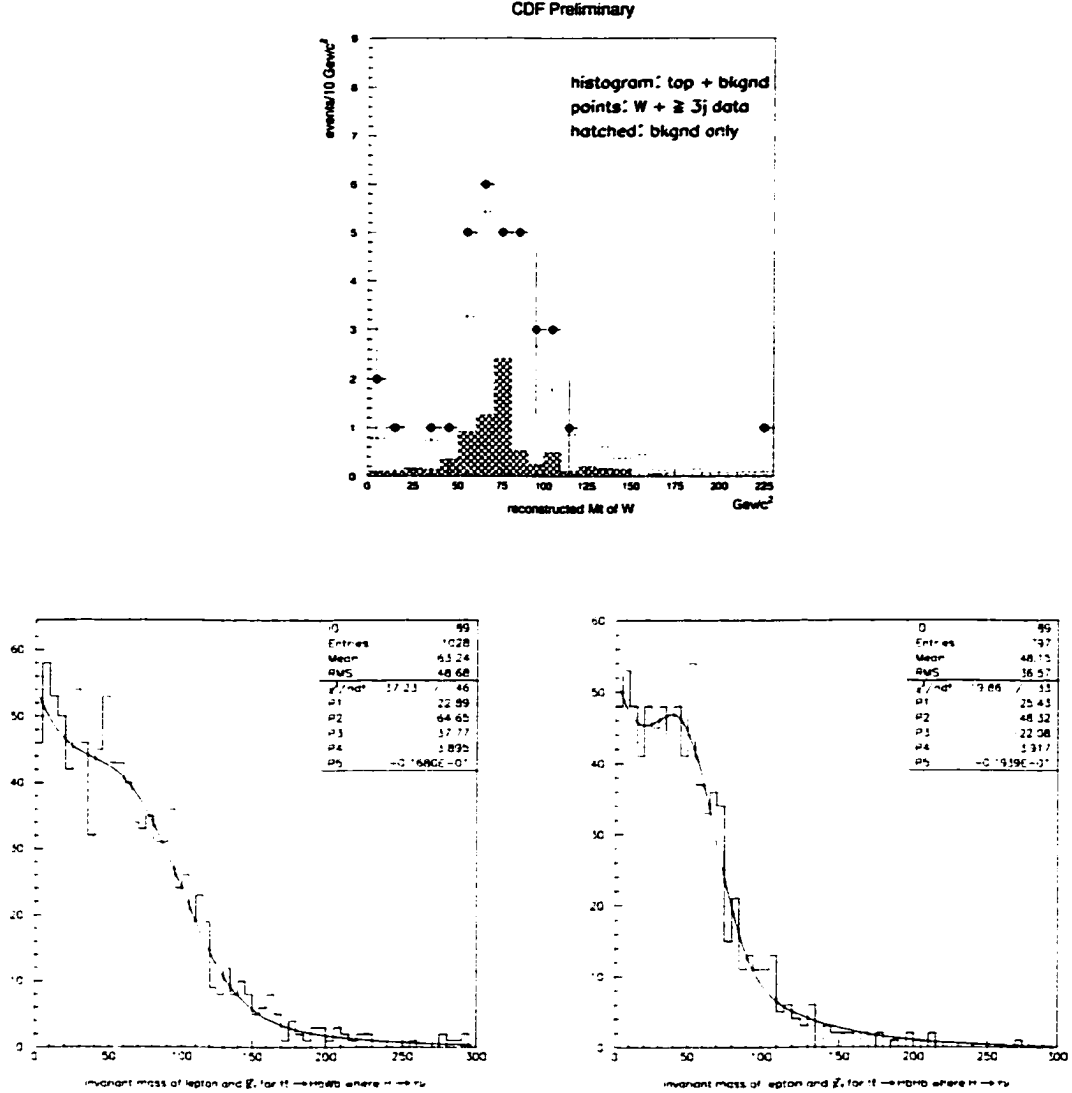
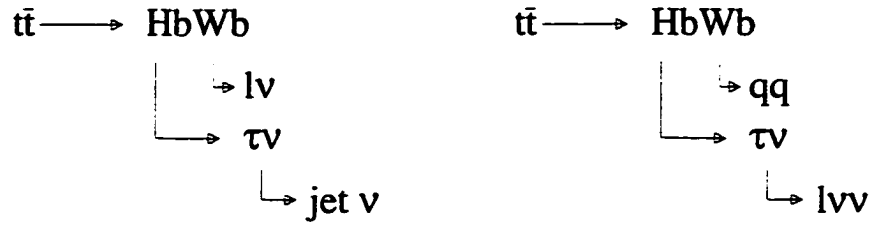


Figure 9.2: Transverse mass M_T formed between the \cancel{E}_T and lepton P_T in lepton+jets events. The upper plot shows the distribution in the data, along with the Monte Carlo prediction for SM $t\bar{t}$ production, and the estimated background contribution from non- $t\bar{t}$ processes. The bottom two plots contain the Monte Carlo M_T distributions for $t\bar{t} \rightarrow HbW\bar{b} \rightarrow \tau\nu bW\bar{b}$ events (left plot) and $t\bar{t} \rightarrow HbH\bar{b} \rightarrow \tau\nu b\tau\nu\bar{b}$ events (right plot).



The bottom two plots in Fig. 9.2 show the transverse mass distribution for $t\bar{t} \rightarrow HbW\bar{b}$ and $t\bar{t} \rightarrow HbH\bar{b}$ events that pass the lepton+jets selection cuts, for $M_{H^\pm} = 80 \text{ GeV}/c^2$. Note that both these distributions are peaked at $M_T = 0 \text{ GeV}/c^2$, in contrast to the expected distribution for the SM decays, which is peaked near $M_T = 80 \text{ GeV}/c^2$.

The observed M_T distribution can be fit to a mixture of the expected background distribution, and a weighted sum of the distributions expected from $t\bar{t} \rightarrow WbW\bar{b}$, $t\bar{t} \rightarrow HbW\bar{b}$, and $t\bar{t} \rightarrow HbH\bar{b}$ decays. I perform a fit for the most likely $\mathcal{B}(t \rightarrow W^\pm b)$ using a log-likelihood technique. Preliminary results for two different charged Higgs masses are given below.

$$\begin{aligned}
 M_{H^\pm} = 80 \text{ GeV}/c^2 & : \quad \mathcal{B}(t \rightarrow Wb) = 1.05^{+0.21}_{-0.24} \\
 M_{H^\pm} = 120 \text{ GeV}/c^2 & : \quad \mathcal{B}(t \rightarrow Wb) = 1.03^{+0.27}_{-0.33}
 \end{aligned}$$

The errors are due to statistical effects alone, which should dominate over the systematic errors. These results indicate that this method is able to exclude $\mathcal{B}(t \rightarrow H^\pm b) \gtrsim 0.60$ at the 95% C.L., for charged Higgs masses in the range of 80-120 GeV/c^2 . This search has the advantage that the results are independent of the absolute value of the $t\bar{t}$ cross section.

One simplification made in this analysis that remains to be justified concerns the exact shape of the M_T distribution for background events from non- $t\bar{t}$ processes.

Most (about 70%) of the background in the lepton+jets channel is expected to originate from the processes with real W^\pm -bosons, such as $Wb\bar{b}$ and $Wc\bar{c}$. For this reason the background distribution for the above fits was assumed to have the same shape as the M_T distribution of $t\bar{t}$ events with one leptonic W^\pm decay. However, including the correct non- $t\bar{t}$ background shape should make only a small difference to the final answer. Limits using this technique should be comparable to those obtained with the direct $H^\pm \rightarrow \tau\nu$ search at CDF.

Appendix A

Partial Widths for the Top Quark and H^\pm

Here I specify the expressions used for the partial widths of the top quark and the H^\pm . As a reminder, the branching fraction for a particular decay mode of a particle is the partial width for that decay mode, divided by the sum of the partial widths for all the possible decay modes of the particle.

A.1 The H^\pm Partial Widths

The partial width for $H^\pm \rightarrow \tau \nu$, which I have derived, is

$$\Gamma_{H^\pm \rightarrow \tau \nu} = \frac{g^2 m_\tau^2 \tan^2 \beta}{32 \pi m_W^2} \left[\frac{M_{H^\pm}^2 - m_\tau^2}{M_{H^\pm}} \right] \approx \frac{g^2 m_\tau^2 \tan^2 \beta M_{H^\pm}}{32 \pi m_W^2} . \quad (\text{A.1})$$

The partial width for $H^\pm \rightarrow cs$ is given in Ref. [38],

$$\Gamma_{H^\pm \rightarrow cs} = \frac{3 g^2 M_{H^\pm} \tan^2 \beta}{32 \pi m_W^2} (\bar{m}_c^2 \cot^2 \beta + \bar{m}_s^2 \tan^2 \beta) . \quad (\text{A.2})$$

This partial width must be corrected for the effect of gluons that can be radiated from the strange and charm quarks, or be exchanged between these quarks. This correction to the width can be absorbed into the quark masses. Thus, in this equation, the charm and strange quark masses \bar{m}_c and \bar{m}_s are the QCD-corrected values, given by Eq. 16 in Ref. [38],

$$\bar{m}_q(\mu) = m_q \left[\frac{\ln(4m_q^2/\Lambda^2)}{\ln(M_{H^\pm}^2/\Lambda^2)} \right]^{1/\beta_0} , \quad (\text{A.3})$$

where $\beta_0 = (33 - 2n_f)/3$. Here, I use the pole mass $m_c = 1.5 \text{ GeV}/c^2$, and I assume that $m_s = 0.30 \text{ GeV}/c^2$ [3]. To calculate the QCD parameter Λ to be used in this

equation, it must be recognized that the QCD corrections are calculated for diagrams with only one loop. Thus, I use the known value of the strong coupling constant at a renormalization scale of the Z^0 mass, $\alpha_s(\mu = M_Z) = 0.119$ [3], and set this equal to the one-loop value of α_s .

$$\alpha_s(\mu = M_Z) = \frac{4\pi}{\beta_0 \ln(\mu^2/\Lambda^2)} \quad (\text{A.4})$$

From this expression, I find that $\Lambda^{(4)} = 0.162 \text{ GeV}/c^2$, needed for calculating \bar{m}_s , and $\Lambda^{(4.5)} = 0.124 \text{ GeV}/c^2$, needed for calculating \bar{m}_c . As an example, for $M_{H^\pm} = 100 \text{ GeV}/c^2$, I find that $\bar{m}_c = 1.03 \text{ GeV}/c^2$ and $\bar{m}_s = 0.140 \text{ GeV}/c^2$.

The partial width for the decay $H^\pm \rightarrow W^\pm b\bar{b}$ [39] has the form [136]

$$\frac{d\Gamma_{H \rightarrow W b \bar{b}}}{dm_{12}^2 dm_{23}^2} = \frac{1}{(2\pi)^3 32 M_{H^\pm}^3} |\mathcal{M}|^2 \quad (\text{A.5})$$

where

$$|\mathcal{M}|^2 = \left(\frac{3g^4 m_t^4 \cot^2 \beta}{4m_W^2 (m_t^2 - m_{23}^2)^2} \right) \times [m_W^2 (m_{13}^2 - 2m_b^{p^2}) + (m_{23}^2 - m_b^{p^2} - m_W^2)(m_{12}^2 - m_b^{p^2} - m_W^2)] \quad (\text{A.6})$$

and m_{12}^2 and m_{23}^2 are the square of the four-momentum transferred to the \bar{b} and b quarks, respectively,

$$m_{12}^2 = (p_{H^\pm} - p_b)^2 \quad (\text{A.7})$$

$$m_{23}^2 = (p_{H^\pm} - p_{\bar{b}})^2 \quad (\text{A.8})$$

$$m_{13}^2 = M_{H^\pm}^2 + 2m_b^{p^2} + m_W^2 - m_{12}^2 - m_{23}^2 \quad (\text{A.9})$$

To find the total partial width, the differential partial width given by Eq. A.5 must be integrated over the two-dimensional phase space in the m_{12}^2 - m_{23}^2 plane, which is shown in Fig. 5.1. There is no QCD correction calculated for this partial width, and m_b^p is the pole mass of $4.7 \text{ GeV}/c^2$.

A.2 The Top Quark Partial Widths

The SM top quark width $\Gamma_{t \rightarrow Wb}$ is given by [38, 45],

$$\begin{aligned} \Gamma_{t \rightarrow Wb} = & \frac{g^2}{64\pi m_t m_W^2} \lambda^{1/2} \left(1, \frac{m_b^2}{m_t^2}, \frac{m_W^2}{m_t^2} \right) \\ & \times [m_W^2 (m_t^2 + m_b^2) + (m_t^2 - m_b^2)^2 - 2m_W^4] \\ & \times (1.0 - 2.5 \alpha_s(\mu = M_{\text{top}})/\pi) \end{aligned} \quad (\text{A.10})$$

$$\text{where} \quad \lambda(a, b, c) = a^2 + b^2 + c^2 - 2ab - 2ac - 2cb$$

The factor of $\lambda^{1/2}$ is a phase-space factor. Since the mass of B -hadrons is about 5 GeV/ c^2 , we expect the phase space factor to go to zero once $M_{\text{top}} - M_{H^\pm} = 5$ GeV/ c^2 . To ensure that this happens, m_b is set to 5 GeV/ c^2 in the factor of $\lambda^{1/2}$. Elsewhere in the expression, the pole mass $m_b^p = 4.7$ GeV/ c^2 is used. The QCD correction to $\Gamma_{t \rightarrow Wb}$ is given by the last term in the product [45], where $\alpha_s(\mu = M_{\text{top}}) = 0.1055$. For $M_{\text{top}} = 175$ GeV/ c^2 , $\Gamma_{t \rightarrow Wb} = 1.41$ GeV.

The expression for the partial width $\Gamma_{t \rightarrow Hb}$ has a similar structure,

$$\begin{aligned} \Gamma_{t \rightarrow Hb} = & \frac{g^2}{64\pi m_t m_W^2} \lambda^{1/2} \left(1, \frac{m_b^2}{m_t^2}, \frac{M_{H^\pm}^2}{m_t^2} \right) \\ & \times [(\tilde{m}_b^2 \tan^2 \beta + m_t^2 \cot^2 \beta)(m_t^2 + \tilde{m}_b^2 - M_{H^\pm}^2) + 4m_t^2 \tilde{m}_b^2] \end{aligned} \quad (\text{A.11})$$

Once again, m_b is set to 5 GeV/ c^2 in the phase-space factor of $\lambda^{1/2}$. However, the QCD correction is taken into account by using \tilde{m}_b , the “running” b -quark mass, for the terms that arise due to the tbH^\pm coupling. This running mass is evaluated at a renormalization scale of M_{top} , $\tilde{m}_b(\mu = 175 \text{ GeV}/c^2) = 3.647$ GeV/ c^2 . The reason for choosing this value is given below. It is very important, because at large values of $\tan \beta$, the partial width $\Gamma_{t \rightarrow Hb}$ is proportional to \tilde{m}_b^2 .

Finally, I will note that these comments, for the partial width $\Gamma_{t \rightarrow Hb}$, also apply to the partial width for the three-body decay $\Gamma_{t \rightarrow \tau \nu b}$. This is given by Eqs. D.20

and D.22 in Appendix D,

$$\Gamma_{t \rightarrow \tau \nu b} = \int d\Gamma_{t \rightarrow \tau \nu b} = \int_{m_\tau}^{m_t - m_b} \frac{d\Gamma_{\text{top}}}{dm_{\tau\nu}} dm_{\tau\nu} \quad (\text{A.12})$$

where

$$\begin{aligned} \frac{d\Gamma}{dm_{\tau\nu}} &= \frac{g^4 m_\tau^2 \tan^2 \beta m_{\tau\nu}}{32^2 \pi^3 m_t m_W^4 [(m_{\tau\nu}^2 - M_{H^\pm}^2)^2 + \Gamma_H^2 m_{\tau\nu}^2]} \times \lambda^{1/2} \left(1, \frac{m_b^2}{m_t^2}, \frac{m_{\tau\nu}^2}{m_t^2}\right) \\ &\times [(\tilde{m}_b^2 \tan^2 \beta + m_t^2 \cot^2 \beta)(m_t^2 + \tilde{m}_b^2 - m_{\tau\nu}^2) + 4m_t^2 \tilde{m}_b^2] [m_{\tau\nu}^2 - m_\tau^2] \\ m_{\tau\nu}^2 &= (p_t - p_b)^2 \end{aligned} \quad (\text{A.13})$$

A.3 The m_b used for the QCD-Corrected $\Gamma_{t \rightarrow Hb}$

This section was written by Michelangelo Mangano.

The partial widths for decays to hadrons, $t \rightarrow H^\pm b$ and $H^\pm \rightarrow cs$, must be corrected for gluon exchange between the quarks, and gluon radiation of these quarks. The first order QCD correction has been calculated in Ref. [38]. The correction is given by Eq. 15 of that reference,

$$\begin{aligned} \Gamma &\rightarrow \Gamma (1 + \Delta) \\ \Delta &= 2\alpha_s / \pi (3/2 - \ln(m_H^2/m_q^2)) \end{aligned} \quad (\text{A.14})$$

This result comes from the loop corrections to the decay width. To know what m_q is, one has to look at the details of the calculation. These are found in Ref. [147] (cited by Ref. [38]), which says that the renormalization is performed for the on-mass-shell scheme. This means that m_q is the pole mass. It turns out that the QCD correction term can be absorbed into the quark mass, by replacing the quark mass with the following expression (Eq. 16 of Ref. [147]).

$$\tilde{m}_q(\mu) = m_q \left[\frac{\ln(4m_q^2/\Lambda^2)}{\ln(\mu^2/\Lambda^2)} \right]^{1/\pi b_0} \quad (\text{A.15})$$

where $b_0 = (33 - 2n_f)/12\pi$, and μ is the renormalization scale. This can be rewritten as follows,

$$\tilde{m}(\mu) = m \exp \left[\frac{1}{\pi b_0} \ln \left(\frac{\ln(4m^2/\Lambda^2)}{\ln(\mu^2/\Lambda^2)} \right) \right] \quad (\text{A.16})$$

Expanded to leading log, this becomes

$$\begin{aligned} \tilde{m}(\mu) &= m \left[1 + \frac{1}{\pi b_0} \ln \left(\frac{\ln(4m^2/\Lambda^2)}{\ln \mu^2/\Lambda^2} \right) \right] \\ &= m \left[1 + \frac{1}{\pi b_0} \ln \left(\frac{\ln(4m^2/\mu^2) + \ln(\mu^2/\Lambda^2)}{\ln \mu^2/\Lambda^2} \right) \right] \\ &= m \left[1 + \frac{1}{\pi b_0} \ln \left(1 + \frac{\ln(4m^2/\mu^2)}{\ln(\mu^2/\Lambda^2)} \right) \right] \\ &= m \left[1 + \frac{1}{\pi b_0} \frac{\ln(4m^2/\mu^2)}{\ln(\mu^2/\Lambda^2)} \right] \\ &= m \left[1 - \frac{\alpha_s(\mu)}{\pi} (\ln(\mu^2/m^2) + \ln 4) \right] \end{aligned} \quad (\text{A.17})$$

where $\alpha_s(\mu) = 1/b_0 \ln(\mu^2/\Lambda^2)$. Squaring this relation, to leading order in α_s ,

$$\Delta = 2\alpha_s/\pi(\ln 4 - \ln(m_H^2/m_q^2)) , \quad (\text{A.18})$$

which corresponds to Eq. A.14, assuming that $\ln 4 = 1.386 \sim 3/2$. Therefore strictly speaking, Eq. A.15 is not the standard running mass (in whose definition the 4 is absent), but something that tries to reproduce also the finite QCD correction. This correction is process dependent - here it appears as part of the mass, but it is really a correction to the top decay width. In other words, we cannot be guaranteed that at higher orders the non-logarithmic corrections to the decay width can be absorbed in the form of a running mass, and whether it gets exponentiated or not has to be proven. It is put in only to ensure that the fixed-order truncation of Eq. A.15 reproduces the exact fixed-order expression in Eq. A.14. The presence of this 4 causes the evaluation of m_q to give a number smaller than the pole mass.

As a result, taking Eq. A.15 at face value would suggest that m_q should be the pole mass (4.5-5 GeV/ c^2). The idea of using the running mass comes from trying to emulate the result of including yet higher order corrections. It could turn out, for example, that Eq. A.15 approximates well the result of the 2-loop calculation provided one uses the running mass instead of the pole mass. Of course it would only be necessary to replace the pole by the running mass in the mass coefficient in front of Eq. A.15, since the change in the arguments of the log would have effects of higher order. While I believe that this is a reasonable expectation, I don't think we should be playing guesses, so I believe it is defensible to use the pole mass in front of Eq. A.15. Using $m_b = 4.7$ GeV/ c^2 (the central value of the range quoted by the PDG) is probably the best choice.

Here follow the results of a numerical study. I calculate the evolved b -quark mass via Eq. A.15, starting from the three mass values 4.5, 4.7 and 4.9 GeV/ c^2 . Two renormalization scales for μ are investigated, $\mu = M_{H^\pm}$ and M_{top} . For $\mu = M_{H^\pm}$ I use the values 120 and 160 GeV/ c^2 . The evolved masses are shown in Table A.1. I study the dependence of these values on Λ . The QCD correction is a one loop correction, so it is best to use $\Lambda_{1\text{loop}}^{(5)}$ for Λ in Eq. A.15. This can be derived by matching the 1-loop value of α_s to the 2-loop value calculated with the measured value $\lambda_{2\text{loop}}^{(5)} = 237$ MeV [3],

$$\alpha_s^{1+2\text{ loop}}(\mu, \lambda_{2\text{loop}}^{(5)}) = \alpha_s^{1\text{ loop}}(\mu, \lambda_{1\text{loop}}^{(5)}) . \quad (\text{A.19})$$

This is done for three different scales ($\mu = 5, 91.2$ and 175 GeV/ c^2) in Table A.1.

The range of values is not very large, and the differences between selecting the value of Λ at the different scales are very small. I choose as a default the value obtained at M_Z , as a fair compromise, and use the renormalization scale of $\mu = M_{\text{top}}$. Thus, I use $m_b = 3.647$ GeV/ c^2 for the Yukawa coupling factor in the expression for $\Gamma_{t \rightarrow Hb}$ (but not for the phase space portion of this partial width).

Λ match at $\mu = 5 \text{ GeV}/c^2$ ($\Lambda=0.107$)			
M_{H^\pm}	m_b	$\tilde{m}(\mu = M_{H^\pm})$	$\tilde{m}(\mu = M_{\text{top}})$
120.0000	4.500000	3.539414	3.444080
160.0000	4.500000	3.466043	3.444080
120.0000	4.700000	3.715600	3.615520
160.0000	4.700000	3.638577	3.615520
120.0000	4.900000	3.892488	3.787643
160.0000	4.900000	3.811798	3.787643
Λ match at $\mu = M_Z$ ($\Lambda=0.0877$)			
M_{H^\pm}	m_b	$\tilde{m}(\mu = M_{H^\pm})$	$\tilde{m}(\mu = M_{\text{top}})$
120.0000	4.500000	3.569027	3.475443
160.0000	4.500000	3.497021	3.475443
120.0000	4.700000	3.745872	3.647650
160.0000	4.700000	3.670298	3.647650
120.0000	4.900000	3.923397	3.820520
160.0000	4.900000	3.844241	3.820520
Λ match at $\mu = 175 \text{ GeV}/c^2$ ($\Lambda=0.0851$)			
M_{H^\pm}	m_b	$\tilde{m}(\mu = M_{H^\pm})$	$\tilde{m}(\mu = M_{\text{top}})$
120.0000	4.500000	3.573348	3.480024
160.0000	4.500000	3.501545	3.480024
120.0000	4.700000	3.750289	3.652344
160.0000	4.700000	3.674930	3.652344
120.0000	4.900000	3.927907	3.825324
160.0000	4.900000	3.848979	3.825324

Table A.1: The QCD-corrected value of m_b , as a function of m_b and renormalization scale μ . All numbers have the units of GeV/c^2 . This is done for three different scales at which $\Lambda_1^{(5)}|_{\text{loop}}$ is derived, used for Λ in Eq. A.15.

Appendix B

Yukawa Couplings for Higgs Bosons

B.1 Standard Model Higgs-Fermion Couplings

Here I continue the discussion in Section 2.3.3. The SM Higgs Boson couples to quarks across generations. As an example, just taking the last term in Eq. 2.14, which corresponds to Higgs couplings to up-type quarks, we substitute $\tilde{\phi} = (v + \eta, 0)/\sqrt{2}$ [30],

$$\begin{aligned}\mathcal{L}_{\text{Yukawa}} &= \sum_{m,n=1}^3 \Gamma_{mn}^u(\bar{u}'_{Lm}, \bar{d}'_{Lm}) \frac{1}{\sqrt{2}} \begin{pmatrix} v + \eta \\ 0 \end{pmatrix} u'_{Rn} + H.C. \\ &= \bar{u}'_L (M^u + h^u \eta) u'_R + H.C.\end{aligned}\tag{B.1}$$

The summation has been replaced by matrix multiplication, in the second step, where $u'_L = (u', c', t')_L$, and $u'_R = (u', c', t')_R$. Also, a up-quark mass matrix M^u and a coupling matrix h^u have been introduced,

$$M_{mn}^u = \Gamma_{mn}^u \frac{v}{\sqrt{2}} \quad \text{and} \quad h_{mn}^u = \frac{1}{v} M_{mn}^u \tag{B.2}$$

In general the Yukawa coupling matrix Γ_{mn}^u , and hence the mass matrix M_{mn}^u , is complex and non-Hermitian [30]. It may be diagonalized by the following transformation

$$A_L^{u\dagger} M^u A_R^u = M_D^u \tag{B.3}$$

where A_L^u and A_R^u are two different 3×3 unitary matrices. To switch from our weak-interaction eigenstate basis to a quark-mass eigenstate basis, we can define

the fields $u_L = (u, c, t)_L$ and $u_R = (u, c, t)_R$ by

$$u'_L = A_L^u u_L, \quad u'_R = A_R^u u_R \quad (\text{B.4})$$

so that the mass and Yukawa terms are diagonalized,

$$\begin{aligned} \bar{u}'_L (M^u + h^u \eta) u'_R + H.C. &= \bar{u}_L (M_D^u + h_D^u \eta) u_R + H.C. \\ &= \bar{u} (M_D^u + h_D^u \eta) u \\ &= (\bar{u}, \bar{c}, \bar{t}) \begin{pmatrix} m_u & 0 & 0 \\ 0 & m_c & 0 \\ 0 & 0 & m_t \end{pmatrix} \left(1 + \frac{g}{2M_W} \eta\right) \begin{pmatrix} u \\ c \\ t \end{pmatrix} \end{aligned}$$

For the first generation only, we have a mass term and a coupling term, analogous to the leptons,

$$\mathcal{L}_{\text{Yukawa up-type quarks}} = m_u \bar{u} u \left(1 + \frac{g}{2M_W} \eta\right) \quad (\text{B.5})$$

Again, we note that the couplings of the Higgs field η are diagonal in flavor. In the two-Higgs-doublet extension to the SM, this does not occur in general. In order to restrict tree-level FCNCs, we must constrain the allowed couplings.

The matrices A_L^u and A_R^u , introduced in Eq. B.3, and the corresponding matrices for the down-type quarks, A_L^d and A_R^d , are related to the CKM matrix. The charged weak currents for quarks are

$$J_{L\mu}^+ = (u', c', t')_L \gamma_\mu \begin{pmatrix} d' \\ s' \\ b' \end{pmatrix}_L = (u, c, t)_L \gamma_\mu A_L^{u\dagger} A_L^d \begin{pmatrix} d \\ s \\ b \end{pmatrix}_L \quad (\text{B.6})$$

By convention, the mixing is ascribed completely to the $T_3 = -1/2$ states [24] by defining $V_{CKM} = A_L^{u\dagger} A_L^d$

$$\begin{pmatrix} d' \\ s' \\ b' \end{pmatrix}_L = V_{CKM} \begin{pmatrix} d \\ s \\ b \end{pmatrix}_L \quad (\text{B.7})$$

so that the weak eigenstates are

$$\begin{pmatrix} u \\ d' \end{pmatrix}_L, \begin{pmatrix} c \\ s' \end{pmatrix}_L, \begin{pmatrix} t \\ b' \end{pmatrix}_L. \quad (\text{B.8})$$

B.2 Couplings of the H^\pm to Fermions

We assume that the doublet Φ_2 gives mass to up-type quarks, and Φ_1 gives mass to down-type quarks and charged leptons. Thus we have

$$\mathcal{L}_{\text{Yukawa}} = \sum_{m=1}^3 \Gamma_{Lm}^\ell \bar{\ell}_m \Phi_1 e_{Rm} + \sum_{m,n=1}^3 \Gamma_{mn}^d \bar{q}'_{Lm} \Phi_1 d'_{Rn} + \sum_{m,n=1}^3 \Gamma_{mn}^d \bar{q}'_{Lm} \tilde{\Phi}_2 u'_{Rn} + H.C. \quad (\text{B.9})$$

As discussed in Section 2.4.3, the most general coupling would have these terms, and terms with Φ_1 exchanged with Φ_2 . However, this would lead to tree-level FCNCs with terms such as $d\bar{s}\phi$, for example. Substituting the physical Higgs states Eqs. 2.33 and 2.34 for Φ_1 and Φ_2 , we find

$$\begin{aligned} \mathcal{L}_{\text{Yukawa}} = & \sum_{m=1}^3 \Gamma_m^\ell (\bar{\nu}_{em}, \bar{e}_{Lm}) \begin{pmatrix} -H^+ \sin\beta \\ v_1 + \sqrt{\frac{1}{2}}(H^0 \cos\alpha - h^0 \sin\alpha - iA^0 \sin\beta) \end{pmatrix} e_{Rm} \\ & + \sum_{m,n=1}^3 \Gamma_{mn}^d (\bar{u}'_{Lm}, \bar{d}'_{Rn}) \begin{pmatrix} -H^+ \sin\beta \\ v_1 + \sqrt{\frac{1}{2}}(H^0 \cos\alpha - h^0 \sin\alpha - iA^0 \sin\beta) \end{pmatrix} d'_{Rm} \\ & + \sum_{m,n=1}^3 \Gamma_{mn}^u (\bar{u}'_{Lm}, \bar{d}'_{Rm}) \begin{pmatrix} v_2 + \sqrt{\frac{1}{2}}(H^0 \sin\alpha + h^0 \cos\alpha - iA^0 \cos\beta) \\ -H^- \cos\beta \end{pmatrix} u'_{Rm} \\ & + H.C. \end{aligned} \quad (\text{B.10})$$

We will be interested only in mass terms, and those terms that involve the coupling of the H^\pm to fermions. The mass term in the Lagrangian is the one proportional to the vacuum expectation values v_1 and v_2 . By introducing the left-handed vectors $e_L = (e, \mu, \tau)_L$, $d_L = (d, s, b)_L$, and $u_L = (u, c, t)_L$, with similar definitions for the

right-handed vectors e_R, d_R and u_R , the mass term can be written as follows,

$$\begin{aligned}
\mathcal{L}_{\text{mass}} &= \bar{e}_L \Gamma^\ell v_1 e_R + \bar{d}_L \Gamma^d v_1 d'_R + \bar{u}_L \Gamma^u v_2 u'_R + H.C. \\
&= \bar{e}_L \Gamma^\ell v_1 e_R + \bar{d}_L A_L^{d\dagger} \Gamma^d v_1 A_R^d d_R + \bar{u}_L A_L^{u\dagger} \Gamma^u v_2 A_R^u u_R + H.C. \\
&= \bar{e}_L M_D^\ell e_R + \bar{d}_L M_D^d d_R + \bar{u}_L M_D^u u_R + H.C. \\
&= \bar{e} M_D^\ell e + \bar{d} M_D^d d + \bar{u} M_D^u u
\end{aligned} \tag{B.11}$$

provided that the diagonal mass matrices $M_D^{\ell,u,d}$ are defined as

$$M_D^\ell = \Gamma^\ell v_1, \quad M_D^d = A_L^{d\dagger} \Gamma^d v_1 A_R^d, \quad M_D^u = A_L^{u\dagger} \Gamma^u v_2 A_R^u. \tag{B.12}$$

The terms in the Lagrangian corresponding to the couplings of the H^\pm to fermions are terms proportional to H^\pm ,

$$\begin{aligned}
\mathcal{L}_{H^\pm ff} &= -\sin\beta \bar{\nu}_L \Gamma^\ell e_R H^+ - \sin\beta \bar{u}_L \Gamma^d d'_R H^+ - \cos\beta \bar{d}_L \Gamma^u u'_R H^- + H.C. \\
&= -\sin\beta \bar{\nu}_L \Gamma^\ell e_R H^+ - \sin\beta \bar{u}_L A_L^{u\dagger} \underbrace{A_L^d A_L^{d\dagger}}_1 \Gamma^d A_R^d d_R H^+ \\
&\quad - \cos\beta \bar{d}_L A_L^{d\dagger} \underbrace{A_L^u A_L^{u\dagger}}_1 \Gamma^u A_R^u u_R H^- + H.C.
\end{aligned} \tag{B.13}$$

We express the matrices in this equation in terms of the diagonal mass matrices M_D given in eq. B.12. Also, we recognize that $A_L^{u\dagger} A_L^d = V_{CKM}$ (see Section B.1). The H^+ coupling term becomes

$$\begin{aligned}
\mathcal{L}_{H^+ ff} &= -\frac{\sin\beta}{v_1} \bar{\nu}_L M_D^\ell e_R H^+ - \frac{\sin\beta}{v_1} \bar{u}_L V_{CKM} M_D^d d_R H^+ \\
&\quad - \frac{\cos\beta}{v_2} \bar{d}_L V_{CKM}^\dagger M_D^u u_R H^- + H.C.
\end{aligned} \tag{B.14}$$

Substituting $v_1 = \sqrt{2} v \cos\beta$, $v_2 = \sqrt{2} v \sin\beta$, and $v = 2M_W/g$, we find

$$\begin{aligned}
\mathcal{L}_{H^\pm ff} &= -\frac{g \tan\beta}{2\sqrt{2}M_W} [\bar{\nu}(1 + \gamma^5) M_D^\ell e H^+ + \bar{e}(1 - \gamma^5) \nu H^-] \\
&\quad - \frac{g \tan\beta}{2\sqrt{2}M_W} [\bar{u} V_{CKM} (1 + \gamma^5) M_D^d d H^+ + \bar{d} V_{CKM}^\dagger (1 - \gamma^5) M_D^d u H^-] \\
&\quad - \frac{g \cot\beta}{2\sqrt{2}M_W} [\bar{d} V_{CKM}^\dagger (1 + \gamma^5) M_D^u u H^- + \bar{u} V_{CKM} (1 - \gamma^5) M_D^u d H^+]
\end{aligned} \tag{B.15}$$

To summarize, the H^\pm couplings to fermion pairs are given by

$$\begin{aligned}
 \mathcal{L}_{e_i \nu_i H^+} &= -\frac{g \tan \beta}{2\sqrt{2}M_W} m_{ei} \nu_i (1 + \gamma^5) e_i H^+ \\
 \mathcal{L}_{\bar{u}_i d_i H^+} &= -\frac{g \{V_{CKM}\}_{ij}}{2\sqrt{2}M_W} \bar{u}_i [(1 - \gamma^5) m_i^u \cot \beta + (1 + \gamma^5) m_j^d \tan \beta] d_j H^+ \\
 \mathcal{L}_{\bar{d}_i u_i H^-} &= -\frac{g \{V_{CKM}^*\}_{ji}}{2\sqrt{2}M_W} \bar{d}_i [(1 - \gamma^5) m_i^d \tan \beta + (1 + \gamma^5) m_j^u \cot \beta] u_j H^-
 \end{aligned}$$

Appendix C

The Fermilab Tevatron

The Tevatron is the highest-energy proton-antiproton ($p\bar{p}$) collider in the world, located at the Fermi National Accelerator Laboratory (Fermilab) in Batavia, Illinois. It is a 1 km radius superconducting synchrotron that performs the last of five separate stages of acceleration in order to produce beams of protons (p) and antiprotons (\bar{p}) that collide at a center-of-mass energy of 1800 GeV, or 1.8 TeV. The Fermilab Accelerator Complex, shown in Fig. C.1, consists of five accelerators (Cockcroft-Walton, Linac, Booster, Main Ring, and the Tevatron), as well as two storage rings (the antiproton Debuncher and Accumulator). Each accelerator in the chain boosts the energy of particles received before passing them off to the next stage. Below, I describe how these individual systems work together to produce counter-rotating beams of protons and antiprotons with 900 GeV of energy each. The acceleration of protons and antiprotons differs significantly, so I describe these processes separately.

C.1 Proton Acceleration

Protons originate from a bottle of hydrogen gas that is ionized to create H^+ ions. These ions are produced at a cathode, extracted through an anode aperture, and accelerated through an extraction plate to 18 keV. The ions are injected into a Cockcroft-Walton electrostatic accelerator where they travel through a potential drop of 750 kV. The maximum voltage, and hence energy, achievable with this

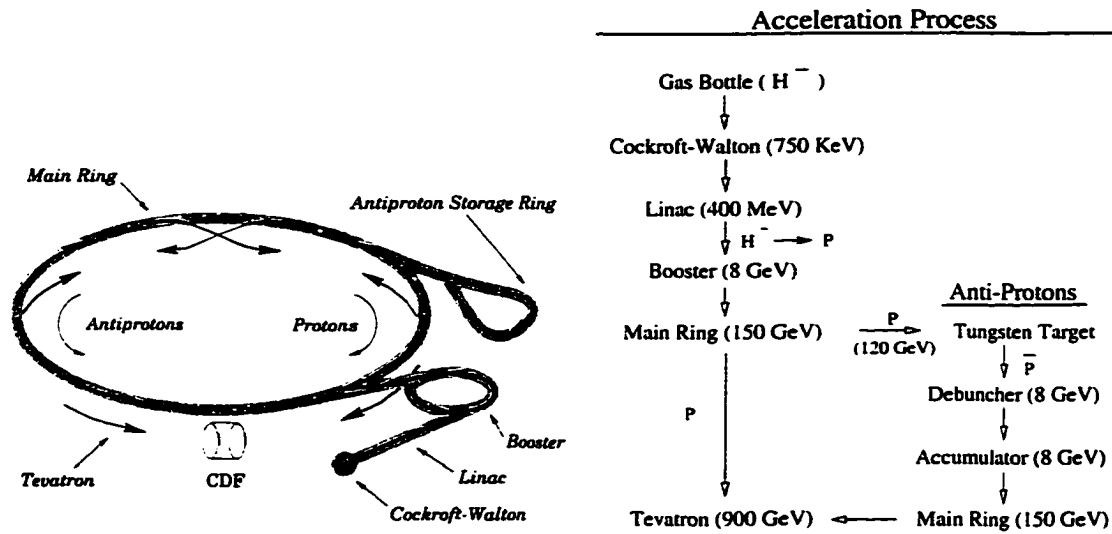


Figure C.1: The Tevatron accelerator complex, and a summary of the steps in the acceleration process of protons and antiprotons.

type of accelerator is limited by the ability of the high-voltage terminal to hold its potential without sparking to its surroundings [148]. This device produces a pulsed beam of 750 keV H^- ions every 67 ms (15 Hz), which is transported 10 m and injected into a two-stage linear accelerator called the Linac.

The Linac increases the ion energy to 401.5 MeV. The first stage of the Linac is an Alvarez accelerator, consisting of 5 radio frequency (RF) electromagnetic cavities resonating at about 201 MHz. Within each cylindrical cavity are a series of collinear conducting drift tubes, alternating in polarity, and separated by small gaps. An RF standing wave with a longitudinal component moves the particles along the axis of the drift tubes. The drift tubes are arranged so that a group of protons will cross the centers of the gaps at the same time that the field across the gap is approximately maximum, which causes the particles to accelerate across the gap [89]. By the time the field decreases and switches polarity the protons have entered the drift tubes and are shielded, so they drift at a constant velocity. To

keep the ions in phase with the accelerating field as their velocity increases, the drift tube length increases, so that the travel time between gaps remains equal to the period of the RF field. When this length becomes equal to half the RF wavelength, the drift tubes act like antennas that radiate the field needed to accelerate the ions, limiting the energy imparted to the ions. The first stage of the Linac reaches an energy of 116 MeV.

The second stage of the Linac is a side-coupled accelerator consisting of seven RF cavities resonating at approximately 804 MHz. This type of accelerator produces a traveling wave that moves along with the ions, so that the field is always in phase with the beam [148]. Thus, drift tube lengths do not increase with distance, in contrast to the Alvarez design. This second stage raises the energy of the ion beam to about 401 MeV. The Linac has the same 67 ms cycle time as the Cockcroft-Walton accelerator.

The H^- ions are then transferred from the Linac to the Booster. They are merged with protons already in the Booster by passing both beams through a dogleg, which consists of two adjacent dipole magnets of opposite polarity [83]. The combined beam is then passed through a carbon foil, which strips the two electrons from the H^- ions. Next, the beam is passed through another dogleg, which restores the protons to the Booster path, while directing remaining H^- ions, H atoms, and anything else to a beam dump. This charge-exchange process is a non-conservative action and allows the two beams to be merged, an act that would otherwise violate Liouville's theorem [149].

The Booster is a 75.5 m radius proton synchrotron with 96 dipole and quadrupole magnets and 17 RF cavities. It bends the beam in a circle, so that it passes through each RF cavity many times, in contrast to a linear design where each cavity is only used once. The dipole magnets are used to keep the protons in their circular path for $\approx 20,000$ revolutions needed to accelerate the protons to 8 GeV.

The acceleration takes about 33 ms, and like the Cockcroft-Walton and Linac, the Booster cycles every 67 ms. With an RF frequency of 52.8 MHz, the Booster provides 84 regions of stable acceleration, referred to as “buckets”. The group of protons in each bucket are referred to as a “bunch”, and all the protons together in the Booster are referred to as a “batch” [150]. When injecting these proton bunches into the Main Ring, at least one is lost during the time when the injection magnet is turned on. When the protons are to be used for $p\bar{p}$ collisions in the Tevatron, 15 of the bunches are injected. However, when the protons are to be used by the Antiproton Source, all 83 bunches are injected into the Main Ring.

The Main Ring is a larger proton synchrotron with a 1 km radius, containing 1113 RF buckets and operating at a frequency of 53 MHz. It is composed of 774 dipole magnets, 240 quadrupole magnets, and 18 RF cavities. The dipole magnets maintain a circular orbit in the Main Ring, while the quadrupole magnets alternatively focus and defocus the beam to contain it in stable oscillations about the ideal closed orbit. For collider operation, the Main Ring accelerates the train of 15 bunches from 8 to 150 GeV before coalescing them into a single bunch occupying the central bucket of the train. Once coalesced, the bunch is “cogged”, or rotated in phase in the Main Ring to match the desired Tevatron bucket for injection. Once inside the Tevatron, which is the final stage of acceleration, the bunch awaits five more proton bunches and six antiproton bunches. A typical proton bunch contains about 150×10^9 protons, while antiproton bunches typically contain about one-third as many antiprotons. Before describing the Tevatron, I will describe the acceleration process for antiprotons, which are produced initially by colliding Main Ring protons with a fixed target.

C.2 Antiproton Acceleration

The most efficient means of making antiprotons is to bombard a target with a proton beam and collect the resulting secondary particles of the collision. At Fermilab, only about 10^7 antiprotons are produced for every bunch of 10^{12} protons striking the target. In order to obtain about 10^{12} protons required for collisions in the Tevatron, it is necessary to “stack” successive pulses of antiprotons into the same beam over several hours until a sufficient number are accumulated. Thus the Antiproton Source at Fermilab is comprised of a target station that protons collide into, two storage synchrotrons called the Debuncher and Accumulator, and the transport lines between these rings and the Main Ring.

Protons are accelerated to 120 GeV in the Main Ring using the process described above, and then directed onto a Nickel target. Antiprotons with 8 GeV of energy, chosen to be equal to the Main Ring injection energy, are extracted from the debris, and collected for storage. A Main Ring energy of 120 GeV is used, rather than the 150 GeV used for proton injection into the Tevatron, as the optimal compromise between 8 GeV antiproton production rate, high repetition rate, constraints from the transport lines, and Main Ring operating cost [151].

Before transferring the protons to the target station, the Main Ring RF cavities are manipulated in order to narrow the bunches in time (or azimuthal spread), which simultaneously increases their momentum spread in accordance with Liouville’s Theorem. This slight smearing in momentum has a negligible effect on the momentum distribution of the antiprotons produced at the target. However, the narrow time spread of the protons is transferred to the antiprotons produced at the target, maximizing their phase space density and lessening the demands of the the antiproton storage rings.

Figure C.2 shows a diagram of the target station. The target is composed of

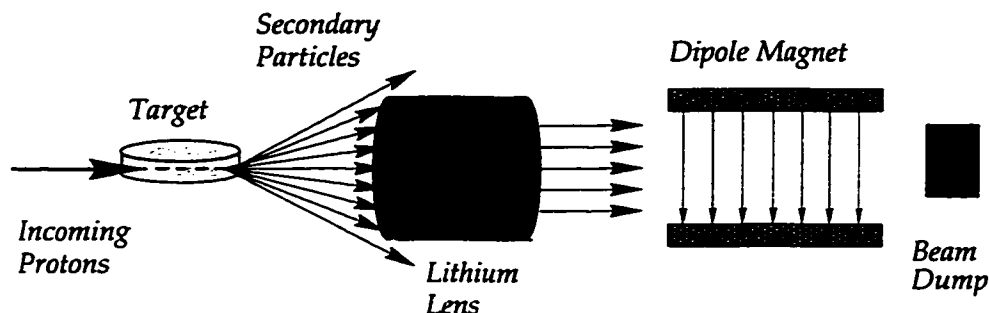


Figure C.2: The proton target station.

nickel disks 10 cm in diameter and 2 cm thick, interleaved with copper disks for cooling purposes. The target translates horizontally in order to tune the proton path length, and thus the \bar{p} flux, and also rotates to evenly distribute heat and radiation damage to the disk. A cylindrical lithium lens with a 2 cm diameter and 15 cm length is used to focus the \bar{p} 's into a parallel beam; this is accomplished with a 750 T/m radial gradient produced by a 0.5 MA current along the axis of the cylinder. Lithium is used since it is the least dense conductor, which limits absorption and multiple scattering of the \bar{p} 's. The \bar{p} beam passes through a 1.5 T dipole magnet that deflects 8 GeV negatively charged particles toward the Antiproton Storage Ring, while deflecting other particles into a beam dump.

The Antiproton Storage Ring confines the \bar{p} 's to a rounded triangular synchrotron with a mean radius of 90 m. It does not accelerate the antiprotons to energies higher than the injection energy of 8 GeV. To maximize the \bar{p} flux, the phase space density of the beam is increased using a technique called stochastic cooling first proposed by van der Meer. To be effective, this technique requires the injected beam to have a small transverse area and momentum spread [151]. However, as previously mentioned, this is not satisfied by the antiproton beam from the target station. Thus the Antiproton storage ring consists of *two* synchrotrons. The first is the Debuncher, which accepts pulses of antiprotons from the target

station and reduces their momentum spread. This allows for efficient momentum cooling in the next synchrotron, the Accumulator. The Accumulator stores \bar{p} 's until enough have been collected to be injected into the Tevatron, via the Main Ring, for $p\bar{p}$ collisions. The Accumulator is about 6% smaller than the Debuncher, and lies just inside it, in the same tunnel.

The Debuncher has the same bunch structure as the Main Ring, and is phase locked to it. To reduce the \bar{p} momentum spread, the Debuncher performs RF manipulations on the beam, and then adiabatically debunches it into a continuous ribbon of antiprotons stretching across 84 buckets, separated by a gap of 6 buckets. These two processes take about 10 ms to complete. Since the Debuncher is on the same cycle as the Main Ring (2.4 sec for \bar{p} production), time remains to reduce the transverse size of the beam and further reduce its momentum spread.

The gap in the antiproton ribbon allows the Debuncher to inject the particles into the Accumulator without \bar{p} loss, since the extraction magnet is turned on as the gap passes by. The Accumulator stores antiprotons in a process referred to as “stacking”, which consists of moving the injected \bar{p} 's in towards a core orbit of about 60 MeV less than the injection orbit, and further reducing the momentum spread and transverse area of the core by stochastic cooling [151].

Stochastic cooling is accomplished through a feedback mechanism that senses the root-mean-square (RMS) deviation of the beam from the central orbit, using electrostatic plates placed at a particular location in the beam path. This information is transmitted across the synchrotron to another set of plates, in time to correct the slope back towards the central orbit once the same portion of beam comes around [93].

When enough antiprotons ($\approx 10^{12}$) are stacked into the accumulator, a portion of the stack is extracted into eleven RF buckets of the Main Ring, which are then accelerated to 150 GeV, coalesced, cogged, and injected into the Tevatron.

Roughly half the antiprotons are used in the six antiproton bunches injected into the Tevatron.

C.3 $p\bar{p}$ Tevatron Collisions

The Tevatron is a $p\bar{p}$ colliding beam synchrotron, the first to use superconducting dipole magnets. The use of superconducting magnet coils eliminates the power lost due to resistive heating of coils, characteristic of conventional dipole magnets, and the resulting monetary savings more than make up for the cost of cooling the magnets with liquid helium to 4 K. The Tevatron lies 65 cm below the Main Ring, in the same 1 km radius tunnel. It is comprised of 774 dipole magnets and 216 quadrupoles, similar in number to the Main Ring, and shares the same 53 MHz, 1113 bucket structure. Bunches are separated by 186 or 187 buckets, which corresponds to about $3.5 \mu\text{s}$.

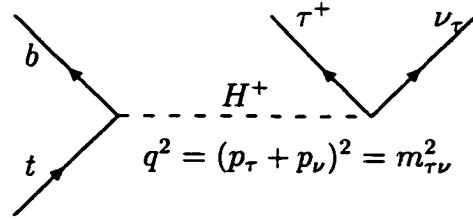
Once the six proton and six antiproton bunches are injected into the Tevatron, the energy is ramped from 150 to 900 GeV in several seconds. The two beams circulate in the same beam pipe, but in opposite directions, and are kept separated most of the time by electrostatic separators in order to increase the beam lifetime. Once the 900 GeV energy is reached, special pairs of quadrupole magnets in each of the CDF and DØ experimental halls are activated to force the two beams to collide at the center (called the interaction point, or IP) of each detector. At each IP, the beam spot size is about $\sigma_{x,y} = 25 \mu\text{m}$ in the transverse plane [82], in order to maximize the luminosity at this point. The bunches have an approximately Gaussian longitudinal profile of about 30 cm. The final phase of the acceleration process involves “scraping” the beam to remove the halo of particles orbiting outside an acceptable radius from the ideal orbit. Such particles can collide with residual gas in the beam pipe and produce background flux in the experimental halls. After

scraping, CDF activates its data acquisition system.

The entire period between bunch injection into the Tevatron and the beam dumping is called a “store”. A store continues until the luminosity drops significantly or until it is lost due to a mishap such as a magnet failure. In Run 1, a store would typically last about 12 hours. When the antiproton stack is sufficient, and the luminosity in the Tevatron is low, the beam in the Tevatron is dumped so new bunches can be injected. Usually about 20 minutes of quiet time follows, during which CDF performs detector calibration. It usually takes at least another hour and a half for injection, cogging and scraping to be completed, making it a minimum of about 2 hours before the data acquisition can be activated between stores. Aside from maintenance periods and access into the collision halls for accelerator repairs, the accelerator complex usually operates 24 hours a day.

Appendix D

The Decay Rate $\Gamma(t \rightarrow H^{+*}b \rightarrow \tau^+\nu b)$



D.1 Setting up the Matrix Element

We calculate the matrix element and the decay rate for the three body top decay shown above. The H^+ acts as a propagator, which contributes a term

$$\frac{i}{m_{\tau\nu}^2 - M_{H^\pm}^2 + i\Gamma_H m_{\tau\nu}}, \quad \text{where } \Gamma_H = \frac{g^2 m_\tau^2 m_{\tau\nu} \tan^2 \beta}{32\pi m_W^2}. \quad (\text{D.1})$$

Here, $m_{\tau\nu}^2 = (p_t - p_b)^2 = (p_\tau + p_\nu)^2$ is the momentum-squared transferred to the τ - ν pair, and is the effective $M_{H^\pm}^2$ of the decay. Note that since Γ_H is itself is proportional to M_{H^\pm} , it exhibits a $m_{\tau\nu}$ dependence when it appears in the denominator of the propagator. The tbH^+ and $H^+\tau^+\nu$ vertex factors,

$$\frac{ig}{2\sqrt{2}m_W} [m_b \tan\beta(1 + \gamma_5) + m_t \cot\beta(1 - \gamma_5)], \quad \frac{ig}{2\sqrt{2}m_W} m_\tau \tan\beta(1 + \gamma_5) \quad (\text{D.2})$$

are derived from the Yukawa coupling of the H^+ to fermions in the Lagrangian.

Putting these factors together, the matrix element for the decay is

$$\begin{aligned} -i\mathcal{M} = & -\frac{g^2}{8m_W^2} \times \frac{i}{m_{\tau\nu}^2 - M_{H^\pm}^2 + i\Gamma_H m_{\tau\nu}} \\ & \times \bar{u}(b) [m_b \tan\beta(1 + \gamma_5) + m_t \cot\beta(1 - \gamma_5)] u(t) \\ & \times \bar{u}(\nu) [m_\tau \tan\beta(1 + \gamma_5)] \bar{\nu}(\tau). \end{aligned} \quad (\text{D.3})$$

The spin-averaged matrix element is

$$\begin{aligned}
\langle |\mathcal{M}|^2 \rangle &= \frac{g^4 m_\tau^2 \tan^2 \beta}{64 m_W^4 [(m_{\tau\nu}^2 - M_{H^\pm}^2)^2 + \Gamma_H^2 m_{\tau\nu}^2]} \times \frac{1}{2} \sum_{\text{final spins}} \\
&\quad (\bar{u}(b)[m_b \tan \beta (1 + \gamma_5) + m_t \cot \beta (1 - \gamma_5)] u(t)) \\
&\quad \times (\bar{u}(b)[m_b \tan \beta (1 + \gamma_5) + m_t \cot \beta (1 - \gamma_5)] u(t))^* \\
&\quad \times [\bar{u}(\nu)(1 + \gamma_5) \bar{\nu}(\tau)] [\bar{u}(\nu)(1 + \gamma_5) \bar{\nu}(\tau)]^* .
\end{aligned} \tag{D.4}$$

The factor of 1/2 in front of the summation sign is the average taken over the initial-state spins of the top quark, and the summation itself is to be performed over the spins of the outgoing particles, the τ and ν . Trace theorems help to evaluate this sum [152],

$$\langle |\mathcal{M}|^2 \rangle = \frac{g^4 m_\tau^2 \tan^2 \beta}{64 m_W^4 [(m_{\tau\nu}^2 - M_{H^\pm}^2)^2 + \Gamma_H^2 m_{\tau\nu}^2]} \times \frac{1}{2} \times \text{Tr}_1 \times \text{Tr}_2 \tag{D.5}$$

where

$$\begin{aligned}
\text{Tr}_1 &= \text{Tr}[(m_b \tan \beta (1 + \gamma_5) + m_t \cot \beta (1 - \gamma_5))(\not{t} + m_t) \\
&\quad \times \overline{[(m_b \tan \beta (1 + \gamma_5) + m_t \cot \beta (1 - \gamma_5))(\not{t} + m_b)}] \tag{D.6}
\end{aligned}$$

$$\text{Tr}_2 = \text{Tr}[(1 + \gamma_5)(\not{\tau} - m_\tau)(1 + \gamma_5)\not{\nu}] . \tag{D.7}$$

D.2 Evaluating the Traces

To evaluate the traces, we use trace theorems, and also recall that

$$\begin{aligned}
\overline{(1 + \gamma_5)} &= \gamma^0 (1 + \gamma_5)^\dagger \gamma^0 = (1 - \gamma_5) \\
\overline{(1 - \gamma_5)} &= \gamma^0 (1 - \gamma_5)^\dagger \gamma^0 = (1 + \gamma_5) .
\end{aligned}$$

Tr₁

$$\begin{aligned}
\text{Tr}_1 &= \text{Tr} \{ [(m_b \tan \beta (1 + \gamma_5) \not{t} + m_b m_t \tan \beta (1 + \gamma_5) \\
&\quad + m_t \cot \beta (1 - \gamma_5) \not{t} + m_t^2 \cot \beta (1 - \gamma_5)] \\
&\quad \times [m_b \tan \beta (1 - \gamma_5) \not{t} + m_b^2 \tan \beta (1 - \gamma_5) \\
&\quad + m_t \cot \beta (1 + \gamma_5) \not{t} + m_b m_t \cot \beta (1 + \gamma_5)] \} \\
&= \text{Tr} \{ m_b^2 \tan^2 \beta (1 + \gamma_5) \not{t} (1 - \gamma_5) \not{t} + m_b^3 \tan^2 \beta (1 - \gamma_5) \not{t} (1 - \gamma_5) \\
&\quad + m_b m_t (1 + \gamma_5) \not{t} (1 + \gamma_5) \not{t} + m_b^2 m_t (1 + \gamma_5) \not{t} (1 + \gamma_5) \\
&\quad + m_b^2 m_t \tan^2 \beta (1 + \gamma_5) (1 - \gamma_5) \not{t} + m_b^3 m_t \tan^2 \beta (1 + \gamma_5) (1 - \gamma_5) \\
&\quad + m_b m_t^2 (1 + \gamma_5) (1 + \gamma_5) \not{t} + m_b^2 m_t^2 (1 + \gamma_5) (1 + \gamma_5) \\
&\quad + m_t m_b (1 - \gamma_5) \not{t} (1 - \gamma_5) \not{t} + m_t m_b^2 (1 - \gamma_5) \not{t} (1 - \gamma_5) \\
&\quad + m_t^2 \cot^2 \beta (1 - \gamma_5) \not{t} (1 + \gamma_5) \not{t} + m_t^2 m_b \cot^2 \beta (1 - \gamma_5) \not{t} (1 + \gamma_5) \\
&\quad + m_t^2 m_b (1 - \gamma_5) (1 - \gamma_5) \not{t} + m_t^2 m_b^2 (1 - \gamma_5) (1 - \gamma_5) \\
&\quad + m_t^3 \cot^2 \beta (1 - \gamma_5) (1 + \gamma_5) \not{t} + m_t^3 m_b \cot^2 \beta (1 - \gamma_5) (1 + \gamma_5) \}
\end{aligned} \tag{D.8}$$

$$\begin{aligned}
&= 8m_b^2 \tan^2 \beta (t \cdot b) + 0 + 0 + 0 + 0 + 0 + 0 + 8m_b^2 m_t^2 + \\
&\quad 0 + 0 + 8m_t^2 \cot^2 \beta (t \cdot b) + 0 + 0 + 8m_t^2 m_b^2 + 0 + 0
\end{aligned} \tag{D.9}$$

$$= 8 [2m_t^2 m_b^2 + m_b^2 \tan^2 \beta (t \cdot b) + m_t^2 \cot^2 \beta (t \cdot b)] \tag{D.10}$$

Tr₂

$$\text{Tr}_2 = \text{Tr} [(1 + \gamma_5) (\not{t} - m_\tau) (1 - \gamma_5) \not{t}]$$

$$\begin{aligned}
&= \text{Tr} \left[(1 + \gamma_5) \not{\tau} (1 - \gamma_5) \not{\nu} - (1 + \gamma_5) (m_\tau) (1 - \gamma_5) \not{\nu} \right] \\
&= \text{Tr} \left[2(1 + \gamma_5) \not{\tau} \not{\nu} \right] \\
&= 8(\tau \cdot \nu)
\end{aligned} \tag{D.11}$$

$$\begin{aligned}
\langle |\mathcal{M}|^2 \rangle &= \frac{g^4 m_\tau^2 \tan^2 \beta}{64 m_W^4 [(m_{\tau\nu}^2 - M_{H^\pm}^2)^2 + \Gamma_H^2 m_{\tau\nu}^2]} \\
&\times \frac{1}{2} \times 64 [(m_b^2 \tan^2 \beta + m_t^2 \cot^2 \beta)(t \cdot b) + 2m_t^2 m_b^2] [(\tau \cdot \nu)] \tag{D.12}
\end{aligned}$$

D.3 The Decay Rate

We follow the treatment given in Ref. [136] for three-body decays. The decay rate can be written in terms of the following two variables.

$$m_{\tau\nu}^2 = (p_t - p_b)^2 = m_t^2 + m_b^2 - 2p_t \cdot p_b \tag{D.13}$$

$$m_{23}^2 = (p_t - p_\nu)^2 \tag{D.14}$$

Using the following relations,

$$p_t \cdot p_b = \frac{m_t^2 + m_b^2 - m_{\tau\nu}^2}{2}, \quad m_{\tau\nu}^2 = m_\tau^2 + 2p_\tau \cdot p_\nu \tag{D.15}$$

the spin-averaged matrix element can be written as

$$\begin{aligned}
\langle |\mathcal{M}|^2 \rangle &= \frac{g^4 m_\tau^2 \tan^2 \beta}{8 m_W^4 [(m_{\tau\nu}^2 - M_{H^\pm}^2)^2 + \Gamma_H^2 m_{\tau\nu}^2]} \times \\
&[(m_b^2 \tan^2 \beta + m_t^2 \cot^2 \beta)(m_t^2 + m_b^2 - m_{\tau\nu}^2) + 4m_t^2 m_b^2] [m_{\tau\nu}^2 - m_\tau^2].
\end{aligned} \tag{D.16}$$

Note that since H^+ is a scalar, the matrix element only depends on $m_{\tau\nu}^2$, which is the effective mass-squared of the H^+ . The differential decay rate is given by

$$d\Gamma = \frac{1}{(2\pi)^3} \frac{1}{32m_t^3} \langle |\mathcal{M}|^2 \rangle dm_{\tau\nu}^2 dm_{23}^2. \tag{D.17}$$

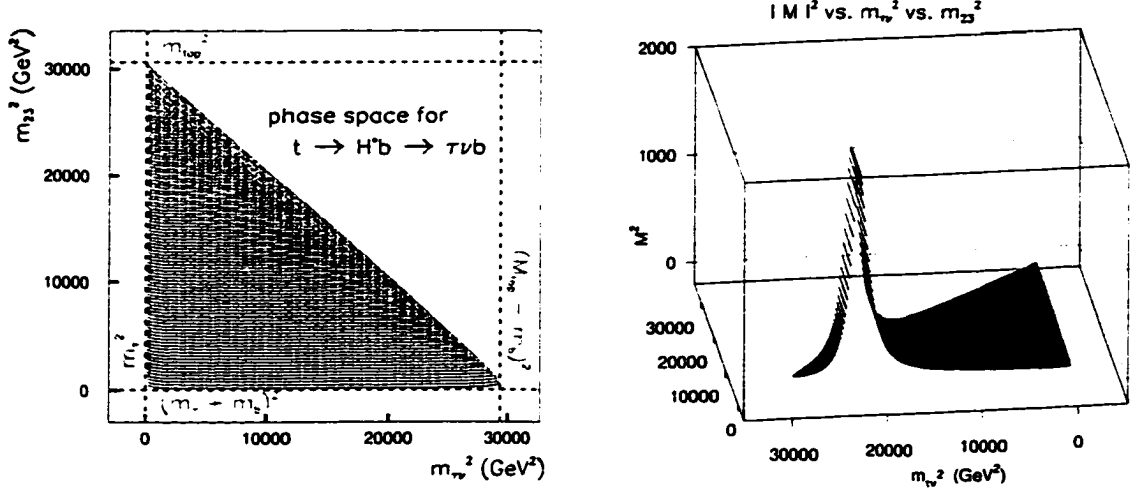


Figure D.1: On the left is the phase space in the m_{23}^2 vs. $m_{\tau\nu}^2$ plane for the three-body decay $t \rightarrow H^*b \rightarrow \tau\nu b$. On the right is the matrix element squared $\langle |\mathcal{M}|^2 \rangle$ shown above this plane for $M_{H^\pm} = 150 \text{ GeV}/c^2$ and $\tan\beta = 150$. The matrix element is peaked around $m_{\tau\nu}^2 = M_{H^\pm}^2$.

D.4 Phase Space

The phase space is a region in the $m_{\tau\nu}^2$ - m_{23}^2 plane. The decay rate is found by integrating $d\Gamma$ over this phase space, which gets weighted by a constant times the probability amplitude $\langle |\mathcal{M}|^2 \rangle$. For a given value of $m_{\tau\nu}^2$, the upper and lower bounds for m_{23}^2 are given by its value when \vec{p}_τ is parallel or antiparallel to \vec{p}_b . The difference between the upper and lower range of integration for the variable m_{23}^2 is a function of $m_{\tau\nu}^2$ [136],

$$\begin{aligned} \Delta(m_{23}^2) &= \frac{1}{m_{\tau\nu}^2} \sqrt{[(m_{\tau\nu}^2 - m_\tau^2)^2] \times [(m_{\tau\nu}^2 - m_b^2 - m_{\text{top}}^2)^2 - (2m_b m_{\text{top}})^2]} \\ &= \frac{(m_{\tau\nu}^2 - m_\tau^2)}{m_{\tau\nu}^2} \lambda^{1/2}(m_t^2, m_b^2, M_{H^\pm}^2) \end{aligned}$$

$$= \frac{(m_{\tau\nu}^2 - m_\tau^2)}{m_{\tau\nu}^2} m_t^2 \lambda^{1/2} \left(1, \frac{m_b^2}{m_t^2}, \frac{M_{H^\pm}^2}{m_t^2}\right) \quad (\text{D.18})$$

$$\text{where } \lambda(a, b, c) = a^2 + b^2 + c^2 - 2ab - 2ac - 2cb.$$

The plane of integration in the $m_{23}^2 - m_{\tau\nu}^2$ plane is shown in Figure D.1, along with the matrix element $\langle |\mathcal{M}|^2 \rangle$.

D.5 Predicted M_{H^\pm} Distribution

We can immediately perform the integral of $d\Gamma$ over dm_{23}^2 since $\langle |\mathcal{M}|^2 \rangle$ doesn't depend on m_{23}^2 . Eq. D.17 can be written

$$\frac{d\Gamma}{dm_{\tau\nu}} = \frac{1}{(2\pi)^3} \frac{1}{32m_t^3} \langle |\mathcal{M}|^2 \rangle \Delta m_{23}^2 2m_{\tau\nu} \quad (\text{D.19})$$

By substituting Eq. D.16 for $\langle |\mathcal{M}|^2 \rangle$ and Eq. D.18 for Δm_{23}^2 , we obtain a differential decay rate for $t \rightarrow \tau\nu b$,

$$\begin{aligned} \frac{d\Gamma}{dm_{\tau\nu}} &= \frac{g^4 m_\tau^2 \tan^2 \beta m_{\tau\nu}}{32^2 \pi^3 m_t m_W^4 [(m_{\tau\nu}^2 - M_{H^\pm}^2)^2 + \Gamma_H^2 m_{\tau\nu}^2]} \times \lambda^{1/2} \left(1, \frac{m_b^2}{m_t^2}, \frac{m_{\tau\nu}^2}{m_t^2}\right) \\ &\times [(m_b^2 \tan^2 \beta + m_t^2 \cot^2 \beta)(m_t^2 + m_b^2 - m_{\tau\nu}^2) + 4m_t^2 m_b^2] [m_{\tau\nu}^2 - m_\tau^2]. \end{aligned} \quad (\text{D.20})$$

This gives an expected distribution for $m_{\tau\nu}$ (the effective M_{H^\pm}) as a function of $\tan\beta$, M_{top} , and some *nominal* value of M_{H^\pm} . For $M_{H^\pm} = 150 \text{ GeV}/c^2$, Figure 5.3 shows $\Gamma_{t \rightarrow \tau\nu b}/dm_{\tau\nu}$ for several values of $\tan\beta$. The expected distribution of $m_{\tau\nu}$ becomes skewed towards smaller values as $\tan\beta$ increases and Γ_H becomes large. This occurs because the phase space factor $\lambda^{1/2}(a, b, c)$ increases as M_{H^\pm} becomes lighter. *The QCD-corrected version of this equation, used in my analysis, is given by Eq. A.12 in Appendix A.*

D.6 Cross Check - The Narrow Width Approximation

We expect that as Γ_H becomes very small, the width for the three-body top decay should reduce to the width for the two-body top decay. In other words,

$$\text{As } \Gamma(H^+) \rightarrow 0, \quad \Gamma(t \rightarrow H^* b \rightarrow \tau \nu b) \rightarrow \Gamma(t \rightarrow H^+ b) \times \mathcal{B}(H^+ \rightarrow \tau \nu). \quad (\text{D.21})$$

For large $\tan\beta$, $\mathcal{B}(H^+ \rightarrow \tau \nu) \approx 1$. The three-body decay width, from Eq. D.20, is

$$\Gamma_{t \rightarrow \tau \nu b} = \int d\Gamma_{t \rightarrow \tau \nu b} = \int_{m_\tau}^{m_t - m_b} \frac{d\Gamma_{\text{top}}}{dm_{\tau\nu}} dm_{\tau\nu} \quad (\text{D.22})$$

A simplification for the integral on the right occurs when one substitutes the Dirac delta function representation for the propagator appearing in Eq. D.20 [24],

$$\text{As } \Gamma_H \rightarrow 0, \quad \frac{1}{(m_{\tau\nu}^2 - M_{H^\pm}^2)^2 + \Gamma_H^2 m_{\tau\nu}^2} \rightarrow \frac{\pi}{m_{\tau\nu} \Gamma_H} \delta(m_{\tau\nu}^2 - M_{H^\pm}^2). \quad (\text{D.23})$$

As a result, the integral is evaluated by calculating the value of the integrand at $m_{\tau\nu}^2 = M_{H^\pm}^2$. Using Eq. D.20, and setting $(M_{H^\pm}^2 - m_\tau^2) = M_{H^\pm}^2$, one has

$$\begin{aligned} \Gamma_{t \rightarrow Hb} &= \frac{1}{(2\pi)^3} \frac{1}{32m_t^3} \frac{g^4 m_\tau^2 \tan^2 \beta}{8m_W^4} \frac{\pi}{M_{H^\pm} \Gamma_H} m_t^2 \lambda^{1/2} \left(1, \frac{m_b^2}{m_t^2}, \frac{M_{H^\pm}^2}{m_t^2}\right) \\ &\times [(m_b^2 \tan^2 \beta + m_t^2 \cot^2 \beta)(m_t^2 + m_b^2 - M_{H^\pm}^2) + 4m_t^2 m_b^2]. \quad (\text{D.24}) \end{aligned}$$

Substituting the proper expression for Γ_H from Eq. D.1, this reduces to

$$\begin{aligned} \Gamma_{t \rightarrow Hb} &= \frac{g^2}{64\pi m_t m_W^2} \lambda^{1/2} \left(1, \frac{m_b^2}{m_t^2}, \frac{M_{H^\pm}^2}{m_t^2}\right) \\ &\times [(m_b^2 \tan^2 \beta + m_t^2 \cot^2 \beta)(m_t^2 + m_b^2 - M_{H^\pm}^2) + 4m_t^2 m_b^2]. \quad (\text{D.25}) \end{aligned}$$

This is the correct expression for $\Gamma_{t \rightarrow Hb}$, given in Ref. [38]. *The QCD-corrected version of this equation, used in my analysis, is given by Eq. A.11 in Appendix A.*

Appendix E

Numerical Values of Efficiencies for $t\bar{t}$ Events With H^\pm Decays

These are the $t\bar{t}$ efficiencies plotted in Figs. 6.1 and 6.7.

Efficiency for $t\bar{t}$ to Pass the Lepton+Jets Selection Criteria, Run 1

M_{H^\pm}	$t\bar{t}$ decay mode			
	$W^+bH^-\bar{b}$ $H^- \rightarrow \bar{c}s$	$W^+bH^-\bar{b}$ $H^- \rightarrow \tau\bar{\nu}$	$H^+bH^-\bar{b}$ $(c\bar{s}b)(\tau\bar{\nu}\bar{b})$	$H^+bH^-\bar{b}$ $H^\pm \rightarrow \tau\nu$
60 GeV/ c^2	(2.27 \pm .05)%	(2.19 \pm .04)%	(1.23 \pm .04)%	(1.30 \pm .03)%
80 GeV/ c^2	(2.31 \pm .05)%	(2.31 \pm .05)%	(1.34 \pm .04)%	(1.34 \pm .03)%
100 GeV/ c^2	(2.42 \pm .06)%	(2.31 \pm .04)%	(1.44 \pm .04)%	(1.44 \pm .03)%
120 GeV/ c^2	(2.29 \pm .05)%	(2.32 \pm .04)%	(1.50 \pm .04)%	(1.29 \pm .03)%
130 GeV/ c^2	(2.26 \pm .05)%	(2.16 \pm .04)%	(1.37 \pm .04)%	(1.12 \pm .03)%
140 GeV/ c^2	(2.04 \pm .05)%	(1.91 \pm .05)%	(1.22 \pm .04)%	(0.77 \pm .02)%
150 GeV/ c^2	(1.77 \pm .05)%	(1.61 \pm .05)%	(0.84 \pm .04)%	(0.41 \pm .02)%
160 GeV/ c^2	(1.63 \pm .05)%	(1.13 \pm .04)%	(0.37 \pm .02)%	(0.11 \pm .01)%

Table E.1: Efficiencies for $t\bar{t}$ with H^\pm decays in the lepton+jets channel, for Run 1. They are plotted in Fig. 6.1. The errors are due to limited Monte Carlo statistics.

Efficiency for $t\bar{t}$ to Pass the Dilepton Selection Criteria, Run 1

M_{H^\pm}	$t\bar{t}$ decay mode			
	$W^+bH^-\bar{b}$ $H^- \rightarrow \bar{c}s$	$W^+bH^-\bar{b}$ $H^- \rightarrow \tau\bar{\nu}$	$H^+bH^-\bar{b}$ $(c\bar{s}b)(\tau\bar{\nu}\bar{b})$	$H^+bH^-\bar{b}$ $H^\pm \rightarrow \tau\nu$
60 GeV	(.014 \pm .005)%	(.358 \pm .017)%	(.008 \pm .004)%	(.203 \pm .013)%
80 GeV	(.017 \pm .005)%	(.380 \pm .021)%	(.008 \pm .004)%	(.214 \pm .013)%
100 GeV	(.011 \pm .003)%	(.419 \pm .018)%	(.010 \pm .004)%	(.250 \pm .014)%
120 GeV	(.008 \pm .003)%	(.453 \pm .024)%	(.005 \pm .003)%	(.276 \pm .015)%
130 GeV	(.017 \pm .003)%	(.457 \pm .024)%	(.014 \pm .003)%	(.273 \pm .015)%
140 GeV	(.011 \pm .004)%	(.424 \pm .020)%	(.011 \pm .004)%	(.238 \pm .014)%
150 GeV	(.014 \pm .004)%	(.408 \pm .026)%	(.005 \pm .004)%	(.175 \pm .017)%
160 GeV	(.014 \pm .005)%	(.291 \pm .022)%	(.006 \pm .002)%	(.086 \pm .011)%

Table E.2: Efficiencies for $t\bar{t}$ with H^\pm decays in the lepton+jets channel, for Run 1, from versions 5.7 and 6.1 of the PYTHIA Monte Carlo generator. The efficiencies plotted in Fig. 6.1 are these values, multiplied by a factor of 1.04 - see the discussion in Section 4.3.1. The errors are due to limited Monte Carlo statistics.

Efficiency for $t\bar{t}$ to Pass the Lepton+Jets Selection Criteria, Run 1

$M_{H^\pm} =$	$t\bar{t}$ decay mode			
	$W^+bH^-\bar{b}$	$W^+bH^-\bar{b}$	$H^+bH^-\bar{b}$	$H^+bH^-\bar{b}$
	$H^- \rightarrow W^-b\bar{b}$	$H^+ \rightarrow W^+b\bar{b}$ $H^- \rightarrow \bar{c}s$	$H^+ \rightarrow W^+b\bar{b}$ $H^- \rightarrow \tau\bar{\nu}$	$H^+ \rightarrow W^+b\bar{b}$ $H^- \rightarrow W^-b\bar{b}$
120 GeV	$(3.99 \pm .10)\%$	$(2.15 \pm .06)\%$	$(2.73 \pm .06)\%$	$(3.97 \pm .07)\%$
130 GeV	$(3.99 \pm .08)\%$	$(2.20 \pm .06)\%$	$(2.81 \pm .06)\%$	$(4.03 \pm .08)\%$
140 GeV	$(3.93 \pm .09)\%$	$(2.07 \pm .06)\%$	$(2.64 \pm .06)\%$	$(4.05 \pm .07)\%$
150 GeV	$(3.92 \pm .07)\%$	$(1.81 \pm .06)\%$	$(2.27 \pm .06)\%$	$(3.93 \pm .07)\%$

Table E.3: Efficiencies for $t\bar{t}$ with H^\pm decays in the lepton+jets channel, for Run 1. They are plotted in Fig. 6.7. The errors are due to limited Monte Carlo statistics.

Efficiency for $t\bar{t}$ to Pass the Dilepton Selection Criteria, Run 1

$M_{H^\pm} =$	$t\bar{t}$ decay mode			
	$W^+bH^-\bar{b}$	$W^+bH^-\bar{b}$	$H^+bH^-\bar{b}$	$H^+bH^-\bar{b}$
	$H^- \rightarrow W^-b\bar{b}$	$H^+ \rightarrow W^+b\bar{b}$ $H^- \rightarrow \bar{c}s$	$H^+ \rightarrow W^+b\bar{b}$ $H^- \rightarrow \tau\bar{\nu}$	$H^+ \rightarrow W^+b\bar{b}$ $H^- \rightarrow W^-b\bar{b}$
120 GeV	$(0.69 \pm .03)\%$	$(0.011 \pm .004)\%$	$(.45 \pm .03)\%$	$(.61 \pm .03)\%$
130 GeV	$(0.67 \pm .03)\%$	$(0.011 \pm .004)\%$	$(.51 \pm .03)\%$	$(.62 \pm .03)\%$
140 GeV	$(0.66 \pm .04)\%$	$(0.011 \pm .004)\%$	$(.51 \pm .03)\%$	$(.57 \pm .03)\%$
150 GeV	$(0.64 \pm .03)\%$	$(0.011 \pm .004)\%$	$(.53 \pm .03)\%$	$(.58 \pm .03)\%$

Table E.4: Efficiencies for $t\bar{t}$ with H^\pm decays in the lepton+jets channel, for Run 1, from version 6.1 of the PYTHIA Monte Carlo generator. The efficiencies plotted in Fig. 6.7 are these values, multiplied by a factor of 1.04 - see the discussion in Section 4.3.1. The errors are due to limited Monte Carlo statistics.

Appendix F

Cross Checks of Efficiencies for $t\bar{t}$ with $H^\pm \rightarrow cs, \tau\nu$ Decays

For the special case $M_{H^\pm} = M_{W^\pm}$, I compare the efficiencies for $t\bar{t}$ decay topologies containing H^\pm bosons, with similar SM topologies where the W^\pm replaces the H^\pm . The comparison is shown in Tables F.1 and F.2.

The decay $t\bar{t} \rightarrow WbX\bar{b}$, where $X \rightarrow cs$, has the same efficiency whether “ X ” is a W^\pm or a H^\pm , despite the differences in angular distribution for the decay products for the bosons.

Decay modes with τ leptons have higher efficiencies if the tau originates from a W^\pm boson, rather than an H^\pm . This is due to τ polarization effects. A tau lepton from the decay of a W^\pm boson will be polarized along its direction of motion in the rest frame of the W^\pm . Electrons and muons from tau decays are emitted preferentially along the direction of the tau polarization, the same direction as the tau momentum. However, the situation is reversed for H^\pm decays, in which electrons and muons are emitted preferentially in the backwards direction (see Fig. F.1). Thus, the P_T spectrum of electrons and muons will be harder for the SM $t\bar{t}$ topologies, as shown in Fig. F.2.

Efficiency of Successive Selection Cuts in the Lepton+Jets Channel

$t\bar{t}$ decay	X ($M_{H^\pm} = 80$ GeV)	efficiency of successive lepton+jets cuts for Run 1B					
		high- P_T e or μ	$E_T > 20$ GeV	#jets ≥ 3	trig	tag	total
$W^+ b X^- \bar{b}$	$X^- = H^-$	$8.49 \pm .1\%$	89%	87%	92%	40%	$(2.42 \pm .06)\%$
$X^- \rightarrow \bar{c}s$	$X^- = W^-$	$8.45 \pm .1\%$	89%	88%	91%	41%	$(2.44 \pm .07)\%$
$X^+ b X^- \bar{b}$	$X^\pm = H^\pm$	$9.59 \pm .1\%$	87%	44%	93%	41%	$(1.40 \pm .04)\%$
$X^\pm \rightarrow \tau\nu$	$X^\pm = W^\pm$	$10.8 \pm .1\%$	89%	41%	93%	41%	$(1.50 \pm .04)\%$

Table F.1: Comparison of lepton+jets channel efficiencies for $t\bar{t}$ topologies with H^\pm decays, and efficiencies for the same decay modes where the W^\pm boson replaces the H^\pm . Note that the decays with W^\pm s are more likely to produce events with high- P_T electrons or muons than decays with H^\pm s.

Efficiency of Successive Selection Cuts in the Dilepton Channel

$t\bar{t}$ decay	X ($M_{H^\pm} = 80$ GeV)	efficiency of successive dilepton cuts in Run 1				
		2 high- P_T e or μ	E_T cuts	# jets ≥ 2	trig	total
$X^+ b X^- \bar{b}$	$X^\pm = H^\pm$	$(.374 \pm .02)\%$	69%	86%	98%	$(.214 \pm .013)\%$
$X^\pm \rightarrow \tau\nu$	$X^\pm = W^\pm$	$(.467 \pm .02)\%$	76%	86%	97%	$(.296 \pm .016)\%$

Table F.2: Comparison of the dilepton channel efficiency for $t\bar{t}$ decays to $\tau\nu b\tau\nu\bar{b}$, mediated by H^\pm decays, and W^\pm decays. Note that the decays with W^\pm s are more likely to produce events with high- P_T electrons or muons than decays with H^\pm s.

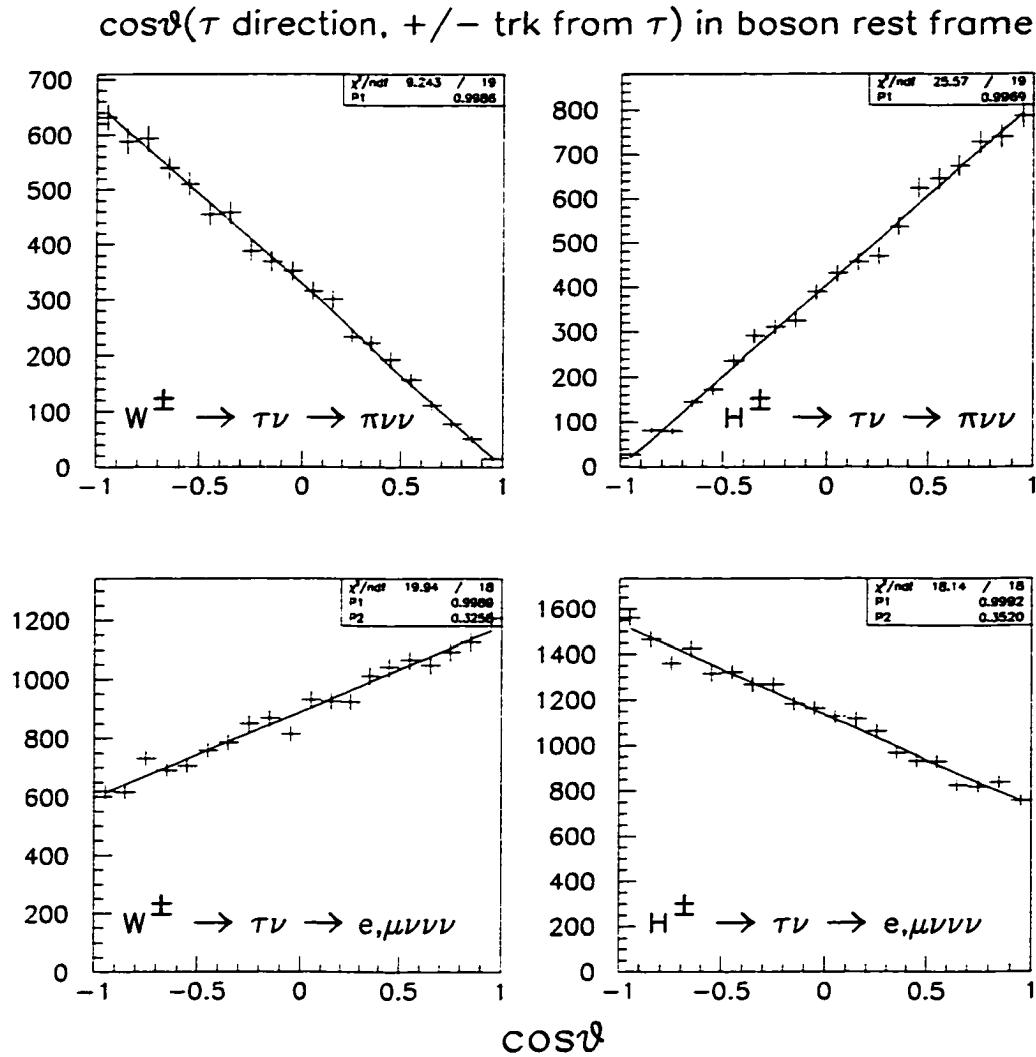


Figure F.1: The angular distribution of charged particles emitted in tau decays. In the rest frame of the tau lepton, I plot the cosine of the angle between the charged track from the tau, and the direction of boost from the boson rest frame to the tau rest frame. The top plots show distributions for the decay $\tau \rightarrow \pi\nu$, while the bottom plots show distributions for $\tau \rightarrow (e \text{ or } \mu)\nu\nu$. Electrons and muons from $W^\pm \rightarrow \tau\nu$ decays are preferentially emitted in the forward direction, while the opposite is true for $H^\pm \rightarrow \tau\nu$ decays.

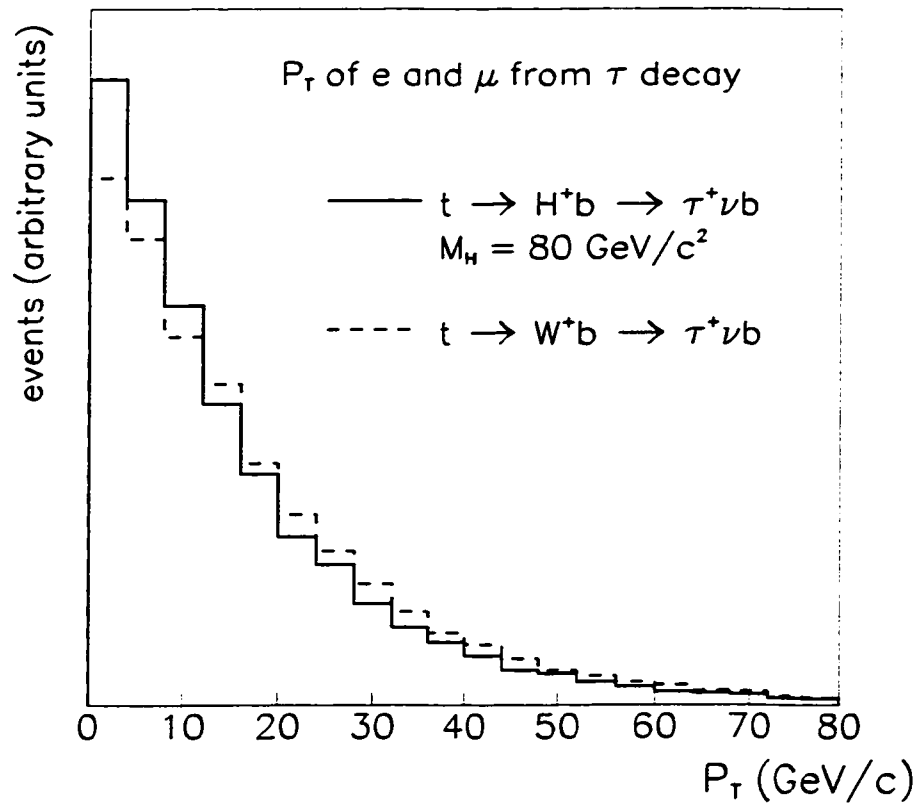


Figure F.2: The P_T spectrums of leptons from tau decay. The two curves correspond to taus that originate from W^+ decay or H^+ decay, where $M_{H^\pm} = M_{W^\pm} = 80 \text{ GeV}/c^2$. About 28% of the leptons from $H^+ \rightarrow \tau^+ \nu$ decay have $P_T > 20 \text{ GeV}/c$, while 33% from $W^+ \rightarrow \tau^+ \nu$ decay have $P_T > 20 \text{ GeV}/c$.

Appendix G

Systematic Errors for $t\bar{t}$ with H^\pm Decay

The efficiencies for $t\bar{t}$ events with H^\pm decays are afflicted with the same systematic errors as SM $t\bar{t}$ decays. These errors are listed in Table 4.5, which is repeated below. For the H^\pm analysis, we use these errors, except for the errors associated with the absolute jet energy scale, and the modeling of initial- and final-state radiation (ISR/FSR) in an event. As I discussed in Section 6.2.1, these errors depend on the topology of the $t\bar{t}$ decay, and M_{H^\pm} . These errors are given in tables that appear below, for the decay topologies that were presented in Chapter 6.

Systematic Errors for the $t\bar{t}$ Efficiency

category	SVX channel	Dilepton channel
lepton ID ϵ	3%	7%
trigger ϵ	8%	2%(trig. only)
SVX b -tag ϵ	8%	-
jet energy scale	5% (SM only!)	3% (SM only!)
ISR/FSR	8% (SM only!)	3% (SM only!)
Luminosity	7%	
z-vertex res. effect	2%	2%
Total	17%	11%

Table G.1: Systematic errors in each channel for the product $\epsilon\mathcal{L}$.

Change in Lepton+Jets Efficiencies Between Extremes of no ISR/FSR

M_{H^\pm}	$t\bar{t}$ decay mode			
	$W^+bH^-\bar{b}$	$W^+bH^-\bar{b}$	$H^+bH^-\bar{b}$	$H^+bH^-\bar{b}$
	$H^- \rightarrow \bar{c}s$	$H^- \rightarrow \tau\bar{\nu}$	$H^+ \rightarrow c\bar{s}, H^- \rightarrow \tau\bar{\nu}$	$H^+ \rightarrow \bar{\tau}\nu, H^- \rightarrow \tau\bar{\nu}$
60 GeV	$(20 \pm 3)\%$	$(16 \pm 2)\%$	$(14 \pm 5)\%$	$(23 \pm 4)\%$
100 GeV	$(15 \pm 3)\%$	$(20 \pm 3)\%$	$(20 \pm 4)\%$	$(25 \pm 3)\%$
140 GeV	$(17 \pm 3)\%$	$(22 \pm 3)\%$	$(20 \pm 5)\%$	$(48 \pm 3)\%$

Change in Dilepton Efficiencies Between Extremes of no ISR/FSR

M_{H^\pm}	$t\bar{t}$ decay mode			
	$W^+bH^-\bar{b}$	$W^+bH^-\bar{b}$	$H^+bH^-\bar{b}$	$H^+bH^-\bar{b}$
	$H^- \rightarrow \bar{c}s$	$H^- \rightarrow \tau\bar{\nu}$	$H^+ \rightarrow c\bar{s}, H^- \rightarrow \tau\bar{\nu}$	$H^+ \rightarrow \bar{\tau}\nu, H^- \rightarrow \tau\bar{\nu}$
60 GeV	-	$(16 \pm 6)\%$	-	$(22 \pm 9)\%$
100 GeV	-	$(8 \pm 6)\%$	-	$(22 \pm 7)\%$
140 GeV	-	$(10 \pm 5)\%$	-	$(26 \pm 6)\%$

Table G.2: Differences in $t\bar{t}$ efficiencies between the extremes of no initial-state radiation and no final-state radiation. Errors are statistical only. The systematic errors for each of the decay modes are taken to be one-half of the values listed in these tables.

Change in Lepton+Jets Efficiencies due to Jet Energy Scale Shifts

M_{H^\pm}	$t\bar{t}$ decay mode			
	$W^+bH^-\bar{b}$	$W^+bH^-\bar{b}$	$H^+bH^-\bar{b}$	$H^+bH^-\bar{b}$
	$H^- \rightarrow \bar{c}s$	$H^- \rightarrow \tau\bar{\nu}$	$H^+ \rightarrow c\bar{s}, H^- \rightarrow \tau\bar{\nu}$	$H^+ \rightarrow \bar{\tau}\nu, H^- \rightarrow \tau\bar{\nu}$
60 GeV	7%	20%	19%	25%
100 GeV	9%	20%	14%	24%
140 GeV	8%	25%	19%	35%

Change in Dilepton Efficiencies due to Jet Energy Scale Shifts

M_{H^\pm}	$t\bar{t}$ decay mode			
	$W^+bH^-\bar{b}$	$W^+bH^-\bar{b}$	$H^+bH^-\bar{b}$	$H^+bH^-\bar{b}$
	$H^- \rightarrow \bar{c}s$	$H^- \rightarrow \tau\bar{\nu}$	$H^+ \rightarrow c\bar{s}, H^- \rightarrow \tau\bar{\nu}$	$H^+ \rightarrow \bar{\tau}\nu, H^- \rightarrow \tau\bar{\nu}$
60 GeV	-	10%	-	18%
100 GeV	-	6%	-	18%
140 GeV	-	10%	-	20%

Table G.3: Shifts in $t\bar{t}$ efficiencies when the jet energy scale is shifted from -10% to +10% of its nominal value. The systematic errors for each of the decay modes are taken to be one-half the values listed in these tables.

Change in Efficiencies due to Jet Energy Scale Shifts

$M_{H^\pm} =$ 130 GeV	$t\bar{t}$ decay mode			
	$W^+bH^-\bar{b}$	$H^+bH^-\bar{b}$	$H^+bH^-\bar{b}$	$H^+bH^-\bar{b}$
	$H^- \rightarrow W^-b\bar{b}$	$H^+ \rightarrow W^+b\bar{b}$	$H^+ \rightarrow W^+b\bar{b}$	$H^+ \rightarrow W^+b\bar{b}$
		$H^- \rightarrow \bar{c}s$	$H^- \rightarrow \tau\bar{\nu}$	$H^- \rightarrow W^-b\bar{b}$
lep.+jets	$(17 \pm 2)\%$	$(20 \pm 3)\%$	$(22 \pm 3)\%$	$(16 \pm 2)\%$
dilepton	$(13 \pm 5)\%$	-	$(8 \pm 4)\%$	$(7 \pm 4)\%$

Table G.4: The change in efficiencies when jet energies are shifted from -10% to +10% of their nominal values. Systematic errors are assigned to be one-half the values shown here.

Change in Efficiencies Between the Extremes of no ISR/FSR

$M_{H^\pm} =$ 130 GeV	$t\bar{t}$ decay mode			
	$W^+bH^-\bar{b}$	$H^+bH^-\bar{b}$	$H^+bH^-\bar{b}$	$H^+bH^-\bar{b}$
	$H^- \rightarrow W^-b\bar{b}$	$H^+ \rightarrow W^+b\bar{b}$	$H^+ \rightarrow W^+b\bar{b}$	$H^+ \rightarrow W^+b\bar{b}$
		$H^- \rightarrow \bar{c}s$	$H^- \rightarrow \tau\bar{\nu}$	$H^- \rightarrow W^-b\bar{b}$
lep.+jets	13%	10%	22%	9%
dilepton	$(7 \pm 1)\%$	-	$(13 \pm 2)\%$	$(6 \pm 1)\%$

Table G.5: The change in efficiencies between the extremes of no initial state radiation and no final state radiation. The systematic errors are assigned to be one-half the values shown in this table

Bibliography

- [1] B. Bevensee for the CDF Collaboration, “Searches for Charged Higgs Bosons and Supersymmetry at CDF”, in *Proceedings of the International Workshop on Quantum Effects in the MSSM*, Ed. J. Solà (Singapore: World Scientific, 1998). An expanded version is preprint FERMILAB-CONF-97-405-E.
- [2] B. Bevensee for the CDF and DØ Collaborations, “Top to Charged Higgs Decays and Top Properties at the Tevatron”, FERMILAB-PUB-98-155-E, To be published in the *Proceedings of 33rd Rencontres de Moriond: QCD and High Energy Hadronic Interactions, Les Arcs, France, 21-28 Mar 1998*.
- [3] C. Caso, *et al.*, *Review of Particle Physics. Particle Data Group*, Eur. Phys. J. **C3**, 1 (1998).
- [4] H. Goldstein, *Classical Mechanics*, (Reading, Ma.: Addison-Wesley Publishing Co., Inc., 2nd Ed., 1980).
- [5] C. Quigg, *Gauge Theories of the Strong, Weak, and Electromagnetic Interactions*, (Reading, Ma.: Addison-Wesley Publishing Co., 1983).
- [6] M. Guidry, *Gauge Field Theories: an Introduction with Applications*, (New York: John Wiley and Sons, Inc., 1991).
- [7] J.D. Jackson, *Classical Electrodynamics (2nd Ed.)*, (New York: John Wiley and Sons, Inc., 1974).
- [8] C.N. Yang and R.L. Mills, *Conservation of Isotopic Spin and Isotopic Gauge Invariance*, Phys. Rev. **96**, 191 (1954).
- [9] S. Weinberg, *A Model of Leptons*, Phys. Rev. Lett. **19**, 1264 (1967).

- [10] F. Halzen and A.D. Martin, *Quarks and Leptons, an Introductory Course in Modern Particle Physics*, (New York: John Wiley and Sons, Inc., 1984).
- [11] J.F. Gunion *et al.*, *The Higgs Hunter's Guide*, (Redwood City, Ca.: Addison-Wesley Publishing Co., 1990).
- [12] S.P. Martin, *A Supersymmetry Primer*, preprint hep-ph/9709356 v2 (1998).
- [13] CDF Collaboration, F. Abe *et al.*, *Observation of Top Quark Production in $p\bar{p}$ Collisions with the Collider Detector at Fermilab*, Phys. Rev. Lett. **74**, 2626 (1995).
- [14] DØ Collaboration, S. Abachi *et al.*, *Observation of the Top Quark*, Phys. Rev. Lett. **74**, 2632 (1995).
- [15] CDF Collaboration, F. Abe *et al.*, *First Observation of the All-Hadronic Decay of $t\bar{t}$ Pairs*, Phys. Rev. Lett. **79**, 1992 (1997).
- [16] We use non- $t\bar{t}$ backgrounds which are slightly higher than those found in Ref. [22], where the portion of the background that is calculated from data is corrected for its top content, assuming $\mathcal{B}(t \rightarrow W^\pm b) = 1.0$. We do not perform such a correction.
- [17] R. Bonciani *et al.*, *NLL Resummation of the Heavy-Quark Hadroproduction Cross Section*, Nucl. Phys. **B529**, 424 (1998).
- [18] E. Berger and H. Contopanagos, *Threshold Resummation of the Total Cross Section for Heavy Quark Production in Hadronic Collisions*, Phys. Rev. **D57**, 253 (1998).
- [19] E. Laenen, J. Smith and W.L. van Neerven, *Top Quark Production Cross Section*, Phys. Lett. **B321**, 254 (1994).

- [20] CDF Collaboration, F. Abe *et al.*, *Measurement of the Top Quark Mass with the Collider Detector at Fermilab*, Phys. Rev. Lett. **82**, 271 (1999).
- [21] DØ Collaboration, S. Abachi *et al.*, *Measurement of the Top Quark Mass in the Dilepton Channel*, preprint hep-ex/9808029, Submitted to Phys. Rev. D (1998).
- [22] CDF Collaboration, F. Abe *et al.*, *Measurement of the $t\bar{t}$ Production Cross-Section in $p\bar{p}$ Collisions at $\sqrt{s} = 1.8$ TeV*, Phys. Rev. Lett. **80**, 2773 (1998).
- [23] CDF Collaboration, F. Abe *et al.*, *Measurement of the Top Quark Mass and $t\bar{t}$ Production Cross-Section from Dilepton Events at the Collider Detector at Fermilab*, Phys. Rev. Lett. **80**, 2779 (1998).
- [24] V. Barger and R. Phillips, *Collider Physics*, (Redwood City, Ca.: Addison-Wesley Publishing Co., 1987).
- [25] S. L. Glashow, *Partial Symmetries of Weak Interactions*, Nucl. Phys. **22**, 579 (1961).
- [26] R. N. Mohapatra, *Unification and Supersymmetry*, (New York: Springer-Verlag, 1992).
- [27] S. Weinberg, “Conceptual Foundations of the Unified Theory of Weak and Electromagnetic Interactions” (1979 Nobel Prize Lecture), in *Selected Papers on Gauge Theory of Weak and Electromagnetic Interactions*, Ed. C.H. Lai (World Scientific Publishing Co., Singapore, 1981), pp. 1-8.
- [28] J. Goldstone, *Field Theories with Superconductor Solutions*, Nuovo Cimento **19**, 154 (1961).

- [29] L. H. Ryder, *Quantum Field Theory*, (Cambridge: Cambridge University Press, 1985).
- [30] P. Langacker, *Grand Unified Theories and Proton Decay*, Phys. Rep. **72**, No. 4, 185 (1981).
- [31] M. Sher, *Electroweak Higgs Potentials and Vacuum Stability*, Phys. Rep. **179**, Nos. 5 & 6, 273 (1989).
- [32] D. Toussaint, *Renormalization Effects from Superheavy Higgs Particles*, Phys. Rev. **D18**, No. 5, 1626 (1978).
- [33] H.E. Haber, G.L. Kane and T. Sterling, *The Fermion Mass Scale and Possible Effects of Higgs Bosons on Experimental Observables*, Nucl. Phys. **B161**, 493 (1979).
- [34] J.F. Gunion and H.E. Haber, *Higgs Bosons (I)*, Nucl. Phys. B **272**, 1 (1986).
- [35] L.J. Hall and M.B. Wise, *Flavor Changing Higgs Boson Couplings*, Nucl. Phys. B **187**, 397 (1981).
- [36] S. Dawson, “Susy and Such”, Lectures given at *NATO Advanced Study Institute on Techniques and Concepts of High-energy Physics*, St. Croix, U.S. Virgin Islands, 10-23 Jul. 1996. Preprint hep-ex/9612229.
- [37] J.F. Gunion *et al.*, *Neutral and Charged Higgs Detection: Heavy Quark Fusion, Top Quark Mass Dependence, and Rare Decays*, Nucl. Phys. **B294**, 621 (1987).
- [38] M. Drees and D.P. Roy, *Effect of QCD Correction on the Charged Higgs Signature in Top Quark Decay*, Phys. Lett. B **269**, 155 (1991). This reference applies a QCD correction to the partial widths Γ_{top} and Γ_H . I use $m_c =$

1.3 GeV/ c^2 , and $m_b = 4.7$ GeV/ c^2 in Eq. 16 of this reference. In the same equation, for m_b only, I use $M_{\text{top}} = 175$ GeV/ c^2 rather than M_{H^\pm} , to get the QCD correction to the partial width $\Gamma_{t \rightarrow Hb}$. See Appendix A.

- [39] E. Ma, D.P. Roy and J. Wudka, *Enhanced Three-Body Decay of the Charged Higgs Boson*, Phys. Rev. Lett. **80**, 1162 (1998).
- [40] D.P. Roy, *Discovery Limit of the Charged Higgs Boson via Top Quark Decay at Future Hadron Colliders*, Phys. Lett. **B283**, 403 (1992).
- [41] J.A. Coarasa, *et al.*, *Top Quark Decay into Charged Higgs Boson in a general Two-Higgs Doublet Model: Implications for the Tevatron Data*, Phys. Lett. **B442**, 326 (1998).
- [42] G. Sterman *et al.*, *Handbook of Perturbative QCD*, Rev. Mod. Phys. **87**, No. 1, 157 (1995).
- [43] R. K. Ellis, W. J. Stirling and B.R. Webber, *QCD and Collider Physics*, (Cambridge: Cambridge University Press, 1996).
- [44] A.D. Martin, R.G. Roberts, W.J. Stirling, *Parton Distributions: A Study of the New HERA Data, Alpha-s, the Gluon and $p\bar{p}$ Jet Production*, Phys. Lett. **B387**, 419 (1996).
- [45] M. Jezabek and J.H. Kuhn, *QCD Corrections to Semileptonic Decays of Heavy Quarks*, Nucl. Phys. **B314**, 1 (1989).
- [46] CDF Collaboration, F. Abe *et al.*, *Evidence for Top Quark Production in $p\bar{p}$ Collisions at $\sqrt{s} = 1.8$ TeV*, Phys. Rev. **D50**, 2966 (1994).
- [47] CDF Collaboration, F. Abe *et al.*, *Kinematics of $t\bar{t}$ events at CDF*, FERMILAB-PUB-98-327-E, Submitted to Phys. Rev. D (1998).

- [48] CDF Collaboration, F. Abe *et al.*, *The $e - \mu$ and $e - \tau$ Decays of Top Quark Pairs Produced in $p\bar{p}$ Collisions at $\sqrt{s} = 1.8$ TeV*, Phys. Rev. Lett. **79**, 3585 (1997).
- [49] DØ Collaboration, B. Abbott *et al.*, *Measurement of the Top Quark Pair Production Cross Section in $p\bar{p}$ Collisions using Multijet Final States*, preprint hep-ex/9808034, Submitted to Phys. Rev. D (1998).
- [50] N. Amos for the CDF and DØ Collaborations, “Measurement of the $t\bar{t}$ Production Cross Section”, To be published in the *Proceedings of 33rd Rencontres de Moriond: QCD and High Energy Hadronic Interactions, Les Arcs, France, 21-28 Mar 1998*.
- [51] S. Blusk for the CDF and DØ Collaborations, “Measurement of the Top Quark Mass”, FERMILAB-PUB-98-151-E, To be published in the *Proceedings of 33rd Rencontres de Moriond: QCD and High Energy Hadronic Interactions, Les Arcs, France, 21-28 Mar 1998*.
- [52] CDF Collaboration, F. Abe *et al.*, *Measurement of the Top Quark Mass*, Phys. Rev. Lett. **80**, 2767 (1998).
- [53] K. A. Tollefson, *A Measurement of the Top Quark Mass*, University of Rochester, Ph.D. Thesis (1997).
- [54] CDF Collaboration, F. Abe *et al.*, *Observation of Hadronic W Decays in $t\bar{t}$ Events with the Collider Detector at Fermilab*, Phys. Rev. Lett. **80**, 5720 (1998).
- [55] DØ Collaboration, B. Abbott *et al.*, *Measurement of the Top Quark Mass at DØ*, Phys. Rev. **D58**, 052001 (1998).

- [56] CDF Collaboration, F. Abe *et al.*, *Search for Charged Higgs Decays of the Top Quark using Hadronic Decays of the Tau Lepton*, Phys. Rev. Lett. **79**, 357 (1997).
- [57] Mark Strovink, for the CDF and DØ Collaborations, “Top Quark Physics: New Experimental Results and Open Questions”, talk given at the *1999 Aspen Winter Conference on Particle Physics*, 22 Jan. 1999.
- [58] OPAL Collaboration, G. Abbiendi *et al.*, *Search for Higgs Bosons in e^+e^- Collisions at 183 GeV*, preprint hep-ex/9811025, Submitted to Eur. Phys. J. C, (1998).
- [59] L3 Collaboration, M. Acciarri *et al.*, *Search for Charged Higgs Bosons in e^+e^- Collisions at Center-of-Mass Energies between 130 GeV and 183 GeV*, preprint CERN-EP-98-149, Submitted to Phys. Lett. B, (1998).
- [60] DELPHI Collaboration, P. Abreu *et al.*, *Search for Charged Higgs Bosons in e^+e^- Collisions at $\sqrt{s} = 172$ GeV.*, Phys. Lett. **B420**, 140 (1998).
- [61] ALEPH Collaboration, R. Barate *et al.*, *Search for Charged Higgs Bosons in e^+e^- Collisions at Center-of-Mass Energies from 130 GeV to 172 GeV*, Phys. Lett. **B418**, 419 (1998).
- [62] G. Altarelli, T. Sjöstrand”, F. Zwirner (Eds.), *Physics at LEP2, Vol. 1*, (CERN, Geneva, 1996).
- [63] K. Chetyrkin, M. Misiak, M. Munz, *Weak Radiative B Meson Decay Beyond Leading Logarithms*, Phys. Lett. **B400**, 206 (1997).
- [64] M. Ciuchini *et al.*, *Next-to-Leading QCD Corrections to $B \rightarrow X_s \gamma$: Standard Model and Two Higgs Doublet Model*, Nucl. Phys. **B527**, 21 (1998).

- [65] S. Stone, “Rare Nonhadronic B decays”, presented at *The 4th International Workshop on Particle Physics Phenomenology*, Kaosiung, Taiwan, China, 18-21 Jun 1998. Preprint hep-ex/9809580.
- [66] G. Eigen, “Measurements of $B \rightarrow X_s \gamma$ and Study of $B \rightarrow X_s \ell^+ \ell^-$ ”, invited talk at *The 4th International Symposium on Radiative Corrections (RADCOR 98): Applications of Quantum Field Theory to Phenomenology*, Barcelona, Catalonia, Spain, 8-12 Sep. 1998. Preprint hep-ex/9901005.
- [67] J.L. Hewett and J.D. Wells, *Searching for Supersymmetry in Rare B Decays*, Phys. Rev. **D55**, 5549 (1997).
- [68] M.S. Alam, *First Measurement of the Rate for the Inclusive Radiative Penguin Decay $b \rightarrow s \gamma$* , Phys. Rev. Lett. **74**, 2885 (1995).
- [69] R. Garisto and J.N. Ng, *Supersymmetric $b \rightarrow s \gamma$ with Large Chargino Contributions*, Phys. Lett. **B315**, 372 (1993).
- [70] M. Ciuchini *et al.*, *Next-to-Leading QCD Corrections to $B \rightarrow X_s \gamma$ in Supersymmetry*, Nucl. Phys. **B534**, 3 (1998).
- [71] J.L. Hewett, T. Takeuchi, and S. Thomas, “Indirect Probes of New Physics”, to appear as a chapter in *Electroweak Symmetry Breaking and Beyond the Standard Model*, T. Barklow *et al.*, (Eds.), 548, (1996). Preprint hep-ph/9603391.
- [72] L3 Collaboration, M. Acciarri *et al.*, *Measurement of $D_s^- \rightarrow \tau^- \bar{\nu}_\tau$ and a New Limit for $B^- \rightarrow \tau^- \bar{\nu}_\tau$* , Phys. Lett. **B396**, 327 (1997).
- [73] ALEPH Collaboration D. Buskulic *et al.*, *Measurement of the $B \rightarrow \tau^- \bar{\nu}_\tau X$ Branching Ratio and an Upper Limit on $B^- \rightarrow \tau^- \bar{\nu}_\tau$* , Phys. Lett. **B343**, 444, (1995).

- [74] Y. Grossman, H.E. Haber and Y. Nir, *QCD Corrections to Charged Higgs Mediated $b \rightarrow c\tau$ Neutrino Decay*, Phys. Lett. **B357**, 630 (1995).
- [75] J.A. Coarasa, R.A. Jimenez and J. Sola, *The $\tan\beta$ - M_{H^\pm} Bound from Inclusive Semitauonic B decays in the MSSM*, Phys. Lett. **B406**, 337 (1997).
- [76] M. Dova, J. Swain and L. Taylor, *Anomalous Charged Current Couplings of the Tau and Implications for Tau Compositeness and Two Higgs Doublet Models*, Phys. Rev. **D58**, 015005 (1998).
- [77] A. Stahl, *Testing the Lorentz Structure of the Charged Weak Current in Tau Decays*, Z. Phys. **C74**, 73 (1997).
- [78] A. Grant, *The Heavy Top Quark in the Two Higgs Doublet Model*, Phys. Rev. **D51**, 207 (1995).
- [79] M. Boulware and D. Finnell, *Radiative Corrections to $BR(Z \rightarrow b\bar{b})$ in the Minimal Supersymmetric Standard Model*, Phys. Rev. **D44**, 2054 (1991).
- [80] W. de Boer *et al.*, *Updated Global Fits of the SM and MSSM to Electroweak Precision Data*, preprint hep-ph/9609209.
- [81] J. Ellis, J.L. Lopez, and D.V. Nanopoulos, *Supersymmetry, Supergravity, and R_b Revisited In the Light of LEP-2*, Phys. Lett. **B397**, 88 (1997).
- [82] F. Abe *et al.*, *Measurement of B Hadron Lifetimes Using J/ψ Final States at CDF*, Phys. Rev. **D57**, 5382 (1998).
- [83] D.A. Edwards and M.J. Syphers, *An Introduction to the Physics of High Energy Accelerators*, (New York: John Wiley and Sons, Inc., 1993).
- [84] D. Amidei *et al.*, *The Silicon Vertex Detector of the Collider Detector at Fermilab*, Nucl. Instrum. Meth. **A350**, 73 (1994).

- [85] P. Azzi *et al.*, *SVXl: The New CDF Silicon Vertex Detector*, Nucl. Instrum. Meth. **A360**, 137 (1995).
- [86] See the file CDF\$DOC:VTVX.MEM, *Vertex Classification*, unpublished.
- [87] F. Bedeschi *et al.*, *Design and Construction of the CDF Central Tracking Chamber*, Nucl. Instrum. Meth. **A268**, 50 (1988).
- [88] C. Fabjan, "Calorimetry in High-Energy Physics", in *Experimental Techniques in High Energy Physics*, Ed. T. Ferbel (Addison Wesley Publishing Company, Inc., Menlo Park, CA, 1987), pp. 257-324.
- [89] R.C. Fernow, *Introduction to Experimental Particle Physics*, (Cambridge: Cambridge University Press, 1986).
- [90] L. Balka *et al.*, *The CDF Central Electromagnetic Calorimeter*, Nucl. Instrum. Meth. **A267**, 272 (1988).
- [91] Y. Yasuoka *et al.*, *Response Maps of the CDF Central Electromagnetic Calorimeter with Electrons*, Nucl. Instrum. Meth. **A267**, 315 (1988).
- [92] S.R. Hahn *et al.*, *Calibration Systems for the CDF Central Electromagnetic Calorimeter*, Nucl. Instrum. Meth. **A267**, 351 (1988).
- [93] D.H. Perkins, *Introduction to High Energy Physics*, (Menlo Park, Ca.: Addison-Wesley Publishing Co., Inc., 3rd Ed., 1987).
- [94] S. Bertolucci *et al.*, *The CDF Central and Endwall Hadronic Calorimeter*, Nucl. Instrum. Meth. **A267**, 301 (1988).
- [95] CDF Collaboration, F. Abe *et al.*, *Topology of Three-jet Events in $p\bar{p}$ Collisions at $\sqrt{s} = 1.8$ TeV*, Phys. Rev. **D45**, 1448 (1992).

- [96] CDF Collaboration, F. Abe *et al.*, *Study of Four-Jet Events and Evidence for Double Parton Interactions in $p\bar{p}$ Collisions at $\sqrt{s} = 1.8$ TeV*, Phys. Rev. **D47**, 4857 (1993).
- [97] N. Eddy, *The New Relative Jet Corrections for Run 1A and 1B Data*, CDF Internal Note 3534 (unpublished).
- [98] S. Behrends, *A Plot of the Systematic Uncertainty on Jet E_T* , CDF Internal Note 3550 (unpublished).
- [99] M. Hohlmann, *Observation of Top Quarks in the Dilepton Decay Channel, using Electrons, Muons and Taus*, University of Chicago, Ph.D. Thesis (1997).
- [100] G. Ascoli *et al.*, *CDF Central Muon Detector*, Nucl. Instrum. Meth. **A268**, 33 (1988).
- [101] CDF Collaboration, F. Abe *et al.*, *Measurement of $\sigma B(W \rightarrow e\nu)$ and $\sigma B(Z^0 \rightarrow e^+e^-)$ in $p\bar{p}$ Collisions at $\sqrt{s} = 1.8$ TeV*, Phys. Rev. Lett. **76**, 3070 (1996).
- [102] CDF Collaboration, F. Abe *et al.*, *Measurement of the Antiproton-Proton Total Cross Section at $\sqrt{s} = 546$ and 1800 GeV*, Phys. Rev. **D50**, 5550 (1994).
- [103] J.D. Olsen, *Measurement of the $b - \bar{b}$ Rapidity Correlations in $p\bar{p}$ Collisions at $\sqrt{s} = 1.8$ TeV*, University of Wisconsin at Madison, Ph.D. Thesis (1998).
- [104] C. Grosso-Pilcher, *Luminosity for Run 1B: How Well do we Know It?*, CDF Internal Note 4350 (unpublished).

- [105] A. Beretvas *et al.*, σ_{BBC} *Accidentals Corrections Update for Run 1B*, CDF Internal Note 3418 (unpublished).
- [106] G. W. Foster *et al.*, *A Fast Hardware Track-Finder for the CDF Central Tracking Chamber*, Nucl. Instrum. Meth. **A269**, 93 (1988).
- [107] L. S. Groer, *A Search for Charged Higgs Boson Decays of the Top Quark using Hadronic Decays of the Tau Lepton in Proton-Antiproton Collisions at $\sqrt{s} = 1.8 \text{ TeV}$ at CDF*, Rutgers, the State University of New Jersey, Ph.D. Thesis (1998).
- [108] The CDF Top Group, *Sample Selection for the Run 1B Top Search*, CDF Internal Note 2966 (unpublished).
- [109] David Gerdes, *Study of Conversion Removal for the Lepton + Jets Sample*, CDF Internal Note 2903 (unpublished).
- [110] CDF Collaboration, F. Abe *et al.*, *Measurement of $\sigma B(W \rightarrow e\nu)$ and $\sigma B(Z^0 \rightarrow e^+e^-)$ in $p\bar{p}$ Collisions at $\sqrt{s} = 1800 \text{ GeV}$* , Phys. Rev. **D44**, 29 (1991).
- [111] M. Kruse, *Observation of Top Quark Pair Production in the Dilepton Decay Channel from Proton-Antiproton Collisions at $\sqrt{s} = 1.8 \text{ TeV}$* , Purdue University, Ph.D. Thesis (1996).
- [112] H. Wenzel, *The Primary Interaction Vertex*, CDF Internal Note 4066 (unpublished).
- [113] F. Bedeschi and S. Dell'Agnello, *Handling Multiple Primary Interactions with the Primary Vertex Finder*, CDF Internal Note 2084 (unpublished).

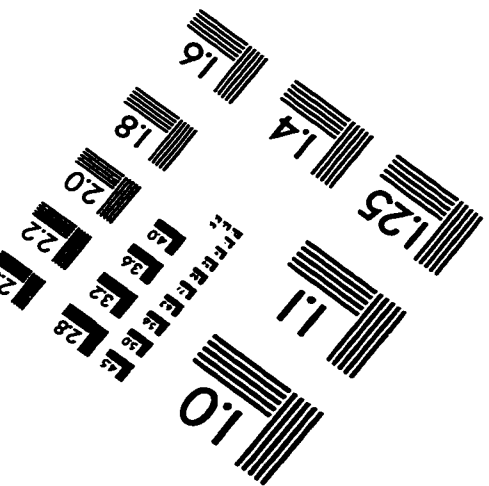
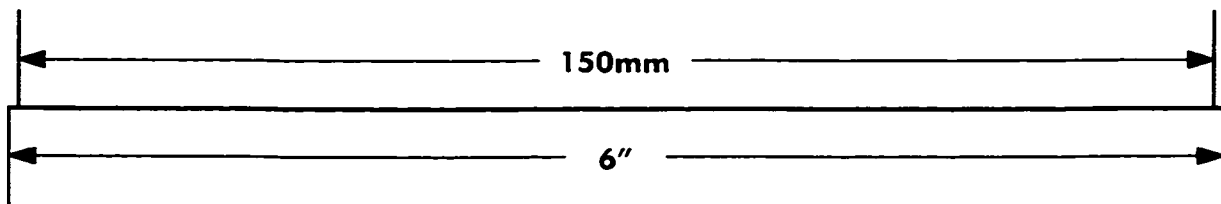
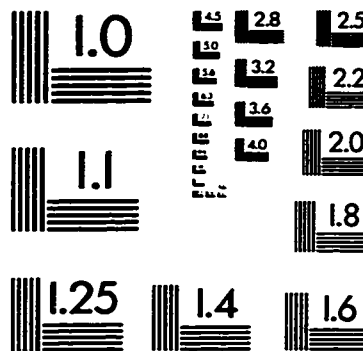
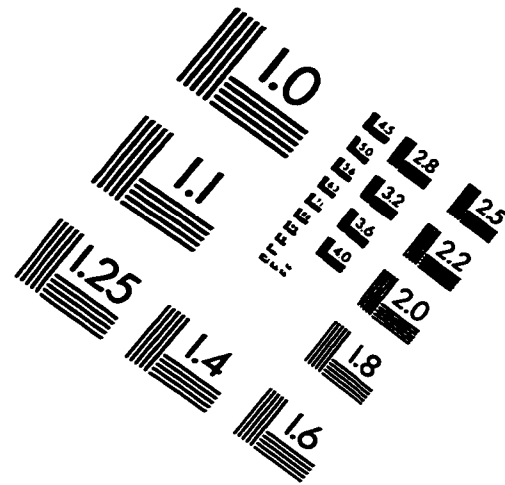
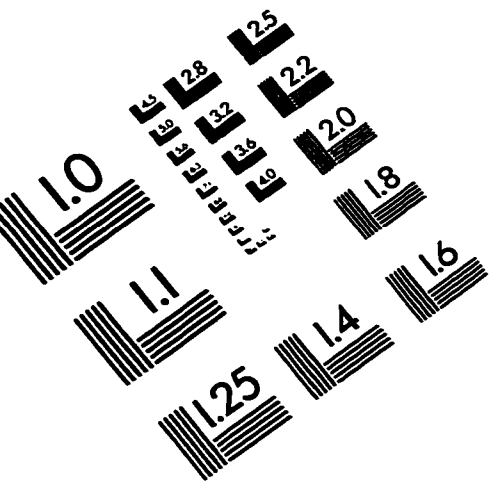
- [114] A. Beretvas, M. Binkley, and W. Yao, *The Effect of the Z Vertex on Top Events*, CDF Internal Note 3636 (unpublished).
- [115] O.R. Long, *A Proper Time Dependent Measurement of Δm_d using Jet Charge and Soft Lepton Flavor Tagging*, The University of Pennsylvania, Ph.D. Thesis (1997).
- [116] The B-tag Group, W. Yao, et al., *Top Search in Lepton + Jets with SECVTX*, CDF Internal Note 2989 (unpublished).
- [117] The B-tag Group, W. Yao, et al., *A Seed-Vertexing b-Tag Algorithm for Top*, CDF Internal Note 2716 (unpublished).
- [118] T. Liss and R. Roser, *$t\bar{t}$ Production Cross Section for 110 pb^{-1}* , CDF Internal Note 3481 (unpublished).
- [119] D. Glenzinski, *$t\bar{t}$ Acceptance Calculation for the Run 1B SVX B-tag Analysis*, CDF Internal Note 3403 (unpublished).
- [120] R. Hughes et. al., *Acceptance for the Top Search using the JETVTX B-tagging Algorithm*, CDF Internal Note 2249 (unpublished).
- [121] T. Liss, R. Roser and A. Martin, *Muon Trigger Simulation changes, and the $W \rightarrow \mu\nu$ Cross Section*, CDF Internal Note 3931 (unpublished).
- [122] T. Liss, private communication.
- [123] G. Unal, *Tracking Efficiency and SVX scale factor*, CDF Internal Note 3563 (unpublished).
- [124] C. Miao and W. Yao, *SECVTX Tagging study with Track-finding Degradation*, CDF Internal Note 3542 (unpublished).

- [125] G. Apollinari *et al.*, *Measurement of the Data to Simulation Scale Factor for the Tagging Efficiency of SECVTX and JPB*, CDF Internal Note 4257 (unpublished).
- [126] R. Hughes and R. Roser, *SVX Resolution and B-Tagging Efficiency in Top Events*, CDF Internal Note 4314 (unpublished).
- [127] S. Kuhlmann, *The 10% Solution*, CDF Internal Note 2506 (unpublished).
- [128] G. Unal, *Background Summary for the Top SVX Analysis*, CDF Internal Note 3513 (unpublished).
- [129] The SVX *b*-Tag Working Group, Y. Cen *et al.*, *Backgrounds for the SVX b-Tag Top Search: Run 1A+1B*, CDF Internal Note 2965 (unpublished).
- [130] G. Unal, *$Wb\bar{b}$ and $Wc\bar{c}$ Backgrounds in Top SVX Channel*, CDF Internal Note 3389 (unpublished).
- [131] B. Bevensee, H.H. Williams and M. Mangano, *A Search for the Charged Higgs Boson using the Top Data*, CDF Internal Note 4295 (unpublished).
- [132] M. Kruse and J. Konigsberg, *Top Dilepton Analysis, Updated for 110 pb^{-1}* , CDF Internal Note 3482 (unpublished).
- [133] J. Konigsberg *et al.*, *Top Dilepton Analysis - June 1995 Update*, CDF Internal Note 3203 (unpublished).
- [134] M. Kruse, *Misreconstructed Z's as a Background in the Top Dilepton Channel*, CDF Internal Note 4148 (unpublished).
- [135] T. Sjöstrand, *High-Energy Physics Event Generation with Pythia 5.7 and Jetset 7.4*, Comput. Phys. Commun. **82**, 74 (1994).

- [136] *The Review of Particle Properties*, Phys. Rev. D **50**, (1994). See the section on 3-body decays in the “Kinematics” chapter.
- [137] D.P. Roy, private communication.
- [138] D.P. Roy and J. Wudka, private communication. See Ref. [39] .
- [139] T. Sjöstrand, private communication.
- [140] M. Mangano, private communication.
- [141] T. Sjöstrand, <http://www.thep.lu.se/tf2/staff/torbjorn/Pythia.html>.
- [142] G. Unal, *Combining Significances of Counting Experiments*, CDF Internal Note 3031 (unpublished).
- [143] G.P. Wadsworth and J.G. Bryan, *Introduction to the Probability and Random Variables*, (New York: McGraw-Hill Book Co., Inc., 1960).
- [144] DØ Collaboration, B. Abbott *et al.*, *Search for Charged Higgs Bosons in the Decay of Top Quark Pairs*, Submitted to Phys. Rev. Lett. (1999). Preprint hep-ex/9902028.
- [145] CDF II Collaboration, R. Blair *et al.*, *The CDF II Detector Technical Design Report*, Preprint FERMILAB-PUB-96/390-E (1996).
- [146] B. Bevensee and H.H. Williams, *A Direct Search for the Hadronic Decay of a Charged Higgs Boson*, CDF Internal Note 3984 (unpublished).
- [147] M. Drees and K. Hikasa, *Note on QCD Corrections to Hadronic Higgs Decay*, Phys. Lett. B **240**, 455 (1990).
- [148] K.S. Krane, *Introductory Nuclear Physics*, (New York: John Wiley and Sons, Inc., 1988).

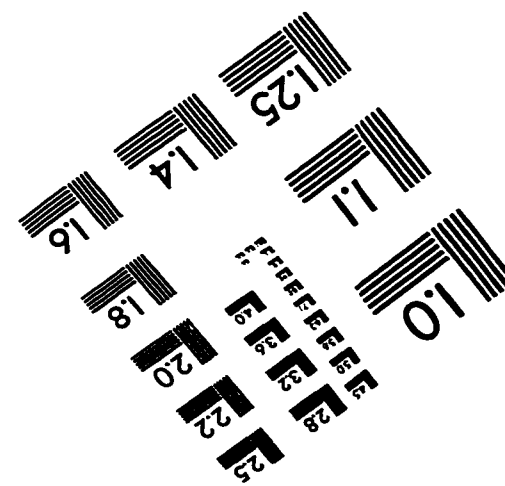
- [149] J. Thompson, *Introduction to Colliding Beams at Fermilab*, Preprint FERMILAB-TM-1909 (1994).
- [150] http://www-bd.fnal.gov/operations/rookie_books/concepts/conceptstoc.html.
- [151] http://www-bd.fnal.gov/operations/rookie_books/pbar_book/contents.html.
- [152] D. Griffiths, *Introduction to Elementary Particles*, (New York: John Wiley and Sons, Inc., 1987).
- [153] P. Langacker, course homework solutions (unpublished).

IMAGE EVALUATION TEST TARGET (QA-3)



APPLIED IMAGE, Inc
1653 East Main Street
Rochester, NY 14609 USA
Phone: 716/482-0300
Fax: 716/288-5989

© 1993, Applied Image, Inc., All Rights Reserved





2017 ProQuest Distribution Agreement

This Agreement is between the author (Author) and ProQuest LLC, through its ProQuest Dissertation Distribution business (formerly ProQuest/UMI). Under this Agreement, Author grants ProQuest certain rights to preserve, archive and distribute the dissertation or thesis (the Work), abstract, and index terms provided by Author to ProQuest.

Section I. License for Inclusion of the Work in ProQuest Publishing Program

Grant of Rights. Author hereby grants to ProQuest the **non-exclusive**, worldwide right to reproduce, distribute, display and transmit the Work (in whole or in part) in such tangible and electronic formats as may be in existence now or developed in the future. Author further grants to ProQuest the right to include the abstract, bibliography and other metadata in the ProQuest Dissertations & Theses database (PQDT) and in ProQuest Dissertation Abstracts International and any successor or related index and/or finding products or services.

ProQuest Publishing Program - Election and Elements. The rights granted above shall be exercised according to the publishing option selected by Author in Section III, Author Options, and subject to the following additional Publishing Program requirements:

- **Distribution of the Work.** Except as restricted by Author in the publishing option selected, the rights granted by Author automatically include (1) the right to allow sale and distribution of the Work, in whole or in part, by ProQuest and its sales agents and distributors and (2) the right to make the Abstract, bibliographic data and any meta data associated with the Work available to search engines and harvesters.
- **Restrictions.** ProQuest will use commercially reasonable efforts to restrict the distribution of the Work as provided under the publishing option selected by Author or *as later elected by Author* through direct contact with ProQuest. Such election is subject to Author's Degree Granting Institution Directives. With respect to restrictions requested after submission of the Work, Author acknowledges that ProQuest cannot recall or amend previously distributed versions of the Work.
- **Removal of Work from the Program.** ProQuest may elect not to distribute the Work if it believes that all necessary rights of third parties have not been secured. Refer to the website http://www.proquest.com/products_umi/dissertations/ for information about copyright and your dissertation or thesis. If Author's degree is rescinded, and/or the degree-granting institution so directs, ProQuest will expunge the Work from its publishing program in accordance with its then current publishing policies.
- **Degree Granting Institution Directives.** Author is solely responsible for any conflict between policies and directions of Author's degree-granting institution, Author's choice of publishing model, and/or any restriction Author places on the use of the Work. For the avoidance of doubt, ProQuest is not responsible for access to the Work that is provided by Author's degree-granting institution through its library or institutional repository. Author must work directly with Author's degree granting institution to ensure application of any restrictions to access relating to the Work by Author's degree granting institution.

Delivery of the Work. Author shall provide to ProQuest the Work and all necessary supporting documents during the online submission process, according to the Instructions accompanying this agreement.

Rights Verification. Author represents and warrants that Author is the copyright holder of the Work and has obtained all necessary rights to permit ProQuest to reproduce and distribute third party materials contained in any part of the Work, including all necessary licenses for any non-public, third party software necessary to access, display, and run or print the Work. Author is solely responsible and will indemnify ProQuest for any third party claims related to the Work as submitted for publication.

Open Access Publishing Plus

- ✓ I want the broadest possible dissemination of my work, and I want to provide free global access to the electronic copy of my work via the internet.
- ✓ I understand that I will not be eligible to receive royalties.

I want major search engines (e.g. Google, Yahoo) to discover my work. Learn more: <http://www.proquest.com/en-US/products/dissertations/google.shtml>

- ✓ Yes
- ☐ No

Acknowledgment: I have read, understand and agree to this ProQuest Publishing Agreement, including all rights and restrictions included within the publishing option chosen by me as indicated above.

REQUIRED Author's signature  Date 9 August 2017

(Print Name) Brendan Bevensee

Institution conferring degree University of Pennsylvania

This page must accompany your manuscript and the rest of the submission materials

Please check type of manuscript:

Dissertation/Master's Thesis Submission Form

Please print clearly in block letters

☐ M (Master's Thesis)

☒ D (Dissertation)

Personal Information

Last Name Bevensee

First Name Brendan

Middle Name or Initial

Elwood

Country (ies) of Citizenship

Degree & Dissertation Information

Title of Dissertation/ Thesis A Search for Top Quark Decays to a Charged Higgs Boson in Proton-Antiproton Collisions at a Center-of-Mass Energy of 1.8 TeV

Institution conferring degree University of Pennsylvania

Degree awarded (abbreviate; e.g., Ph.D.) PhD

College, School, or Division College of Arts and Sciences

Year degree awarded 1999

Department or Program Department of Physics and Astronomy

Year manuscript completed 1999

Advisor/Committee Chair Professor H.H. Williams

Committee Member Nigel Lockyer

Committee Member

Joe Kroll

Committee Member Larry Gladney

Committee Member

Committee Member

Committee Member

Language of manuscript English

Primary Subject Category: Enter the 4-digit code and category name from the Subject Category Guide that most closely describes the area of your research.

Code 0605

Category Physics

You may suggest two additional subject categories that may aid in the discovery of your work in our digital database.

Code _____

Category _____

Code _____

Category _____

Provide up to 6 keywords or short phrases for citation indices, library cataloging, and database searching.

Top Quark

Charged Higgs

Higgs Boson

Current Contact Information

Current Email Address

Street Address

Please provide your postal address if you are interested in receiving royalties on sales of your thesis.

Permanent Contact Information

City	San Jose	Province	CA	Future Phone	██████████
Country	USA	Postal Code	95128	Alternate Future Phone	1-800-Call-Earth

THIS PAGE MUST ACCOMPANY YOUR MANUSCRIPT AND THE REST OF YOUR SUBMISSION MATERIALS

The ProQuest Dissertations & Theses (PQDT) database and the ProQuest citation indices are arranged by subject categories. Please select the one category below that best describes your field of research or creative work. You may add one or two additional categories on your submission form that will also be associated with your work as secondary subjects.

Arts, Business, Education, Humanities, and Social Sciences

African American studies	0296
African studies	0293
American studies	0323
Asian American studies	0343
Asian studies	0342
Baltic studies	0361
Black studies	0325
Canadian studies	0385
Caribbean studies	0432
Classical studies	0434
East European studies	0437
Ethnic studies	0631
European studies	0440
French Canadian culture	0482
Gender studies	0733
GLBT studies	0492
Hispanic American studies	0737
Holocaust studies	0507
Islamic culture	0512
Judaic studies	0751
Latin American studies	0550
Middle Eastern studies	0555
Native American studies	0740
Near Eastern studies	0559
North African studies	0560
Pacific Rim studies	0561
Regional studies	0604
Scandinavian studies	0613
Slavic studies	0614
South African studies	0654
South Asian studies	0638
Sub Saharan Africa studies	0639
Women's studies	0453

Accounting	0272
Arts management	0424
Banking	0770
Business	0310
Entrepreneurship	0429
Finance	0508
Management	0454
Marketing	0338
Sports management	0430

Communication	0459
Information science	0723
Journalism	0391
Library science	0399
Mass communication	0708
Technical communication	0643
Web studies	0646

Art criticism	0365
Art history	0377
Cinematography	0435
Dance	0378
Design	0389
Film studies	0900
Fine arts	0357
Music	0413
Performing arts	0641
Theater	0465
Theater history	0644

Adult education	0516
Art education	0273
Bilingual education	0282
Business education	0688
Community college education	0275
Continuing education	0651
Curriculum development	0727
Early childhood education	0518
Education	0515
Education finance	0277
Education policy	0458
Educational administration	0514
Educational evaluation	0443
Educational leadership	0449
Educational psychology	0525
Educational technology	0710
Educational tests & measurements	0288
Elementary education	0524
English as a second language	0441
Foreign language instruction	0444
Gifted education	0445
Health education	0680
Higher education	0745
Higher education administration	0446
History of education	0520
Home economics education	0278
Industrial arts education	0521
Instructional design	0447
Language arts	0279
Mathematics education	0280
Middle school education	0450
Multicultural education	0455
Music education	0522
Pedagogy	0456
Performing arts education	0457
Philosophy of education	0998
Physical education	0523
Reading instruction	0535
Religious education	0527

School counseling	0519
Science education	0714
Secondary education	0533
Social sciences education	0534
Sociology of education	0340
Special education	0529
Teacher education	0530
Vocational education	0747

HUMANITIES

HISTORY

African history	0331
American history	0337
Ancient history	0579
Asian history	0332
Black history	0328
Canadian history	0334
European history	0335
History	0578
History of Oceania	0504
History of science	0585
Latin American history	0336
Medieval history	0581
Middle Eastern history	0333
Military history	0772
Modern history	0582
Russian history	0724
World history	0506

LANGUAGE & LITERATURE

African literature	0316
American literature	0591
Ancient languages	0289
Asian literature	0305
British and Irish literature	0593
Canadian literature	0352
Caribbean literature	0360
Classical literature	0294
Comparative literature	0295
English literature	0593
French Canadian literature	0355
Germanic literature	0311
Icelandic & Scandinavian literature	0362
Language	0679
Latin American literature	0312
Linguistics	0290
Literature	0401
Literature of Oceania	0356
Medieval literature	0297
Middle Eastern literature	0315
Modern language	0291
Modern literature	0298
Rhetoric	0681
Romance literature	0313
Slavic literature	0314

PHILOSOPHY AND RELIGION

Aesthetics	0650
Biblical studies	0321
Canon law	0375
Clerical studies	0319
Comparative religion	0618
Divinity	0376
Epistemology	0393
Ethics	0394
Logic	0395
Metaphysics	0396
Pastoral counseling	0397
Philosophy	0422
Philosophy of Religion	0322
Philosophy of science	0402
Religion	0318
Religious history	0320
Spirituality	0647
Theology	0469

LAW AND LEGAL STUDIES

Alternative dispute resolution	0649
Intellectual property	0513
International law	0616
Law	0398
Patent law	0562

SOCIAL SCIENCES

Archaeology	0324
Area planning and development	0341
Criminology	0627
Cultural anthropology	0326
Demography	0938
Economic history	0509
Economic theory	0511
Economics	0501
Economics, Commerce-Business	0505
Economics, Labor	0510
Folklore	0358
Forensic anthropology	0339
Geography	0366
Individual & family studies	0628
International relations	0601
Labor relations	0629
Military studies	0750
Organization theory	0635
Organizational behavior	0703
Peace studies	0563
Physical anthropology	0327
Political Science	0615
Public administration	0617
Public policy	0630
Recreation and tourism	0814
Social research	0344
Social structure	0700
Social work	0452
Sociolinguistics	0636
Sociology	0626
Transportation planning	0709
Urban planning	0999

INTERDISCIPLINARY

Alternative energy	0363
Biographies	0304
Climate change	0404

Cultural resources management	0436
Energy	0791
Food science	0359
Home economics	0386
Information technology	0489
Multimedia	0558

Museum studies	0730
Sustainability	0640
Textile research	0994
Wood sciences	0746

Behavioral, Natural, and Physical Sciences

AGRICULTURE

Agriculture	0473
Agronomy	0285
Animal diseases	0476
Animal sciences	0475
Fisheries and aquatic sciences	0792
Forestry	0478
Horticulture	0471
Plant pathology	0480
Plant sciences	0479
Range management	0777
Soil sciences	0481
Urban forestry	0281
Wildlife management	0286

ARCHITECTURE

Architecture	0729
Architectural engineering	0462
Landscape architecture	0390

BEHAVIORAL SCIENCES

Animal behavior	0602
Behavioral sciences	0384
Clinical psychology	0622
Cognitive psychology	0633
Counseling psychology	0603
Developmental psychology	0620
Experimental psychology	0623
Occupational psychology	0624
Personality psychology	0625
Physiological psychology	0989
Psychobiology	0349
Psychology	0621
Quantitative psychology and psychometrics	0632
Social psychology	0451

BIOLOGICAL SCIENCES

Biochemistry	0487
Bioinformatics	0715
Biology	0306
Biomechanics	0648
Biophysics	0786
Biostatistics	0308
Cellular biology	0379
Developmental biology	0758
Endocrinology	0409
Entomology	0353
Evolution & development	0412
Genetics	0369
Histology	0414
Limnology	0793
Microbiology	0410
Molecular biology	0307
Morphology	0287
Neurosciences	0317
Parasitology	0718

Physiology	0719
Plant biology	0309
Systematic biology	0423
Virology	0720
Zoology	0472

ECOSYSTEM SCIENCES

Ecology	0329
Macroecology	0420
Paleoecology	0426

ENGINEERING

Aerospace engineering	0538
Artificial intelligence	0800
Automotive engineering	0540
Biomedical engineering	0541
Chemical engineering	0542
Civil engineering	0543
Computer engineering	0464
Computer science	0984
Electrical engineering	0544
Engineering	0537
Geological engineering	0466
Geophysical engineering	0467
Geotechnology	0428
Industrial engineering	0546
Mechanical engineering	0548
Mining engineering	0551
Naval engineering	0468
Nanotechnology	0652
Nuclear engineering	0552
Ocean engineering	0547
Operations research	0796
Packaging	0549
Petroleum engineering	0765
Plastics	0795
Robotics	0771
System science	0790

ENVIRONMENTAL SCIENCES

Conservation biology	0408
Environmental economics	0438
Environmental education	0442
Environmental engineering	0775
Environmental geology	0407
Environmental health	0470
Environmental justice	0619
Environmental law	0439
Environmental management	0474
Environmental philosophy	0392
Environmental science	0768
Environmental studies	0477
Land use planning	0536
Natural resource management	0528
Water resources management	0595
Wildlife conservation	0284

GEOSCIENCES

Aeronomy	0367
Atmospheric chemistry	0371
Atmospheric sciences	0725
Biogeochemistry	0425
Biological oceanography	0416
Chemical oceanography	0403
Continental dynamics	0406
Geobiology	0483
Geochemistry	0996
Geographic information science and geodesy	0370
Geology	0372
Geomorphology	0484
Geophysics	0373
Hydrologic sciences	0388
Marine geology	0556
Meteorology	0557
Mineralogy	0411
Paleoclimate science	0653
Paleontology	0418
Petroleum geology	0583

**MATHEMATICAL AND
PHYSICAL SCIENCES**

Acoustics	0986
Analytical chemistry	0486
Applied mathematics	0364
Astronomy	0606
Astrophysics	0596
Atomic physics	0748
Chemistry	0485
Condensed matter physics	0611
Electromagnetics	0607
High temperature physics	0597
Inorganic chemistry	0488
Low temperature physics	0598
Materials science	0794
Mathematics	0405
Mechanics	0346
Molecular chemistry	0431
Molecular physics	0609
Nanoscience	0565
Nuclear chemistry	0738
Nuclear physics	0756
Optics	0752
Organic chemistry	0490
Particle physics	0798
Physical chemistry	0494
Physics	0605
Plasma physics	0759
Polymer chemistry	0495
Quantum physics	0599
Statistics	0463
Theoretical mathematics	0642
Theoretical physics	0753

Petrology	0584
Physical geography	0368
Physical oceanography	0415
Planetology	0590
Plate tectonics	0592
Remote sensing	0799
Sedimentary geology	0594

**HEALTH AND MEDICAL
SCIENCES**

Aging	0493
Alternative medicine	0496
Audiology	0300
Dentistry	0567
Epidemiology	0766
Gerontology	0351
Health care management	0769
Health sciences	0566
Immunology	0982
Kinesiology	0575
Medical ethics	0497
Medical imaging and radiology	0574

Medicine	0564
Mental health	0347
Nursing	0569
Nutrition	0570
Obstetrics and gynecology	0380
Occupational health	0354
Occupational therapy	0498
Oncology	0992
Ophthalmology	0381
Osteopathic medicine	0499
Pathology	0571
Pharmaceutical sciences	0572
Pharmacology	0419
Physical therapy	0382
Public health	0573
Public health occupations education	0500
Speech therapy	0460
Surgery	0576
Toxicology	0383
Veterinary medicine	0778